REMOTE SENSING FOR AQUACULTURE

EDITED BY: Pierre Gernez, Stephanie C. J. Palmer, Yoann Thomas and Rodney Forster

PUBLISHED IN: Frontiers in Marine Science

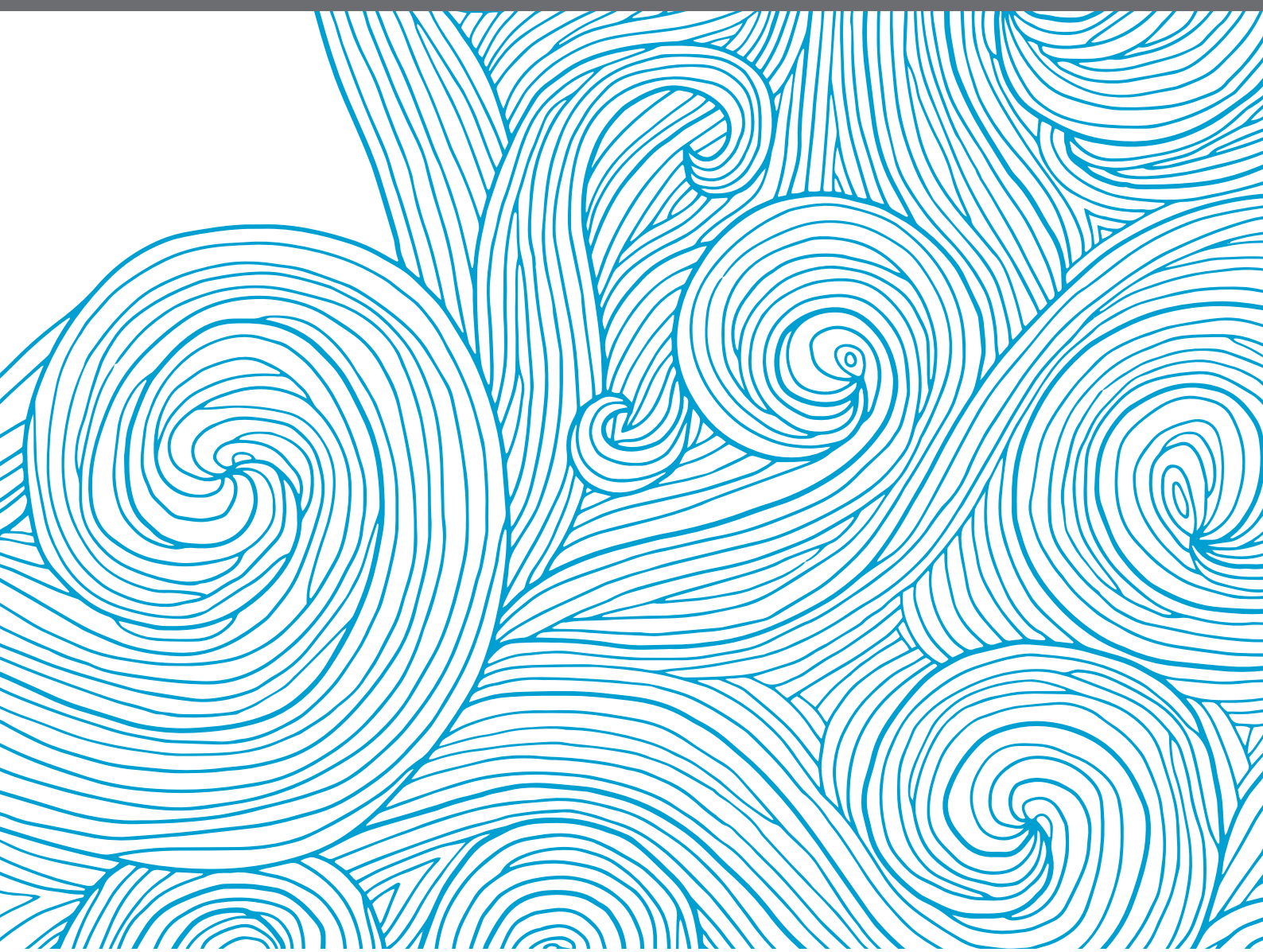

frontiers Research Topics

ISSN 1664-8714
ISBN 978-2-88966-562-4
DOI 10.3389/978-2-88966-562-4

About Frontiers

Frontiers is more than just an open-access publisher of scholarly articles: it is a pioneering approach to the world of academia, radically improving the way scholarly research is managed. The grand vision of Frontiers is a world where all people have an equal opportunity to seek, share and generate knowledge. Frontiers provides immediate and permanent online open access to all its publications, but this alone is not enough to realize our grand goals.

Frontiers Journal Series

The Frontiers Journal Series is a multi-tier and interdisciplinary set of open-access, online journals, promising a paradigm shift from the current review, selection and dissemination processes in academic publishing. All Frontiers journals are driven by researchers for researchers; therefore, they constitute a service to the scholarly community. At the same time, the Frontiers Journal Series operates on a revolutionary invention, the tiered publishing system, initially addressing specific communities of scholars, and gradually climbing up to broader public understanding, thus serving the interests of the lay society, too.

Dedication to Quality

Each Frontiers article is a landmark of the highest quality, thanks to genuinely collaborative interactions between authors and review editors, who include some of the world's best academicians. Research must be certified by peers before entering a stream of knowledge that may eventually reach the public - and shape society; therefore, Frontiers only applies the most rigorous and unbiased reviews.
Frontiers revolutionizes research publishing by freely delivering the most outstanding research, evaluated with no bias from both the academic and social point of view. By applying the most advanced information technologies, Frontiers is catapulting scholarly publishing into a new generation.

What are Frontiers Research Topics?

Frontiers Research Topics are very popular trademarks of the Frontiers Journals Series: they are collections of at least ten articles, all centered on a particular subject. With their unique mix of varied contributions from Original Research to Review Articles, Frontiers Research Topics unify the most influential researchers, the latest key findings and historical advances in a hot research area! Find out more on how to host your own Frontiers Research Topic or contribute to one as an author by contacting the Frontiers Editorial Office: frontiersin.org/about/contact

REMOTE SENSING FOR AQUACULTURE

Topic Editors:
Pierre Gernez, Université de Nantes, France
Stephanie C. J. Palmer, Université de Nantes, France
Yoann Thomas, Institut de Recherche Pour le Développement (IRD), France
Rodney Forster, University of Hull, United Kingdom

Citation: Gernez, P., Palmer, S. C. J., Thomas, Y., Forster, R., eds. (2021). Remote Sensing for Aquaculture. Lausanne: Frontiers Media SA.
doi: 10.3389/978-2-88966-562-4

Table of Contents

frontiers in Marine Science

EDITORIAL
published: 22 January 2021
doi: 10.3389/fmars.2020.638156

Editorial: Remote Sensing for Aquaculture

Pierre Gernez[1]*, *Stephanie C. J. Palmer*[1], *Yoann Thomas*[2] and *Rodney Forster*[3]

[1] University of Nantes, Mer Molécules Santé, Nantes, France, [2] IRD, University of Brest, CNRS, Ifremer, LEMAR, Plouzané, France, [3] Hull Marine Laboratory, Department of Biological and Marine Sciences, University of Hull, Hull, United Kingdom

Keywords: earth observation, site selection, HAB risk assessment, production monitoring, ecological modeling, kelp, fish, shellfish

Editorial on the Research Topic

Remote Sensing for Aquaculture

While the sustainability of aquaculture is crucial for global food security, aquaculture development faces major threats and challenges, such as the increasing competition for land, water, and energy resources, as well as vulnerability to global warming, sea level rise, water pollution, increased occurrence of extreme events, harmful algal blooms (HABs), and disease outbreaks (Froehlich et al., 2018; Soto et al., 2019). Compared to land-based aquaculture where suitable areas are limited by space constraints, there is immense potential for the expansion of aquaculture in the coastal and open oceans (Gentry et al., 2017). The intensification of marine aquaculture, if not managed properly, could, however, lead to serious environmental impacts and socio-economic conflicts, and there is a clear need for ecosystem-based approaches to aquaculture planning in the marine realm (Lester et al., 2018).

In the ocean, most aquaculture species, equipment, and operations are sensitive to the variability of environmental parameters, such as sea surface temperature (SST), currents, wave height, underwater irradiance, and/or water quality in terms of suspended particulate matter (SPM) and phytoplankton. All of these parameters are highly variable over time and space, adding to the complexity of planning and management. Due to its ability to map essential variables at multiple scales and resolutions, Earth Observation (EO) can help to comprehensively optimize aquaculture location and type in both the nearshore and offshore oceans (Meaden and Aguilar-Manjarrez, 2013). Spatially-explicit time-series of remotely-sensed parameters have been used for site selection of fish (IOCCG, 2009), shellfish (Saitoh et al., 2011; Thomas et al., 2011; Gernez et al., 2014; Snyder et al., 2017), and kelp aquaculture (Radiarta et al., 2010). Remote sensing can also contribute to aquaculture planning, with the integration of EO into Geographic Information Systems (GIS) (Falconer et al., 2020) and spatial multi-criteria evaluation (SMCE) methodologies to resolve complex environmental and socioeconomic constraints (Kapetsky and Aguilar-Manjarrez, 2007; Radiarta et al., 2008; Brigolin et al., 2017; Barillé et al., 2020). Besides site-selection and planning, aquaculture could also benefit from EO for water quality monitoring (Gernez et al., 2017; Soriano-González et al., 2019), notably in the case of HAB detection (Gokul et al., 2020; Rodríguez-Benito et al., 2020; Torres Palenzuela et al., 2020), assessment of fish farming environmental impact (Bengil and Bizel, 2014), and modeling of species invasion associated with aquaculture (Thomas et al., 2016).

The objectives of this Research Topic were to assess the use of advanced EO products over a variety of scales and resolutions, and to document the latest developments in coupling EO with biological and ecological models applied to a variety of aquaculture contexts. All articles focused on offshore marine aquaculture, with the exception of one article dedicated to nearshore intertidal waters. All types of mariculture were investigated: fish, shellfish, and macroalgae aquaculture.

OPEN ACCESS

Edited and reviewed by:
Griet Neukermans, Ghent University, Belgium

***Correspondence:**
Pierre Gernez
pierre.gernez@univ-nantes.fr

Specialty section:
This article was submitted to Ocean Observation, a section of the journal Frontiers in Marine Science

Received: *05 December 2020*
Accepted: *30 December 2020*
Published: *22 January 2021*

Citation:
Gernez P, Palmer SCJ, Thomas Y and Forster R (2021) Editorial: Remote Sensing for Aquaculture. Front. Mar. Sci. 7:638156. doi: 10.3389/fmars.2020.638156

Although most articles were based on satellite remote sensing, the use of unmanned aerial vehicle (UAV) was also tackled, and a large range of spatial scales considered. Overall, the articles concerned three types of study: site selection, risk to aquaculture (HABs), and production monitoring.

The use of EO for site suitability and selection was addressed in four articles. In Porporato et al., EO-derived SST data was coupled with an ecophysiological model based on a dynamic energy budget (DEB) and incorporated into a SMCE framework to optimize the design of allocated aquaculture zones for fish farming (European seabass and gilthead seabream) in the Italian offshore waters. In Palmer et al., EO-derived SST, Chlorophyll and SPM concentration were also coupled with DEB modeling for Pacific oyster aquaculture site selection in a French macrotidal bay, demonstrating the potential of strategically selected offshore sites compared to the traditionally-farmed, albeit less productive, intertidal zone. In Jossart et al., statistical spatial autocorrelation techniques were incorporated into the planning framework, improving upon conventional site selection approaches. Two approaches were demonstrated for northeastern US case studies; one assessing the relative suitability for mussel farming, the other assessing patterns in modeled and remotely-sensed oceanographic data important to aquaculture. High-resolution SST imagery from Landsat-8 was used as a proxy for surface nitrate concentration by Snyder et al., in their study of offshore kelp farm optimal placement.

The Research Topic also documented some of the latest developments in HAB remote sensing using the new generation of Sentinel-3 satellites. In Smith and Bernard, an indicator to identify the bloom-dominant phytoplankton type was developed for aquaculture risk mitigation. Spectral features in the red and NIR were used to discriminate two types of HABs (high biomass dinoflagellate vs. *Pseudo-nitzschia* blooms) from other phytoplankton assemblages in South Africa. The red-edge spectral signature of various HAB types was also documented in Wolny et al., where promising algorithms to detect common marine and estuarine HAB species (*Alexandrium monilatum*, *Karlodinium veneficum*, *Margalefidinium polykrikoides*, and *Prorocentrum minimum*) were investigated in the Chesapeake Bay (US).

Finally, the performance of several remote-sensing platforms to monitor offshore kelp farming along the eastern Pacific coastline was compared in Bell et al.: satellite sensors, UAV-mounted optical sensors, underwater imagery and sonar scanning. Using field observations and deep learning, this study provided a valuable analysis of strength, weakness, opportunity, and threat for future developments in the monitoring of far-field kelp production.

In summary, this Research Topic compiled some of the latest remote sensing developments for aquaculture. While three types of studies were addressed (site selection, production monitoring, and HAB remote sensing), there is no doubt that EO could also benefit other aquaculture topics, notably environmental impact assessment. EO-based analyses of land cover changes associated with aquaculture (Proisy et al., 2018) could, for example, be translated to the seascape. Whatever the topic, future developments of innovative EO products (habitat mapping, phytoplankton groups, species identification, particulate organic carbon, or nitrogen content), as well as advances in data processing (process-based modeling approach, deep learning, and big data analysis) are expected to further improve aquaculture studies. Concurrent to such progress, the uptake of EO data by the aquaculture industry, environmental managers, and policy makers will certainly increase as higher temporal and spatial imagery become available, including very high-resolution observations and services from commercial providers.

AUTHOR CONTRIBUTIONS

PG, SP, YT, and RF organized this Research Topic and wrote the editorial. All authors contributed to the article and approved the submitted version.

FUNDING

This work has received funding from the European Union's Horizon 2020 research and innovation programme (Grant agreement No. 678396—Tools for Assessment and Planning of Aquaculture Sustainability, No. 776342—DataCube Services for Copernicus, and No. 776348—Commercial service platform for user-relevant coastal water monitoring services based on Earth observation).

REFERENCES

Barillé, L., Le Bris, A., Goulletquer, P., Thomas, Y., Glize, P., Kane, F., et al. (2020). Biological, socio-economic, and administrative opportunities and challenges to moving aquaculture offshore for small French oyster-farming companies. *Aquaculture* 521:735045. doi: 10.1016/j.aquaculture.2020.735045

Bengil, F., and Bizel, K. C. (2014). Assessing the impact of aquaculture farms using remote sensing: an empirical neural network algorithm for Ildiri Bay, Turkey. *Aquacult. Env. Interact.* 6, 67–79. doi: 10.3354/aei00115

Brigolin, D., Porporato, E. M. D., Prioli, G., and Pastres, R. (2017). Making space for shellfish farming along the Adriatic coast. *ICES J. Mar. Sci.* 74, 1540–1551. doi: 10.1093/icesjms/fsx018

Falconer, L., Middelboe, A. L., Kaas, H., Ross, L. G., and Telfer, T. C. (2020). Use of geographic information systems for aquaculture and recommendations for development of spatial tools. *Rev. Aquacult.* 12, 664–677. doi: 10.1111/raq.12345

Froehlich, H. E., Gentry, R. R., and Halpern, B. S. (2018). Global change in marine aquaculture production potential under climate change. *Nat. Ecol. Evol.* 2, 1745–1750. doi: 10.1038/s41559-018-0669-1

Gentry, R. R., Froehlich, H. E., Grimm, D., Kareiva, P., Parke, M., Rust, M., et al. (2017). Mapping the global potential for marine aquaculture. *Nat. Ecol. Evol.* 1, 1317–1324. doi: 10.1038/s41559-017-0257-9

Gernez, P., Barillé, L., Lerouxel, A., Mazeran, C., Lucas, A., and Doxaran, D. (2014). Remote sensing of suspended particulate matter in turbid oyster-farming ecosystems. *J. Geophys. Res. Oceans* 119, 7277–7294. doi: 10.1002/2014JC010055

Gernez, P., Doxaran, D., and Barillé, L. (2017). Shellfish aquaculture from space: potential of Sentinel2 to monitor tide-driven changes in turbidity, chlorophyll

concentration and oyster physiological response at the scale of an oyster farm. *Front. Mar. Sci.* 4:137. doi: 10.3389/fmars.2017.00137

Gokul, E. A., Raitsos, D. E., Gittings, J. A., and Hoteit, I. (2020). Developing an atlas of harmful algal blooms in the red sea: linkages to local aquaculture. *Remote Sens.* 12:3695. doi: 10.3390/rs12223695

IOCCG (2009). "Remote sensing in fisheries and aquaculture," in *Reports of the International Ocean-Colour Coordinating Group, No. 8*, eds M.-H. Forget, V. Stuart, and T. Platt (Dartmouth, NS: IOCCG).

Kapetsky, J. M., and Aguilar-Manjarrez, J. (2007). *Geographic Information Systems, Remote Sensing and Mapping for the Development and Management of Marine Aquaculture*. Rome: Food and Agriculture Organization, No. 458.

Lester, S. E., Stevens, J. M., Gentry, R. R., Kappel, C. V., Bell, T. W., Costello, C. J., et al. (2018). Marine spatial planning makes room for offshore aquaculture in crowded coastal waters. *Nat. Comm.* 9:945. doi: 10.1038/s41467-018-03249-1

Meaden, G. J., and Aguilar-Manjarrez, J. (Eds.) (2013). *Advances in Geographic Information Systems and Remote Sensing for Fisheries and Aquaculture*. Rome: FAO Fisheries and Aquaculture Technical Paper, No. 552.

Proisy, C., Viennois, G., Sidik, F., Andayani, A., Enright, J. A., Guitet, S., et al. (2018). Monitoring mangrove forests after aquaculture abandonment using time series of very high spatial resolution satellite images: a case study from the Perancak estuary, Bali, Indonesia. *Mar. Pollut. Bull.* 131, 61–71. doi: 10.1016/j.marpolbul.2017.05.056

Radiarta, I. N., Saitoh, S. I., and Miyazono, A. (2008). GIS-based multi-criteria evaluation models for identifying suitable sites for Japanese scallop (*Mizuhopecten yessoensis*) aquaculture in Funka Bay, southwestern Hokkaido Japan. *Aquaculture* 284, 127–135. doi: 10.1016/j.aquaculture.2008.07.048

Radiarta, I. N., Saitoh, S. I., and Yasui, H. (2010). Aquaculture site selection for Japanese kelp (*Laminaria japonica*) in southern Hokkaido, Japan, using satellite remote sensing and GIS-based models. *ICES J. Mar. Sci.* 68, 773–780. doi: 10.1093/icesjms/fsq163

Rodríguez-Benito, C. V., Navarro, G., and Caballero, I. (2020). Using Copernicus Sentinel-2 and Sentinel-3 data to monitor harmful algal blooms in Southern Chile during the COVID-19 lockdown. *Mar. Pollut. Bull.* 161:111722. doi: 10.1016/j.marpolbul.2020.111722

Saitoh, S. I., Mugo, R., Radiarta, I. N., Asaga, S., Takahashi, F., Hirawake, T., et al. (2011). Some operational uses of satellite remote sensing and marine GIS for sustainable fisheries and aquaculture. *ICES J. Mar. Sci.* 68, 687–695 doi: 10.1093/icesjms/fsq190

Snyder, J., Boss, E., Weatherbee, R., Thomas, A. C., Brady, D., and Newell, C. (2017). Oyster aquaculture site selection using Landsat 8-Derived Sea surface temperature, turbidity, and chlorophyll *a*. *Front. Mar. Sci.* 4:190. doi: 10.3389/fmars.2017.00190

Soriano-González, J., Angelats, E., Fernández-Tejedor, M., Diogene, J., and Alcaraz, C. (2019). First results of phytoplankton spatial dynamics in two NW-Mediterranean bays from chlorophyll-*a* estimates using Sentinel 2: potential implications for aquaculture. *Remote Sens.* 11:1756. doi: 10.3390/rs11151756

Soto, D., Ross, L. G., Handisyde, N., Bueno, P. B., Beveridge, M. C., Dabbadie, L., et al. (2019). *Climate Change and Aquaculture: Vulnerability and Adaptation Options*. Rome: Impacts of Climate Change on Fisheries and Aquaculture, FAO Fisheries and Aquaculture Technical Paper No. 627, 465–490.

Thomas, Y., Mazurié, J., Alunno-Bruscia, M., Bacher, C., Bouget, J. F., Gohin, F., et al. (2011). Modelling spatio-temporal variability of *Mytilus edulis* (L.) growth by forcing a dynamic energy budget model with satellite-derived environmental data. *J. Sea Res.* 66, 308–317. doi: 10.1016/j.seares.2011.04.015

Thomas, Y., Pouvreau, S., Alunno-Bruscia, M., Barillé, L., Gohin, F., Bryère, P., and Gernez, P. (2016). Global change and climate-driven invasion of the Pacific oyster (*Crassostrea gigas*) along European coasts: a bioenergetics modelling approach. *J. Biogeogr.* 43, 568–579. doi: 10.1111/jbi.12665

Torres Palenzuela, J. M., Vilas, L. G., Bellas Aláez, F. M., and Pazos, Y. (2020). Potential application of the new Sentinel satellites for monitoring of harmful algal blooms in the galician aquaculture. *Thalassas* 36, 85–93. doi: 10.1007/s41208-019-00180-0

Conflict of Interest: The authors declare that the research was conducted in the absence of any commercial or financial relationships that could be construed as a potential conflict of interest.

frontiers in Marine Science

ORIGINAL RESEARCH
published: 09 January 2020
doi: 10.3389/fmars.2019.00772

Site Suitability for Finfish Marine Aquaculture in the Central Mediterranean Sea

Erika M. D. Porporato[1], Roberto Pastres[1,2] and Daniele Brigolin[1,2,3]*

[1] Dipartimento di Scienze Ambientali, Informatica e Statistica, Università Ca' Foscari Venezia, Mestre, Italy, [2] Bluefarm S.r.l., Marghera, Italy, [3] Università Iuav di Venezia, Venice, Italy

Farm site selection plays a critical role in determining the productivity, environmental impact, and interactions of aquaculture activities with ecosystem services. Satellite Remote Sensing (SRS) provide spatially extensive datasets at high temporal and spatial resolution, which can be useful for aquaculture site selection. In this paper we mapped a finfish aquaculture Suitability Index (SI) applying the Spatial Multi-criteria Evaluation (SMCE) methodology. The robustness of the outcome of the SMCE was investigated using Uncertainty Analysis (UA), and in parallel we evaluate a set of alternative scenarios, aimed at minimizing the subjectivity associated with the decision process. The index is based on the outputs of eco-physiological models, which were forced using time series of sea surface temperature data, and on data concerning Significant Wave Height (SWH), distance to harbor, current sea uses, and cumulative impacts. The methodology was applied to map the suitability for farming of European seabass (*Dicentrarchus labrax*) and gilthead seabream (*Sparus aurata*) within the Italian Economic Exclusive Zone (EEZ), under three scenarios: Blue Growth, Economic and Environment. Tyrrhenian and Ionian coastal areas were found to be more suitable, compared to the Northern Adriatic and southern Sicilian ones. In the latter, and in the western Sardinia, the index is also affected by higher uncertainty. The application presented suggests that SRS data could play a significant role in designing the Allocated Zones for Aquaculture, assisting policy makers and regulators in including aquaculture within maritime spatial planning.

Keywords: aquaculture zoning, offshore aquaculture, spatial multi-criteria evaluation, maritime spatial planning, deterministic models, sea surface temperature, significant wave height, remote sensing

OPEN ACCESS

Edited by:
Stephanie C. J. Palmer, Université de Nantes, France

Reviewed by:
Lennon Thomas, University of California, Santa Barbara, United States
Seth Theuerkauf, The Nature Conservancy, United States

****Correspondence:***
Erika M. D. Porporato
erika.porporato@unive.it;
erika.porporato@gmail.com

Specialty section:
This article was submitted to Ocean Observation, a section of the journal Frontiers in Marine Science

Received: *26 July 2019*
Accepted: *28 November 2019*
Published: *09 January 2020*

Citation:
Porporato EMD, Pastres R and Brigolin D (2020) Site Suitability for Finfish Marine Aquaculture in the Central Mediterranean Sea. Front. Mar. Sci. 6:772. doi: 10.3389/fmars.2019.00772

INTRODUCTION

Human population growth and changes in eating habits are leading to a global increase in fish protein demand (Delgado et al., 2003; World Bank, 2013; FAO, 2018), generating an increased interest in sustainable aquaculture and fisheries to guarantee food security (e.g., Béné et al., 2015; Longo et al., 2019). The potential for the development of marine fish culture is high (Gentry et al., 2017) and could play an important role in reducing the fishing pressure on wild fish stocks (see for example Little et al., 2016), the majority of which are fully exploited or overexploited (Branch et al., 2011; Costello et al., 2016; FAO, 2018). The presence of an aquaculture farm can alter health and productivity of the surrounding marine ecosystem in diverse and complex ways (Black, 2001; McKindsey et al., 2006). The effects of farms on the environments include eutrophication, chemicals

and medicines release, modification of the benthic community (Ahmed and Thompson, 2019). Moreover, preserving water quality assures provisions of high-quality aquaculture products (Gentry et al., 2017; Clavelle et al., 2019). Therefore, the site selection process should take into account a set of criteria in order to avoid negative effects on the local environment. The identification of Allocated Zones for Aquaculture (AZAs – FAO, 2012), following the principles of the ecosystem approach (Soto et al., 2008), can boost the integration of this industry with other existing marine uses, allowing a better and profitable coordination among decision makers involved in licensing and monitoring processes (FAO and World Bank, 2015).

Aquaculture is strongly supported by the policies and initiatives of the European Union, i.e., the EU Blue Growth strategy (European Commission [EC], 2012) and the strategic guidelines for the sustainable development of EU aquaculture (European Commission [EC], 2013). Offshore aquaculture (i.e., aquaculture located in open water; Gentry et al., 2017), instead of coastal aquaculture, may help mitigating and avoiding some of the well-known local environmental impact of cage culture, due to the higher carrying and assimilative capacity of open water sites (Tacon and Metian, 2016; Gentry et al., 2017; Troell et al., 2017). However, to date, little is known about the spatial extent and potential expansion of this activity (Froehlich et al., 2017; Gentry et al., 2017). Scientists and policymakers have recommended Maritime Spatial Planning (MSP – EC Directive, 2014/89/EU) as an approach to harmonize multiple uses of the marine environment. In this context, current marine uses should be integrated together with the human impacts (da Luz Fernandes et al., 2017), to develop sustainable spatial management plans (Stelzenmüller et al., 2008; Halpern et al., 2009, 2015; Micheli et al., 2013; Kelly et al., 2014). The implementation of the MSP Directive can assume a critical role in the effective management of marine resources (Margules and Pressey, 2000; Pressey et al., 2007; Ban et al., 2010; da Luz Fernandes et al., 2017). In the MSP context, the marine space rationalization requires a multisectoral approach and the AZAs evaluation represent only one component.

At the operational level, the implementation of the site selection procedure can make use of valuable methodologies, such as the Spatial Multi-Criteria Evaluation (SMCE), being able to support the stakeholders in complex decisions procedure, through the combination of different criteria (Radiarta et al., 2008). In this framework, the increasing availability of Earth Observation data created opportunities for aquaculture suitability evaluation, farming management, and ecosystem studies (Saitoh et al., 2011; Gernez et al., 2014, 2017). Beginning in the 1980s, Satellite Remote Sensing (SRS) technologies represented a very effective means for providing data for aquaculture site selection at high temporal and spatial resolution (Kapetsky and Aguilar-Manjarrez, 2007). More recently, starting from 2017, the Copernicus Marine Environment Monitoring Service (CMEMS) EU initiative made available data from 5 new satellites (Sentinel-3, Jason-3, Saral Altika, Cryosat-2, and Jason-2N). The above-mentioned SRS data can be used as an input for dynamic models, simulating growth and physiology of farmed organisms, in order to determine the suitability for aquaculture activities through growth performance indicators, such as the organisms weight at harvest (Thomas et al., 2011), or the condition index (e.g., Filgueira et al., 2013). Together with consolidated environmental variables (i.e., sea surface temperature and Chlorophyll-*a* concentration data), Significant Wave Height (SWH) data are now accessible. These latter data can be useful for evaluating which areas have higher probability of being affected by storms.

The present study focuses on the estimation of a Suitability Index (SI) for new marine finfish aquaculture offshore activities, using SRS data and the SMCE methodology. The analysis was performed under three different scenarios of growth for the aquaculture industry. The robustness of the outcome of the SMCE was assessed based on an Uncertainty Analysis (UA), which was carried out by treating the weights in the SMCE as stochastic variables.

Spatial multi-criteria evaluation was applied for mapping suitability indices for seabass and seabream over the whole Italian Economic Exclusive Zone (EEZ). The methodology, previously applied to shellfish farming (Brigolin et al., 2017), was tested for identifying AZA for seabass/seabream farming. In particular, specific objectives were: (i) evaluating the suitability for finfish aquaculture in areas subjected to multiple human impacts; (ii) estimate the uncertainty in the suitability indices. The following methodological section will present: (1) the study area in which the application was performed and the SRS data used; (2) details for SMCE application, including scenarios construction and UA; (3) the definition of criteria and constraints used in the analysis.

MATERIALS AND METHODS

Study Area and Data Description

The SMCE methodology was applied to the Italian EEZ, which covers different sub-basins of the Mediterranean Sea, namely Adriatic, Ionian and Tyrrhenian Seas (see **Figure 1**). In accordance with the definition of offshore aquaculture given by Gentry et al. (2017), areas deeper than 100 m and farther than 25 nm from the coast were excluded "*a priori*" from the analysis (**Figure 1**).

The two farmed species considered were European seabass (herein seabass) and gilthead seabream (herein seabream). These are among the most important species for the EU marine aquaculture, along with salmon, mussels and oysters, and in 2015 they together accounted, respectively, for 21% and 12% of the total production, in terms of value and volume (European Commission, 2018). Italy is the third European producer of these species, after Greece and Spain (8% and 7%, respectively; EUMOFA database[1]; last access 07/01/2019). In 2015–2016 Italy produced 6800 metric tonnes of seabass and 7400 tonnes of seabream: these productions are far from satisfying the internal demand, as the import amounted to 26500 tonnes of seabass and 26000 of seabream (EUMOFA, 2017, 2019).

[1]https://www.eumofa.eu

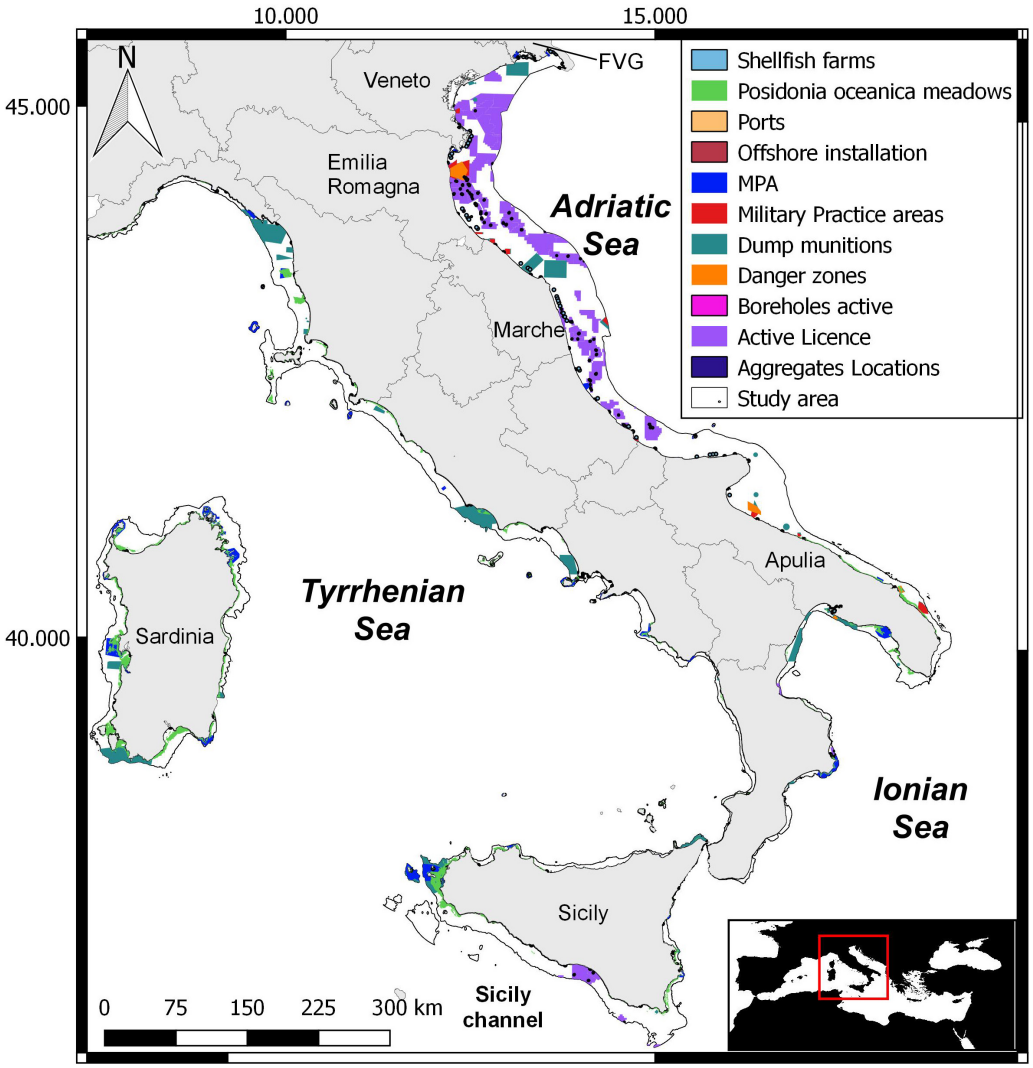

FIGURE 1 | Study area within the Italian EEZ and maps of anthropogenic and natural constraints: commercial harbor, shellfish farm, *Posidonia oceanica* meadows, Marine Protected Area (MPA), dredging, military practice area, danger zones, hydrocarbon extraction (active licenses), and dump munitions.

SRS data were obtained from the CMEMS data portal[2], selecting the Level 4 data (i.e., model output resulting from the statistical analysis of multiple measurements), cloud free and gridded continuously over time and space, from January 2016 until December 2017. Time series of SST daily data at 1 km^2 spatial resolution were selected. These data are based on the night-time images recorded by the infrared sensors of different satellites and, subsequently interpolated by means of the algorithm described by Buongiorno Nardelli et al. (2013). Sea surface SWH data are produced by the Hellenic Center for Marine Research (HCMR), also available through the CMEMS data portal. This dataset provides hourly data at a spatial resolution of ca. 4 km^2, and is based on satellite altimetry data, including wave products derived from Jason-3 and Sentinel-3A altimeters, assimilated within the CMEMS numerical real-time Mediterranean Waves Model (Med-waves), a coupled hydrodynamic-wave model implemented in the Mediterranean Sea, and based on the WAM Cycle 4.5.4 wave model.

SMCE, Scenarios Considered and Uncertainty Analysis

The finfish aquaculture suitability was assessed by applying the SMCE methodology (Malczewski, 2006), which is based on the analytic hierarchical process (Saaty, 1980). The present study considered 2 macro-criteria: Economic (EC) and Environmental (EN). As presented in **Figure 2**, aquaculture was assumed to develop under 3 scenarios, reflecting different social perceptions of this activity. These were defined by initially assigning the same weight to EC and EN (Blue Growth, EC 0.5/EN 0.5), and therefore decreasing by 50% each macro-criterion (Economic, EC 0.75/EN 0.25; Environmental, EC 0.25/EN 0.75). EC macro-criterion

[2]http://marine.copernicus.eu/

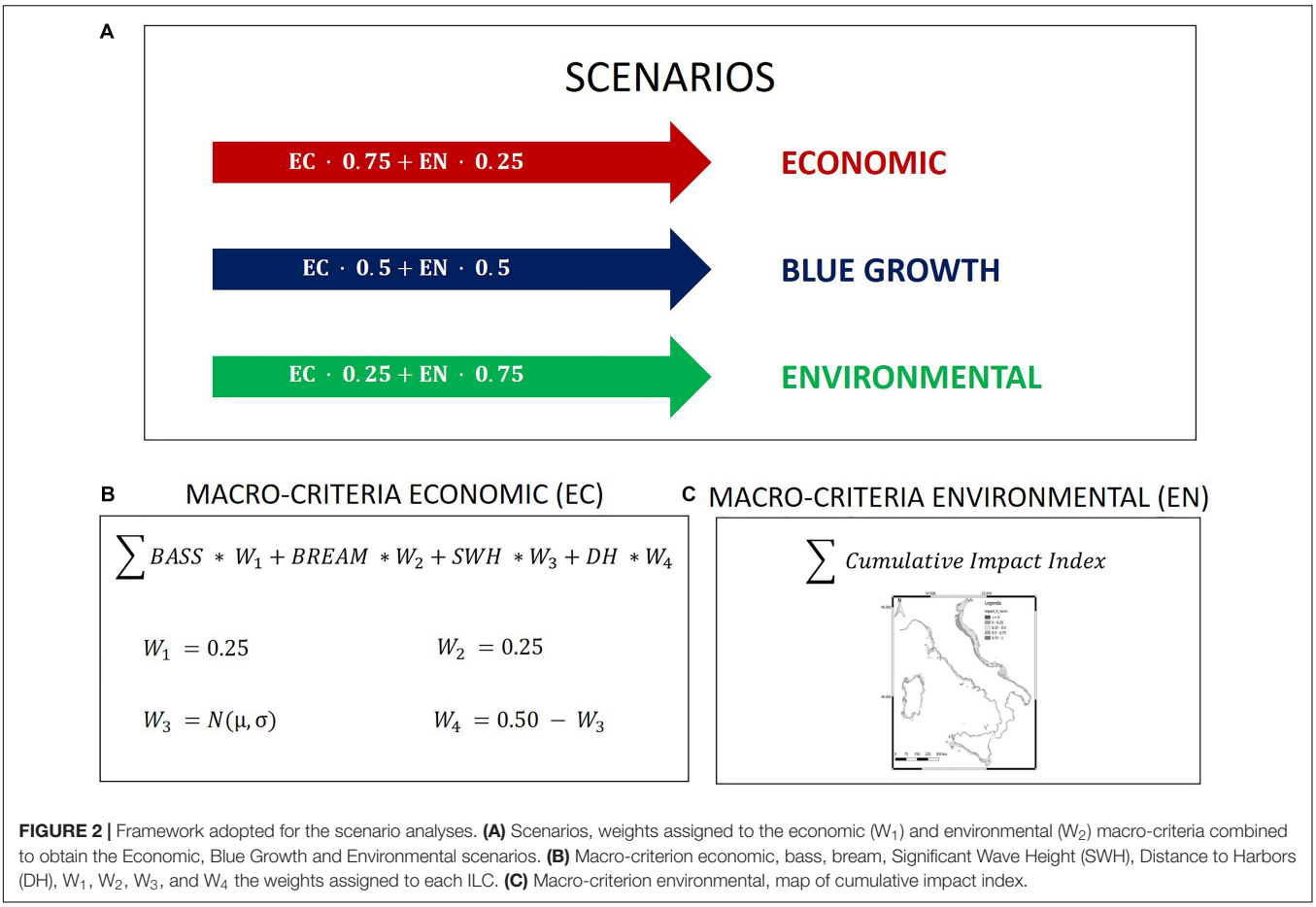

FIGURE 2 | Framework adopted for the scenario analyses. **(A)** Scenarios, weights assigned to the economic (W_1) and environmental (W_2) macro-criteria combined to obtain the Economic, Blue Growth and Environmental scenarios. **(B)** Macro-criterion economic, bass, bream, Significant Wave Height (SWH), Distance to Harbors (DH), W_1, W_2, W_3, and W_4 the weights assigned to each ILC. **(C)** Macro-criterion environmental, map of cumulative impact index.

included the following Intermediate Level Criteria [ILC – *sensu* Radiarta et al. (2008)]: (i) number of days required to reach the market size for seabass (BASS), (ii) number of days required to reach the market size for seabream (BREAM), (iii) distance of the farm facilities from harbors (DH), and (iv) SWH. EN was based on a single criterion, the multiple impact index estimated by Micheli et al. (2013). The raster used for site suitability, the data used for the analysis, the spatial resolution and data sources were reported in **Supplementary Material**.

In order to perform the SMCE analysis, criteria were normalized, weighted and combined linearly, thus obtaining a SI ranging from 0 to 1, where values close to 1 indicate the highest suitability. Each criterion was normalized by linearly re-scaling each value in the range 0–1, by subtracting the minimum value and dividing by the range of the raw data (Eastman, 1999). Finally, in order to rank the areas, SI was aggregated in 5 suitability classes: 0.0 – 0.2, not suitable; 0.2 – 0.4, low suitability; 0.4 – 0.6, medium suitability; 0.6 – 0.8, high suitability; 0.8 – 1.0, very high suitability. This partitioning was performed by choosing the same number of classes, namely 5, considered by current European directives (see e.g., WFD, European Community, 2000), and equally spacing SI among these.

The robustness of the outcome of the SMCE was therefore evaluated by means of an UA, which allows one to quantify the output variability with respect to a set of input factors, e.g., driving function, model parameters. The results of UA are very relevant in decision making, as they provide information about the confidence in model output (Gómez-Delgado and Tarantola, 2006): in this paper, we used UA for investigating how the weighting of criteria could affect the SI. This point could be very relevant in the implementation of the MSP Directive, which requires a participatory process, involving different stakeholders: weights could, therefore, be selected on the basis of the indications provided by expert panels. To this regard, it would be very relevant to understand in advance how the ranking provided by the index could change, as a consequence of different weighting. In order to demonstrate the use of this methodology, we focused on the EC macro-criterion. Two of the ILC weights, i.e., seabass and seabream days to harvest, were fixed in this analysis, respectively, $w_1 = 0.25$ and $w_2 = 0.25$, assuming that there is no "*a priori*" reason for preferring the farming of one species. In order to perform the UA, the weights w_3 and w_4 were treated as stochastic variables, normally distributed with mean $\mu = 0.25$ and standard deviation $\sigma = 0.05$. Their joint probability density function (pdf) was randomly sampled by extracting 100 values of w_3 and calculating w_4 from the following Equation,

$$w_3 + w_4 = 0.5 \quad (1)$$

This procedure generated 100 independent results for the SI, from which the median and the interquartile range (i.e., distance between the 25th and 75th percentile) were calculated. Within the Blue Growth scenario we also identified those areas in which SI resulted to be stable within 0.8 and 1.0 in all the 100 results. These areas were called "high-suitability stable areas."

Definition of Criteria and Constraints

The spatial resolution of the SI map, 1 km^2, was determined by the resolution of SST data, which represent a key input for the eco-physiological models of the two farmed species. The latter were used for estimating the number of days required to reach the market size of 400 g both for seabream and seabass[3] using the R package RAC[4] (Baldan et al., 2018). Fish growth was simulated for each grid point, assuming that fish are fed *ad libitum*. Feed composition, in terms of proteins, lipids, and carbohydrates, was set on the basis of values which were considered to be representative of currently used commercial formulations for the two species[5,6] (last access 15/04/2019). The simulations were run for a period of 18 months, with a juvenile stocking size of 6 g, and a rearing cycle starting in July 2016, and ending in December 2017. Model formulations and parameters, both for seabass and seabream, are reported in previously published papers (Brigolin et al., 2010, 2014; Baldan et al., 2018), and in the demo dataset provided within the RAC package. Only one parameter was modified with respect to these works, namely the seabream fasting catabolism at 0°C, for which the value of $k_0 = 0.0012$ day^{-1} was used, as suggested by Libralato and Solidoro (2008). The distance to harbor criterion was estimated by measuring the distance, in km, from each center of the grid to the nearest harbor, through the nearest neighbor analysis in QGIS (version Las Palmas, 2.18.24). The SWH criterion, providing a measure of the roughness of the sea at each specific site, selected to evaluate which areas have higher probability of being affected by storms, was estimated on the basis of the 90th percentile of the sea surface SWH, estimated for each center grid, by interpolating the data downloaded from the CMEMS website though a nearest neighbor interpolation algorithm. It is important to notice that downscaling satellite data implies several issues, depending on the algorithms applied, which influence the accuracy, outputs resolution and robustness (see for example Ramírez Villegas and Jarvis, 2010). We decided to use the nearest neighbor interpolation algorithm based on the consideration that this simple technique, taking the value of the nearest observed point does not change the input raster values (Hengl and Reuter, 2008). The SWH data were downscaled to the same spatial resolution of SST data allowing us to run the SMCE analysis at 1 km^2.

The estimation of EN macro-criterion was based on the results presented in Micheli et al. (2013), who produced a cumulative human impacts index for the Mediterranean coasts, following the approach described by Halpern et al. (2008). The impacts were calculated considering multiple drivers (e.g., temperature, acidification, nutrient input, and risk of hypoxia) and ecosystems, which values were combined and weighted. The sum of these weighted combinations represented the relative cumulative impacts of human activities on ecosystems (Halpern et al., 2008; Micheli et al., 2013). Data were extracted from the NCEAS website[7] (last access 15/04/2019).

Spatial constraints imposed by existing anthropogenic activities considered to be in conflict with the presence of aquaculture were also considered. Data on uses such as hydrocarbon extraction, dump munition areas, danger zones, and military practice area, were downloaded from EMODnet[8] and Adriplan portals[9]. Moreover, we considered the *Posidonia oceanica* meadows distribution, extracted for the study area from the Mediterranean Sensitive Habitats (MediSeH) project (Giannoulaki et al., 2013; Telesca et al., 2015), and the Marine Protected Areas, which were downloaded from the World Database on Protected Areas[10]. Under a precautionary approach, around marine protected areas and seagrass meadows a security distance buffer of 500 meters was considered (see Holmer et al., 2008).

As a final step, all the constraints were merged, in order to identify unavailable space for aquaculture, and superimposed to the suitability map for finfish aquaculture, by using a Boolean classification scheme (suitable areas 1, unsuitable areas 0) (Falconer et al., 2013). Analyses were performed using free open software R 3.5.1, R packages RAC – R package for AquaCulture, raster, ncdf4 and maptools (R Core Team, 2018), and QGIS 2.18.24 Las Palmas (Quantum GIS Development Team, 2018).

RESULTS

All the considered constraints, together with Marine Protected Areas and seagrass meadows are mapped in **Figure 1**. The Central and North Adriatic Sea is the area with most anthropogenic activities, while in the southern part of the Tyrrhenian Sea, along the Sicilian and Calabrian coasts these activities are almost absent. **Figures 3A–C** shows the median values of the SI with the constraints superimposed for the three considered scenarios: Environmental (EC 0.25/EN 0.75), Blue Growth (EC 0.5/EN 0.5), and Economic (EC 0.75/EN 0.25). The "constraints-free" maps are reported in **Supplementary Figures S2A–C**. **Figures 4A–C** shows the uncertainty in terms of interquartile range for the Environmental, Blue Growth and Economic scenarios. Low SI values with similar uncertainties for the three considered scenarios are estimated in the following two areas: (1) offshore area of the Northern Adriatic Sea, along the coasts of Friuli Venezia Giulia, Veneto, Emilia-Romagna and Apulia regions; (2) offshore area of the Southern part of Sicily. Globally, the Italian

[3]http://www.fao.org/fishery/culturedspecies/search/en

[4]https://cran.r-project.org/package=RAC

[5]http://www.fao.org/fishery/affris/species-profiles/gilthead-seabream/gilthead-seabream-home/en/

[6]http://www.fao.org/fishery/affris/species-profiles/european-seabass/european-seabass-home/en/

[7]https://www.nceas.ucsb.edu/globalmarine

[8]http://www.emodnet-humanactivities.eu/about.php#humanactivities

[9]http://data.adriplan.eu/

[10]https://protectedplanet.net/

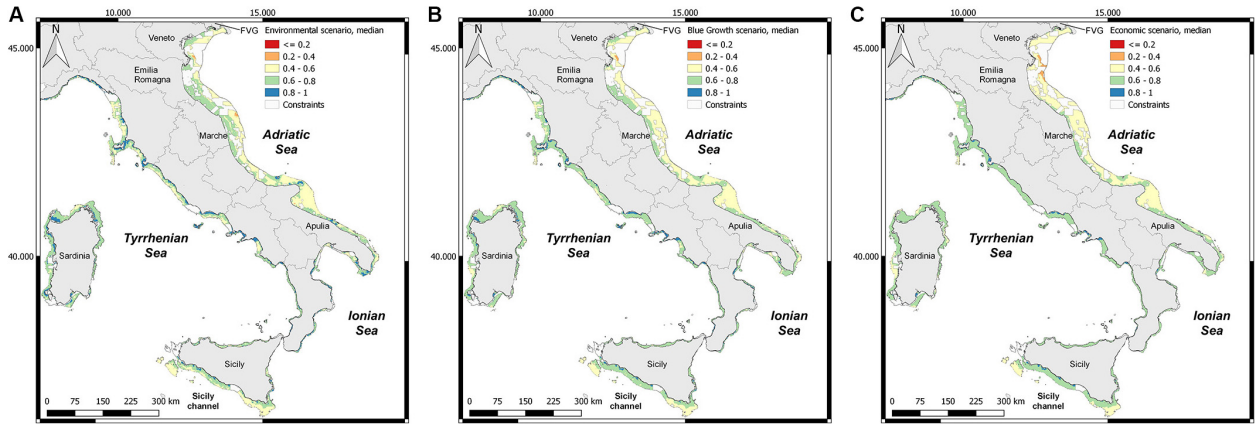

FIGURE 3 | Spatial multi-criteria evaluation median results for the 3 scenarios considering the current sea uses and protected areas. **(A)** Environmental. **(B)** Blue Growth. **(C)** Economic. Scenarios were defined by initially assigning the same weight to EC and EN (Blue growth, EC 0.5/EN 0.5), and therefore decreasing by 50% each macro-criterion (Economic, EC 0.75/EN 0.25; Environmental, EC 0.25/EN 0.75).

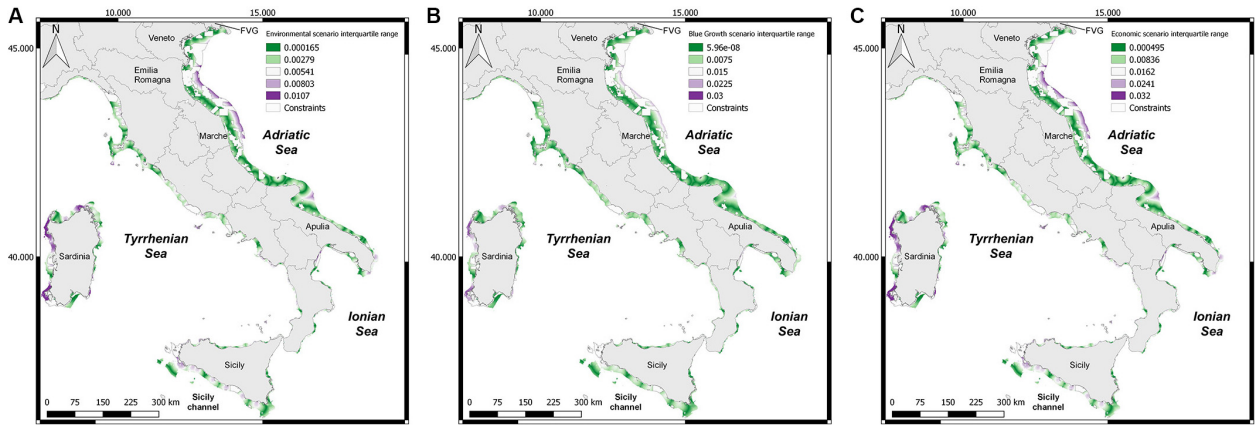

FIGURE 4 | Spatial multi-criteria evaluation uncertainty (interquartile range/median) for the 3 scenarios considering the current sea uses and protected areas: **(A)** Environmental. **(B)** Blue Growth. **(C)** Economic.

EEZ, both inshore and offshore, results to be suitable for seabass and seabream farming, with the notable exception of the Adriatic Sea offshore areas. Indeed, the lowest SI values (0.2 – 0.4) are estimated for this area, in front of the Po river outlet. Most of the investigated marine space presents SI values comprised between 0.6 and 0.8, while the highest SI values (0.8 – 1.0) are recorded in the Tyrrhenian and Ionian area. In particular, the suitable space (SI > 0.6) results around 60% of the total space for the Environmental and Blue Growth scenarios, while is ca. 54% for the Economic scenario (**Supplementary Figure S3A**). In details, in the Environmental scenario 59.87% of the total space (53,412 km^2) presents high and very high suitability values, followed by the Blue Growth scenario with the 58.63% of the total space (52,301 km^2), and the Economic scenario with 53.73% (47,928 km^2) of the total space.

The highest uncertainties were found in the Economic and Blue Growth scenarios, with very similar values, followed by the Environmental scenario (**Figure 4**). The UA highlighted low values with a common uncertainty for all considered scenarios in three areas: (1) offshore area of the Northern Adriatic Sea, along the coasts of Veneto, Emilia-Romagna and Marche regions; (2) inshore and offshore Western and Northern coasts of Sardinia region; (3) inshore areas of the Southern part of Sicily. Considering the Blue Growth scenario, the uncertainty values and the current marine sea uses are represented in **Figure 5**, along with the high-suitability stable areas (areas in which the SI scored between 0.8 and 1.0, see section "SMCE analysis and scenarios construction"). The high-suitability stable areas are located in the Tyrrhenian and Ionian Seas, and almost in the whole area the lowest uncertainty is recorded with the exception of the Sardinian and western Sicilian coasts. In particular, in **Figure 5A** is possible to highlight in the Southern part, two stable areas, one with low uncertainty values and the other with high uncertainty values. Moreover, in the Sicilian area (**Figure 5B**), the highest uncertainty is recorded in two stable areas, where is located the Egadi Island Marine Protected Area.

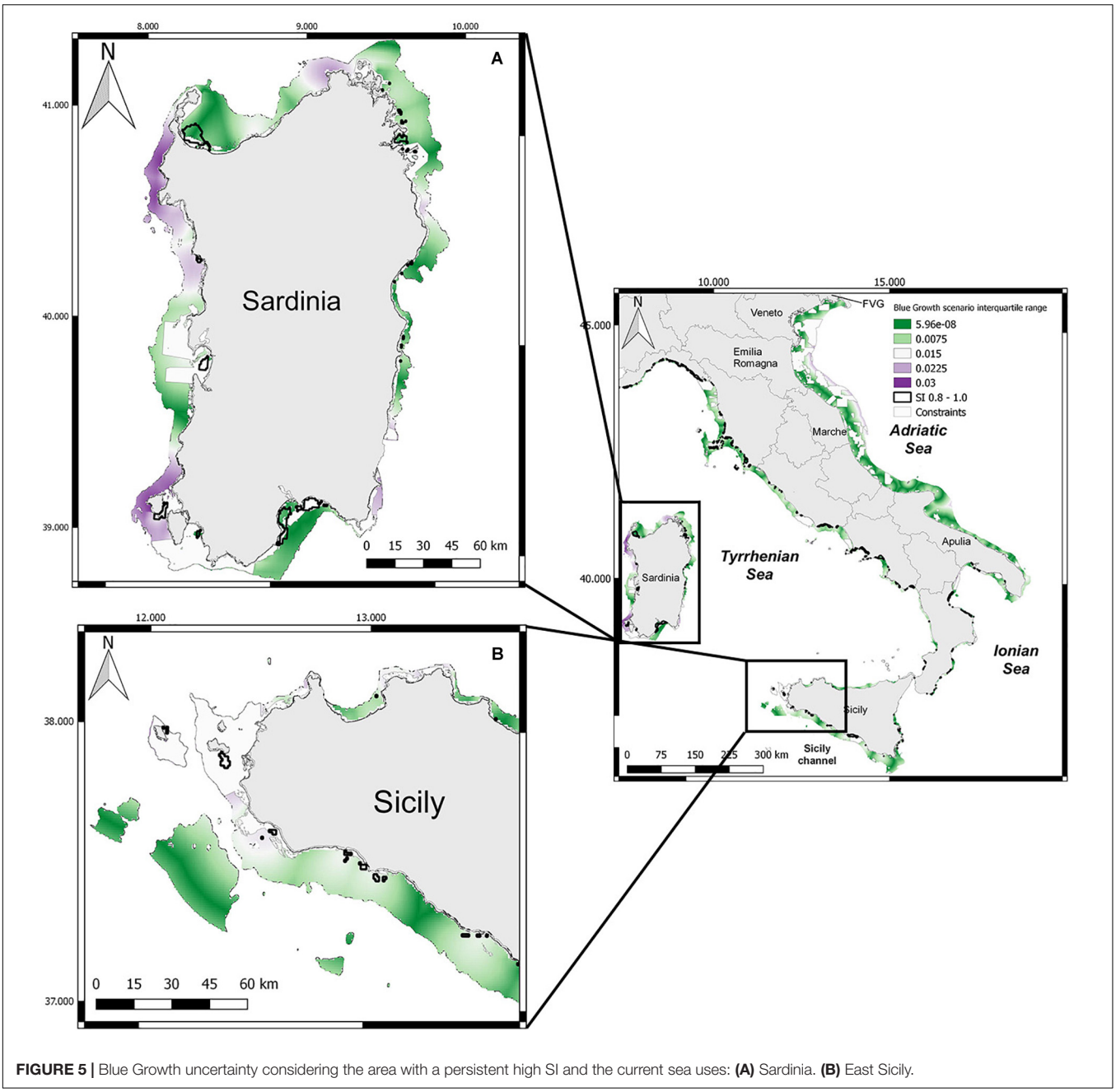

FIGURE 5 | Blue Growth uncertainty considering the area with a persistent high SI and the current sea uses: **(A)** Sardinia. **(B)** East Sicily.

DISCUSSION

The first step in a process for aquaculture site selection is related with the identification of priority areas at the national level, afterward detailed plans are developed at regional level (FAO and World Bank, 2015). The Strategic Guidelines for Aquaculture delivered by the (European Commission [EC], 2013) considered spatial planning for aquaculture as a key issue and all EU Member States developed the Multi-annual aquaculture plans with the aim to increase their productions. In this context, the first objective of the Italian national strategic plan for aquaculture (PSA, 2014-2020) is to develop the aquaculture activity in the Italian seas in order to create economy, employment and social benefits. Considering also the Blue Growth strategy perspective, the Italian national growth objective for the 2013 – 2025 is to increase of 58% in volume the current marine fish farming production (PSA, 2014-2020). The response to the EU strategic guidelines to achieve this objective includes the coordinated spatial planning (macro-objective 2 of the PSA, 2014-2020), through the implementation of the MSP Directive and coherently with the FAO-GFCM resolution of 2012 (Recommendation GFCM/36/2012/1; GFCM, 2012), with the aim to identify the priority areas for aquaculture activities. In particular, there is a need of national guidelines

for the identification of AZAs able to support regions in the adoption of MSP plans.

As highlighted by our results, the Italian EEZ is a complex system in which different users coexist, with a wide range of purposes and conflicts of interest (tourism, industry, fisheries and transport). Understanding and quantifying the spatial distribution of constraints and multiple stressors should help to improve and rationalize the spatial management of human activities, considering both the Water Framework Directive (WFD; Directive 2000/60/EC) and the Marine Strategy Framework Directive (MSFD; Directive 2008/56/EC). The identification of suitable areas for the expansion of aquaculture presents both purely technical-scientific aspects, linked to the current scientific knowledge, and problems connected to the decision-making aspects and the planning process. In recent years, there was a rise in the usage of "virtual technologies" (*sensu* Ferreira et al., 2012) for the sustainable development and management of aquaculture activities, also related mainly with the increasing availability of SRS data (see e.g., Radiarta et al., 2008; Brigolin et al., 2015, 2017; Gernez et al., 2017). The application presented in this study confirms the potential of SRS for MSP and, based on the generality and transferability of the applied methodology, could be both tested in other areas and extended to different species. With respect to this latter point, it is worth remarking that the present work used SST satellite data as inputs for mechanistic models simulating eco-physiology and growth of seabass and seabream, while recent studies considered directly the water temperature values in relation to the thermal tolerance of the selected species (e.g., Longdill et al., 2008; Radiarta et al., 2008; Gentry et al., 2017; Weiss et al., 2018). The advantage of using a mechanistic model is related to the possibility of obtaining the integrated assessment of the temperature effects on fish physiology and growth over time. Consistently with the results from a mechanistic model based on the dynamic energy budget theory (Sarà et al., 2018), our analysis showed that, fixing the husbandry practices, fish growth appeared strongly related to the spatio-temporal variability in SST. Indeed, a latitudinal gradient was highlighted for both species, with a better growth performance highlighted in the southern part of the Italian EEZ.

SI and Estimated Criteria

Consistently with the approach promoted by the EU Directive on Maritime Spatial Planning, the definition of weights should be the results of a participatory process involving different stakeholders. Indeed, as remarked by Radiarta et al. (2008), weighting is one of the primary challenges when a multicriteria evaluation is applied. To the knowledge of the authors, a univocal and objective procedure to determine the importance of each criterion does not exist.

According to the results obtained in this work, the areas less suitable were the Adriatic Sea and the southern part of Sicily, were a high uncertainty was also recorded. On the opposite side, the western and northern Sardinian coasts were classified as highly suitable but, in these areas, high uncertainty values were also estimated. Considering current constraints, the areas not available for seabass, and seabream farming are located in the Northern Adriatic Sea, in the same areas where the estimated SI presents lower values. High suitability was the most represented class for all the scenarios analyzed, (**Supplementary Figures S3A,B**) (*ca*. 50% of the EEZ), followed by the medium suitability (around 40%). SI maps before and after considering constraints, highlight that available areas with very high suitability were, respectively, reduced by 2500, 1300, and 750 km^2 under the Environmental, Blue Growth and Economic scenarios (**Supplementary Figure S3B**). Few areas resulted highly suitable for seabass/seabream cage culture, in particular 2%, 5%, and 9% of the study area for the Economic, Blue Growth and Environmental scenario, respectively. Noteworthy, for this suitability class, very similar values were recorded both taking and not taking into account the current sea uses and constraints. Low suitability area, SI values comprised between 0.2 and 0.4, resulted marginally represented with values comprised between 2.5% and 0.5% of the total area, while SI values below 0.2 were never recorded.

In general, the most constraining Intermediate Level Criteria (ILC), was Bream, followed by DH, Bass, SWH, and Impact (see **Supplementary Figure S4**). Maps of EC and EN criteria used to calculate the SI are reported in **Figure 6** (raw values) and in **Supplemetary Figure S1** (normalized values), and briefly presented in the following. Days required to reach the commercial size (400 g) were estimated and mapped for the entire study area (**Figures 6A,B** and **Supplementary Figures S1A,B**). The values are comprised between 320 and 443 for seabream, and 385 and 518 days for seabass. For seabream, the lowest growth values were found in the Northern Adriatic Sea, with a decreasing tendency moving offshore. The highest growth values are located in the southern part of the Sicily channel, followed by the western part of Sardinia island, and the Tyrrhenian Sea, showing fewer variable values, of *ca.* 330 days. The growth performance estimated for seabass are comparable to those described for seabream but, in general, a higher number of days is required to reach the commercial size. Distance to harbor (**Figure 6C** and **Supplementary Figure S1C** normalized values) results homogenously distributed in the whole study area, with the highest values in the Adriatic Sea and Sicily channel. The most exposed areas, through the SWH analysis (**Figure 3D** and **Supplementary Figure S1D**), are located in the western and northern Sardinia, and in the southern part of Sicily. Regarding the cumulative impact index (**Figure 6E** and **Supplementary Figure S1E**), the highest values are present offshore, both in the Adriatic and Sicily channel areas, and in the Central and North Tyrrhenian areas.

SMCE Use for Aquaculture Planning

In the aquaculture suitability analysis presented in this work, the UA performed allows to understand the SI variability depending on the respective weights assigned to distance of the farm facilities from harbors and SWH criteria (**Figure 6**). Overall, the introduction of the UA marks an element of novelty of this work with respect to previous similar applications (e.g., Radiarta et al., 2008; Brigolin et al., 2015, 2017). With respect to this, results obtained in the present application highlight that the average map could provide an incomplete view, if not integrated

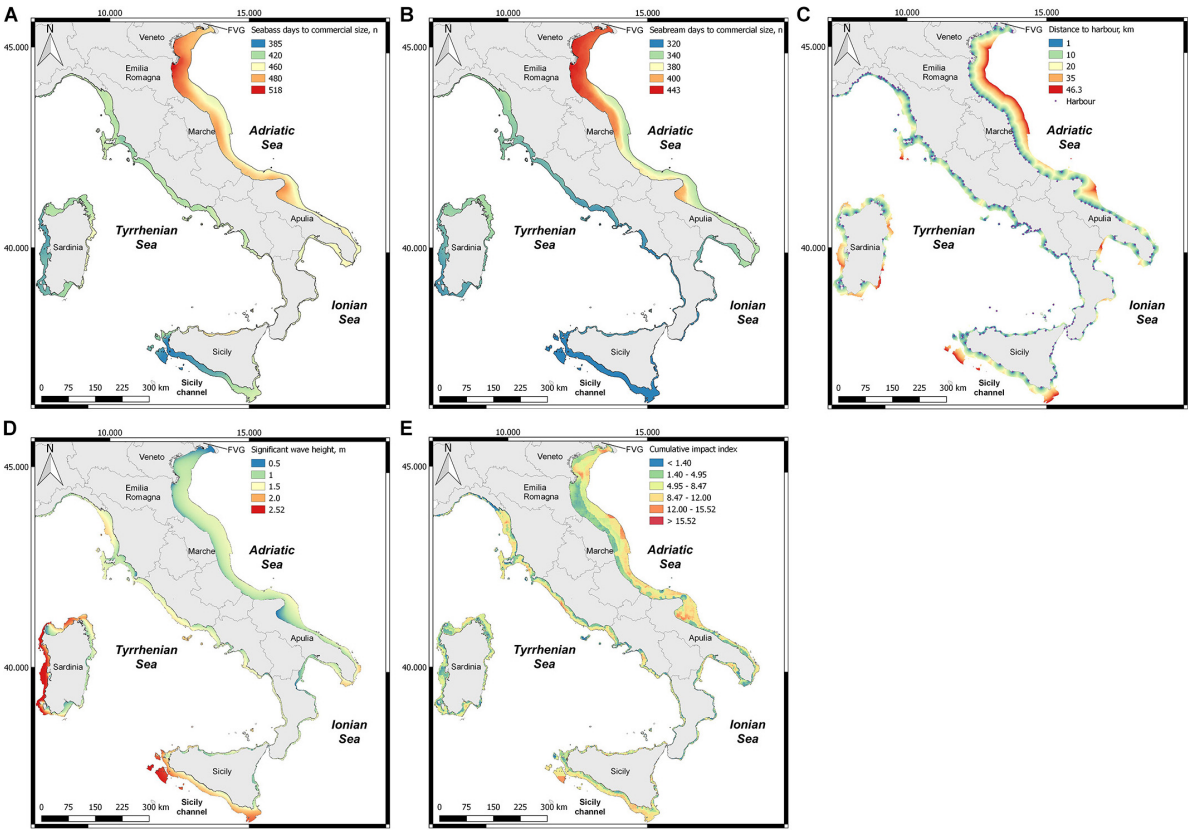

FIGURE 6 | Maps of criteria considered in the analyses. **(A)** Days required by seabass to reach the commercial size. **(B)** Days required by seabream to reach the commercial size. **(C)** Distance to harbor. **(D)** SWH. **(E)** Cumulative impact within the study area.

with the uncertainty associated, which can provide a measure of the stability of results under criteria weights modifications. This is easily detectable in the Western and Northern Sardinian coasts under the Blue Growth scenario, where we estimated high suitability but also the highest uncertainty. To this regard, it is worth noting that high values of uncertainty are detected in the areas were the two criteria SWH and DH, for which the respective weights were treated as stochastic variables in the analysis, show the more pronounced spatial gradients. This suggests, as a general rule, to carefully identify the factors considered in the UA.

In this work we used the cumulative human impact map (Halpern et al., 2008; Micheli et al., 2013), which allowed us to take advantage of an indicator of ecosystem status to identify which areas are already heavily impacted, and in which a new anthropogenic activity could push the system beyond the resilience limits. Indeed, these impacted areas have high priority for management and conservation actions (Coll et al., 2012; Micheli et al., 2013) and it could be difficult to integrate new aquaculture activities with the impacts already present. We are aware that this approach has two main limitations related with (i) the linear combination of the impacts, that does not consider the different combinations of drivers which can also determine a non-linear response to cumulative impacts, and (ii) the variable quality of the available data (see for example comments by Halpern et al., 2008; Micheli et al., 2013; Stock and Micheli, 2016). At the same time, the wide spatial scale and the completeness of the drivers considered, represented a great opportunity for the implementation in this study of the environmental components within the design of AZAs. In agreement with the procedure suggested by FAO (FAO and World Bank, 2015), we remark that the *a priori* evaluation of cumulative impacts presented here should be accompanied by a quantification of the local interaction of the planned facilities, once the location of aquaculture management areas is established. This step, which goes in the direction of characterizing the Allowable Zone of Effect (AZE), should be based on a more comprehensive set of environmental data, including time series of local currents, dissolved oxygen concentrations, and water transparency (e.g., through light extinction coefficient, K_d).

Offshore aquaculture activities are increasing in other European Seas (e.g., Buck and Langan, 2017): our findings could provide a basis for feasibility studies, aimed at evaluating the possibility of developing them also in Mediterranean areas. The co-use and development of offshore aquaculture in combination with other activities (e.g., wind farms, oil, and gas decommissioned platforms, etc.) could boost this industry helping in different aspects, including attachment points for cages, less cost in maintenance operation, and sharing of

infrastructural costs (Buck and Langan, 2017). In the meantime, future development of control-engineering farming practices (i.e., Precision Fish Farming – Føre et al., 2018) can help overcoming some of the logistic problems, potentially related to the distance from the harbors (Naylor and Burke, 2005). Finally, it is worth remarking that economic and social-acceptability aspects (see e.g., Gentry et al., 2017; Kluger et al., 2019), may limit aquaculture production. Therefore, we advocate for the inclusion of social carrying capacity considerations (McKindsey et al., 2006; Gentry et al., 2017; Kluger et al., 2019) in the future applications of the methodology presented in this work, in order to obtain more realistic expansion scenarios.

Management Recommendations

Our results estimated a potential suitability for marine aquaculture within most of the Italian EEZ, above all in the Tyrrhenian and Ionian Seas, suggesting the potential development of this activity. Less suitable marine space was recorded in the northern Adriatic Sea, in western Sardinia, and southern Sicily, were the highest uncertainty was also recorded. The application highlights the possibility of providing an estimation of the suitability of different areas, along with an uncertainty associated, through the Spatial Multi-Criteria analysis and making use of SRS data, mechanistic models, existing impacts and uses of marine space. This could assist policy makers and regulators in promoting a development of aquaculture which follows the ecosystem approach. Indeed, spatial planning will be only the first step of this process, which will also include environmental impact assessment and monitoring programs (Sanchez-Jerez et al., 2016). We believe that the approach and the findings reported in this work can contribute to the identification of priority areas for aquaculture activities within the Italian EEZ. It is worth remarking that the identification carried out here with respect to finfish aquaculture needs, must be extended to consider also the potential for extractive aquaculture (shellfish and macroalgae). This step should take into account interactions and possibilities for Integrated Multi-Trophic Aquaculture (IMTA) development in this area. IMTA implementation is seen as a possible way to develop an ecological intensification of aquaculture activities (BLUEMED Italian White Paper Working Group, 2018). Once identified suitable areas, as in the present study, a more downscaled approach could allow to deeply examine the complex mosaic of local factors interacting with aquaculture installations. Specifically, the availability of local data, such as marine currents, and the application of depositional models, could determine a more precise and site-specific results allowing to highlight possible obstacles for seabass and seabream aquaculture development at the finest spatial scale. After the AZAs identification, carrying capacity, cost/benefit analysis and environmental quality standards should be taken into account to define the Allowable Zone Effect and the Aquaculture Management Area (Sanchez-Jerez et al., 2016). These evaluations, being site-specific and depending on both environmental and socio-economic factors, should be considered as a further development of the analysis presented here.

The set of indicators used in this study could be expanded in different ways, however, this should be carried out by taking into account the availability of data, and the reliability of the models needed to derive the indicators. In perspective, model results could be improved by the development of new algorithms and new SRS products, such as organic fraction of the suspended matter and the detection of Harmful Algal Blooms, which will provide new opportunities in this area (Gernez et al., 2014, 2017). Future availability of SRS at highest resolution could improve the accuracy of suitability predictions, allowing to disentangle the complex mosaic of site-specific factors influencing the aquaculture activities. Finally, we remark that eco-physiological mathematical models, which within this work were forced by using SST data, could in perspective be applied for forecasting the effects of climate changes, by using as an input the downscaling simulation produced by hydrodynamic numerical models (e.g., Euro-CORDEX initiative[11]).

DATA AVAILABILITY STATEMENT

The spatial raster generated for this study can be found in the **Supplementary Material**.

AUTHOR CONTRIBUTIONS

EP, RP, and DB conceptualized the study, wrote the manuscript, contributed to the manuscript revision, and read and approved the submitted version. EP ran the analysis.

FUNDING

This work was partially supported by PORTODIMARE project, project number 205, Priority Axis 2 Sustainable Region, funding program Interreg V B 2014–2020: Adriatic-Ionian Program – ADRION.

SUPPLEMENTARY MATERIAL

The Supplementary Material for this article can be found online at: https://www.frontiersin.org/articles/10.3389/fmars.2019.00772/full#supplementary-material

[11] https://euro-cordex.net/

REFERENCES

Ahmed, N., and Thompson, S. (2019). The blue dimensions of aquaculture: a global synthesis. *Sci. Total Environ.* 652, 851–861. doi: 10.1016/j.scitotenv.2018.10.163

Baldan, D., Porporato, E. M. D., Pastres, R., and Brigolin, D. (2018). An R package for simulating growth and organic wastage in aquaculture farms in response to environmental conditions and husbandry practices. *PLoS One* 13:e0195732. doi: 10.1371/journal.pone.0195732

Ban, N. C., Alidina, H. M., and Ardron, J. A. (2010). Cumulative impact mapping: advances, relevance and limitations to marine management and conservation, using Canada's Pacific waters as a case study. *Mar. Pol.* 34, 876–886. doi: 10.1016/j.marpol.2010.01.010

Béné, C., Barange, M., Subasinghe, R., Pinstrup-Andersen, P., Merino, G., Hemre, G. I., et al. (2015). Feeding 9 billion by 2050–Putting fish back on the menu. *Food Secur.* 7, 261–274. doi: 10.1007/s12571-015-0427-z

Black, K. D. (2001). *Environmental Impacts of Aquaculture*. Sheffield: Sheffield Academic Press.

BLUEMED Italian White Paper Working Group (2018). *The BLUEMED Italian White Paper: An Overview of Relevance, Obstacles and Proposals of the Key Sectors for a Blue Growth*. Roma: CNR Edizioni.

Branch, T. A., Jensen, O. P., Ricard, D., Yimin, Y., and Hilborn, R. (2011). Contrasting global trends in marine fishery status obtained from catches and from stock assessments. *Conserv. Biol.* 25, 777–786. doi: 10.1111/j.1523-1739.2011.01687.x

Brigolin, D., Lourguioui, H., Taji, M. A., Venier, C., Mangin, A., and Pastres, R. (2015). Space allocation for coastal aquaculture in North Africa: data constraints, industry requirements and conservation issues. *Ocean Coast. Manage.* 116, 89–97. doi: 10.1016/j.ocecoaman.2015.07.010

Brigolin, D., Meccia, V. L., Venier, C., Tomassetti, P., Porrello, S., and Pastres, R. (2014). Modelling biogeochemical fluxes across a mediterranean fish cage farm. *Aquac. Environ. Interact.* 5, 71–88. doi: 10.3354/aei00093

Brigolin, D., Pastres, R., Tomassetti, P., and Porrello, S. (2010). Modelling the biomass yield and the impact of seabream mariculture in the adriatic and tyrrhenian seas (Italy). *Aquac. Int.* 18, 149–163. doi: 10.1007/s10499-008-9232-4

Brigolin, D., Porporato, E. M. D., Prioli, G., and Pastres, R. (2017). Making space for shellfish farming along the adriatic coast. *ICES J. Mar. Sci.* 74, 1540–1551. doi: 10.1093/icesjms/fsx018

Buck, B. H., and Langan, R. (2017). *Aquaculture Perspective of Multi-Use Sites in the Open Ocean: The Untapped Potential for Marine Resources in the Anthropocene*. New York, NY: Springer.

Buongiorno Nardelli, B., Tronconi, C., Pisano, A., and Santoleri, R. (2013). High and Ultra-high resolution processing of satellite Sea Surface temperature data over Southern European Seas in the framework of MyOcean project. *Remote Sens. Environ.* 129, 1–16. doi: 10.1016/j.rse.2012.10.012

Clavelle, T., Lester, S. E., Gentry, R., and Froehlich, H. E. (2019). Interactions and management for the future of marine aquaculture and capture fisheries. *Fish. Fish.* 20, 368–388. doi: 10.1111/faf.12351

Coll, M., Piroddi, C., Albouy, C., Ben Rais Lasram, F., Cheung, W. W. L., Christensen, V., et al. (2012). The mediterranean Sea under siege: spatial overlap between marine biodiversity, cumulative threats and marine reserves. *Glob. Ecol. Biogeogr.* 21, 465–480. doi: 10.1111/j.1466-8238.2011.00697.x

Costello, C., Ovando, D., Clavelle, T., Strauss, C. K., Hilborn, R., Melnychuk, M. C., et al. (2016). Global fishery prospects under contrasting management regimes. *Proc. Natl. Acad. Sci. U.S.A.* 113, 5125–5129. doi: 10.1073/pnas.1520420113

da Luz Fernandes, M., Esteves, T. C., Oliveira, E. R., and Alves, F. L. (2017). How does the cumulative impacts approach support maritime spatial planning? *Ecol. Indic.* 73, 189–202. doi: 10.1016/j.ecolind.2016.09.014

Delgado, C. L., Wada, N., Rosegrant, M. W., Meijer, S., and Ahmed, M. (2003). *Fish to 2020: Supply and Demand in Changing Global Markets*. Penang: World Fish Center.

Eastman, J. R. (1999). Multi-criteria evaluation and GIS. *Geograph. Inf. Syst.* 1, 493–502.

EC Directive (2014). *2014/89/EU of the European Parliament and of the Council of 23 July 2014 Establishing a Framework for Maritime Spatial Planning*.

EUMOFA (2017). *Highlights the EU in the World EU Market Supply, Consumption, trade, EU Landings, Aquaculture Production*. Belgium: EUMOFA.

EUMOFA (2019). *Seabass in the EU. Price Structure in the Supply Chain for Seabass*. Belgium: EUMOFA.

European Commission (2018). *Facts and Figures on the Common Fisheries Policy. Basic statistical data*. Brussels: European Commission.

European Commission [EC] (2012). *Communication from the Commission to the European Parliament, the Council, the European Economic and Social Committee and the Committee of the Regions. Blue Growth Opportunities for Marine and Maritime Sustainable Growth*. Brussels: European Commission.

European Commission [EC] (2013). *Communication from the Commission to the European Parliament, the Council, the European Economic and Social Committee and the Committee of the Regions: Strategic Guidelines for the Sustainable Development of EU Aquaculture*. Brussels: European Commission.

European Community (2000). *Directive 2000/60/EC of the European Parliament and of the Council of 23 October 2000 Establishing a Framework for Community Action in the Field OF Water Policy*. Bruxelles: European Community.

Falconer, L., Hunter, D. C., Scott, P. C., Telfer, T. C., and Ross, L. G. (2013). Using physical environmental parameters and cage engineering design within GIS-based site suitability models for marine aquaculture. *Aquac. Environ. Interact.* 4, 223–237. doi: 10.3354/aei00084

FAO (2012). *Report of the Thirty-Sixth Session of the General Fisheries Commission for the Mediterranean*. Rome: FAO.

FAO (2018). *The State of World Fisheries and Aquaculture 2018. Meeting the Sustainable Development Goals*. Rome: FAO.

FAO and World Bank (2015). *Aquaculture Zoning, Site Selection and Area Management Under the Ecosystem Approach to Aquaculture*. Rome: World Bank.

Ferreira, J. G., Aguilar-Manjarrez, J., Bacher, C., Black, K., Dong, S. L., Grant, J., et al. (2012). "Progressing aquaculture through virtual technology and decision-support tools for novel management," in *Proceedings of the Global Conference on Aquaculture 2010, Farming the Waters for People and Food* eds R. P. Subasinghe, J. R. Arthur, D. M. Bartley, S. S. De Silva, M. Halwart, N. Hishamunda, C. V. Mohan, and P. Sorgeloos (Rome: FAO), 643–704.

Filgueira, R., Comeau, L. A., Landry, T., Grant, J., Guyondet, T., and Mallet, A. (2013). Bivalve condition index as an indicator of aquaculture intensity: a meta-analysis. *Ecol. Indic.* 25, 215–229. doi: 10.1016/j.ecolind.2012.10.001

Føre, M., Frank, K., Norton, T., Svendsen, E., Alfredsen, J. A., Dempster, T., et al. (2018). Precision fish farming: a new framework to improve production in aquaculture. *Biosyst. Eng.* 173, 176–193. doi: 10.1016/j.biosystemseng.2017.10.014

Froehlich, H. E., Smith, A., Gentry, R. R., and Halpern, B. S. (2017). Offshore aquaculture: i know it when I see it. *Front. Mar. Sci.* 4:154. doi: 10.3389/fmars.2017.00154

Gentry, R. R., Froehlich, H. E., Grimm, D., Kareiva, P., Parke, M., Rust, M., et al. (2017). Mapping the global potential for marine aquaculture. *Nat. Ecol. Evol.* 1:1317. doi: 10.1038/s41559-017-0257-9

Gernez, P., Barillé, L., Lerouxel, A., Mazeran, C., Lucas, A., and Doxaran, D. (2014). Remote sensing of suspended particulate matter in turbid oyster-farming ecosystems. *J. Geophys. Res. Oceans* 119, 7277–7294. doi: 10.1002/2014JC010055

Gernez, P., Doxaran, D., and Barillé, L. (2017). Shellfish aquaculture from space: potential of Sentinel2 to monitor tide-driven changes in turbidity, chlorophyll concentration and oyster physiological response at the scale of an oyster farm. *Front. Mar. Sci.* 4:137. doi: 10.3389/fmars.2017.00137

GFCM (2012). *Resolution GFCM/36/2012/1 on Guidelines on Allocated Zones for Aquaculture (AZA)*. Rome: GFCM.

Giannoulaki, M., Belluscio, A., Colloca, F., Fraschetti, S., Scardi, M., Smith, C., et al. (2013). *Mediterranean Sensitive Habitats (MEDISEH), Final Project Report. DG MARE Specific Contract SI2.600741*. Anavyssos: Hellenic Centre for Marine Research.

Gómez-Delgado, M., and Tarantola, S. (2006). GLOBAL sensitivity analysis, GIS and multi-criteria evaluation for a sustainable planning of a hazardous waste disposal site in Spain. *Int. J. Geogr. Inf. Sci.* 20, 449–466. doi: 10.1080/13658810600607709

Halpern, B. S., Frazier, M., Potapenko, J., Casey, K. S., Koenig, K., Longo, C., et al. (2015). Spatial and temporal changes in human impacts on the world's ocean. *Nat. Commun.* 6:7615. doi: 10.1038/ncomms8615

Halpern, B. S., Kappel, C., Selkoe, K., Micheli, F., Ebert, C., Kontgis, C., et al. (2009). Mapping cumulative human impacts to California current marine ecosystems. *Conserv. Lett.* 2, 138–148. doi: 10.1111/j.1755-263X.2009.00058.x

Halpern, B. S., Walbridge, S., Selkoe, K. A., Kappel, C. V., Micheli, F., D'Agrosa, C., et al. (2008). A global map of human impact on marine ecosystems. *Science* 319, 948–952. doi: 10.1126/science.1149345

Hengl, T., and Reuter, H. I. (eds) (2008). *Geomorphometry: Concepts, Software, Applications*. Amsterdam: Elsevier.

Holmer, M., Argyrou, M., Dalsgaard, T., Danovaro, R., Diaz-Almela, E., Duarte, C. M., et al. (2008). Effects of fish farm waste on *Posidonia oceanica* meadows:

synthesis and provision of monitoring and management tools. *Mar. Pollut. Bull.* 56:e1629. doi: 10.1016/j.marpolbul.2008.05.020

Kapetsky, J. M., and Aguilar-Manjarrez, J. (2007). *Geographic Information Systems, Remote Sensing and Mapping for the Development and Management of Marine Aquaculture*. Rome: Food & Agriculture Org.

Kelly, C., Gray, L., Shucksmith, R. J., and Tweddle, J. F. (2014). Investigating options on how to address cumulative impacts in marine spatial planning. *Ocean Coast. Manage.* 102, 139–148. doi: 10.1016/j.ocecoaman.2014.09.019

Kluger, L. C., Filgueira, R., and Byron, C. J. (2019). Using media analysis to scope priorities in social carrying capacity assessment: a global perspective. *Mar. Pol.* 99, 252–261. doi: 10.1016/j.marpol.2018.10.042

Libralato, S., and Solidoro, C. (2008). A bioenergetic growth model for comparing *Sparus aurata* feeding experiments. *Ecol. Model.* 214, 325–337. doi: 10.1016/j.ecolmodel.2008.02.024

Little, D. C., Newton, R. W., and Beveridge, M. C. M. (2016). Aquaculture: a rapidly growing and significant source of sustainable food? Status, transitions and potential. *Proc. Nutr. Soc.* 75, 274–286. doi: 10.1017/S0029665116000665

Longdill, P. C., Healy, T. R., and Black, K. P. (2008). An integrated GIS approach for sustainable aquaculture management area site selection. *Ocean Coast. Manage.* 51, 612–624. doi: 10.1016/j.ocecoaman.2008.06.010

Longo, S. B., Clark, B., York, R., and Jorgenson, A. K. (2019). Aquaculture and the displacement of fisheries captures. *Conserv. Biol.* 33, 832–841. doi: 10.1111/cobi.13295

Malczewski, J. (2006). GIS-based multicriteria decision analysis: a survey of the literature. *Int. J. Geogr. Inf. Sci.* 20, 703–726. doi: 10.1080/13658810600661508

Margules, C. R., and Pressey, R. L. (2000). Systematic conservation planning. *Nature* 405, 243–253. doi: 10.1038/35012251

McKindsey, C. W., Thetmeyer, H., Landry, T., and Silvert, W. (2006). Review of recent carrying capacity models for bivalve culture and recommendations for research and management. *Aquaculture* 261, 451–462. doi: 10.1016/j.aquaculture.2006.06.044

Micheli, F., Halpern, B. S., Walbridge, S., Ciriaco, S., Ferretti, F., Fraschetti, S., et al. (2013). Cumulative human impacts on mediterranean and black sea marine ecosystems: assessing current pressures and opportunities. *PLoS One* 8:e79889. doi: 10.1371/journal.pone.0079889

Naylor, R., and Burke, M. (2005). Aquaculture and ocean resources: raising tigers of the sea. *Annu. Rev. Environ. Resour.* 30, 185–218. doi: 10.1146/annurev.energy.30.081804.121034

Pressey, R. L., Cabeza, M., Watts, M. E. J., Cowling, R. M., and Wilson, K. A. (2007). Conservation planning in a changing world. *Trends Ecol. Evol.* 22, 583–592. doi: 10.1016/j.tree.2007.10.001

PSA (2014-2020). *Piano Strategico per l'Acquacoltura in Italia 2014-2020*. Available at: https://www.politicheagricole.it/flex/cm/pages/ServeAttachment.php/L/IT/D/b%252F1%252Ff%252FD.428bdb5bca0aa9cf42e1/P/BLOB%3AID%3D8752/E/pdf (accessed November 18, 2019).

Quantum GIS Development Team (2018). *Quantum GIS Geographic Information System. Open Source Geospatial Foundation Project*. Available at: http://qgis.osgeo.org (accessed September 15, 2018).

R Core Team, (2018). *R: A language and environment for Statistical Computing. R Foundation for Statistical Computing*. Vienna: R Core Team.

Radiarta, I. N., Saitoh, S. I., and Miyazono, A. (2008). GIS-based multi-criteria evaluation models for identifying suitable sites for Japanese scallop (*Mizuhopecten yessoensis*) aquaculture in Funka Bay, southwestern Hokkaido Japan. *Aquaculture* 284, 127–135. doi: 10.1016/j.aquaculture.2008.07.048

Ramírez Villegas, J., and Jarvis, A. (2010). *Downscaling Global Circulation Model Outputs: The Delta Method Decision and Policy Analysis Working Paper No. 1*. Available at: https://hdl.handle.net/10568/90731 (accessed November 18, 2019).

Saaty, T. L. (1980). *The Analytic Hierarchy Process: Planning, Priority Setting, Resources Allocation*. New York, NY: RWS Publications.

Saitoh, S.-I., Mugo, R., Radiarta, I. N., Asaga, S., Takahashi, F., Hirawake, T., et al. (2011). Some operational uses of satellite remote sensing and marine GIS for sustainable fisheries and aquaculture. *ICES J. Mar. Sci.* 68, 687–695. doi: 10.1093/icesjms/fsq190

Sanchez-Jerez, P., Karakassis, I., Massa, F., Fezzardi, D., Aguilar-Manjarrez, J., Soto, D., et al. (2016). Aquaculture's struggle for space: the need for coastal spatial planning and the potential benefits of Allocated Zones for Aquaculture (AZAs) to avoid conflict and promote sustainability. *Aquac. Environ. Interact.* 8, 41–54. doi: 10.3354/aei00161

Sarà, G., Gouhier, T. C., Brigolin, D., Porporato, E. M. D., Mangano, M. C., Mirto, S., et al. (2018). Predicting shifting sustainability tradeoffs in aquaculture under climate change. *Glob. Change Biol.* 24, 3654–3665. doi: 10.1111/gcb.14296

Soto, D., Aguilar-Manjarrez, J., and Hishamunda, N. (eds) (2008). *Building an Ecosystem Approach to Aquaculture: FAO/Universitat de Les Illes Balears Expert Workshop, 7-11 May, 2007, Palma de Mallorca, Spain*. Rome: FAO Fisheries and Aquaculture.

Stelzenmüller, V., Rogers, S. I., and Mills, C. M. (2008). Spatio-temporal patterns of fishing pressure on UK marine landscapes, and their implications for spatial planning and management. *ICES J. Mar. Sci.* 65, 1081–1091. doi: 10.1093/icesjms/fsn073

Stock, A., and Micheli, F. (2016). Effects of model assumptions and data quality on spatial cumulative human impact assessments. *Glob. Ecol. Biogeogr.* 25, 1321–1332. doi: 10.1111/geb.12493

Tacon, A. G. J., and Metian, M. (2016). Fish matters: importance of aquatic foods in human nutrition and global food supply. *Rev. Fish. Sci.* 21, 22–38. doi: 10.1080/10641262.2012.753405

Telesca, L., Belluscio, A., Criscoli, A., Ardizzone, G., Apostolaki, E. T., Fraschetti, S., et al. (2015). Seagrass meadows (*Posidonia oceanica*) distribution and trajectories of change. *Sci. Rep.* 5:12505. doi: 10.1038/srep12505

Thomas, Y., Mazurié, J., Alunno-Bruscia, M., Bacher, C., Bouget, J. F., Gohin, F., et al. (2011). Modelling spatio-temporal variability of *Mytilus edulis* (L.) growth by forcing a dynamic energy budget model with satellite-derived environmental data. *J. Sea Res.* 66, 308–317. doi: 10.1016/j.seares.2011.04.015

Troell, M., Jonell, M., and Henriksson, P. (2017). Ocean space for seafood. *Nat. Ecol. Evol.* 1, 1224–1225. doi: 10.1038/s41559-017-0304-6

Weiss, C. V., Ondiviela, B., Guanche, R., Castellanos, O. F., and Juanes, J. A. (2018). A global integrated analysis of open sea fish farming opportunities. *Aquaculture* 497, 234–245. doi: 10.1016/j.aquaculture.2018.07.054

World Bank (2013). *Fish to 2030: Prospect for Fisheries and Aquaculture*. Washington, DC: World Bank.

Conflict of Interest: EP, RP, and DB are researchers employed at the Department of Environmental Sciences, Informatics and Statistics, University of Venice (DAIS). RP and DB are shareholders of Bluefarm S.r.l., a spin-off company of DAIS. There are no patents, products in development or marketed products to declare.

frontiers in Marine Science

ORIGINAL RESEARCH
published: 14 January 2020
doi: 10.3389/fmars.2019.00802

Remote Sensing-Driven Pacific Oyster (*Crassostrea gigas*) Growth Modeling to Inform Offshore Aquaculture Site Selection

Stephanie C. J. Palmer[1], Pierre M. Gernez[1], Yoann Thomas[2], Stefan Simis[3], Peter I. Miller[3], Philippe Glize[4] and Laurent Barillé[1]*

[1] Mer Molécules Santé, Faculté des Sciences et des Techniques, Université de Nantes, Nantes, France, [2] Univ Brest, CNRS, IRD, Ifremer, LEMAR, Plouzane, France, [3] Plymouth Marine Laboratory, Plymouth, United Kingdom, [4] Syndicat Mixte pour le Développement de l'Aquaculture et de la Pêche en Pays de la Loire (SMIDAP), Nantes, France

OPEN ACCESS

Edited by:
Astrid Bracher, Alfred Wegener Institute Helmholtz Centre for Polar and Marine Research (AWI), Germany

Reviewed by:
Erika M. D. Porporato, Ca' Foscari University of Venice, Italy
Marie Elizabeth Smith, Council for Scientific and Industrial Research (CSIR), South Africa
Jordan Snyder, University of California, Santa Barbara, United States

***Correspondence:**
Stephanie C. J. Palmer
Stephanie.Palmer@univ-nantes.fr

Specialty section:
This article was submitted to Ocean Observation, a section of the journal Frontiers in Marine Science

Received: *25 September 2019*
Accepted: *12 December 2019*
Published: *14 January 2020*

Citation:
Palmer SCJ, Gernez PM, Thomas Y, Simis S, Miller PI, Glize P and Barillé L (2020) Remote Sensing-Driven Pacific Oyster (Crassostrea gigas) Growth Modeling to Inform Offshore Aquaculture Site Selection. Front. Mar. Sci. 6:802. doi: 10.3389/fmars.2019.00802

Aquaculture increasingly contributes to global seafood production, requiring new farm sites for continued growth. In France, oyster cultivation has conventionally taken place in the intertidal zone, where there is little or no further room for expansion. Despite interest in moving production further offshore, more information is needed regarding the biological potential for offshore oyster growth, including its spatial and temporal variability. This study shows the use of remotely-sensed chlorophyll-a and total suspended matter concentrations retrieved from the Medium Resolution Imaging Spectrometer (MERIS), and sea surface temperature from the Advanced Very High Resolution Radiometer (AVHRR), all validated using *in situ* matchup measurements, as input to run a Dynamic Energy Budget (DEB) Pacific oyster growth model for a study site along the French Atlantic coast (Bourgneuf Bay, France). Resulting oyster growth maps were calibrated and validated using *in situ* measurements of total oyster weight made throughout two growing seasons, from the intertidal zone, where cultivation currently takes place, and from experimental offshore sites, for both spat (R^2 = 0.91; RMSE = 1.60 g) and adults (R^2 = 0.95; RMSE = 4.34 g). Oyster growth time series are further digested into industry-relevant indicators, such as time to achieve market weight and quality index, elaborated in consultation with local producers and industry professionals, and which are also mapped. Offshore growth is found to be feasible and to be as much as two times faster than in the intertidal zone ($p < 0.001$). However, the potential for growth is also revealed to be highly variable across the investigated area. Mapping reveals a clear spatial gradient in production potential in the offshore environment, with the northeastern segment of the bay far better suited than the southwestern. Results also highlight the added value of spatiotemporal data, such as satellite image time series, to drive modeling in support of marine spatial planning. The current work demonstrates the feasibility and benefit of such a coupled remote sensing-modeling approach within a shellfish farming context, responding to real and current interests of oyster producers.

Keywords: satellite image, time series, bivalve, dynamic energy budget, growth modeling, MERIS, AVHRR, marine spatial planning

INTRODUCTION

Marine aquaculture (mariculture) now accounts for more than half of the world's total seafood production (FAO, 2018). It is responsible for the overall increase in production observed over recent decades, and is expected to continue to bridge the gap between the ever-growing demand for seafood and supply by capture fisheries, which have been stagnant since the 1980s (FAO, 2018). Whereas nearly all mariculture currently takes place in the nearshore environment, the combination of increased demand for seafood, and environmental impacts, overcrowding and conflicting uses in the near-coastal zone has resulted in increasing interest in moving mariculture further offshore (Kapetsky et al., 2013). At the same time, technical advances, including in offshore submerged structures and multi-use platforms, render offshore mariculture increasingly feasible (Buck and Langan, 2017).

French shellfish production has taken place in the intertidal zone for over a century, and now occupies much of the suitable area (Goulletquer and Le Moine, 2002). Moving production further offshore, in this case beyond the intertidal area, has been considered for several commercial species in France as a means to expand and improve production, beginning with scallops (Buestel et al., 1982) and mussels (Prou and Goulletquer, 2002) in the 1980s, and eventually offshore oyster cultivation (Goulletquer and Le Moine, 2002). Results from experimental offshore oyster cultivation have been promising, generally characterized by faster growth compared with that in the intertidal zone and yielding a product of good quality (e.g., Mille et al., 2008; Glize and Guissé, 2009; Glize et al., 2010; Louis, 2010). Although offshore cultivation is still not commonplace, due largely to administrative barriers (Barillé et al., submitted), it continues to be of interest to producers who seek to optimize production and an alternative to the overcrowded intertidal zone.

Aquaculture is not necessarily feasible everywhere, however, and appropriate site selection for new mariculture farms is key to their success and sustainability. Several socioeconomic (e.g., existing tourism, military, or fishing uses) and environmental (e.g., existing protected areas, adequate ranges of temperature, and other parameters) constraints and influences need to be considered as part of spatial multicriteria evaluation and marine spatial planning endeavors (Falconer et al., 2019). Several recent studies have thusly aimed to determine the potential for various mariculture subsectors at the global scale using such criteria, and at identifying "hot spots" of potential production at the country level (e.g., Kapetsky et al., 2013; Gentry et al., 2017; Oyinlola et al., 2018). Other studies have placed aquaculture site selection within the context of use conflicts and potential environmental impacts at the regional scale (e.g., Falconer, 2013; Brigolin et al., 2017; Depellegrin et al., 2017; Gimpel et al., 2018; Barillé et al., forthcoming). The biological growth potential for a given species is another key factor for site selection and is expected to vary spatially (Barillé et al., forthcoming), likely at even finer, local scales. Spatially-explicit methods are therefore essential to assess farmed species' growth potential across areas of interest, and to thereby inform site selection in the offshore as well as in the nearshore environment.

Satellite remote sensing is increasingly well-suited for mapping the biological potential of various aquaculture subsectors at the local scale, given recent improvements to spatial, temporal, and spectral resolutions of sensors. Shellfish growth is governed by environmental parameters, including inorganic particulate matter and phytoplankton concentrations in the water column, proxies for which can now be mapped by the European Space Agency (ESA) Sentinel-3 Ocean and Land Color Imager (OLCI) at a 300 m scale, with satellite overpasses for a given location occurring every two days or less. This extends the ESA Medium Resolution Imaging Spectrometer (MERIS) legacy from 2002 to 2012 of the same spatial resolution and 2–3-day overpass frequency. Other images are available at a higher spatial, but lower temporal resolution (e.g., Sentinel-2 MultiSpectral Instrument (MSI); 20–60 m every five days for most coastal locations), or vice versa [e.g., NASA Moderate Resolution Imaging Spectroradiometer (MODIS); 1km every day], with other trade-offs in terms of spectral and/or radiometric resolutions. Water temperature is also critical to shellfish growth, survival, and reproduction. Frequent measurements, via sea surface temperature, are also possible using satellite thermal infrared data, from sensors such as the ESA Sentinel-3 Sea and Land Surface Temperature Radiometer (SLSTR; near-daily revisit at 1 km spatial resolution) and the NOAA Advanced Very High Resolution Radiometer (AVHRR; daily revisit at 1 km spatial resolution). The use of remote sensing time series to drive ecophysiological modeling of shellfish growth, including the use of Dynamic Energy Budget (DEB) theory, has been demonstrated for several species and sites, for both aquaculture and environmental applications (e.g., Thomas et al., 2011, 2016; Brigolin et al., 2017; Porporato et al., 2019), but with coarser-resolution data. Satellite imagery has more often been used to generally constrain areas that fall within known tolerance ranges of farmed species and rate suitability in this way (e.g., Radiarta and Saitoh, 2009; Kapetsky et al., 2013; Aura et al., 2016; Snyder et al., 2017).

The current work makes use of a nine-year archive of MERIS and AVHRR time series remote sensing products along with experimental *in situ* oyster growth measurements to demonstrate the feasibility and benefit of such an approach at higher resolutions within a shellfish farming context. We thereby respond to real and current interest by existing oyster producers in Bourgneuf Bay, France, who are considering offshore production as a possible response to overcrowding in the intertidal zone and related issues. Calibration and validation of satellite-derived chlorophyll-a (Chl-a), total suspended matter (TSM), and sea surface temperature (SST) products, used to drive ecophysiological growth modeling, is followed by the calibration and validation of the Pacific oyster DEB model itself. Several industry-relevant production scenarios and performance indicators have been elaborated from the oyster growth time series results, selected with input from producers and industry professionals to provide realistic insight into how offshore production can be expected to compare to existing intertidal production. These are mapped for Bourgneuf Bay, for each full year for which all satellite data products were available (2003–2011), and spatial patterns, contrasting potential new sites,

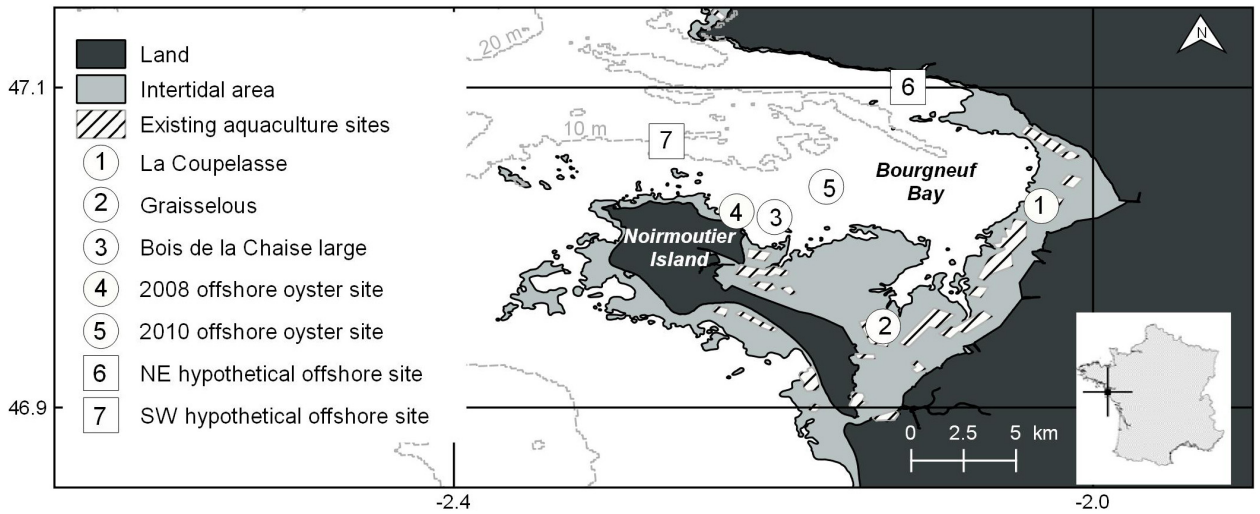

FIGURE 1 | The study site, Bourgneuf Bay, on the French Atlantic coast (indicated in subset). Intertidal (light gray) and offshore (white) zones, in addition to the locations of current aquaculture farms in the intertidal zone and *in situ* water and experimental oyster sampling sites are indicated.

and interannual variation in these growth indicators are explored with respect to the feasibility and site selection of future offshore Pacific oyster farms.

MATERIALS AND METHODS

Study Site

Bourgneuf Bay, located on the French Atlantic coast in the Pays de la Loire region (**Figure 1**), is a 340 km^2 macrotidal embayment (maximal tidal range of 6 m during spring tides and 2 m during neap tides). It is open to the Atlantic Ocean to the northwest, and largely enclosed by the mainland and the Noirmoutier island otherwise, except for a 800 m-wide channel separating the two. Strong spatial gradients in the turbidity of the water column have been observed, with highly turbid conditions [TSM typically > 10 g m^{-3}, and up to more than an order of magnitude higher (Gernez et al., 2017)] in parts of the intertidal zone related to tidal- and wind-driven resuspension of surface sediment at shallower water depths, and relatively clear conditions offshore (Gernez et al., 2014). A predominant intertidal-offshore gradient similar to that of turbidity also exists for Chl-a concentration, related to the contribution of microphytobenthos resuspension at shallow depths (Hernández Fariñas et al., 2017), as well as nutrient loading in the nearshore environment via river discharge and overland runoff, and subsequent dilution and progressive uptake by phytoplankton toward the offshore environment. Chl-a concentration in Bourgneuf Bay has been reported to span several orders of magnitude, and typically ranges from 0.1 mg m^{-3} to occasionally > 5 mg m^{-3} offshore (data from the French Observation and Monitoring program for Phytoplankton and Hydrology in coastal waters database (REPHY, 2017); Bois de la Chaise large sampling site) to ∼1–30 mg m^{-3} across the intertidal zone (Barillé-Boyer et al., 1997; Dutertre et al., 2009; Gernez et al., 2017). From northeast to southwest within the intertidal zone, La Coupelasse (site 1, **Figure 1**) is on average five times more turbid and comprises an overall smaller sediment grain size (Dutertre et al., 2009; Gernez et al., 2014), as well as a higher concentration of particulate inorganic matter (PIM) than Graisselous (site 2, **Figure 1**; Méléder et al., 2005). Chl-a concentration also tends to be two to four times higher at La Coupelasse than at Graisselous (Dutertre et al., 2009). Superimposed on the general patterns of turbidity and productivity are the effects of currents, bathymetry, and sediment type within the bay.

There are currently 283 mainly small oyster farms occupying leases over approximately 10% of the 100 km^2 intertidal zone, producing Pacific oysters (*Crassostrea gigas*) in approximately three-year growth cycles for sale in the local market (Guillotreau et al., 2018). Expanding production to the offshore environment has been of interest to Bourgneuf Bay farmers for some time now, as there is no more room to expand in the intertidal zone. Furthermore, successful offshore experiments in the nearby Marennes-Olérons Bay in the 1990s (Mille et al., 2008) and in Bourgneuf Bay since the late 2000s (Glize and Guissé, 2009; Glize et al., 2010; Louis, 2010) suggest enhanced growth conditions in the offshore environment. Offshore production is seen as a means to increase and diversify production and to shorten the overall production cycle duration within the bay. It is also thought to have the potential to decrease the density of production in the over-crowded intertidal zone, thereby decreasing the probability of disease and related mortality (Pernet et al., 2018).

Satellite Data and Processing

All environmental variables, namely SST, TSM concentration, and Chl-a concentration, were derived from satellite observations. Although more recent satellite data are now available, for example from Sentinel-2 MSI, Sentinel-3 OLCI, and Landsat 8 Operational Land Imager sensors, these are only available for later periods (i.e., from 2015 and 2013 respectively),

and as such do not coincide with our earlier *in situ* data (described in detail below) needed for algorithm validation. MERIS and AVHRR data from 2003 to 2011 were therefore used here. For SST retrieval, the operational non-linear split-window algorithm (Brewin et al., 2017) was applied to data from the US National Oceanic and Atmospheric Administration (NOAA) AVHRR daytime and nighttime scenes with a 1 km spatial resolution. Data from the ESA MERIS have been widely used for the retrieval of optical water quality parameters, including Chl-a as a proxy for phytoplankton concentration and TSM, in a variety of inland and coastal settings (e.g., Matthews, 2011; Odermatt et al., 2012; Blondeau-Patissier et al., 2014; Mouw et al., 2015; Palmer et al., 2015). Nevertheless, there exist no globally-validated retrieval algorithms for the optically dynamic and near-coast environment studied here. Therefore, we investigated full resolution and swath (FRS; spatial resolution 300 m) MERIS data, processed using the Calimnos processing chain, which is designed to dynamically resolve optical water quality parameters in a variety of optically complex inland waters (Simis et al., 2018). Version 1.21 of the processing chain was applied to the 1934 level 1 (L1b) FRS images including our site from the period 2003–2011, and comprised Polymer atmospheric correction with a mineral absorption model, the removal of flagged invalid and suspect pixels, and the application of Chl-a and TSM retrieval algorithms to obtain L2 products.

The MERIS Chl-a and TSM products available through Calimnos and tuned to lake optical properties according to the water types described by Spyrakos et al. (2018) were not found to adequately match the concentrations measured *in situ* at our site, but several had robust linear relationships with the *in situ* data. We therefore recalibrated these algorithms for Bourgneuf Bay to improve confidence in the results and applied the recalibrated algorithms to the full time series of interest. The overall best performing algorithms for the detection of water column constituents including both offshore and intertidal matchups (highest coefficient of determination, R^2, for model fit) were OC2 (O'Reilly et al., 2000) for Chl-a retrieval, which is a fourth-order polynomial relationship between the ratio of the MERIS band centered at 490 nm to that centered at 560 nm and Chl-a, and the Binding et al. (2010) algorithm for TSM, which uses the MERIS band centered at 754 nm in semi-analytical inverse modeling. Recalibration and validation of Chl-a and TSM retrieval algorithms was carried out by splitting our *in situ* data set into two groups at random; one (70%) to determine the tuning coefficients (i.e., recalibration) and the other (30%) to assess how accurately the tuned algorithm retrieved the absolute concentrations (i.e., validation), in terms of mean bias and absolute and relative root mean square error (RMSE):

$$\text{Bias} = \frac{1}{n}\sum_{1}^{n}(M - O)$$

$$\text{RMSE} = \sqrt{\frac{\sum_1^n (M-O)^2}{n}}$$

$$\text{Rel. RMSE}(\%) = \text{RMSE}/(\max(O) - \min(O)) \times 100,$$

where M refers to the model-predicted value, O refers to the observed, or *in situ*-measured value, and n to the number of validation matchups. The original SST retrieval algorithm calibration was similarly validated, but without splitting the matchup dataset into calibration and validation subsets for recalibration.

The archive *in situ* datasets used to recalibrate and validate the satellite products used in this work comprised measurements made at three locations across the bay; the northern La Coupelasse (47.026 N; -2.032 E) and the southern Graisselous (46.951 N; -2.132 E) sites in the intertidal zone, and Bois de la Chaise large (47.042 N; -2.061 E), located offshore near Noirmoutier island (**Figure 1**). Multi-parameter water quality probes (YSI 6600) were attached to oyster racks at a height of approximately 0.6 m from the bottom for a duration of two years (2005–2006) at La Coupelasse and Graisselous. These were cleaned manually of biofouling every two months, and turbidity and fluorescence sensors were cleaned with an automatic brush system every 15 min. Hourly measurements of temperature, Chl-a fluorescence, and turbidity, as well as salinity were recorded, and fluorescence and turbidity converted to Chl-a and TSM concentration respectively using field-calibrated relationships obtained and provided in Dutertre et al. (2009). Approximately bi-weekly samples acquired from Bois de la Chaise large for Chl-a quantification by monochromatic spectrophotometry and *in situ* temperature measurements collected from the surface layer (0–1 m depth) beginning in March 2007 were used here (REPHY, 2017). For all three sites, same-day matchup data were selected from within a 3 h window of the corresponding MERIS overpass, with the closest hour to overpass chosen in the case of the hourly probe data, and comprise the value obtained from the MERIS pixel coinciding with the given *in situ* sampling location. The total number of matchup points for each parameter and per site, which span all seasons of multiple years, are provided in **Table 1**.

Following recalibration and validation using daily matchups, all Earth Observation-derived data were processed at and provided by Plymouth Marine Laboratory, and aggregated to L3 ten-day averages from 2003 to 2011 to create the full-year, regular time series data to run the DEB model, given irregular

TABLE 1 | Total and per site numbers of *in situ*-satellite retrieval matchups for each of the variables used as input into DEB modeling.

Variable	Site	# of matchups
Chl-a	La Coupelasse	23
	Graisselous	23
	Bois de la Chaise large	16
	Total	62
TSM	La Coupelasse	22
	Graisselous	24
	Bois de la Chaise large	0
	Total	46
SST	La Coupelasse	17
	Graisselous	23
	Bois de la Chaise large	78
	Total	119

overpass frequency (2–3 days) and gaps from cloud cover in the original data.

Pacific Oyster Dynamic Energy Budget (DEB) Model

DEB theory was used here to model the growth of Pacific oyster. This is a generic (i.e., non-species specific) approach to mechanistically model the uptake and flow of energy through, and eventual growth and reproduction of an organism, based on its environmental conditions (Kooijman, 2010; Sousa et al., 2010). DEB models have been adapted and published for a broad range of species[1].

The DEB model equations and parameters applied here for Pacific oyster are detailed in Thomas et al. (2016), building on previous work by Bernard et al. (2011) and Pouvreau et al. (2006). Essentially, food availability (mainly phytoplankton and resuspended microphytobenthos, represented here using satellite image-derived Chl-a) and water temperature (using satellite image-derived SST in this well-mixed water column) interactively and variably influence rates of ingestion, assimilation, storage, and metabolism, resulting in energy for growth and/or reproduction depending on reserves and additional conditions being met (**Figure 2**; Thomas et al., 2016). In coastal areas, highly turbid conditions can also have a substantial impact on clearance rate, food consumption, and ingestion (Barillé et al., 1997; Gernez et al., 2014, 2017), subsequently limiting growth. Thomas et al. (2016) have included the effect of high turbidity in Pacific oyster DEB modeling through the inclusion of PIM, which we have also done here (represented using satellite image-derived TSM). The degree to which the ingestion rate is influenced by food availability and TSM in the current work is modeled using calibrated ingestion half-saturation coefficients, X_k and X_{ky} respectively; all other equations and parameters are those reported in Thomas et al. (2016, S1). Model output is dry flesh mass (DFM; g) and shell length (L; cm) at the same spatial and temporal resolutions as the MERIS input data (i.e., 300 m and every ten days here). To compare with *in situ* measurements of oyster morphology and to transform into the industry-relevant indicators described below, L was converted to total weight (TW; g) using the biometric relationship found between measurements of the two variables from the extensive Réseau d'observations conchylicoles database (RESCO; Fleury et al., 2018; Equation 1). Flesh weight (FW; g) was likewise calculated from DFM, using the relationship obtained between RESCO measurements from Bourgneuf Bay specifically (n = 2943, R^2 = 0.83; 2008–2017) (Equation 2).

$$TW = 0.076 \times L^3 \quad (1)$$

$$FW = 3.99 \times DFM + 0.97 \quad (2)$$

For calibration and validation of the ingestion half saturation coefficients (X_k and X_{ky}; see above), the DEB model was initialized with oyster measurements made at the beginning of *in situ* experiments carried out by the Syndicat Mixte pour le Développement de l'Aquaculture et de la Pêche en Pays de la Loire (SMIDAP), a regional association supporting shellfish farmers and fishers, over the course of two growing seasons (2008; 2010) (Glize and Guissé, 2009; Glize et al., 2010; Louis, 2010). The model was run for the specific date range of the *in situ* measurements for the years in question. The 2010 measurements (May 6 through October 17) were used in the iterative optimization-based calibration, as more data were available and over a longer period for this year. The 2008 measurements and corresponding date range (May 20 through August 14) were then used to independently validate model output with calibration results applied. The model was run for an immersion time of 100% for the offshore site (i.e., constant immersion) and of 75% for the intertidal zone (i.e., under water 75% of the time on average), as calculated by Thomas et al. (2016).

Resulting total oyster weight was extracted for the locations and dates coinciding with the *in situ* measurements, and model-predicted values were evaluated through regression against measured *in situ* values. Ingestion half-saturation coefficients were selected in the calibration process as the combination of X_k and X_{ky} that maximized the coefficient of determination (i.e., R^2). Model performance was validated through the mean bias and absolute and relative RMSE. This was carried out for adult and spat life stages separately, given morphological differences between them that may affect ingestion efficiency,

[1]https://www.bio.vu.nl/thb/deb/deblab/add_my_pet/

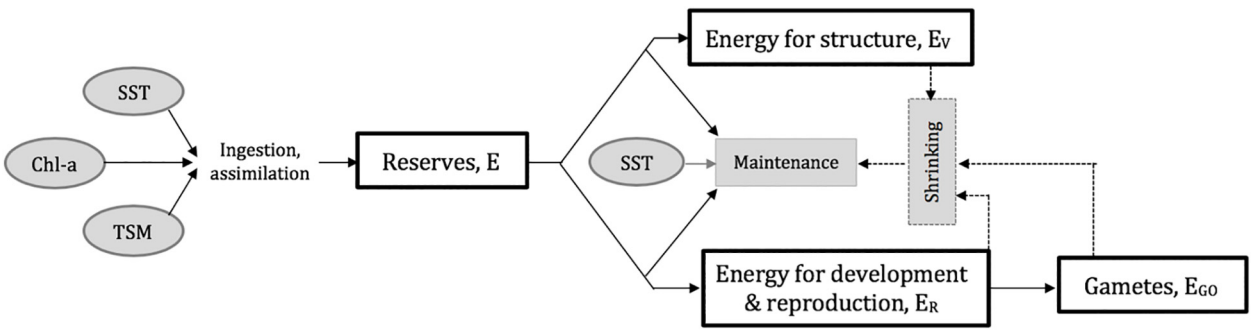

FIGURE 2 | Schematic of the Dynamic Energy Budget (DEB) modified and parameterized from Thomas et al. (2016).

TABLE 2 | Total Pacific oyster weight ranges and quality indices corresponding to French market calibers and classes (AFNOR, 1985; Gosling, 2003).

Caliber	Total weight range (g)	Quality index (%)
0	>150	NA
1	121–150	NA
2	86–120	NA
3	66–85	NA
4	46–65	NA
5	30–45	NA
Normales	>30	<6.5
Fines	>30	6.5–10.5
Spéciales	>30	>10.5

and for offshore and intertidal sites, to obtain the ingestion half-saturation coefficients to be used to model the growth of each under various production cycle scenarios.

Pacific Oyster Production Cycle Scenarios and Growth Performance Indicators

Pacific oyster production is typically divided into three stages. The first is pre-growing, whereby spat, often weighing less than 1 g, are grown out to a certain size range (on the order of 10–20 g) for resale, or are then thinned out to allow for sufficient space to continue to grow on the same farm. Here, spat of the industrial size scale T6/T8, corresponding to a total weight of 0.5 g, grown out to size T20/T25, or 14 g total weight, are considered. Although this can take place in marine water or in nurseries, only the former is considered here. From this stage, adults are grown-out to final market size, which ranges from a minimum of 30 g (caliber 5 in France; **Table 2**) to upward of 150 g (caliber 0 in France; **Table 2**; Gosling, 2003). Finally, for a short period (several weeks to months) following grow-out, many producers undertake finishing or fattening, which aims to increase the quality index, essentially the fleshiness of the oyster (i.e., ratio of flesh weight to total weight), rather than the total weight, starting with an already market-weight product (i.e., ≥30 g). In France, defined quality index thresholds correspond to certain classes: *Normales*, *Fines*, and *Spéciales*, with *Fines* obtaining higher market prices than *Normales*, and *Spéciales* obtaining higher market prices than *Fines* (AFNOR, 1985; Gosling, 2003).

Validated half-saturation coefficients were used in DEB modeling of the scenarios described in **Table 3**, and resulting oyster growth curves were transformed into the associated industry-relevant growth performance indicators (**Figure 3**). In addition to the initial oyster sizes and scenario dates (**Table 3**), which were chosen in consultation with regional oyster producers and professionals, indicators were also elaborated based on producer and professional input and feedback. These include the time required to reach a target marketable size for both spat (sale to another farm) and adults (sale to market for consumption); total weight achieved by a particular date (here, the main December market corresponding to the traditional peak of oyster consumption for Christmas and New Year celebrations (Buestel et al., 2009), is selected for demonstration); quality index after targeted finishing periods; and the number and timing of spawning events. The latter could be seen as either favorable (i.e., for including or optimizing spat settling and collection as a complementary economic avenue within a grower's production) or unfavorable (i.e., resulting in additional biofouling as spat settle on cages or other equipment, and (at least temporarily) reducing the quality index of the animal) to production and operations, depending on a particular grower's specialization and objectives. Overall, our goal was to provide a suite of industry-relevant indicators of which locations would be best suited for oyster farming, and this for various stages and considerations of production.

Oyster growth curves were generated for each MERIS pixel and for each year of input data (2003–2011). The indicators described above were mapped for each year, and the interannual means and standard deviations were then calculated and mapped, with a single-iteration 3 × 3 pixel median filter applied. By using this multi-year approach, we reduced the chance of unintentionally only mapping an uncharacteristic year (i.e., substantially more or less productive or turbid than usual; much higher or lower temperatures) and thereby capture more typically representative conditions across Bourgneuf Bay. This also allowed us to explicitly consider the interannual variability in the indicators, which is of interest to the farmers, as they seek to optimize production, reducing unnecessary inputs and losses, and therefore seek consistent (akin to

TABLE 3 | Scenarios and indicators for different production cycle stages (spat; adult grow-out; finishing/fattening) processed from Pacific oyster DEB growth modeling.

Production stage	*Initial oyster size	Scenarios	Indicators
Spat pre-growing	0.5 g total weight, 1.9 cm shell length, 0.05 g dry flesh mass	Apr. 1 start date (Dec. 6 end) Jun. 30 start date (Dec. 6 end) Aug. 29 start date (Dec. 6 end)	Days to reach T20/T25 (14g)
Adult grow-out	14 g total weight, 5.7 cm shell length, 0.3 g dry flesh mass	Jun. 30 start date (Dec. 6 end)	Time to reach minimum market weight (30 g), Total weight at end date, Number of spawning events
Finishing/fattening	76 g total weight, 10 cm shell length, 0.9 g dry flesh mass	Jul. 30 start date (Dec. 6 end) Aug. 29 start date (Dec. 6 end) Sep. 28 start date (Dec. 6 end)	Quality index (QI = flesh weight/total weight)

**Initial sizes correspond to commercial ratings of T6–T8 for spat pre-growing, T20–T25 for adult grow-out, and Caliber 3 for finishing.*

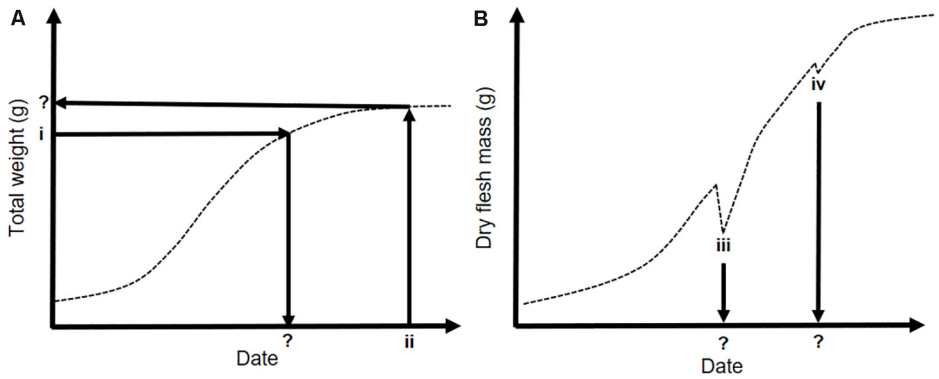

FIGURE 3 | Conceptual schematics of the types of growth performance indicators developed in consultation with oyster growers and professionals and extracted from our modeled growth time series maps. **(A)** Total oyster weight as a function of time throughout the growing season. (i) Represents the date a target weight is achieved as the parameter of interest, e.g., minimum market weight (30 g). (ii) Takes a given date of interest as the starting point (e.g., early December, in time for the main French oyster market), and looks at what total weight is achieved by this date. **(B)** Dry flesh mass (DFM) over time throughout the growing season; sharp decreases in DFM indicate spawning events. (iii) and (iv) Indicate the timing of these spawning events, and can also be summed to determine the number of spawning events at a given site in a given year.

more reliable) and stable conditions in addition to higher growth potential.

Demonstration of Offshore and Intertidal Farm Site Comparison

Two hypothetical lease sites were considered; one situated in the northeast and the other in the southwest, near the mouth of the bay (**Figure 1**). The sites were selected in order to appraise the diversity of growth conditions in the offshore area, the northeastern site being located in more turbid and Chl-a-rich waters than the southeastern site. Each comprised a five-by-five-pixel region of interest, corresponding to approximately 2.25 km^2 and similar in size to some of the existing leases in the intertidal zone (**Figure 1**). Descriptive statistics were then extracted and visualized for each hypothetical offshore farm and for the existing intertidal leases for comparison, for each selected growth indicator. Following testing for normality (Shapiro–Wilk) and equal variance, the annual means of each indicator were also compared between sites through parametric one-way ANOVA, or using the Kruskall–Wallis one-way ANOVA by ranks when either normality (Shapiro–Wilk) or equal variance testing failed, with *post hoc* Tukey tests for pairwise comparison. In all cases, an $\alpha = 0.05$ was selected for significance.

RESULTS

Satellite Input Data Calibration, Validation, and Mapping

Results from the empirical recalibration and validation of Chl-a (OC2) and TSM (Binding et al., 2010) retrieval algorithms, and the validation of the original SST (operational NOAA AVHRR) calibration, can be found in **Figure 4**. For Chl-a and TSM, retrievals using the original algorithm parameterization showed either a strong linear over- or underestimation (**Figures 4A,C**), and linear recalibration (n = 44 and 32 respectively) was therefore performed (**Figures 4B,D**), improving retrievals of the three parameters, with only slight positive mean bias in the satellite retrievals for each (Chl-a = 0.74 mg m^{-3}, n = 18; TSM = 2.6 g m^{-3}, n = 14). The original SST calibration (n = 119) was found to sufficiently reproduce *in situ* measurements from the three sites (**Figure 4E**), and was therefore applied as-is to the nine-year time series.

Maps of the interannual mean and standard deviation of the three parameters (**Figure 5**) highlight the general spatial patterns observed and their interannual variability across Bourgneuf Bay. As expected, both Chl-a (**Figures 5a,b**) and TSM (**Figures 5c,d**) are higher on average and more variable in the intertidal and adjacent areas than further offshore at greater water depths, with both the absolute concentration range and variability of the latter being much greater. Likewise, higher average SST (**Figure 5e**) is found in the nearshore areas, with higher variability in the central bay (**Figure 5f**).

DEB Model Calibration and Validation

A good fit was found between DEB-modeled spat and adult oyster total weight growth and weights measured *in situ* throughout the growing season following calibration of the ingestion half saturation coefficients, X_k and X_{ky} (**Figure 6** and **Table 4**). Modeled spat (0.5–13.45 g) and adult (20.9–47.1 g) total weight corresponded to a RMSE of 1.30 g (13.4%) and 4.34 g (17.4%) and mean biases of 0.55 and -3.37 g respectively, compared with measured *in situ* values. In both *in situ* measurements and modeled values (in both 2010 and 2008), we see higher weight gain offshore compared with the same amount of time in the intertidal zone. This is most notable for 2010, for which *in situ* measurements were taken over a longer period than in 2008 (May 1 through October 17 versus May 20 through August 14), thereby allowing growth

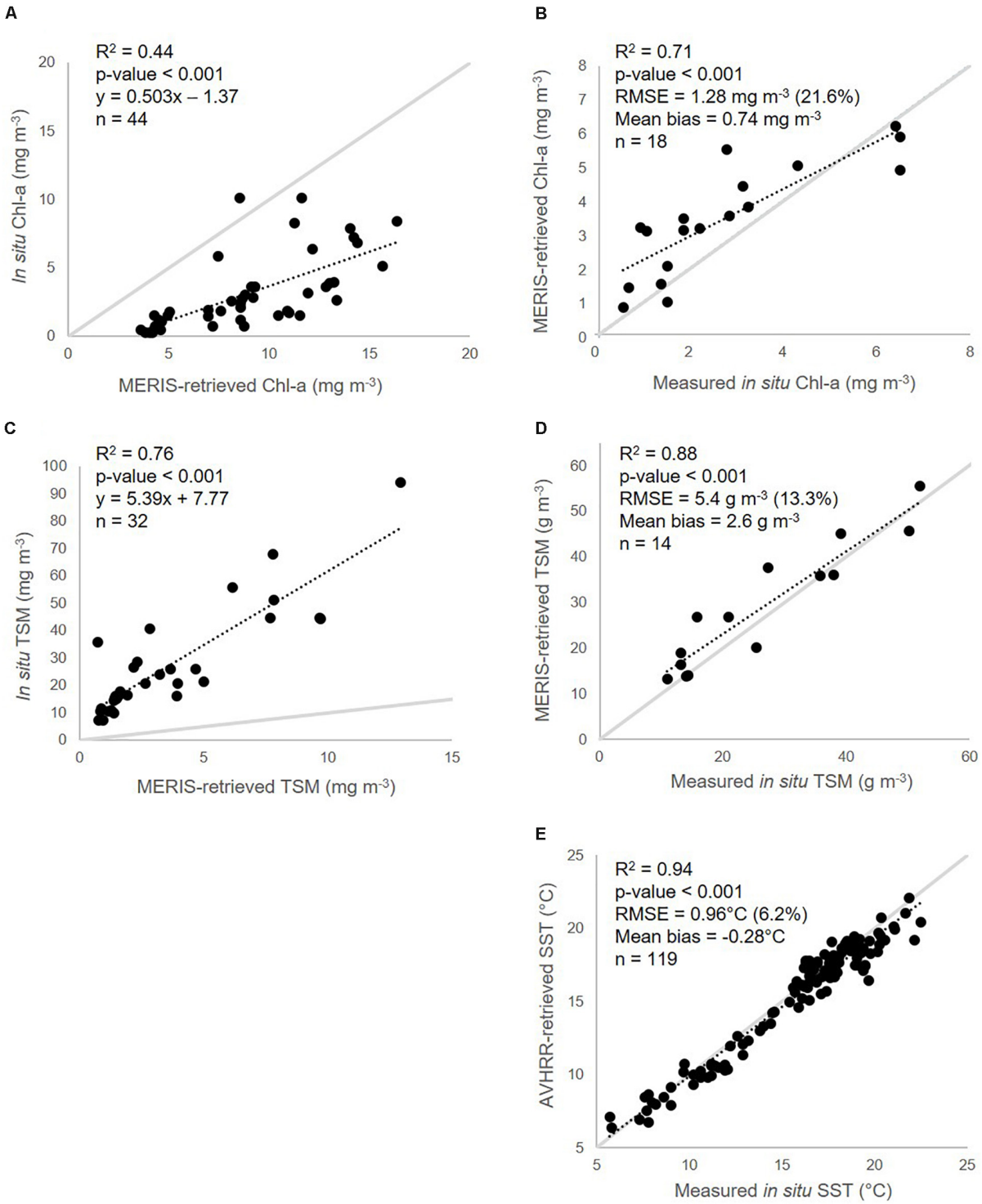

FIGURE 4 | Recalibration **(A,C)** and validation **(B,D)** of MERIS OC2 Chl-a **(A,B)** and Binding et al. (2010) TSM **(C,D)** retrieval algorithms, and validation of original SST **(E)** retrieval algorithm calibration, used to drive the DEB model, with corresponding *in situ* data from Bourgneuf Bay (**Figure 1**).

to heavier weights to be achieved. Even spat grown from an initial weight of < 1 g were able to reach market weight offshore by mid-September (**Figure 6A**) in 2010, although this was slightly underestimated by the MERIS-DEB-modeled results. Note that initial measurements (i.e., from May 1, 2010 and May 20, 2008) were used in model initialization for calibration

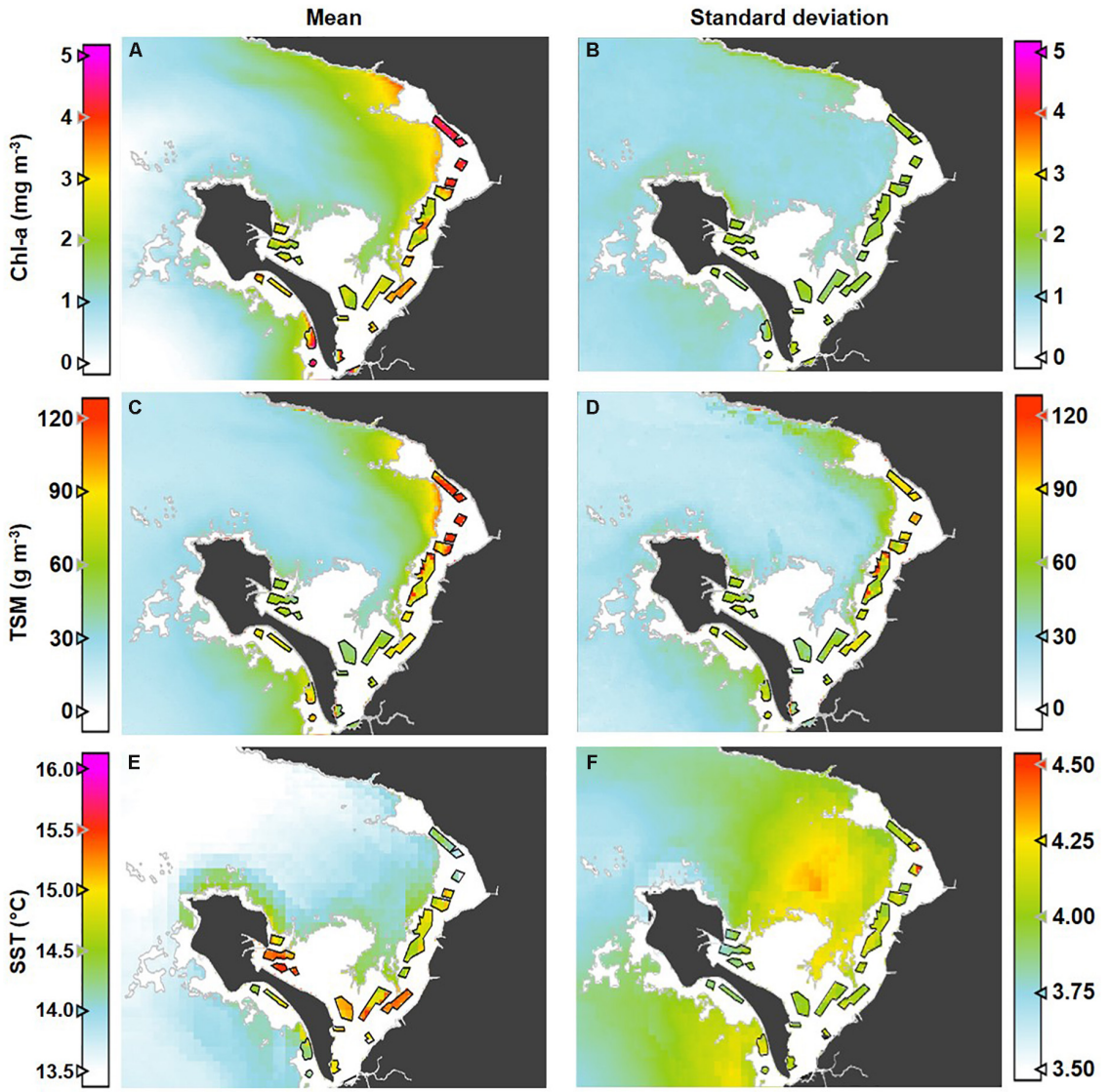

FIGURE 5 | Maps of interannual mean (left) and standard deviation (right) for input products across the full nine-year time series; **(A,B)** Chl-a, **(C,D)** TSM, and **(E,F)** SST. In the intertidal zone, the Chl-a, TSM, and SST mean and standard deviation are shown within the farming sites only (i.e., unmapped for the white area).

and validation respectively, and therefore were not included in matchup statistics or graphing.

Growth Indicator Mapping

The Pacific oyster production scenarios and growth indicators detailed in **Table 3** were modeled for each of the nine full years of satellite image input data. For each scenario, the resulting interannual mean and standard deviation are mapped in **Figures 7**, **8** respectively. Mapping trends across the nine indicators and three production cycles suggest generally enhanced growth in the northeastern offshore segment of the bay across all indicators, higher than in the intertidal zone where production is currently practiced and higher than in the southwestern offshore segment (**Figure 7**).

For the spat pre-growing phase, industry size T6–T8 spat (initial total weight of 0.5 g) were put in place at staggered start times (April 1, June 30, and August 29) and highlight that, in the northeastern offshore segment of the bay, it would be possible to begin this phase at later dates than in the southwestern offshore and intertidal areas, as late as the end of August (**Figure 7C**), and still achieve the target size (T20–T25; 14 g) for sale in under 2 months. Indeed, in the intertidal area, pre-growing must begin in the spring to achieve the target weight gain of a T20–T25 spat by October, over 6 months later. In the southwestern offshore segment, it must begin by early summer at the latest (i.e., June 30; **Figure 7B**), to reach the target weight within 6 months, by late November/early December.

For adult grow-out, a single time frame was considered (June 30 through December 6), but three different growth indicators

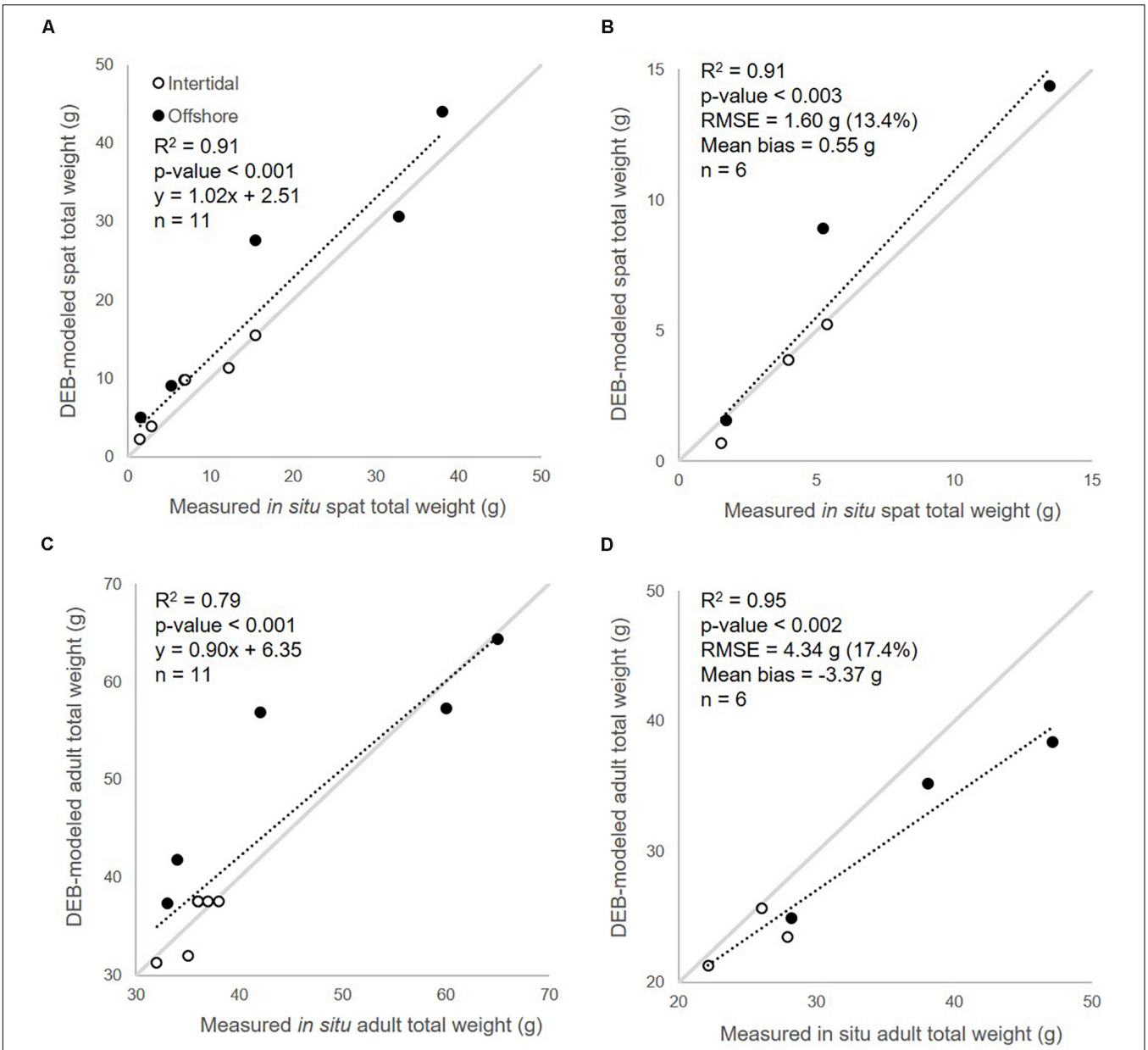

FIGURE 6 | Calibration of DEB-modeled **(A)** spat and **(C)** adult growth using corresponding 2010 *in situ* data from intertidal and offshore zones; validation for spat **(B)** and adult **(D)** growth modeled with calibrated coefficients using *in situ* data from 2008 (see **Figure 1** for sampling locations).

were of interest. First, the time to reach the minimum market size for consumption (30 g; **Figure 7D**) as well as the total weight by early December (**Figure 7E**) were jointly assessed as they are of primary interest for the industry. Although minimum market weight was able to be reached for a few, dispersed areas in the intertidal zone for an average year, this took until the end of the growing season considered here (i.e., early December, after 160 days), which was also the case for the southwestern offshore segment (**Figure 7D**). Instead, 30 g (i.e., minimum market weight) is achieved by mid-August to early October on average on the northeastern offshore segment (**Figure 7D**). Total weight by early December, for the initial conditions and dates considered here, tends to remain on the order of 15–25 g (**Figure 7E**) for the southwestern offshore area and the existing intertidal farms, and oysters would require another season before marketable. In contrast, total weight by the end of the season for the northwestern offshore segment is on average greater than 45 g for some areas (i.e., Caliber 4 oysters; **Table 2** and **Figure 7E**). Certain offshore areas, notably the eastern and central portion of the bay, are associated with slightly more spawning activity on average (**Figure 7F**), which could indicate areas to avoid or to target for farm placement,

TABLE 4 | Calibrated half-saturation coefficients (X_k, X_{ky}) used in MERIS-driven DEB modeling of Pacific oyster spat and adult growth, and applied to all nine modeled years.

Production stage	Zone	Parameter	Value
Spat (T6–T8)	Intertidal	X_k	1.9
		X_{ky}	23.7
	Offshore	X_k	0.6
		X_{ky}	27.2
Final year adult	Intertidal	X_k	2.5
		X_{ky}	17.0
	Offshore	X_k	1.1
		X_{ky}	16.8

All other parameters used in the model are from Thomas et al. (2016, S1).

depending on whether spat collection is foreseen as part of a given production cycle.

The quality index and classification according to French standards (*Normales*, *Fines*, or *Spéciales*) for sale to the main French market in early December that was achieved by starting at three different dates, from large Caliber 3 (76 g) *Normales* oysters (QI = 6%) was considered for a final fattening phase (**Figures 7G–I**). Throughout most of the intertidal area, only *Normales* classification was achieved on average (orange in **Figures 7G–I**), whereas at least *Fines* was possible throughout much of the offshore area (pale yellow in **Figures 7G–I**). An early start to fattening (late July/early August) resulted in *Spéciales* classification over a large part of the offshore area (blue in **Figure 7G**).

Intertidal and Offshore Farm Site Comparison

Modeled growth indicators were compared statistically for the two potential offshore farm sites located in contrasting conditions, one in the northeastern segment of the bay, the other in the southwestern segment, with average values across existing farms in the intertidal zone (**Figure 9**). Although these hypothetical sites were chosen here to simplify

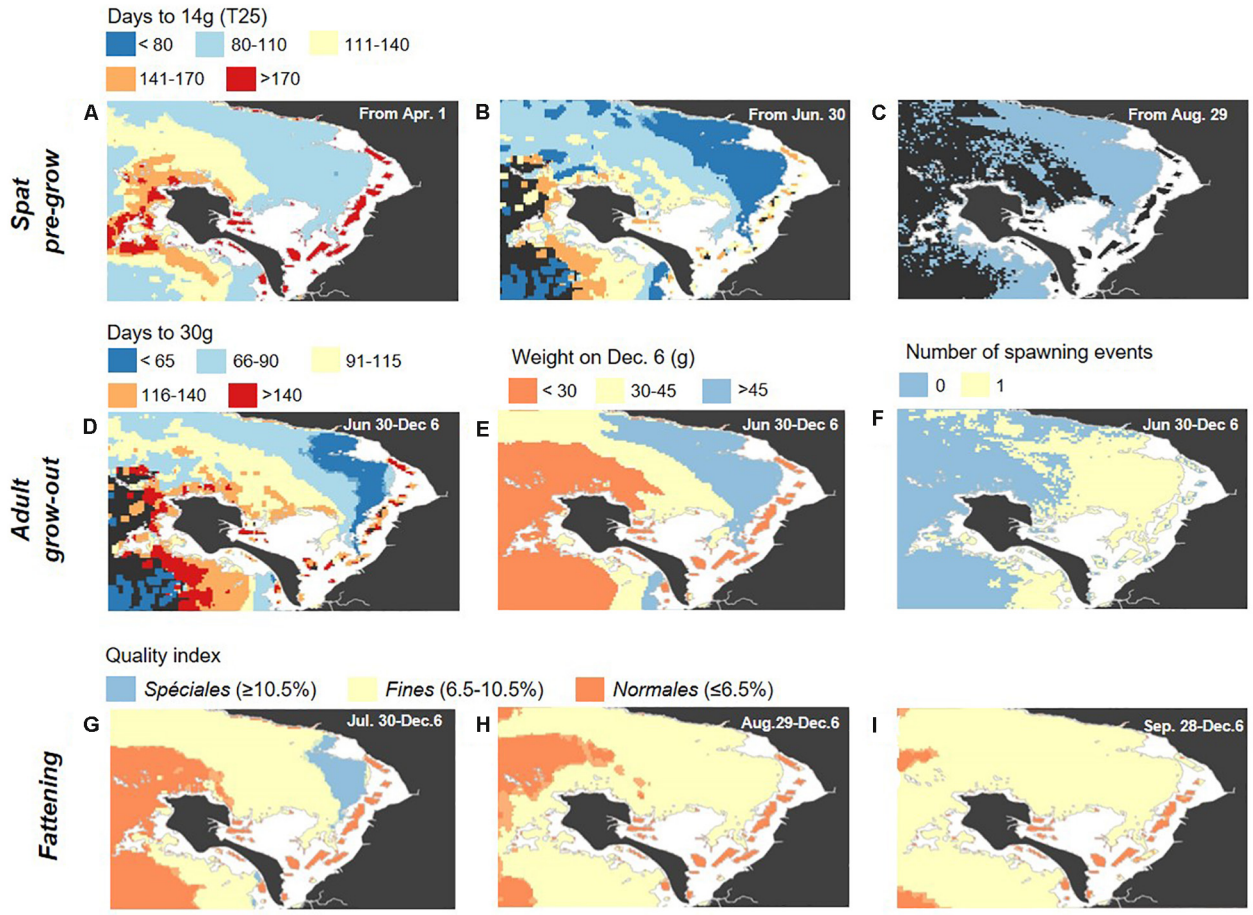

FIGURE 7 | Maps of the nine-year interannual means for the scenarios and growth indicators detailed in **Table 3**, for the spat pre-growing phase **(A–C)**, from an initial T6–T8 (0.5 g) size, adult grow-out phase **(D–F)**, from an initial T25 (14 g) size, and final fattening phase **(G–I)**, from an initial Caliber 3 *Normale* size (76 g; QI = 6%). Note that dark gray water areas in a-d correspond to areas where the target weight (i.e., 14 g for spat and 30 g for adults) was not achieved by the end of the growing season.

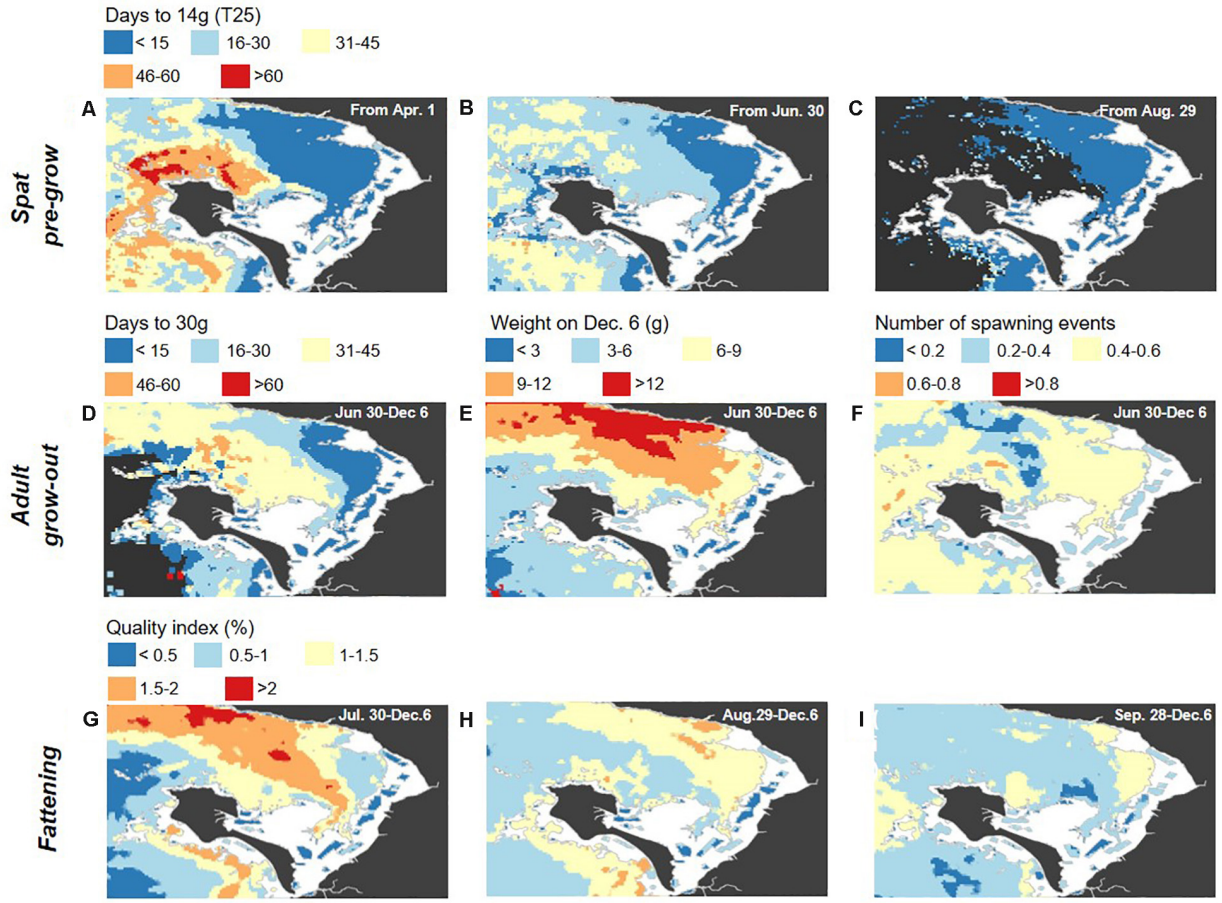

FIGURE 8 | Maps of the nine-year interannual standard deviations for the scenarios and growth indicators detailed in **Table 3**, for the spat pre-growing phase **(A–C)**, from an initial T6–T8 (0.5 g) size, adult grow-out phase **(D–F)**, from an initial T25 (14 g) size, and final fattening phase **(G–I)**, from an initial Caliber 3 Normale size (76 g; QI = 6%). These correspond to the means presented in **Figure 7**. Note that dark gray water areas in **(A–D)** correspond to areas where the target weight (i.e., 14 g for spat and 30 g for adults) was not achieved by the end of the growing season.

the demonstration of our approach, such a comparison could be made for any selected site, and these findings are expected to extend beyond the hypothetical new farm sites considered here, with similar findings mapped across larger areas in **Figures 7**, **8**.

It is clear that although enhanced growth is expected in the offshore environment, as already observed in *in situ* experimental data for single point locations (**Figure 6**) and in mapped interannual average indicator values (**Figure 7**), this is highly variable across the approximately 240 km^2 of the offshore area considered. Notably, we consistently see faster growth and higher quality products at the northeastern site (**Figure 9**; dark blue box), with the southwestern site (**Figure 9**; turquoise box) most often either statistically indistinguishable (KW and Tukey test $p < 0.005$) from growth on the existing intertidal farms (**Figure 9**; magenta), or falling in between the NE and intertidal sites. Exceptions are the number of days for spat to reach 14 g from the second start date, June 30, where this is reached for the SW site, but not in the intertidal zone (**Figure 9B**), and the slightly higher average number of spawning events per year observed in the intertidal zone, with the two offshore sites statistically indifferent (**Figure 9F**).

DISCUSSION

DEB Input and Output Validation: General Findings and Limitations

Due to the empirical calibration of Chl-a and TSM algorithms, these are only considered to be valid for Bourgneuf Bay without wider validation, and specifically for the conditions encountered in the *in situ* matchup dataset. This remains an important consideration here, and in the use of calibrated satellite products for water quality parameter retrieval generally. Ongoing work on automatized algorithm selection based on satellite-observed optical characteristics promises a robust solution to this issue through the provision of more globally-valid products (e.g., work of Spyrakos et al., 2018; Neil et al., 2019 for lakes), but was not yet adapted for the optical conditions of our site for use in this work. Similar validation, and possibly calibration,

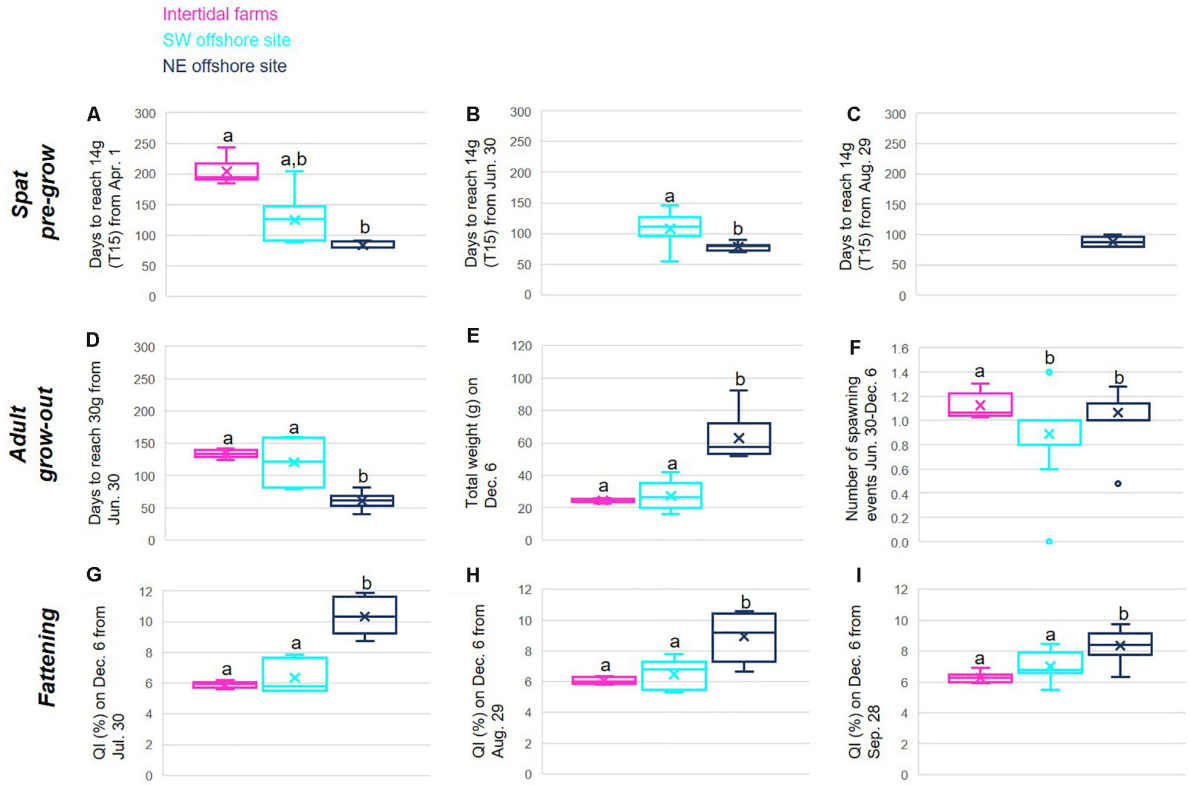

FIGURE 9 | Comparison of interannual indicator values for two hypothetical offshore sites (see **Figure 1**) (dark blue (NE) and turquoise (SW)) and existing intertidal farms (pink) for the scenarios and growth indicators detailed in **Table 3**, for the spat pre-growing phase **(A–C)**, from an initial T6–T8 (0.5 g) size, adult grow-out phase **(D–F)**, from an initial T25 (14 g) size, and final fattening phase **(G–I)**, from an initial Calibre 3 Normale size (76 g; QI = 6%). Different letters above boxes are associated with statistically different groups (Kruskall–Wallis one-way ANOVA on ranks and Tukey test $p < 0.05$). Note that missing boxes associated with given sites **(B,C)** correspond to the target weight not being achieved for that site within the defined time range.

of satellite products would also be required in future work at other sites until a more automated approach is available, and limits the spatial range over which results can be expected to be valid. Given the range of conditions and temporal coverage (i.e., interseasonal and interannual; spanning all seasons of several years, as well as multiple sites within the bay comprised of contrasting conditions) of the *in situ* matchup dataset, such local calibration was possible in the current work and the resulting satellite products are expected to adequately represent the conditions for the area and time period of interest for the current modeling application.

For both DEB modeling results and input parameter validation, single-point measurements taken *in situ* are compared with satellite pixel data integrating the signal of 0.09 km^2, which is a well-known source of error inherent to the methodology. In addition, whereas same-day matchups were used to calibrate and validate the input products, in the DEB modeling, daily images were aggregated to ten-day mean products to reduce gaps and noise in the data. Modeled oyster growth extracted for matchup validation are then the ten-day modeled periods within which the given *in situ* measurements were taken, and represent an additional, temporal source of uncertainty. More recent satellite image data, for example from the ESA Sentinel-2 MultiSpectral Instrument and Sentinel-3 Ocean and Land Color Imager, improve upon the spatial and temporal resolutions respectively of the data used here and the availability and use of such higher resolution data will offer potential new insights and directions for future work. It is also worth noting that although the oyster growing season typically begins in March and ends in December, *in situ* data were only available from May through August (2008) and October (2010), which corresponds to the period of most and most rapid growth in the year. Nonetheless, growth dynamics were found to be well-captured here using the coupled MERIS-DEB results. Following the calibration of the half-saturation coefficients (X_k, X_{ky}), modeled results were found to robustly capture oyster growth over time, for spat as well as for adults, and for both intertidal and offshore sites alike. The differences in the half-saturation coefficients resulting for the two life stages may be explained by developmental differences in their gills and labial palp morphologies affecting their respective ingestion efficiencies (Dutertre et al., 2007, 2017). With regard to site differences, food quality (and phytoplankton composition in particular) is recognized to be key to bivalve nutrition (Picoche et al., 2014). Differences in the composition of phytoplankton communities between the intertidal and offshore sectors could therefore explain the differences in X_k, which were

higher in the intertidal sector for both spat and adult oysters. The high Chl-a concentrations measured in the intertidal zone may therefore be associated with phytoplankton or resuspended microphytobenthos of poorer food quality, in addition to the negative impact of the higher turbidity on oysters' filtering ability.

Given the investigative and experimental nature of offshore oyster cultivation in this area, *in situ* data for model calibration and validation are limited to only the two periods presented here (2008 and 2010), each with only one intertidal and one offshore site. These are, however, expected to represent the main component of variability in the input parameters, and therefore in oyster growth, within the bay overall. As for the satellite input data, however, empirical DEB model calibration using this local *in situ* data means that application of this model and similar methods at other sites would require recalibration with data from the given site. As offshore shellfish production remains quite experimental in nature and is not common either commercially or experimentally, such data are very seldom available and may present a barrier to carrying out similar future work elsewhere. Monaco et al. (2019) observed the inability to transfer DEB parameterization of the Mediterranean mussel (*Mytilus galloprovincialis*) validated at a native site to a South African site and suggested unaccounted environmental variables and phenotypic plasticity as underlying this observation. Proposed alternatives to address the issue related to the former explanation are by adapting the ingestion half-saturation coefficients as a function of the given phytoplankton density (Alunno-Bruscia et al., 2011) or the ratio of Chl-a to TSM (Thomas and Bacher, 2018), providing a means to apply such work across larger spatial scales without needing to manually recalibrate the half-saturation coefficients.

Spatial Trends in Growth Parameters to Inform Site Selection

In all of the mapped oyster growth indicators (**Figure 7**) and their interannual variability (**Figure 8**), variability across the bay is clearly observed, including between farmed intertidal sites and the offshore environment, as well as across the offshore environment itself. Although oyster growth clearly has high potential offshore, improving greatly upon the intertidal *status quo* in some areas, this is not spatially uniform. Instead, this is highly variable, and there are large areas of the offshore environment where production is expected to not be even as good as in the intertidal area where farming currently takes place, in addition to the areas where higher growth would be expected. Generally, there is a consistent spatial gradient, with greater growth potential in the northeast offshore segment of the bay and less in the southwest offshore segment, found to be comparable or sometimes even less favorable than in the intertidal zone. This highlights the value of using spatialized data in such an approach, as the finding from *in situ* data alone that growth is higher offshore is limited spatially and may be misleading when proceeding to either future experimental work or commercial operations offshore, depending on where in the bay they are located. For example, locating a new cage or farm where the 2010 experimental cage was located (**Figure 1**) would not result in the most optimal growth possible within the bay, and locating it further west (e.g., just north of Noirmoutier island) would result in even more limited growth (**Figure 7**). The results from the current work then guide more optimal offshore cage or long-line placement as a result of their spatially-explicit nature.

The overall spatial structure in the resulting mapped indicators is, expectedly, due to the variability observed in satellite image input parameters, Chl-a, TSM, and SST, which underlie oyster growth. The very high TSM concentrations in the intertidal zone are at levels that substantially limit oyster growth in this area (Gernez et al., 2014). TSM concentrations gradually become lower and reach sub-impacting levels offshore, but Chl-a also decreases toward the offshore environment in a similar fashion. The spatial patterns in both TSM and Chl-a are expected to be related to benthic resuspension only possible at shallower depths, with water column Chl-a concentrations comprising phytoplankton and resuspended microphytobenthos (Hernández Fariñas et al., 2017), as well as current and water circulation patterns. Concentrations of both in the offshore waters are higher in the northeastern segment of the bay, but the yearly average TSM seems to be low enough to not hinder growth. In the southwestern segment, however, where TSM concentrations are lower, Chl-a concentration is also too low to support accelerated growth compared with the intertidal zone. At the temperatures observed for Bourgneuf Bay, higher SST is generally expected to promote oyster growth, and there is a more linear gradient from near- to offshore compared with Chl-a or TSM, with overall warmer temperatures in shallower waters. Multiple spawning events (**Figure 7F**) are also associated with these generally warmer shallower areas (**Figure 5E**) and with areas with higher SST variability (**Figure 5F**), likely due to the required 18°C spawning threshold being met or exceeded more frequently (Barillé et al., 2011). Additionally, outside of the intertidal zone, oysters are immersed in the water full-time (i.e., 100% immersion), whereas the average immersion time for intertidal zone farms is only 75% (Thomas et al., 2016, Suppl. Info). This means that on average oysters are able to ingest food 25% less of the time in the intertidal zone compared with offshore. In preliminary sensitivity analyses carried out ahead of this work, the variability of immersion time was also found to significantly affect resulting oyster growth, and to play a role in the higher growth observed offshore.

For spat, the consistently faster growth observed in the northeastern offshore segment over the different timeframes tested suggests that pre-growing multiple batches of spat within the same year may be possible there. For example, starting pre-growing in early April, as in **Figure 7A**, the target 14 g is achieved within approximately 90 days, corresponding to late June, potentially allowing for a second or even third pre-growth cycle for those farmers choosing to specialize in spat production for resale or to stock other concessions within their own production. Likewise, the later start of a single offshore pre-growth cycle may be chosen to better fit within a farmer's overall production, which may include other phases, or to better coincide with sale or thinning (i.e., when oyster densities are reduced to allow continued growth on the same farm) dates of interest. Comparatively, to achieve the target spat weight (14 g) over the

full time period (eight months) considered here, spat cultivation would need to begin in the spring in the intertidal zone, or early summer at the latest in the southwestern offshore segment (**Figures 7A–C**), and only one cycle per year would be possible.

Alternatively, rapid adult oyster growth offshore (**Figures 7D,E**) may allow producers to purchase pre-grown spat, specialize in the offshore adult production stage, and either move adults to a fattening pond within their own operation or sell to a fattening-specialized grower, keeping this part of their production cycle to within a single year. Overall, in moving either adult or spat production offshore, approximately a full year of the total production cycle can be saved, reducing this from approximately three to two years. Producers may also consider areas with higher spawning potential (in the central-eastern and intertidal areas of the bay; **Figure 7F**) as either favorable, in cases where spat capture is targeted as part of their overall production and therefore desirable, or unfavorable, where capture is not intended and rather leads to issues of biofouling, requiring added maintenance, and decreased quality index, at least temporarily.

Fattening may also be possible offshore, in the northeastern segment of Bourgneuf Bay (**Figures 7G–I**), allowing *Fines*, if not *Spéciales*, classification, and removing the need for a separate fattening facility (ponds, typically located inshore and with high concentrations of phytoplankton). Although interannual variability was found to be slightly higher at the northeastern offshore hypothetical site considered here than elsewhere in the bay (**Figures 8**, **9G–I**), it is still relatively low, such that at least *Fines* and possibly *Spéciales* class oysters could be expected from year to year, compared with consistently *Normales* in the intertidal zone. However, attaining the higher *Spéciales* classification was found to only be possible by beginning fattening in the summer months, suggesting that flesh weight gain during the late summer/early fall months can be critical in natural waters under the scenarios considered. All options are to be considered by producers in terms of the cost-benefit balance of moving offshore for their given situation, for any production stage of interest, and with particular consideration for risks, infrastructure and technical investment, and additional (or less) labor that would be required of them (Buck and Langan, 2017).

Adaptability of Growth Indicators and Production Scenarios

Given the nature of the DEB model outputs driven by remote sensing data, mapped and at regular time steps, oyster growth can be transformed to provide meaningful information to producers or other decision-makers or professionals, and targeted to their specific cases and interests. A suite of indicators was selected here to demonstrate the broad range of indicator types possible to easily adapt to a particular production specialization of interest. For example, Bourgneuf Bay oysters are sold for consumption primarily within the local market, with peak sales and therefore target peak production, occurring in December, in association with the French tradition of eating oysters at Christmas and New Year celebrations (Buestel et al., 2009). An additional summer market was indicated as being of secondary interest in France, and may be the primary domestic market in other oyster-producing countries. Although not demonstrated here, a similar exercise could be undertaken targeting, for example, starting production in spring and assessing adult oyster weight achieved in July, or another date deemed to be of interest for a particular site. Likewise, whereas minimum weight for the French market (30 g) was considered here, a range of different production targets could be considered, in terms of product size and weight, notably considering the different market calibers (**Table 2**), where the most popular size is typically considered to be Caliber 3 (ranging from 66 to 85 g total weight). Several examples, for spat, adult, and finishing stages have been demonstrated in a mapping and statistical application here, but weight thresholds and timings can easily be adjusted to correspond to specific calibers or other targets.

Likewise, various scenario combinations could be considered, including different start dates and moving oysters between offshore and intertidal concessions at different stages. The start and end dates considered are part of model initialization and can be modified to correspond to a particular scenario of interest. Faster growth is observed for both spat and adults in the northeastern offshore segment compared with the intertidal zone, and other noted benefits include reduced mortality from viral disease (Pernet et al., 2018). However, it is generally considered unfavorable to complete an entire production cycle (i.e., spat through market size) offshore. This is due to observed physiological effects (e.g., underdeveloped adductor muscles; relatively weak or malformed shell) and parasite damage, such as from the shell-boring worm, *Polydora* sp. (e.g., Glize et al., 2010), associated with constant immersion, and the negative impact on the marketability of the resulting product. Given the various possible offshore and intertidal production cycle stage combinations (e.g., beginning with pre-growing in the intertidal zone, then moving offshore for grow-out or finishing or vice versa), and this imperative to choose which production cycle stage would best be moved offshore, potential time savings and other gains generated by completing different stages within the full production cycle offshore versus in the intertidal zone can be assessed and compared. Again, the farmer can then determine if such gains are worth the various investments that would be required in moving part of their production offshore and optimize which phases take place where (i.e., offshore or in the intertidal zone).

Additional Considerations for Site Selection and Future Directions

An important consideration that is beyond the scope of the current work is the effect of stocking density and carrying capacity on growth potential (Smaal and Van Duren, 2019). Trophic interactions and population dynamics are not considered here, and carrying capacity is known to be a limitation to production within the bay (Le Grel and Le Bihan, 2009). Indeed, the current modeling is based on a calibration where quite dense oyster cultivation takes place in the intertidal zone, where more than 5,000 tons of Pacific oyster are harvested per year (Agreste, 2015), but no cultivation takes place offshore (i.e., the current results relate to a single cage with no

additional cultivation in the vicinity, as per the experimental data used for DEB calibration and validation). This can be expected to have an impact on modeled results, favorably biasing offshore growth potential. Were stocking density to increase offshore, through adding concessions there, growth potential could reasonably be expected to decline as carrying capacity is met or especially if it is exceeded. Furthermore, the addition of more farms to the bay could be expected to impact the overall carrying capacity at the bay level, and adding farms offshore may also negatively affect existing cultivation in the intertidal zone. Offshore leases could be offset by requiring that an equivalent lease be ceded in the intertidal zone (Le Bihan and Le Grel, 2008). As a next step, the inclusion of carrying capacity assessments (e.g., Filgueira et al., 2015) to inform farm and stocking density would be invaluable. Likewise, the environmental impacts of shellfish farms, via their enrichment of surface sediment organic matter, have been modeled using spatialized data elsewhere (Brigolin et al., 2017), and should be considered in offshore site selection for Bourgneuf Bay in terms of overall sustainability.

The value of using remote sensing data has been demonstrated here for modeling growth potential, and its use could be extended to coupling with other models to inform shellfish aquaculture [e.g., scope for growth (e.g., Barillé et al., 2011), the R package for AquaCulture (RAC; Baldan et al., 2018), ShellSim (Ferreira et al., 2008; Hawkins et al., 2013), Farm Aquaculture Resource Model models (FARM; Ferreira et al., 2007)]. DEB modeling, like several of these alternative or complementary models, is generic, simulates the entire life cycle of species, and elsewhere has been parameterized for a variety of species, including several of interest from an aquaculture perspective and in Bourgneuf Bay in particular. These include blue mussel (Thomas et al., 2011) and great scallop (Gourault et al., 2019). Given *in situ* data for the location and species of interest, other potential opportunities for farmers could be similarly assessed and compared, and included in broader feasibility and economic analyses.

Whereas the use of satellite remote sensing only allows the retrospective consideration of conditions at potential or current aquaculture sites, coastal zones and shellfish are known to be sensitive to the effects of climate change (Thomas et al., 2016, 2018; FAO, 2018). A similar approach as presented here could also make use of spatialized data from ecological models, such as the Finite Volume Coastal Ocean Model (FVCOM; Cowles, 2008) or the Proudman Oceanographic Laboratory Coastal Ocean Modeling System (POLCOMS; Holt and James, 2001) coupled with the European Regional Seas Ecosystem Model ERSEM (Baretta et al., 1995; Butenschön et al., 2016), to consider present-day as well as various future climate change scenarios to more fully plan for these potential effects in choosing and developing new aquaculture sites (e.g., Palmer et al., 2019). Such data often provide fuller spatial and temporal coverage than satellite observations, since issues like cloud cover do not apply. Like satellite data, such data are associated with their own inherent error and uncertainty and with trade-offs in terms of their spatial resolutions and coverage (i.e., POLCOMS-ERSEM spans all of the western North Atlantic and Mediterranean, but at a 0.1° spatial resolution; Ciavatta et al., 2016).

In addition to the growth potential, assessed here, which is crucial and underlies the potential success of a given operation at a given location, such results should eventually be combined with other environmental, technical, and socioeconomic considerations (Longdill et al., 2008; Brigolin et al., 2017). Barillé et al. (forthcoming) have assessed a suite of these for offshore Pacific oyster cultivation at the regional scale within which Bourgneuf Bay is located, and note in particular that bathymetry, as well as distance to and harbor capacity entail real constraints to which locations the small-scale producers of Bourgneuf could consider in terms of what upgrades to materials, boats, and then boat licenses would be required should certain ranges be exceeded (i.e., bathymetry ranging from 5 to 10 m for cages and from 10 to 20 m for longlines, and within 5 nm of a harbor with sufficient capacity). Certain other environmental and socioeconomic factors were likewise found to impose constraints as to where aquaculture would be feasible (e.g., areas where protected habitat or fishing areas are found, of seabed mining, sand deposits, or commercial traffic channels). Others were considered in terms of their favorable or unfavorable impact, but were not considered preclusive to oyster cultivation (i.e., presence of underwater pipes or cables, militarized zones, current rates and benthic substrate type) in resulting suitability indices. Whereas physical conditions (e.g., wave height, swell) will substantially limit which sites are suitable in more exposed open ocean sites (Buck and Langan, 2017), for the relatively sheltered conditions within Bourgneuf Bay, even offshore, this is not expected to be a major issue. Barillé et al. (forthcoming) also considered DEB-modeled oyster growth, but using reduced resolution input products more relevant to the regional-scale analysis they undertook, and therefore at a much coarser scale than is demonstrated here. The combination of a GIS-based spatial multi-criteria evaluation with the oyster growth indicator mapping at a finer spatial scale relevant to site selection at the bay scale, as demonstrated here, will be invaluable next step in moving Pacific oyster production offshore in Bourgneuf Bay.

CONCLUSION

Here, medium-resolution satellite data were coupled with ecophysiological DEB modeling to demonstrate the feasibility, but also the high degree of spatial variability of offshore Pacific oyster growth potential in Bourgneuf Bay, France, where cultivation currently takes place in the intertidal zone with little to no room for further expansion. Both satellite (MERIS and AVHRR)-derived input products, Chl-a, TSM, and SST, and DEB modeled outputs were successfully validated with coinciding *in situ* measurements, and mapped across existing farm sites in the intertidal zone and the full offshore extent of the bay. The use of DEB modeling allowed us to integrate the non-linear effects of Chl-a, TSM, and SST throughout the production cycle. Mapped oyster growth at regular time intervals was then transformed into a suite of industry-relevant indicators established in consultation with oyster producers and professionals, and tailored to different production stages; spat pre-growing, adult grow-out, and fattening. Across all indicators,

a large area of the northeast offshore segment of the bay was found to be characterized by particularly enhanced growth potential, suggesting the potential to reduce the current total production cycle duration by up to a full year, whereas the southwest offshore segment was found to perform similarly to or less well than existing intertidal farms. Such spatially-explicit data are crucial as part of site selection, to be included with other environmental and socioeconomic considerations, with as much as a threefold difference in growth potential revealed across the ∼200 km^2 of the offshore Bourgneuf Bay.

DATA AVAILABILITY STATEMENT

The datasets generated for this study are available on request to the corresponding author.

AUTHOR CONTRIBUTIONS

SP, PG, and LB designed the study. SS, PM, PG, and LB contributed to the data collection. SP, SS, and YT contributed to the data analysis. SP, PG, YT, SS, and LB contributed to the data interpretation. SP wrote the manuscript. All authors contributed to the writing and revision, and gave their approval to the final version of the manuscript.

FUNDING

This work was part of the EU H2020 project *Tools for Assessment and Planning of Aquaculture Sustainability* (TAPAS), funded by the EU H2020 Research and Innovation Program under Grant Agreement No. 678396.

ACKNOWLEDGMENTS

Financial support from the project Tools for Assessment and Planning of Aquaculture Sustainability (TAPAS; http://tapas-h2020.eu/), funded by the EU H2020 Research and Innovation Program under Grant Agreement No. 678396, is gratefully acknowledged. We thank the oyster producers Florence Buzin and Richard Chaigneau (Benth'Ostrea), and David Lecossois (L'huîtrière de Vendée), as well as Laurent Champeau, director of the Shellfish Production Regional Committee of Marennes-Oléron for insightful discussions. The Région Pays de la Loire is acknowledged for funding the SMIDAP, which collected oyster growth data, as are ESA/Copernicus and NOAA for providing satellite imagery.

REFERENCES

AFNOR (1985). *Norme Française Huîtres Creuses. Dénomination et Classification* (Paris: AFNOR), 45–56.

Agreste (2015). *Recensement de la Conchyliculture 2012*. Available at http://agreste.agriculture.gouv.fr/IMG/pdf/R7215A01.pdf (accessed December 18, 2019).

Alunno-Bruscia, M., Bourlès, Y., Maurer, D., Robert, S., Mazurié, J., Gangnery, A., et al. (2011). A single bio-energetics growth and reproduction model for the oyster *Crassostrea gigas* in six Atlantic ecosystems. *J. Sea Res.* 66, 340–348. doi: 10.1016/j.seares.2011.07.008

Aura, C. M., Saitoh, S. I., Liu, Y., Hirawake, T., Baba, K., and Yoshida, T. (2016). Implications of marine environment change on Japanese scallop (*Mizuhopecten yessoensis*) aquaculture suitability: a comparative study in Funka and Mutsu Bays, Japan. *Aquacult. Res.* 47, 2164–2182. doi: 10.1111/are.12670

Baldan, D., Porporato, E. M. D., Pastres, R., and Brigolin, D. (2018). An R package for simulating growth and organic wastage in aquaculture farms in response to environmental conditions and husbandry practices. *PLoS One* 13:e0195732. doi: 10.1371/journal.pone.0195732

Baretta, J. W., Ebenhöh, W., and Ruardij, P. (1995). The European regional seas ecosystem model, a complex marine ecosystem model. *Netherl. J. Sea Res.* 33, 233–246. doi: 10.1016/0077-7579(95)90047-0

Barillé, L., Héral, M., and Barillé-Boyer, A.-L. (1997). Modélisation de l'écophysiologie de l'huître *Crassostrea gigas* dans un environnement estuarien. *Aquat. Living Res.* 10, 31–48. doi: 10.1051/alr:1997004

Barillé, L., Le Bris, A., Goulletquer, P., Thomas, Y., Glize, P., Kane, F., et al. (forthcoming). Biological, socio-economic, and administrative opportunities and challenges to moving aquaculture offshore for small French oyster-farming companies.

Barillé, L., Lerouxel, A., Dutertre, M., Haure, J., Barillé, A. L., Pouvreau, S., et al. (2011). Growth of the Pacific oyster (*Crassostrea gigas*) in a high-turbidity environment: comparison of model simulations based on scope for growth and dynamic energy budgets. *J. Sea Res.* 66, 392–402. doi: 10.1016/j.seares.2011.07.004

Barillé-Boyer, A. L., Haure, J., and Baud, J. P. (1997). *L'ostréiculture en Baie de Bourgneuf. Relation Entre la Croissance des huîtres Crassostrea gigas et le Milieu Naturel: Synthèse de 1986 à 1995*. IFREMER Rep. DRV/RA/RST/97–16. Paris: IFREMER.

Bernard, I., de Kermoysan, G., and Pouvreau, S. (2011). Effect of phytoplankton and temperature on the reproduction of the Pacific oyster *Crassostrea gigas*: investigation through DEB theory. *J. Sea Res.* 66, 349–360. doi: 10.1016/j.seares.2011.07.009

Binding, C. E., Jerome, J. H., Bukata, R. P., and Booty, W. G. (2010). Suspended particulate matter in Lake Erie derived from MODIS aquatic colour imagery. *Int. J. Remote Sens.* 31, 5239–5255. doi: 10.1080/01431160903302973

Blondeau-Patissier, D., Gower, J. F., Dekker, A. G., Phinn, S. R., and Brando, V. E. (2014). A review of ocean color remote sensing methods and statistical techniques for the detection, mapping and analysis of phytoplankton blooms in coastal and open oceans. *Prog. Oceanogr.* 123, 123–144. doi: 10.1016/j.pocean.2013.12.008

Brewin, R. J. W., de Mora, L., Billson, O., Jackson, T., Russell, P., Brewin, T. G., et al. (2017). Evaluating operational AVHRR sea surface temperature data at the coastline using surfers. *Estuar. Coast. Shelf Sci.* 196, 276–289. doi: 10.1016/j.ecss.2017.07.011

Brigolin, D., Porporato, E. M. D., Prioli, G., and Pastres, R. (2017). Making space for shellfish farming along the Adriatic coast. *ICES J. Mar. Sci.* 74, 1540–1551. doi: 10.1093/icesjms/fsx018

Buck, B. H., and Langan, R. (2017). *Aquaculture Perspective of Multi-Use Sites in the Open Ocean*. Berlin: SpringerOpen.

Buestel, D., Gérard, A., and Morize, E. (1982). Elevage de naissains de pectinidés: description des filières flottantes de préélevage. *La Pêche Maritime* 1247, 83–87.

Buestel, D., Ropert, M., Prou, J., and Goulletquer, P. (2009). History, status, and future of oyster culture in France. *J. Shellfish Res.* 28, 813–821.

Butenschön, M., Clark, J., Aldridge, J. N., Allen, J. I., Artioli, Y., Blackford, J., et al. (2016). ERSEM 15.06: a generic model for marine biogeochemistry and the ecosystem dynamics of the lower trophic levels. *Geosci. Model Dev.* 9, 1293–1339. doi: 10.5194/gmd-9-1293-2016

Ciavatta, S., Kay, S., Saux-Picart, S., Butenschön, M., and Allen, J. I. (2016). Decadal reanalysis of biogeochemical indicators and fluxes in the North West European shelf-sea ecosystem. *J. Geophys. Res. Oceans* 121, 1824–1845. doi: 10.1002/2015jc011496

Cowles, G. W. (2008). Parallelization of the FVCOM coastal ocean model. *Int. J. High Perform. Comput. Appl.* 22, 177–193. doi: 10.1177/1094342007083804

Depellegrin, D., Menegon, S., Farella, G., Ghezzo, M., Gissi, E., Sarretta, A., et al. (2017). Multi-objective spatial tools to inform maritime spatial planning in the Adriatic Sea. *Sci. Total Environ.* 609, 1627–1639. doi: 10.1016/j.scitotenv.2017.07.264

Dutertre, M., Barillé, L., Haure, J., and Cognie, B. (2007). Functional responses associated with pallial organ variations in the Pacific oyster *Crassostrea gigas* (Thunberg, 1793). *J. Exp. Mar. Biol. Ecol.* 352, 139–151. doi: 10.1016/j.jembe.2007.07.016

Dutertre, M., Beninger, P. G., Barillé, L., Papin, M., Rosa, P., Barillé, A. L., et al. (2009). Temperature and seston quantity and quality effects on field reproduction of farmed oysters, *Crassostrea gigas*, in Bourgneuf Bay, France. *Aquat. Living Resour.* 22, 319–329. doi: 10.1051/alr/2009042

Dutertre, M., Ernande, B., Haure, J., and Barillé, L. (2017). Spatial and temporal adjustments in gill and palp size in the oyster *Crassostrea gigas*. *J. Mollus. Stud.* 83, 11–18. doi: 10.1093/mollus/eyw025

Falconer, L. (2013). *Spatial Modelling and GIS-Based Decision Support Tools to Evaluate the Suitability of Sustainable Aquaculture Development in Large Catchments*. Doctoral dissertation, University of Stirling, Stirling.

Falconer, L., Middelboe, A. L., Kaas, H., Ross, L. G., and Telfer, T. C. (2019). Use of geographic information systems for aquaculture and recommendations for development of spatial tools. *Rev. Aquacult.* doi: 10.1111/raq.12345

FAO (2018). *The State of World Fisheries and Aquaculture 2018 - Meeting the Sustainable Development Goals*. Rome: FAO.

Ferreira, J. G., Hawkins, A. J. S., and Bricker, S. B. (2007). Management of productivity, environmental effects and profitability of shellfish aquaculture—the farm aquaculture resource management (FARM) model. *Aquaculture* 264, 160–174. doi: 10.1016/j.aquaculture.2006.12.017

Ferreira, J. G., Hawkins, A. J. S., Monteiro, P., Moore, H., Service, M., Pascoe, P. L., et al. (2008). Integrated assessment of ecosystem-scale carrying capacity in shellfish growing areas. *Aquaculture* 275, 138–151. doi: 10.1016/j.aquaculture.2007.12.018

Filgueira, R., Comeau, L. A., Guyondet, T., McKindsey, C. W., and Byron, C. J. (2015). *Modelling Carrying Capacity of Bivalve Aquaculture: A Review of Definitions and Methods. Encyclopedia of Sustainability Science and Technology*. New York, NY: Springer.

Fleury, E., Normand, J., Lamoureux, A., Bouget, J.-F., Lupo, C., Cochennec-Laureau, N., et al. (2018). *RESCO REMORA Database: National monitoring Network of Mortality and Growth Rates of the Sentinel Oyster Crassostrea gigas*. France: SEANOE.

Gentry, R. R., Froehlich, H. E., Grimm, D., Kareiva, P., Parke, M., Rust, M., et al. (2017). Mapping the global potential for marine aquaculture. *Nat. Ecol. Evol.* 1, 1317–1324. doi: 10.1038/s41559-017-0257-9

Gernez, P., Barillé, L., Lerouxel, A., Mazeran, C., Lucas, A., and Doxaran, D. (2014). Remote sensing of suspended particulate matter in turbid oyster-farming ecosystems. *J. Geophys. Res. Oceans* 119, 7277–7294. doi: 10.1002/2014jc010055

Gernez, P., Doxaran, D., and Barillé, L. (2017). Shellfish aquaculture from space: potential of Sentinel2 to monitor tide-driven changes in turbidity, chlorophyll concentration and oyster physiological response at the scale of an oyster farm. *Front. Mar. Sci.* 4:137. doi: 10.3389/fmars.2017.00137

Gimpel, A., Stelzenmüller, V., Töpsch, S., Galparsoro, I., Gubbins, M., Miller, D., et al. (2018). A GIS-based tool for an integrated assessment of spatial planning trade-offs with aquaculture. *Sci. Total Environ.* 627, 1644–1655. doi: 10.1016/j.scitotenv.2018.01.133

Glize, P., and Guissé, S.-N. (2009). *Approche Zootechnique de L'élevage Conchylicole au Large en Baie de Bourgneuf: Essais Préliminaires*. France: SMIDAP.

Glize, P., Tetard, X., and Dreux, D. (2010). *Elevage Conchylicole au Large en Baie de Bourgneuf: Approche Zootechnique et Cartographique*. France: SMIDAP.

Gosling, E. M. (2003). *Bivalve Molluscs*. Hoboken, NJ: Blackwell Publishing.

Goulletquer, P., and Le Moine, O. (2002). Shellfish farming and coastal zone management (CZM) in the Marennes-Oléron Bay and the charentais sounds (Charente-Maritime, France): a review of recent developments. *Aquacult. Int.* 10, 507–525.

Gourault, M., Lavaud, R., Leynaert, A., Pecquerie, L., Paulet, Y. M., and Pouvreau, S. (2019). New insights into the reproductive cycle of two great scallop populations in brittany (France) using a DEB modelling approach. *J. Sea Res.* 143, 207–221. doi: 10.1016/j.seares.2018.09.020

Guillotreau, P., Le Bihan, V., and Pardo, S. (2018). "Mass mortality of farmed oysters in France: bad responses and good results," in *Global Change in Marine Systems, Integrating Societal and Governing Responses*, eds P. Guillotreau, A. Bundy, and R. I. Perry, (Abingdon: Routledge), 54–64. doi: 10.4324/9781315163765-4

Hawkins, A. J. S., Pascoe, P. L., Parry, H., Brinsley, M., Black, K. D., McGonigle, C., et al. (2013). Shellsim: a generic model of growth and environmental effects validated across contrasting habitats in bivalve shellfish. *J. Shellfish Res.* 32, 237–253. doi: 10.2983/035.032.0201

Hernández Fariñas, T., Ribeiro, L., Soudant, D., Belin, C., Bacher, C., Lampert, L., et al. (2017). Contribution of benthic microalgae to the temporal variation in phytoplankton assemblages in a macrotidal system. *J. Phycol.* 53, 1020–1034. doi: 10.1111/jpy.12564

Holt, J. T., and James, I. D. (2001). An s coordinate density evolving model of the northwest European continental shelf: 1. Model description and density structure. *J. Geophys. Res. Oceans* 106, 14015–14034. doi: 10.1029/2000jc000304

Kapetsky, J. M., Aguilar-Manjarrez, J., and Jenness, J. (2013). A global assessment of potential for offshore mariculture development from a spatial perspective. *Paper presented FAO Fisheries and Aquaculture Technical Paper No. 549*, Rome.

Kooijman, S. A. L. M. (2010). *Dynamic Energy Budget Theory for Metabolic Organisation*. Cambridge: Cambridge University Press.

Le Bihan, V., and Le Grel, L. (2008). *Quels Impacts Socioéconomiques du Développement des Techniques d'élevage des Huîtres en eau Profonde ? AGLIA – Observatoire des Pêches et des Cultures Marines du Golfe de Gascogne*. Rochefort: Université de Nantes.

Le Grel, L., and Le Bihan, V. (2009). Oyster farming and externalities: the experience of the Bay of Bourgneuf. *Aquacult. Econ. Manag.* 13, 112–123. doi: 10.1080/13657300902881690

Longdill, P. C., Healy, T. R., and Black, K. P. (2008). An integrated GIS approach for sustainable aquaculture management area site selection. *Ocean Coast. Manage.* 51, 612–624. doi: 10.1016/j.ocecoaman.2008.06.010

Louis, R. (2010). *Elevage Conchylicole au Large en Baie de Bourgneuf: Potentialité de Diversification*. Ph.D. thesis, Agrocampus Ouest, Rennes.

Matthews, M. W. (2011). A current review of empirical procedures of remote sensing in inland and near-coastal transitional waters. *Int. J. Remote Sens.* 32, 6855–6899. doi: 10.1080/01431161.2010.512947

Méléder, V., Barillé, L., Rincé, Y., Morançais, M., Rosa, P., and Gaudin, P. (2005). Spatio-temporal changes in microphytobenthos structure analysed by pigment composition in a macrotidal flat (Bourgneuf Bay, France). *Mar. Ecol. Prog. Ser.* 297, 83–99. doi: 10.3354/meps297083

Mille, D., Oudot, G., Dubillot, E., and Geay, A. (2008). *Étude de Faisabilité de L'élevage D'huîtres en eau Profonde Dans la Baie de la Malconche*. Prise de Terdoux: CREAA.

Monaco, C. J., Porporato, E. M., Lathlean, J. A., Tagliarolo, M., Sarà, G., and McQuaid, C. D. (2019). Predicting the performance of cosmopolitan species: dynamic energy budget model skill drops across large spatial scales. *Mar. Biol.* 166:14.

Mouw, C. B., Greb, S., Aurin, D., DiGiacomo, P. M., Lee, Z., Twardowski, M., et al. (2015). Aquatic color radiometry remote sensing of coastal and inland waters: challenges and recommendations for future satellite missions. *Remote Sens. Environ.* 160, 15–30. doi: 10.1016/j.rse.2015.02.001

Neil, C., Spyrakos, E., Hunter, P. D., and Tyler, A. N. (2019). A global approach for chlorophyll-a retrieval across optically complex inland waters based on optical water types. *Remote Sens. Environ.* 229, 159–178. doi: 10.1016/j.rse.2019.04.027

Odermatt, D., Gitelson, A., Brando, V. E., and Schaepman, M. (2012). Review of constituent retrieval in optically deep and complex waters from satellite imagery. *Remote Sens. Environ.* 118, 116–126. doi: 10.1016/j.rse.2011.11.013

O'Reilly, J. E., Maritorena, S., Siegel, D. A., O'Brien, M. C., Toole, D., Mitchell, B. G., et al. (2000). *Ocean Color Chlorophyll a Algorithms for SeaWiFS, OC2, and OC4: Version 4*.

Oyinlola, M. A., Reygondeau, G., Wabnitz, C. C., Troell, M., and Cheung, W. W. (2018). Global estimation of areas with suitable environmental conditions for mariculture species. *PLoS One* 13:e0191086. doi: 10.1371/journal.pone.0191086

Palmer, S., Barillé, L., Gernez, P., Ciavatta, S., Evers-King, H., Kay, S., et al. (2019). *Earth Observation and Model-Derived Aquaculture Indicators Report*. TAPAS project Deliverable 6.6 report, 65. doi: 10.5281/zenodo.3581506

Palmer, S. C. J., Kutser, T., and Hunter, P. D. (2015). Remote sensing of inland waters: challenges, progress and future directions. *Remote Sens. Environ.* 157, 1–8. doi: 10.1016/j.rse.2014.09.021

Pernet, F., Fuhrmann, M., Petton, B., Mazurié, J., Bouget, J.-F., Fleury, E., et al. (2018). Determination of risk factors for herpesvirus in oysters using a broad-scale spatial epidemiological framework. *Sci. Rep*. 8:10869. doi: 10.1038/s41598-018-29238-4

Picoche, C., Le Gendre, R., Flye-Sainte-Marie, J., Françoise, S., Maheux, F., Simon, B., et al. (2014). Towards the determination of mytilus edulis food preferences using the dynamic energy budget (DEB) theory. *PLoS One* 9:e109796. doi: 10.1371/journal.pone.0109796

Porporato, E. M., Pastres, R., and Brigolin, D. (2019). Site suitability for finfish marine aquaculture in the central Mediterranean Sea. *Front. Mar. Sci.* 6:772.

Pouvreau, S., Bourles, Y., Lefebvre, S., Gangnery, A., and Alunno-Bruscia, M. (2006). Application of a dynamic energy budget model to the Pacific oyster, *Crassostrea gigas*, reared under various environmental conditions. *J. Sea Res.* 56, 156–167. doi: 10.1016/j.seares.2006.03.007

Prou, J., and Goulletquer, P. (2002). *The French Mussel Industry: Present Status and Perspectives. First international Mussel Forum*. Charlottetown: Aquaculture Canada.

Radiarta, I. N., and Saitoh, S. I. (2009). Biophysical models for Japanese scallop, *Mizuhopecten yessoensis*, aquaculture site selection in Funka Bay, Hokkaido, Japan, using remotely sensed data and geographic information system. *Aquacult. Int.* 17:403. doi: 10.1007/s10499-008-9212-8

REPHY (2017). *REPHY Dataset - French Observation and Monitoring Program for Phytoplankton and Hydrology in Coastal Waters. 1987-2016 Metropolitan Data*. Paris: IFREMER.

Simis, S., Stelzer, K., and Müller, D. (2018). *Copernicus Global Land Operations "Cryosphere and Water" "CGLOPS-2" Framework Service Contract N° 199496 (JRC): Lake waters 300m and 1km products. Version 1.2.0*.

Smaal, A. C., and Van Duren, L. A. (2019). "Bivalve aquaculture carrying capacity: concepts and assessment tools," in *Goods and Services of Marine Bivalves*, eds. A. C. Smaal, J. G. Ferreira, J. Grant, J. K. Petersen, and Ø. Strand (Cham: Springer), 451–483.

Snyder, J., Boss, E., Weatherbee, R., Thomas, A. C., Brady, D., and Newell, C. (2017). Oyster aquaculture site selection using Landsat 8-Derived Sea surface temperature, turbidity, and chlorophyll a. *Front. Mar. Sci.* 4:190. doi: 10.3389/fmars.2017.00190

Sousa, T., Domingos, T., Poggiale, J. C., and Kooijman, S. A. L. M. (2010). Dynamic energy budget theory restores coherence in biology. *Philos. Trans. R. Soc. B* 365, 3413–3428. doi: 10.1098/rstb.2010.0166

Spyrakos, E., O'Donnell, R., Hunter, P. D., Miller, C., Scott, M., Simis, S. G., et al. (2018). Optical types of inland and coastal waters. *Limnol. Oceanogr.* 63, 846–870. doi: 10.1364/AO.55.002312

Thomas, Y., and Bacher, C. (2018). Assessing the sensitivity of bivalve populations to global warming using an individual-based modelling approach. *Glob. Change Biol.* 24, 4581–4597. doi: 10.1111/gcb.14402

Thomas, Y., Cassou, C., Gernez, P., and Pouvreau, S. (2018). Oysters as sentinels of climate variability and climate change in coastal ecosystems. *Environ. Res. Lett.* 13:104009. doi: 10.1088/1748-9326/aae254

Thomas, Y., Mazurié, J., Alunno-Bruscia, M., Bacher, C., Bouget, J. F., Gohin, F., et al. (2011). Modelling spatio-temporal variability of *Mytilus edulis* (L.) growth by forcing a dynamic energy budget model with satellite-derived environmental data. *J. Sea Res.* 66, 308–317. doi: 10.1016/j.seares.2011.04.015

Thomas, Y., Pouvreau, S., Alunno-Bruscia, M., Barillé, L., Gohin, F., Bryère, P., et al. (2016). Global change and climate-driven invasion of the Pacific oyster (*Crassostrea gigas*) along European coasts: a bioenergetics modelling approach. *J. Biogeogr.* 43, 568–579. doi: 10.1111/jbi.12665

Conflict of Interest: The authors declare that the research was conducted in the absence of any commercial or financial relationships that could be construed as a potential conflict of interest.

frontiers in Marine Science

ORIGINAL RESEARCH
published: 22 January 2020
doi: 10.3389/fmars.2019.00806

Applications of Spatial Autocorrelation Analyses for Marine Aquaculture Siting

Jonathan Jossart[1], Seth J. Theuerkauf[2], Lisa C. Wickliffe[1] and James A. Morris Jr.[3]*

[1] CSS, Inc., for National Oceanic and Atmospheric Administration, Fairfax, VA, United States, [2] The Nature Conservancy, Arlington, VA, United States, [3] National Oceanic and Atmospheric Administration, National Ocean Service, National Center for Coastal Ocean Sciences, Beaufort, NC, United States

Interest and growth in marine aquaculture are increasing around the world, and with it, advanced spatial planning approaches are needed to find suitable locations in an increasingly crowded ocean. Standard spatial planning approaches, such as a Multi-Criteria Decision Analysis (MCDA), may be challenging and time consuming to interpret in heavily utilized ocean spaces. Spatial autocorrelation, a statistical measure of spatial dependence, may be incorporated into the planning framework, which provides objectivity and assistance with the interpretation of spatial analysis results. Here, two case studies highlighting applications of spatial autocorrelation analyses in the northeast region of the United States of America are presented. The first case study demonstrates the use of a local indicator of spatial association analysis within a relative site suitability analysis – a variant of a MCDA – for siting a mussel longline farm. This case study statistically identified 17% of the area as highly suitable for a mussel longline farm, relative to other locations in the area of interest. The use of a clear, objective, and efficient analysis provides improved confidence for industry, coastal managers, and stakeholders planning marine aquaculture. The second case study presents an incremental spatial autocorrelation analysis with Moran's I that is performed on modeled and remotely sensed oceanographic data sets (e.g., chlorophyll *a*, sea surface temperature, and current speed). The results are used to establish a maximum area threshold for each oceanographic variable within the online decision support tool, OceanReports, which performs an automated spatial analysis for a user-selected area (i.e., drawn polygon) of ocean space. These thresholds provide users guidance and summary statistics of relevant oceanographic information for aquaculture planning. These two case studies highlight practical uses and the value of spatial autocorrelation analyses to improve the siting process for marine aquaculture.

Keywords: spatial planning, marine aquaculture, spatial autocorrelation, Local Indicator of Spatial Association, Moran's I, Multi-Criteria Decision Analysis

OPEN ACCESS

Edited by:
Stephanie C. J. Palmer, Université de Nantes, France

Reviewed by:
Daniele Brigolin, Università Iuav di Venezia, Italy
John David Icely, Independent Researcher, Vila do Bispo, Portugal
Tom William Bell, University of California, Santa Barbara, United States

****Correspondence:***
Jonathan Jossart
jonathan.jossart@noaa.gov

Specialty section:
This article was submitted to Ocean Observation, a section of the journal Frontiers in Marine Science

Received: *30 September 2019*
Accepted: *13 December 2019*
Published: *22 January 2020*

Citation:
Jossart J, Theuerkauf SJ, Wickliffe LC and Morris JA Jr (2020) Applications of Spatial Autocorrelation Analyses for Marine Aquaculture Siting. Front. Mar. Sci. 6:806. doi: 10.3389/fmars.2019.00806

INTRODUCTION

The demand for marine aquaculture products in the United States is growing, with domestic sales from 2007 to 2012, increasing 13% per year (National Marine Fisheries Service [NMFS], 2017). Marine aquaculture development in the United States has been increasing 3.3% annually from 2009 to 2011 (National Marine Fisheries Service [NMFS], 2017) and the use of traditional siting analyses will aid development by identifying

optimal locations that minimize conflict with other industries and environmental constraints. Spatial autocorrelation, a statistical measure of spatial dependence, has emerged as a powerful means to improve the siting of marine aquaculture development in areas with high competition for ocean space. Spatial autocorrelation analyses may be incorporated into planning for marine aquaculture to increase the confidence of spatial planners, stakeholders, and coastal managers overseeing development.

Marine Spatial Planning (MSP) provides a framework for the responsible siting of marine aquaculture and relies on representative and authoritative data. Remote sensing platforms – such as satellites, Global Positioning System based technologies (e.g., Vessel Monitoring Systems (VMS), data buoy networks), or other similar devices – provide data with a broad spatio-temporal range and resolution to inform the MSP process. For example, vessel traffic information derived from VMS or Automatic Identification Systems (AIS) is used to characterize navigation-related ocean space-use conflicts among ocean industries, such as renewable energy (Rawson and Rogers, 2015), commercial fishing (Rouse et al., 2017), and marine aquaculture (Tlusty et al., 2018). Satellite derived oceanographic variables are frequently used to site marine aquaculture. For example, Radiarta et al. (2011) created a suitability model for Japanese kelp (*Laminaria japonica*) in Hokkaido, Japan, using Moderate Resolution Imaging Spectroradiometer (MODIS) Sea Surface Temperature (SST) data and suspended solid concentrations calculated from Sea-viewing Wide Field-of-view Sensor (SeaWiFS) data to identify suitable locations. Reliable remote sensing data combined with authoritative or regulatory data, such as shipping lanes or marine protected areas, are essential for MSP.

Following the collection of reliable data, the next step in the MSP framework is to evaluate an area for potential environmental impacts, conflicts with other ocean industries, and compliance with applicable laws (Douvere, 2008; Collie et al., 2013; Stelzenmüller et al., 2017). A Multi-Criteria Decision Analysis (MCDA), also referred to as Multi-Criteria Decision Making or Multi-Criteria Evaluation, is a commonly used spatial analysis technique for the MSP of aquaculture (Longdill et al., 2008; Radiarta et al., 2008; Gimpel et al., 2015; Bwadi et al., 2019). MCDA allows for numerous environmental and stakeholder interests to be evaluated within an area of ocean space and has demonstrated value for the siting of marine aquaculture (Aguilar-Manjarrez et al., 2017; Lester et al., 2018). Variants of a MCDA have been conducted to guide aquaculture management decisions around the world (Aguilar-Manjarrez et al., 2017); examples include shellfish aquaculture siting in South America (Silva et al., 2011), siting of kelp in Japan (Radiarta et al., 2011), and siting for marine fish farms in Italy (Dapueto et al., 2015). The results of a MCDA are used by resource managers and regulatory authorities to understand potential environmental or space-use conflicts associated with a proposed operation while allowing industry to identify prospective sites with the highest return on investment.

A limitation of using a MCDA within the MSP framework is the ease and lack of data accessibility, which may be overcome through the use of an online Decision Support Tool (DST). Viewing and analyzing spatial data sets requires technical knowledge of Geographic Information Science and software, which may prevent stakeholders, industry, or coastal managers from being able to examine remote sensing or authoritative data efficiently. Online DSTs provide users of varying skill levels a rapid and cost-effective method to interactively explore spatial data and receive summarized results for an area of interest (Pınarbaşı et al., 2017). Online DSTs may be used to screen an area of interest prior to a MCDA, to remove areas with known constraints to reduce computer processing time. Puniwai et al. (2014) demonstrates the use of an online DST to present the results of a MCDA identifying areas in the nearshore and offshore waters of Hawai'i to inform aquaculture sector development and management. Online DSTs assist planners by providing quick access and simplified results to various user groups during the MSP process.

Both MCDA and online DSTs may incorporate spatial autocorrelation analyses, which have been developed by geostatisticians and applied to numerous fields of study, to improve the quality and confidence of results. Landscape ecologists commonly use spatial autocorrelation analyses, and have shown that not including a measure of spatial dependence into an analysis may lead to erroneous results (Legendre, 1993; Diniz-Filho et al., 2003; Hawkins et al., 2007; Kühn, 2007). Increasingly, spatial autocorrelation is incorporated into MSP and marine aquaculture siting analyses as part of a model or statistical analysis to improve reliability and rigor (Tavornpanich et al., 2012; Brager et al., 2015; Overton et al., 2018). Spatial autocorrelation also provides the foundation for identifying statistically significant high and low clusters, with analytical approaches being utilized within a variety of fields, including ecology (Nelson and Boots, 2008), epidemiology (Izumi et al., 2015), and spatial planning (Truong and Somenahalli, 2011). For example, Rauner et al. (2016) demonstrated how high and low clusters of demand for electricity and the supply of renewable energy systems may be used to guide renewable energy development in Germany. Similar methods of identifying clusters within a data set and siting analysis may be applied to the results of a MCDA. Furthermore, knowledge of cluster sizes within a data set may be leveraged for use within a DST to provide users with additional information regarding remotely sensed or modeled data sets.

Two case studies displaying how spatial autocorrelation analyses improve on the standard MSP framework for marine aquaculture are presented. The first case study presents a MCDA that uses a Local Indicator of Spatial Association (LISA) analysis to enhance the interpretation of the results. The second case study demonstrates how an incremental spatial autocorrelation analysis may be used to calculate area thresholds for key oceanographic parameters by identifying distances when clustering is most significant. These area thresholds are used within OceanReports[1], a recently released online DST co-developed by the United States National Oceanic and Atmospheric Administration (NOAA) and Bureau of Ocean Energy Management (BOEM). Both case studies demonstrate how the siting process and planning for

[1]https://coast.noaa.gov/digitalcoast/tools/ort.html

marine aquaculture may be enhanced by the inclusion of spatial autocorrelation analyses.

MATERIALS AND METHODS

Case Study 1: MCDA With Cluster and Outlier Analysis

A relative suitability analysis, a variant of a MCDA, was conducted to evaluate potential sites for a hypothetical mussel longline aquaculture operation in and around Buzzards Bay in the state waters of Massachusetts, United States (**Figure 1A**). This location was selected for use within this case study because of data availability, known potential conflicts (e.g., extensive vessel traffic and industrial activities), and increasing regional interest in marine aquaculture. **Table 1** provides the generalized steps followed for performing the relative suitability analysis used here. The presented results are for demonstrative purposes and do not guarantee a location's suitability with aquaculture. Further investigation and analysis should be executed if an aquaculture operation is proposed within this area. Incorporation of additional data sets and considerations relevant to the type of aquaculture and geographic setting should be performed when using this or similar methods that evaluate a location's compatibility for marine aquaculture.

With the project goal of siting a mussel longline farm and target geography identified, a grid with 1 ha grid cells (100 m by 100 m) was established for an area of interest, containing a total of 133,776 grid cells (**Figure 1A**). Cell size for the grid was determined based on the resolution of available spatial data for the analysis, inherent spatial variability of the data, and an industry-standard farm footprint size (Hengl, 2006). Grid cells shallower than 10 m were removed, leaving 98,369 grid cells within the acceptable depth range for this aquaculture siting exercise. Spatial data sets containing potential space-use conflicts with marine aquaculture operations, such as active military areas, maritime navigation, ocean industries, and natural resource management, were collated (**Table 2** and **Figures 1B–D**). Data sets were individually assigned a score ranging from 0 (low suitability) to 1 (high suitability) determined by its compatibility with mussel longlines (**Table 2**).

TABLE 1 | Generalized steps performed for the relative suitability analysis, including the Local Indicator of Spatial Association (LISA) analysis.

Steps for relative suitability analysis workflow
1. Define project goal.
2. Identify area of interest.
3. Select grid cell size and create grid.
4. Refine grid based on known constraints.
5. Evaluate spatial data sets relationship with each grid cell.
6. Score each spatial data sets relationship (0–1 Scale).
7. Calculate relative suitability scores.
8. Run a LISA analysis on the relative suitability scores.
9. Extract significantly high clusters of grid cells.
10. Review extracted clusters for further evaluation or site surveys.

Each data set was subsequently evaluated to determine if a spatial data set was present or absent within each grid cell. For example, a shipping lane was considered to be present if it intersected a grid cell, and that grid cell would receive a score of 0. For continuous data, such as bathymetry, fishing effort, and sediment grain size, the mean value for each grid cell was calculated and scores were assigned based on operational constraints associated with mussel longlines (e.g., low suitability scores were assigned for areas corresponding with high fishing effort because of the potential for space-use conflict; **Tables 3**, **4**). Vessel traffic from 2017 was categorized by type, and the sum of vessel transits per grid cell was calculated[2]. The 25th, 50th, and 75th, percentiles for each vessel type were calculated for the values in the grid and used to create and categorize the scoring schema (**Tables 5**, **6**). Any grid cell that contained a data set with a score of 0 was considered to be unsuitable regardless of the other scores as that single conflict is completely incompatible for siting. All data sets were integrated by summing all individual scores for each grid cell across all data sets and dividing the sum by the total number of data sets, providing a proportion from 0 to 1, with 0 representing "low suitability" and 1 representing "high suitability" relative to other grid cells. This final proportion provides the relative suitability of that cell to all other grid cells in the area of interest.

A LISA analysis, which is used to identify statistically significant clusters and outliers within a data set, is then performed on the final proportion of the relative suitability analysis (Anselin, 1995). Esri ArcGIS Pro's "Cluster and Outlier Analysis" tool was used to perform the LISA analysis (ESRI, 2019)[3]. The inverse distance spatial conceptualization with a 100 m search distance is used as it includes all grid cells; however, proximal cells have more influence than distant cells. Row standardization, application of a false discovery rate correction, and 999 iterations were all applied for more conservative and robust results. Statistically significant clusters of the highest suitable scores were identified, and any clusters smaller than 20 ha were excluded. A minimum size of 20 ha was used as smaller mussel farms have less economic sustainability and less flexibility for optimal farm configuration (Ahsan and Roth, 2010; Rosland et al., 2011). The LISA analysis is similar to the Getis–Ord Gi* statistic, but in addition to identifying significant high and low clusters, this method identifies outliers (Getis and Ord, 1992; Anselin, 1995). Knowledge of outliers is useful when interpreting results of a MCDA as it highlights areas that may need to be avoided when identifying suitable locations for an aquaculture operation. For example, a sewage discharge pipe or piece of unexploded ordnance may be surrounded by otherwise suitable locations.

Case Study 2: Incremental Spatial Autocorrelation Analysis With Moran's I

OceanReports enables the public to explore an ocean neighborhood by drawing a polygon anywhere within the

[2]https://marinecadastre.gov/ais/

[3]https://pro.arcgis.com/en/pro-app/tool-reference/spatial-statistics/cluster-and-outlier-analysis-anselin-local-moran-s.htm

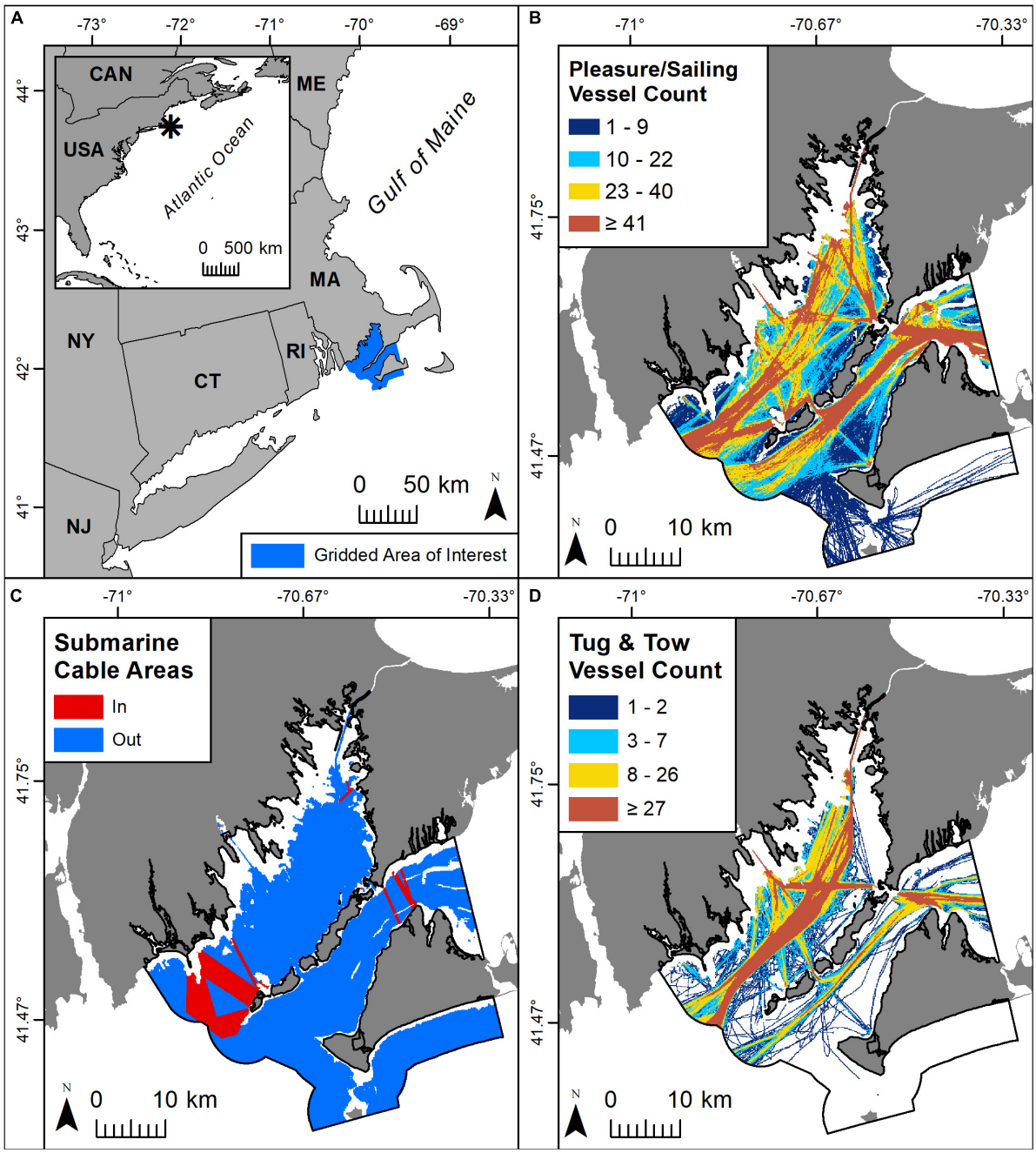

FIGURE 1 | (A) Area of interest (133,776 ha) located in the state waters of Massachusetts, United States. **(B)** Pleasure and sailing vessel traffic sum of transits per 1 ha for 2017. **(C)** Submarine cable area presence (in) or absence (out) for each 1 ha grid cell. **(D)** Tug and tow vessel traffic sum of transits per 1 ha for 2017.

United States Exclusive Economic Zone (EEZ) to visualize spatial data within that polygon. An immediate report is provided that includes location-based, regulatory, abiotic, biotic, cultural, and geophysical characteristics specific to the user-defined area. Within the Oceanographic and Biophysical information section of the tool, descriptive statistics from a variety of remotely sensed oceanographic data sets are generated for the custom area (**Figure 2A**). A user could draw a polygon to inspect and visualize a large area (e.g., the East Coast of the United States), however, the summary statistics of oceanographic data for this expansive area may provide inconsequential information. On the other hand, drawing a smaller polygon would produce more useful localized descriptive statistics of oceanographic parameters for MSP. To address this issue maximum area thresholds were developed for all oceanographic data sets by identifying the amount of area at which spatial dependence or clustering was the

TABLE 2 | Discrete spatial data sets included in the relative suitability analysis with scores ranging from 0 (low suitability) to 1 (high suitability) and proportion of grid cells that the parameter is present in along with the data source.

Parameter/data set	Score	Proportion of grid	Data source*
Active renewable energy leases	0.5	0	BOEM
Aids to navigation	0	<0.01	NOAA OCM
Anchorage area	0.1	0.27	NOAA OCM
Aquaculture	0.1	<0.01	NROC
Artificial reefs	0	0	NOAA OCM
Audubon important bird areas	0.9	0.01	NAS
Coastal barrier resource system	0.5	0.02	US FWS
Coastal critical habitat designations	0.5	0	NOAA OCM
Coastal wetlands	0.5	<0.01	US FWS
Coastally maintained channel	0	0.01	NOAA OCS
Danger and restricted zones	0.1	0.01	NOAA OCM
Eelgrass	0	<0.01	NROC
MA wind energy areas	0.5	0.07	MA CZM
Military operating area	0.5	0.02	USN
Military range complex	0.5	0.02	USN
Obstructions	0	<0.01	NOAA OCS
Ocean disposal sites	0	<0.01	NOAA OCM
Pipeline areas	0	<0.01	NOAA OCM
Pipelines	0	0	NOAA/BOEM
Protected areas	0.5	1.00	US DOI
Recreational SCUBA diving areas	0.1	0.17	NROC
Right whale seasonal management area	0.5	0.06	NFMS SERO
Shellfish habitats	0.5	0.52	MA DMF
Shipping lane	0	0.03	NOAA OCS
Shipwreck	0	<0.01	NOAA OCS
Submarine cable	0	<0.01	NOAA CSC
Submarine cable areas	0	0.08	NOAA OCM
Unexploded ordnance	0.5	<0.01	NOAA OCM
Unexploded ordnance FUDS**	0.5	0.30	NOAA OCM

**Bureau of Ocean Energy Management (BOEM), National Oceanic and Atmospheric Administration (NOAA), Office for Coastal Management (OCM), Northeast Regional Ocean Council (NROC), National Audubon Society (NAS), Fish and Wildlife Service (FWS), Office of Coast Survey (OCS), Massachusetts (MA) Office of Coastal Zone Management (CZM), United States Navy (USN), Department of the Interior (DOI), National Marine Fishery Service (NMFS), Southeast Regional Office (SERO), Division of Marine Fisheries (DMF), Coastal Services Center (CSC). **Formerly Used Defense Sites (FUDS).*

most pronounced using an incremental spatial autocorrelation analysis with Moran's I. OceanReports will not return descriptive statistics for an oceanographic variable if the user-drawn area is greater than the maximum area threshold for that data set. Rather, the tool informs the user to draw a smaller area to receive summary statistics for that variable (**Figure 2B**). Thus, the likelihood of a user receiving meaningless or misrepresentative summary statistics is reduced.

For this case study, long-term monthly climatologies of remotely sensed chlorophyll *a*, SST, and current speed, were evaluated within the northeast region of the United States, including state waters to the 200 nm federal waters boundary of the EEZ (**Table 7**). These three environmental variables are commonly used in siting analyses for marine aquaculture (Radiarta et al., 2008; Snyder et al., 2017; Tung and Son, 2019). Monthly climatologies of surface chlorophyll *a* concentrations produced by the National Aeronautics and Space Administration (NASA) MODIS-Aqua from July 2002 to February 2019 provide insight into an area's potential food availability (i.e., phytoplankton biomass) or possible nutrient loading (Gentry et al., 2017; NASA Goddard Space Flight Center, 2018; Theuerkauf et al., 2019). Monthly climatologies of water temperature and current magnitude from October 1992 to December 2012 were derived from the three-dimensional, physical oceanographic Hybrid Coordinate Ocean Model (HYCOM) and Navy Coupled Ocean Data Assimilation (NCODA) 1/12° reanalysis daily 1200 hr measurement (Bleck et al., 2002; Halliwell, 2004). Water temperature is critical for evaluating optimal growth ranges, approximate harvest times, and potential thermal stress thresholds for finfish, shellfish, and macroalgae aquaculture (Gentry et al., 2017). Oceanographic current speed is important to consider when siting aquaculture as well, and is useful for understanding shellfish food availability, equipment limitations, and fish welfare (Ferreira et al., 2007; Huang et al., 2008; Jónsdóttir et al., 2019).

An incremental spatial autocorrelation analysis using the global Moran's I spatial autocorrelation index with a fixed distance spatial conceptualization was performed for each monthly climatology using the "spdep" library in R v3.6.1 (R Core Team, 2019). An incremental spatial autocorrelation analysis calculates the Moran's I index and *z* score at multiple distances for a single data set. The fixed distances analyzed were derived from each possible distance between one data point and all other data points. For example, if 100 possible distances existed in a data set, Moran's I index would be run 100 times or once for each distance. The resulting *z* scores are then plotted by distance, rather than using the Moran's I index value, as the *z* scores allow for a standardized comparison of significance by distance (i.e., larger positive *z* scores have more significant clustering). The distances at the first peak and

TABLE 3 | Continuous spatial data sets included in the relative suitability analysis with scores ranging from 0 (low suitability) to 1 (high suitability) and proportion of grid cells that the parameter is present in.

Parameter	Value	Score	Proportion of grid	Data source*
Mean bathymetry (m)	>−10	0.1	0.04	NOAA NCEI
	≤−10	1	0.96	
Sediment grain size (mm)	≤2	1	0.87	TNC
	>2	0.5	0.13	

** United States National Oceanic and Atmospheric Administration (NOAA) National Centers for Environmental Information (NCEI), The Nature Conservancy (TNC).*

TABLE 4 | Commercial fishing effort 2015–2016 Vessel Monitoring System (VMS) derived (Northeast Regional Ocean Council 2019) categories and scoring schema ranging from 0 (low suitability) to 1 (high suitability), and the proportion of grid cells in each category by fishery (NMS = Multispecies groundfish, Pelagic includes mackerel, squid, and herring, SCO = Quahog, SES = Scallop).

Fishing effort	Score	Proportion of grid by fishery						
		Herring	Monkfish	NMS	Pelagic	SCO	SES	Squid
<−1	1	0.007	0.017	0.094	0.055	0.074	0.090	0.041
−1 – 0	0.8	0.013	0.027	0.130	0.079	0.025	0.215	0.070
0 – 1	0.6	0.000	0.017	0.039	0.043	0.002	0.034	0.043
1 – 2	0.4	0.001	0.015	0.021	0.029	0.000	0.004	0.028
>2	0.2	0.001	0.005	0.003	0.037	0.001	0.001	0.036
NA	1	0.978	0.920	0.714	0.757	0.898	0.657	0.782

TABLE 5 | Automatic Identification System (AIS) vessel counts by vessel type categories is the count of vessels that passed through a grid cell over the course of 2017 with the corresponding scores ranging from 0 (low suitability) to 1 (high suitability).

Vessel count categories by type				Score	Proportion of grid by type			
Fishing	Passenger	Pleasure	Other		Fishing	Passenger	Pleasure	Other
0	0	0	0	1	0.26	0.38	0.13	0.13
1–3	1–2	1–9	1–4	0.8	0.23	0.22	0.22	0.23
4–9	3–5	10–22	5–10	0.6	0.15	0.11	0.21	0.24
10–31	6–16	23–40	11–21	0.4	0.18	0.14	0.22	0.19
≥32	≥17	≥41	≥22	0.2	0.18	0.15	0.21	0.21

The proportion of grid cells in each category by vessel type; for example, 26% of the grid cells had 0 fishing vessel transits and received a score of 1.

TABLE 6 | Larger vessels with limited maneuverability associated with established shipping lanes from the 2017 Automatic Identification System (AIS) data.

Vessel count categories by type			Score	Proportion of grid by type		
Cargo	Tanker	Tug/Tow		Cargo	Tanker	Tug/Tow
0	0	0	1	0.92	0.96	0.51
1	1–2	1–2	0.5	0.04	0.01	0.15
2	3–6	3–7	0.3	0.01	0.01	0.10
3–9	7–14	8–26	0.1	0.02	0.01	0.12
≥10	≥15	≥27	0	0.02	0.01	0.12

With scores ranging from 0 (low suitability) to 1 (high suitability) and the proportion of grid cells in each category by vessel type.

maximum peak were identified for each plot. The first peak indicates smaller significant clustering and the maximum peak indicates the distance that clustering or spatial autocorrelation was most significant in the data set. The distance of the first *z* score peak, which also was the maximum peak for all data sets, provided a radius, and the standard formula for the area of a circle was performed to calculate an area for each monthly climatology.

OceanReports provides descriptive statistics for each month in a user drawn area, and therefore, the smallest area threshold or the most conservative estimate was chosen as the threshold for each oceanographic parameter. Using the smallest area threshold from all monthly climatologies assists in ensuring a user defined area contains appropriate summary statistics within the online DST. A temporal component was not included within this spatial dependence analysis, because the objective was simply to identify the smallest or most conservative area as determined by the distance at which spatial clustering was most significant. Therefore each monthly climatology was treated as an independent data set. Methodologies for using a spatio-temporal Moran's I index have been developed, and examine how spatial dependence patterns change over time or at different time scales. For example, Shen et al. (2016) demonstrate how a temporally detrended global spatio-temporal Moran's I index, which accounts for temporal data that is not stationary, may be used to examine changes in the spatial and temporal dependence of daily precipitation data sets in China.

RESULTS

Case Study 1: MCDA With Cluster and Outlier Analysis

The MCDA identified roughly 26% of the area of interest as unsuitable (i.e., received a score of 0) for mussel longlines. Vessel traffic, specifically "tug and tow" vessel traffic, and submarine

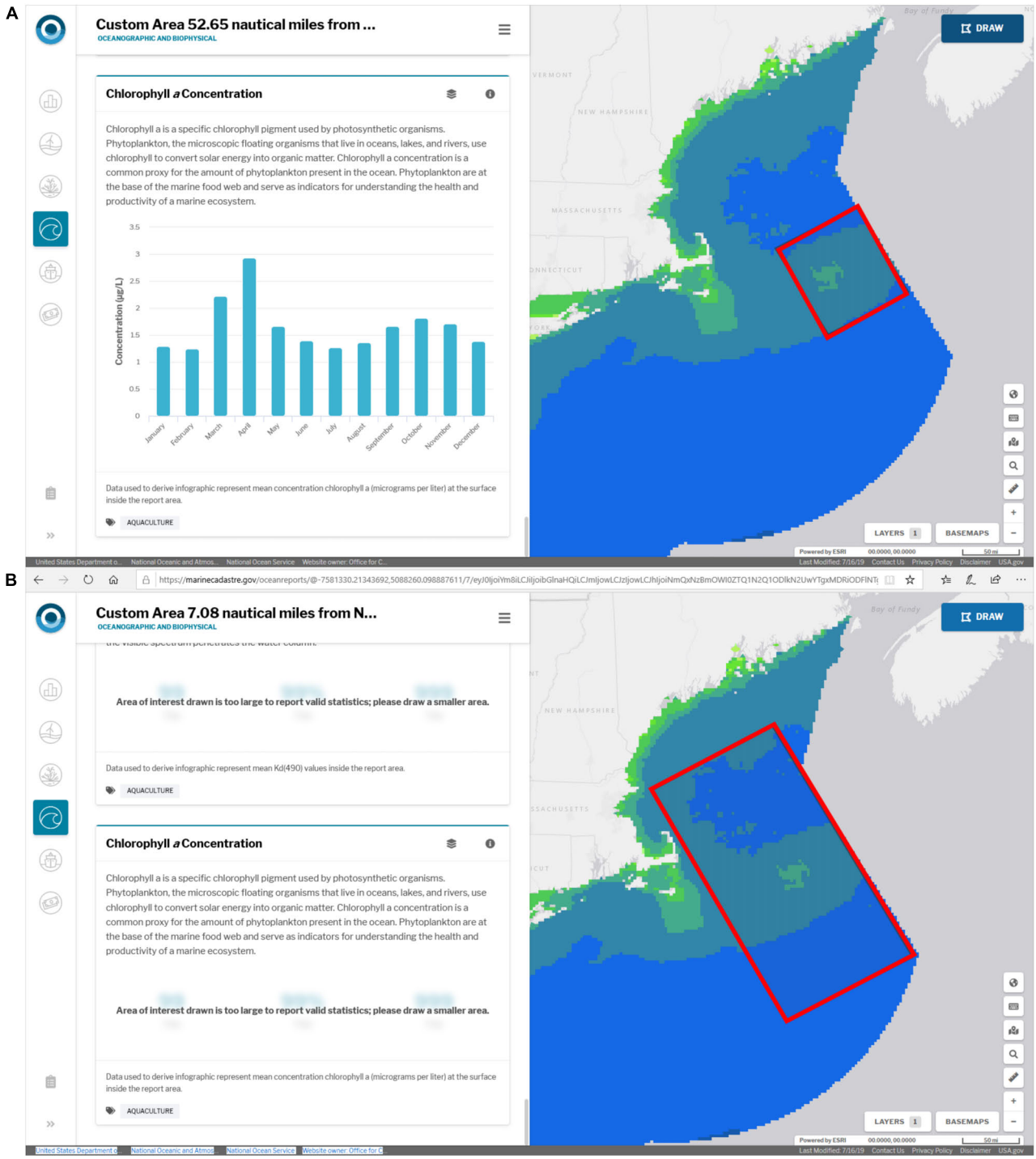

FIGURE 2 | Example output from OceanReports providing **(A)** descriptive statistics for a number of oceanographic variables based on a custom drawn area and **(B)** an error message indicating the maximum area threshold has been exceeded.

cable areas removed the greatest amount of suitable area (**Figures 1C,D**). The remaining 74% varied in levels of suitability (i.e., suitability scores ranging from >0 to 1; **Figure 3A**). The LISA analysis identified statistically significant highly suitable clusters with at least 20 ha of a contiguous area within 17% of the total area (**Figure 3D**). Within these highly suitable grid cells, the most considerable constraints were "pleasure and sailing craft" and "other" vessel traffic, as well as the presence of protected

TABLE 7 | Oceanographic data sets examined with units, spatial resolution, and source of data.

Data set	Resolution (km)	Min. distance (km)	Max. area (km^2)	Data source*
Surface chlorophyll *a* (mg m^{-3})	4.6	103	33,329	NASA
Surface water temperature (°C)	9.4	255	204,282	HYCOM NCODA
Surface current speed (m s^{-1})	9.4	217	147,934	HYCOM NCODA

**National Aeronautics and Space Administration (NASA), Hybrid Coordinate Ocean Model (HYCOM), and Navy Coupled Ocean Data Assimilation (NCODA). The minimum distance is the smallest value of the first peak over all months from the incremental spatial autocorrelation analysis. The maximum area is the area of a circle using the minimum distance as the radius. All distance and area calculations performed in North America Albers Equal Area Conic (WKID 102008).*

areas and shellfish habitats (**Figure 1B**; **Tables 2**, **5**). A few outliers with unsuitable cells adjacent to highly suitable cells were identified; these were either aids to navigation or other navigational obstructions (e.g., shipwrecks; **Figure 4**).

Case Study 2: Incremental Spatial Autocorrelation Analysis With Moran's I

The Moran's I *z* scores plotted by distance identified the distances at which clustering was most significant for the three oceanographic variables presented. Throughout the monthly climatologies, the distances of the first peak for chlorophyll *a z* scores ranged from 103 to 124 km, with the smallest distance of 103 km occurring in April, May, and July (**Figures 5A,B**). Water temperature distances had a range of 255 to 453 km, with the shortest distance in February at 255 m (**Figures 5C,D**). The first peak distances for current magnitude ranged from 217 to 245 km, exhibiting the shortest distance of 217 km in July, August, and October (**Figures 5E,F**). Plotting the distance values at the first peak for all variables by month demonstrates how the sizes of clusters within a data set fluctuates throughout the year. The smallest distance is used to calculate the maximum area threshold used by OceanReports (**Table 7** and **Figure 6**).

DISCUSSION

As global interest in "blue economy" initiatives and strategies expands, the MSP framework and associated geospatial analyses will be increasingly relied upon to minimize anthropogenic impacts on the ocean environment and space-use conflicts (Golden et al., 2017). Spatial autocorrelation approaches improve the reliability, rigor, and utility of the decision support guidance provided by MSP analyses. The two presented case studies showcase the utility of spatial autocorrelation analyses to (1) inform identification of clusters of highly suitable ocean areas for marine aquaculture that minimizes space-use conflict, and (2) prevent users from receiving misrepresentative summary statistics for oceanographic parameters within an online DST by defining maximum area thresholds. The potential applications of spatial autocorrelation analyses to help resource managers and industry better understand and apply these analyses are diverse and hold great promise to reduce uncertainty and provide a data-driven approach to the interpretation of results.

The first case study successfully identifies areas that are completely unsuitable (received a score of 0) for mussel longline aquaculture. Submarine cable areas, ocean disposal sites, and other navigational constraints were present; however, the "cargo", "tanker," and "tug and tow" vessel traffic in transit to the Cape Cod Canal in the area of interest was the most considerable constraint (**Figure 1D** and **Table 6**). Quantifying vessel traffic from AIS land-based or satellite data ensures vessel-related considerations are adequately characterized within spatial analyses to reduce potential conflict with other ocean industries, such as shipping, fishing, or recreation (Metcalfe et al., 2018; Tlusty et al., 2018). Any grid cells with values greater than 0 in the relative suitability analysis are considered negotiable ocean space.

The LISA analysis identified statistically significant clusters of cells that have low conflict relative to other grid cells, which is an improvement over other methods. Typically, the results of a MCDA for marine aquaculture (e.g., suitability maps) are visually and qualitatively assessed to identify areas with high potential for compatibility with marine aquaculture (**Figure 3A**). The simplest approach is to exclude areas that were completely unsuitable and evaluate all other areas by examining constraints (**Figure 3B**). Additionally, a threshold may be applied to the score; for example, grid cell values greater than the 75th percentile could be considered highly suitable and examined apart from the other grid cells (**Figure 3C**). Both approaches may aid in identifying potential areas, however, simply excluding unsuitable areas generally leaves a large area that must be sifted through, cell by cell, to identify sites. Establishing a score threshold reduces the amount of area; however, choosing a "good" suitability score threshold may be difficult to establish and justify.

Use of a LISA analysis identified 17% of the total area as having statistically higher suitable scores relative to the other grid cells (**Figure 3D**) and identified outliers that should be avoided (**Figure 4**). Compared to the two other approaches described, the LISA analysis identified a smaller area by means of spatial statistics, which provides decision makers and coastal managers increased confidence when examining the results of a spatial planning analysis. Regardless of the analysis used, further review of the highly suitable locations is required for the creation and evaluation of alternative sites for any marine aquaculture operation. The benefit of the LISA analysis is the standardized process and method for identifying statistically significant clusters, which serves as a basis for discussion with local managers and stakeholders.

Regardless of the methods used to calculate the suitability scores, a LISA analysis can be used to identify statistically significant clusters of high values and detect outliers. Methods range from a simple exclusion analysis (i.e., excluding areas representing known constraints) to more complicated MCDA

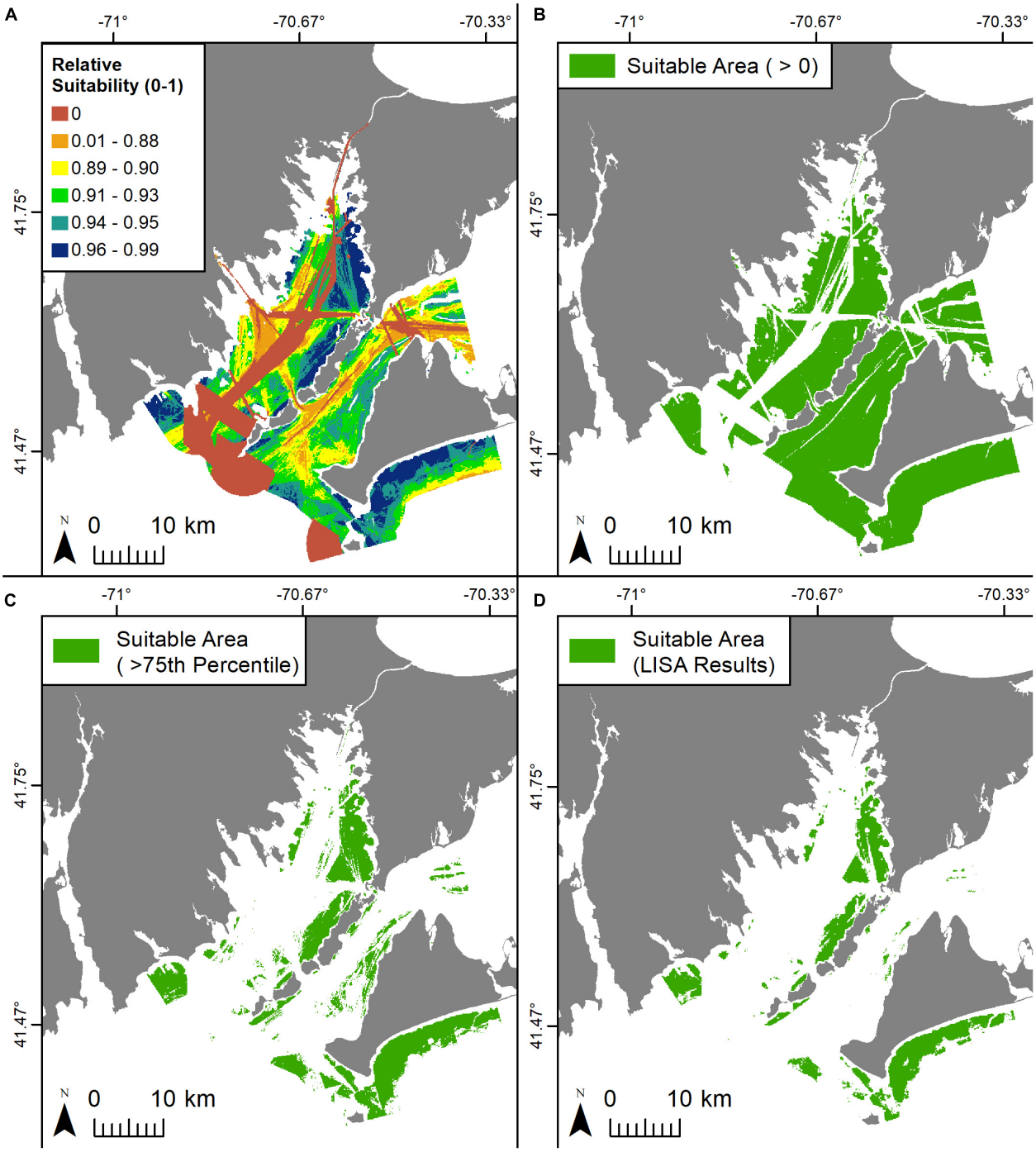

FIGURE 3 | (A) The relative suitability analysis results. A score of 0 indicates completely unsuitable, while a score closer to 1 indicates higher relative suitability with aquaculture. **(B)** Suitable area using a traditional binary exclusion analysis (Suitability score >0). **(C)** Suitable area using a threshold (Suitability score >75th percentile). **(D)** Highly suitable areas greater than 20 ha based on the Local Indicator of Spatial Association (LISA) analysis using the relative suitability score.

suitability modeling that include weighted variables. For example, Pérez et al. (2005) used a weighted linear combination method for development of a MCDA whereby decision makers assign weights to each factor considered within the analysis, with the final output being a weighted average. Weighted variables provides more confidence in determining what a "good" score is; however, setting a score threshold (e.g., 0.80) and interpreting the results may still be challenging. Thus, a LISA analysis provides a robust approach that may be used to guide interpretation of suitability analysis outputs by identifying

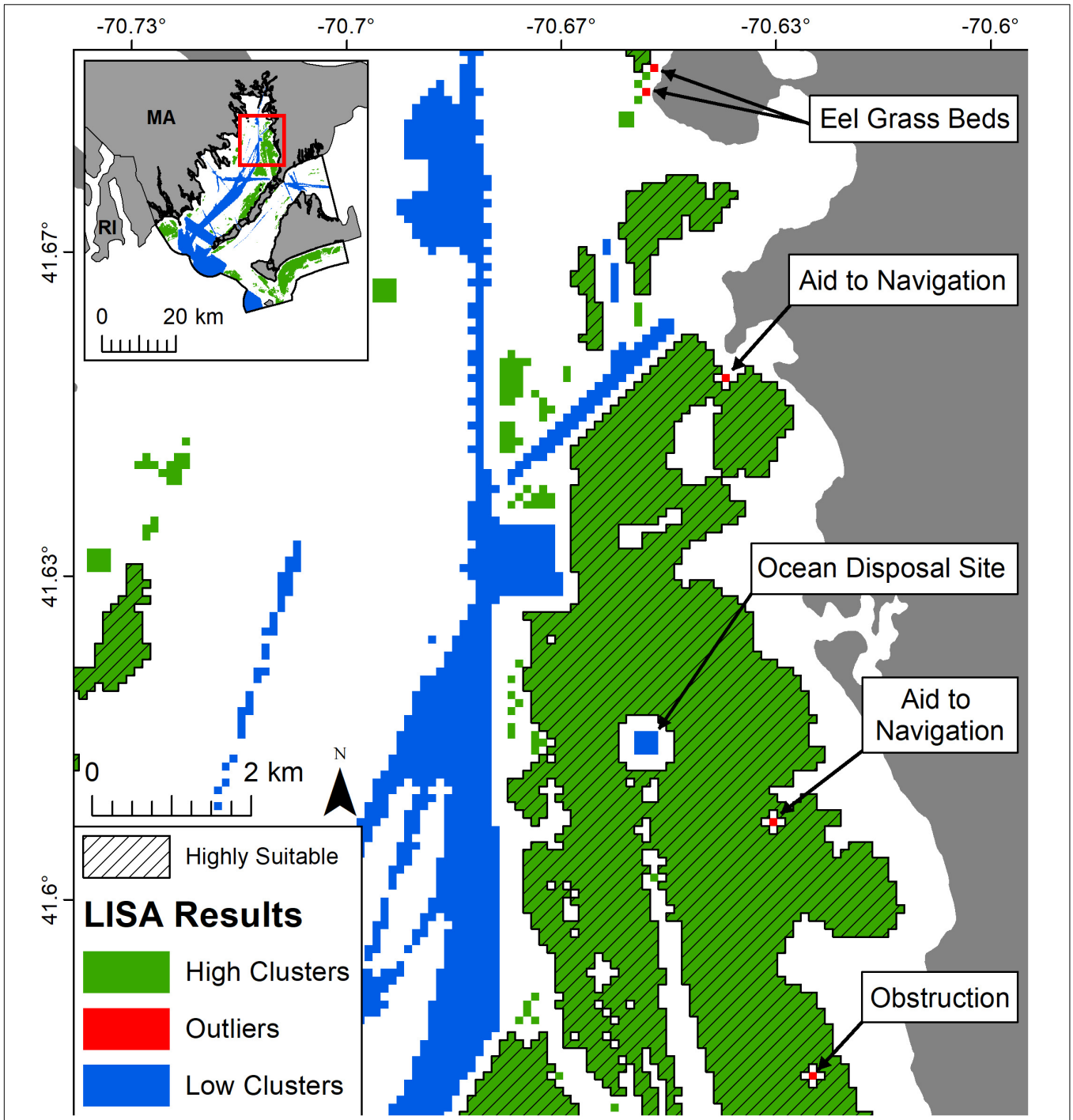

FIGURE 4 | Results of the Local Indicator of Spatial Association (LISA) analysis displaying the highly suitable high clusters, with outliers and low clusters. Groups of high clusters less than 20 ha were not considered highly suitable.

statistically significant clusters and outliers. In the presented case study, all data sets were equally weighted, however, if weights were applied, standardized methods of collecting stakeholder input or expert knowledge should be used over arbitrary assignment of values (Alexander et al., 2012; Klain and Chan, 2012; Teniwut et al., 2019).

Similar to other MSP analyses, the relative suitability and LISA analyses presented here have various assumptions and limitations. Marine aquaculture spatial planning projects typically rely upon the best available data for planning despite known data limitations and gaps (Longdill et al., 2008). For example in this case study, the most recent and best available

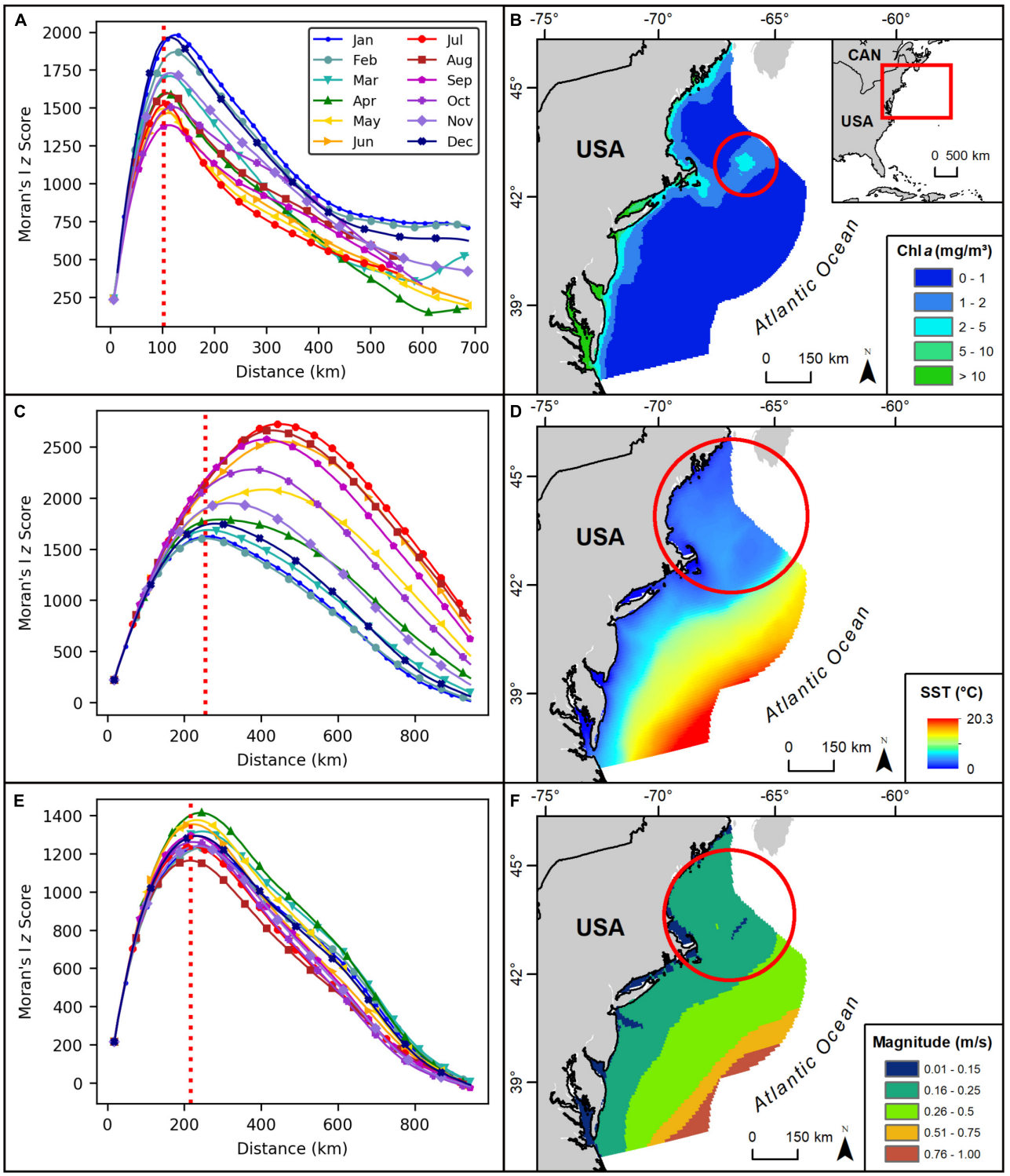

FIGURE 5 | (A) Chlorophyll *a z* scores plotted by distance band for each month, vertical red dotted line indicates the smallest distance of the first peak, 103 km. **(B)** June chlorophyll *a* climatology with the red circle having an area of 33,329 km^2. **(C)** Sea Surface Temperature (SST) *z* scores plotted by distance band for each month, vertical red dotted line indicates the smallest distance of the first peak, 255 km. **(D)** February SST climatology, red circle with area of 204,282 km^2. **(E)** Surface current speed *z* scores plotted by distance band for each month, vertical red dotted line indicates the smallest distance of the first peak, 217 km. **(F)** October current speed climatology, red circle with area of 147,934 km^2.

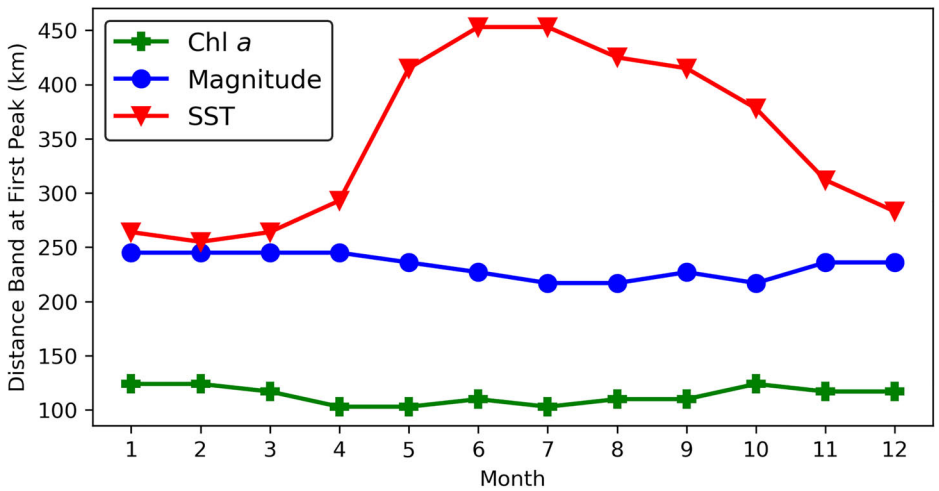

FIGURE 6 | Distance band at first peak by month for the three oceanographic variables examined. The month with the smallest minimum distance band was used to calculate the maximum area threshold to be used within the decision support tool, OceanReports.

vessel traffic data was used, however, vessels not required to carry an AIS transponder were not represented. Using the best available data and noting any assumptions or limitations can improve trust and reliability in the results, while also highlighting future data needs. Appropriate grid cell size and search distances are required, and should be based on the data and size of area being examined, as using inappropriate sizes or distances may provide limited results. Additionally a relative suitability analysis was performed, which means a highly suitable cluster does not guarantee a location is highly suitable for aquaculture, only that it is highly suitable relative to the other locations examined. Regardless of the type of spatial planning analysis, onsite surveys will be required to ensure a site's compatibility with marine aquaculture.

Within the second case study, the distance at which the Moran's I index *z* score first peaked for chlorophyll *a*, SST, and current speed, was identified for each month. These distances are consistent with known regional oceanographic patterns. Monthly climatological values for chlorophyll *a*, which is frequently used as a surrogate variable for phytoplankton biomass, displayed a general pattern of phytoplankton blooms in early spring and summer, which is typical in the North Atlantic (Friedland et al., 2016; **Figure 5A**). The surface water temperature displayed higher clustering in the winter months when temperature differences increase among the estuaries, the Gulf of Maine, and the Gulf Stream, while in the summer months, the water temperatures are more uniform throughout the northeast region (Shearman and Lentz, 2010; **Figure 5C**). Surface current speeds had higher clustering in late summer, which may be related to increased storm activity (Fewings et al., 2008; **Figure 5E**). The area threshold for each oceanographic parameter was calculated by using the smallest distance observed over the 12 months (**Figure 6** and **Table 7**). The incorporation of these into OceanReports lessen the possibility of a user receiving potentially misrepresentative descriptive statistics.

Alternative methods of establishing maximum area thresholds exist, but the target audience and industry of the DST should be used to guide any thresholds. For example, a DST built solely for marine aquaculture planning could use an area threshold determined by industry or regulatory standards. Since OceanReports was designed for a variety of industries with varying needs, determining area thresholds that accommodate different user groups was required. The incremental spatial autocorrelation analysis is able to accomplish this by producing thresholds for each oceanographic variable based on cluster sizes within that data set. For example, different descriptive statistics (i.e., changes in the mean concentration of chlorophyll *a*) are obtained as the area of interest changes, and once the area exceeds the threshold the results begin to mean less for localized planning (**Figures 7A,B**). When the custom area is smaller than the threshold a user may still receive inconsequential descriptive statistics for an oceanographic variable within OceanReports, because of where and how the area is drawn. However, the use of a maximum area threshold reduces the likelihood of this occurring. Inclusion of maximum area thresholds for oceanographic parameters used by OceanReports provides guidance for users, especially those unfamiliar with descriptive statistics and oceanographic parameters, during exploratory analysis of an area.

Several other pragmatic applications of spatial autocorrelation analyses may be assimilated into the MSP process for marine aquaculture, such as spacing of environmental monitoring stations or farms. Key environmental variables, such as nutrient input and impact to benthic habitat, may require monitoring to be performed (Holmer et al., 2008). Environmental variables with significant spatial autocorrelation (i.e., High clustering of a variable) around a farm should be sampled at additional locations, while variables with no significant spatial autocorrelation (i.e., Random distribution of a variable) require less spatial coverage for monitoring (Foster et al., 2018). The

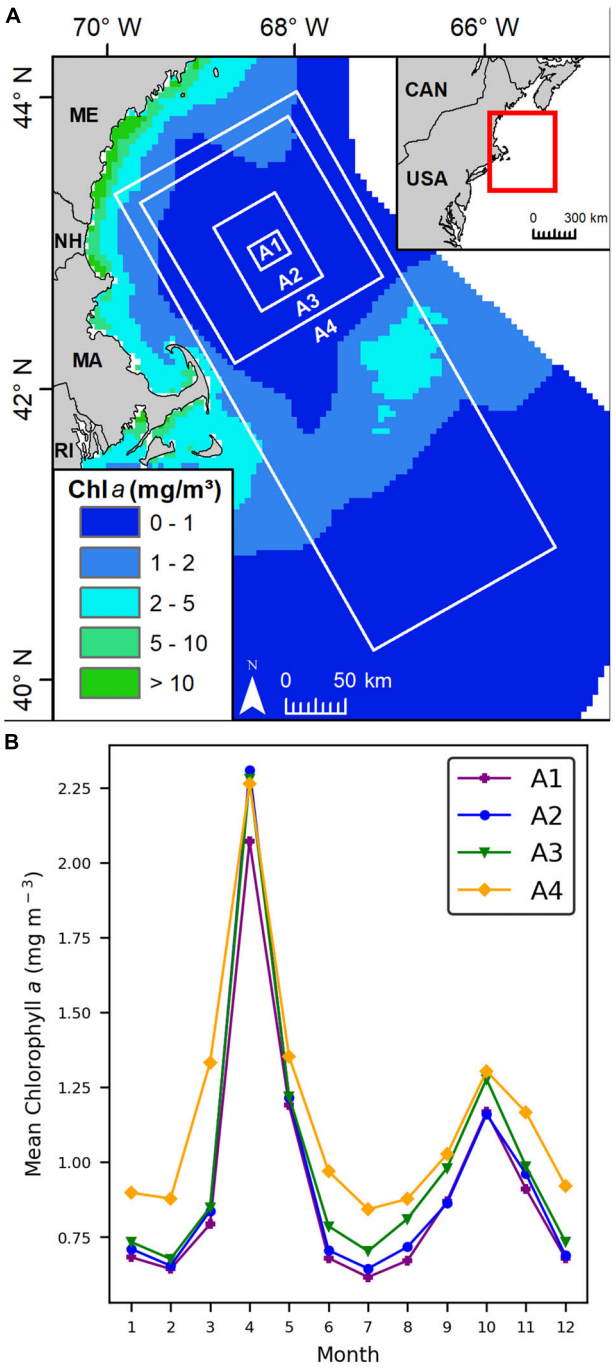

FIGURE 7 | (A) Example of different hypothetical areas of interest (A1 = 625 km^2, A2 = 4,778 km^2, A3 = 22,428 km^2, A4 = 76,995 km^2). **(B)** Mean chlorophyll *a* concentration for each of the area sizes, A1, A2, A3, and A4.

spacing and distance of sample points may be calculated after initial survey data has been collected, using a semivariogram or an incremental spatial autocorrelation analysis. The resulting distances may be used to space farm sites as well. As marine aquaculture development continues, so too will the need for rigorous analysis to provide assurance to stakeholders and coastal managers that a location is suitable.

CONCLUSION

The marine aquaculture industry needs efficient, objective, and accessible spatial planning tools in order to responsibly and efficiently plan for aquaculture. In the first case study, the relative suitability analysis and LISA analysis identified highly suitable locations for a hypothetical mussel longline farm in 17% of the area examined. The use of these analyses to statistically identify high clusters provides confidence and reliability for industry, coastal managers, and stakeholders, that these locations are the most suitable for a mussel longline farm in the area of interest. The second case study calculated maximum area thresholds using an incremental spatial autocorrelation analysis for chlorophyll *a*, SST, and current speed, to be used within OceanReports. These area thresholds were determined by the distance that spatial dependence or clustering was greatest within each data set, rather than arbitrarily assigning an area threshold. These maximum area thresholds provide users guidance and descriptive statistics that are meaningful for MSP activities. Incorporating spatial autocorrelation analyses into the MSP process improves efficiency and confidence when planning for marine aquaculture.

DATA AVAILABILITY STATEMENT

The datasets generated for this study are available upon request to the corresponding author.

AUTHOR CONTRIBUTIONS

JJ, ST, and LW conceived the idea for the manuscript and developed the methods. JJ executed the analysis. JJ, ST, LW, and JM reviewed and discussed the results. JJ, ST, LW, and JM wrote the manuscript. JM reviewed the final manuscript.

FUNDING

This work was supported by the NOAA National Ocean Service, National Centers for Coastal Ocean Science; NOAA National Marine Fisheries Service, Office of Aquaculture; and Department of Energy, Advanced Research Projects Agency-Energy.

ACKNOWLEDGMENTS

The authors thank Samantha Binion-Rock and Daniel Martin who provided comments and input to an early version of the manuscript. The authors also thank the NOAA/NMFS Office of Aquaculture, NOAA National Centers for Coastal Ocean Service (NCCOS) and the DOE ARPA-E program for support of this publication.

REFERENCES

Aguilar-Manjarrez, J., Soto, D., and Brummett, R. (2017). *Aquaculture Zoning, Site Selection and Area Management Under the Ecosystem Approach to Aquaculture. A Handbook*. Italy: Food and Agriculture Organization of the United Nations.

Ahsan, D. A., and Roth, E. V. A. (2010). Farmers' perceived risks and risk management strategies in an emerging mussel aquaculture industry in Denmark. *Mar. Resour. Econ.* 25, 309–323. doi: 10.5950/0738-1360-25.3.309

Alexander, K. A., Janssen, R., Arciniegas, G., O'Higgins, T. G., Eikelboom, T., and Wilding, T. A. (2012). Interactive marine spatial planning: siting tidal energy arrays around the Mull of Kintyre. *PLoS One* 7:e0030031. doi: 10.1371/journal.pone.0030031

Anselin, L. (1995). Local indicators of spatial association—LISA. *Geog. Anal.* 27, 93–115. doi: 10.1186/s12942-017-0119-3

Bleck, R., Halliwell, G., Wallcraft, A., Carroll, S., Kelly, K., and Rushing, K. (2002). *HYbrid Coordinate Ocean Model (HYCOM) User's Manual: Details of the Numerical Code. HYCOM*. Available at: https://www.hycom.org/attachments/063_hycom_users_manual.pdf (accessed June 3, 2019).

Brager, L. M., Cranford, P. J., Grant, J., and Robinson, S. M. (2015). Spatial distribution of suspended particulate wastes at open-water Atlantic salmon and sablefish aquaculture farms in Canada. *Aquacult. Environ. Interact.* 6, 135–149. doi: 10.3354/aei00120

Bwadi, B. E., Mustafa, F. B., Ali, M. L., and Bhassu, S. (2019). Spatial analysis of water quality and its suitability in farming giant freshwater prawn (*Macrobrachium rosenbergii*) in Negeri Sembilan region, Peninsular Malaysia. *Singapore J. Trop. Geog.* 40, 71–91. doi: 10.1111/sjtg.12250

Collie, J. S., Beck, M. W., Craig, B., Essington, T. E., Fluharty, D., Rice, J., et al. (2013). Marine spatial planning in practice. *Estuarine Coastal Shelf Sci.* 117, 1–11.

Dapueto, G., Massa, F., Costa, S., Cimoli, L., Olivari, E., Chiantore, M., et al. (2015). A spatial multi-criteria evaluation for site selection of offshore marine fish farm in the Ligurian Sea, Italy. *Ocean Coastal Manage.* 116, 64–77. doi: 10.1016/j.ocecoaman.2015.06.030

Diniz-Filho, J. A. F., Bini, L. M., and Hawkins, B. A. (2003). Spatial autocorrelation and red herrings in geographical ecology. *Glob. Ecol. Biogeogr.* 12, 53–64. doi: 10.1046/j.1466-822x.2003.00322.x

Douvere, F. (2008). The importance of marine spatial planning in advancing ecosystem-based sea use management. *Mar. Policy* 32, 762–771. doi: 10.1016/j.marpol.2008.03.021

ESRI (2019). *ArcGIS Pro: Release 2.4.0*. Redlands, CA: Environmental Systems Research Institute.

Ferreira, J. G., Hawkins, A. J. S., and Bricker, S. B. (2007). Management of productivity, environmental effects and profitability of shellfish aquaculture—the Farm Aquaculture Resource Management (FARM) model. *Aquaculture* 264, 160–174. doi: 10.1016/j.aquaculture.2006.12.017

Fewings, M., Lentz, S. J., and Fredericks, J. (2008). Observations of cross-shelf flow driven by cross-shelf winds on the inner continental shelf. *J. Phys. Oceanogr.* 38, 2358–2378. doi: 10.1175/2008jpo3990.1

Foster, S. D., Monk, J., Lawrence, E., Hayes, K. R., Hosack, G. R., and Przeslawski, R. (2018). "Statistical considerations for monitoring and sampling," in *Field Manuals for Marine Sampling to Monitor Australian Waters*, eds R. Przeslawski, and S. Foster, (Canberra ACT: National Environmental Science Programme, Marine Biodiversity Hub), 23–41.

Friedland, K. D., Record, N. R., Asch, R. G., Kristiansen, T., Saba, V. S., Drinkwater, K. F., et al. (2016). Seasonal phytoplankton blooms in the North Atlantic linked to the overwintering strategies of copepods. *Elem. Sci. Anth.* 4:000099. doi: 10.12952/journal.elementa.000099

Gentry, R. R., Lester, S. E., Kappel, C. V., White, C., Bell, T. W., Stevens, J., et al. (2017). Offshore aquaculture: spatial planning principles for sustainable development. *Ecol. Evol.* 7, 733–743. doi: 10.1002/ece3.2637

Getis, A., and Ord, J. K. (1992). The analysis of spatial association by use of distance statistics. *Geog. Anal.* 24, 189–206. doi: 10.1111/j.1538-4632.1992.tb00261.x

Gimpel, A., Stelzenmüller, V., Grote, B., Buck, B. H., Floeter, J., Núñez-Riboni, I., et al. (2015). A GIS modelling framework to evaluate marine spatial planning scenarios: Co-location of offshore wind farms and aquaculture in the German EEZ. *Mar. Policy* 55, 102–115. doi: 10.1016/j.marpol.2015.01.012

Golden, J. S., Virdin, J., Nowacek, D., Halphin, P., Bennear, L., and Patil, P. G. (2017). Making sure the blue economy is green. *Nat. Ecol. Evol.* 1:17. doi: 10.1038/s41559-016-0017

Halliwell, G. R. (2004). Evaluation of vertical coordinate and vertical mixing algorithms in the HYbrid-Coordinate Ocean Model (HYCOM). *Ocean Model.* 7, 285–322. doi: 10.1016/j.ocemod.2003.10.002

Hawkins, B. A., Diniz-Filho, J. A. F., Mauricio Bini, L., De Marco, P., and Blackburn, T. M. (2007). Red herrings revisited: spatial autocorrelation and parameter estimation in geographical ecology. *Ecography* 30, 375–384. doi: 10.1111/j.2007.0906-7590.05117.x

Hengl, T. (2006). Finding the right pixel size. *Comput. Geosci.* 32, 1283–1298. doi: 10.1016/j.cageo.2005.11.008

Holmer, M., Hansen, P. K., Karakassis, I., Borg, J. A., and Schembri, P. J. (2008). "Monitoring of environmental impacts of marine aquaculture," in *Aquaculture in the Ecosystem*, eds M. Holmer, K. Black, C. M. Duarte, N. Marbà, and I. Karakassis, (Berlin: Springer Science & Business Media), 47–85. doi: 10.1007/978-1-4020-6810-2_2

Huang, C. C., Tang, H. J., and Liu, J. Y. (2008). Effects of waves and currents on gravity-type cages in the open sea. *Aquacult. Eng.* 38, 105–116. doi: 10.1016/j.aquaeng.2008.01.003

Izumi, K., Ohkado, A., Uchimura, K., Murase, Y., Tatsumi, Y., Kayebeta, A., et al. (2015). Detection of tuberculosis infection hotspots using activity spaces based spatial approach in an urban Tokyo, from 2003 to 2011. *PLoS One* 10:e0138831. doi: 10.1371/journal.pone.0138831

Jónsdóttir, K. E., Hvas, M., Alfredsen, J. A., Føre, M., Alver, M. O., Bjelland, H. V., et al. (2019). Fish welfare based classification method of ocean current speeds at aquaculture sites. *Aquacult. Environ. Interact.* 11, 249–261. doi: 10.3354/aei00310

Klain, S. C., and Chan, K. M. (2012). Navigating coastal values: participatory mapping of ecosystem services for spatial planning. *Ecol. Econ.* 82, 104–113. doi: 10.1016/j.ecolecon.2012.07.008

Kühn, I. (2007). Incorporating spatial autocorrelation may invert observed patterns. *Divers. Distrib.* 13, 66–69.

Legendre, P. (1993). Spatial autocorrelation: trouble or new paradigm? *Ecology* 74, 1659–1673. doi: 10.2307/1939924

Lester, S. E., Stevens, J. M., Gentry, R. R., Kappel, C. V., Bell, T. W., Costello, C. J., et al. (2018). Marine spatial planning makes room for offshore aquaculture in crowded coastal waters. *Nat. Commun.* 9:945. doi: 10.1038/s41467-018-03249-1

Longdill, P. C., Healy, T. R., and Black, K. P. (2008). An integrated GIS approach for sustainable aquaculture management area site selection. *Ocean Coastal Manag.* 51, 612–624. doi: 10.1016/j.ocecoaman.2008.06.010

Metcalfe, K., Bréheret, N., Chauvet, E., Collins, T., Curran, B. K., Parnell, R. J., et al. (2018). Using satellite AIS to improve our understanding of shipping and fill gaps in ocean observation data to support marine spatial planning. *J. Appl. Ecol.* 55, 1834–1845. doi: 10.1111/1365-2664.13139

NASA Goddard Space Flight Center (2018). *Ocean Ecology Laboratory, Ocean Biology Processing Group. Data from: Moderate-Resolution Imaging Spectroradiometer (MODIS) Aqua chlorophyll data*. Greenbelt, MD: NASA OB.DAAC, doi: 10.5067/AQUA/MODIS/L3B/CHL/2018

National Marine Fisheries Service [NMFS] (2017). *Fisheries of the United States, 2016. U.S. Department of Commerce, NOAA Current Fishery Statistics No. 2016*. Available at: https://www.fisheries.noaa.gov/resource/document/fisheries-united-states-2016-report (accessed July 10, 2019).

Nelson, T. A., and Boots, B. (2008). Detecting spatial hot spots in landscape ecology. *Ecography* 31, 556–566. doi: 10.1111/j.0906-7590.2008.05548.x

Overton, K., Dempster, T., Oppedal, F., Kristiansen, T. S., Gismervik, K., and Stien, L. H. (2018). Salmon lice treatments and salmon mortality in Norwegian aquaculture: a review. *Rev. Aquacult.* 11, 1398–1417. doi: 10.1111/raq.12299

Pérez, O. M., Telfer, T. C., and Ross, L. G. (2005). Geographical information systems-based models for offshore floating marine fish cage aquaculture site selection in Tenerife. *Canary Islands. Aquacult. Res.* 36, 946–961. doi: 10.1111/j.1365-2109.2005.01282.x

Pınarbaşı, K., Galparsoro, I., Borja, Á, Stelzenmüller, V., Ehler, C. N., and Gimpel, A. (2017). Decision support tools in marine spatial planning: present applications, gaps and future perspectives. *Mar. Policy* 83, 83–91. doi: 10.1016/j.marpol.2017.05.031

Puniwai, N., Canale, L., Haws, M., Potemra, J., Lepczyk, C., and Gray, S. (2014). Development of a GIS-based tool for aquaculture siting. *ISPRS Int. J. Geo-Inf.* 3, 800–816. doi: 10.3390/ijgi3020800

R Core Team, (2019). *R: A Language and Environment for Statistical Computing*. Vienna: R Foundation for Statistical Computing.

Radiarta, I. N., Saitoh, S. I., and Miyazono, A. (2008). GIS-based multi-criteria evaluation models for identifying suitable sites for Japanese scallop (*Mizuhopecten yessoensis*) aquaculture in Funka Bay, southwestern Hokkaido. *Japan. Aquacult.* 284, 127–135. doi: 10.1016/j.aquaculture.2008.07.048

Radiarta, I. N., Saitoh, S. I., and Yasui, H. (2011). Aquaculture site selection for Japanese kelp (*Laminaria japonica*) in southern Hokkaido, Japan, using satellite remote sensing and GIS-based models. *ICES J. Mar. Sci.* 68, 773–780. doi: 10.1093/icesjms/fsq163

Rauner, S., Eichhorn, M., and Thrän, D. (2016). The spatial dimension of the power system: investigating hot spots of smart renewable power provision. *Appl. Energy* 184, 1038–1050. doi: 10.1016/j.apenergy.2016.07.031

Rawson, A., and Rogers, E. (2015). Assessing the impacts to vessel traffic from offshore wind farms in the Thames Estuary. *Sci. J. Marit. Univ. Szczecin* 43, 99–107.

Rosland, R., Bacher, C., Strand, Ø, Aure, J., and Strohmeier, T. (2011). Modelling growth variability in longline mussel farms as a function of stocking density and farm design. *J. Sea Res.* 66, 318–330. doi: 10.1016/j.seares.2011.04.009

Rouse, S., Kafas, A., Hayes, P., and Wilding, T. A. (2017). Development of data layers to show the fishing intensity associated with individual pipeline sections as an aid for decommissioning decision-making. *Underwater Technol.* 34, 171–178. doi: 10.3723/ut.34.171

Shearman, R. K., and Lentz, S. J. (2010). Long-term sea surface temperature variability along the U.S. East Coast. *J. Phys. Oceanogr.* 40, 1004–1017. doi: 10.1175/2009jpo4300.1

Shen, C., Li, C., and Si, Y. (2016). Spatio-temporal autocorrelation measures for nonstationary series: a new temporally detrended spatio-temporal Moran's index. *Phys. Lett. A* 380, 106–116. doi: 10.1016/j.physleta.2015.09.039

Silva, C., Ferreira, J. G., Bricker, S. B., DelValls, T. A., Martín-Díaz, M. L., and Yáñez, E. (2011). Site selection for shellfish aquaculture by means of GIS and farm-scale models, with an emphasis on data-poor environments. *Aquaculture* 318, 444–457. doi: 10.1016/j.aquaculture.2011.05.033

Snyder, J., Boss, E., Weatherbee, R., Thomas, A. C., Brady, D., and Newell, C. (2017). Oyster aquaculture site selection using Landsat 8-derived sea surface temperature, turbidity, and chlorophyll a. *Front. Mar. Sci.* 4:190. doi: 10.3389/fmars.2017.00190

Stelzenmüller, V., Gimpel, A., Gopnik, M., and Gee, K. (2017). "Aquaculture site-selection and marine spatial planning: the roles of GIS-based tools and models," in *Aquaculture Perspective of Multi-Use Sites in the Open Ocean*, eds B. H. Buck, and R. Langan, (Cham: Springer), 131–148. doi: 10.1007/978-3-319-51159-7_6

Tavornpanich, S., Paul, M., Viljugrein, H., Abrial, D., Jimenez, D., and Brun, E. (2012). Risk map and spatial determinants of pancreas disease in the marine phase of Norwegian Atlantic salmon farming sites. *BMC Vet. Res.* 8:172. doi: 10.1186/1746-6148-8-172

Teniwut, W., Marimin, M., and Djatna, T. (2019). GIS-Based multi-criteria decision making model for site selection of seaweed farming information centre: a lesson from small islands. *Indonesia. Decis. Sci. Lett.* 8, 137–150. doi: 10.5267/j.dsl.2018.8.001

Theuerkauf, S. J., Eggleston, D. B., and Puckett, B. J. (2019). Integrating ecosystem services considerations within a GIS-based habitat suitability index for oyster restoration. *PLoS One* 14:e0212936. doi: 10.1371/journal.pone.0210936

Tlusty, M. F., Wikgren, B., Lagueux, K., Kite-Powell, H., Jin, D., Hoagland, P., et al. (2018). Co-occurrence mapping of disparate data sets to assess potential aquaculture sites in the Gulf of Maine. *Rev. Fish. Sci. Aquacult.* 26, 70–85. doi: 10.1080/23308249.2017.1343798

Truong, L. T., and Somenahalli, S. V. (2011). Using GIS to identify pedestrian-vehicle crash hot spots and unsafe bus stops. *J. Public Transp.* 14, 99–114. doi: 10.5038/2375-0901.14.1.6

Tung, N. T., and Son, T. P. H. (2019). GIS-based multi-criteria evaluation models for selection of suitable sites for pacific oyster (*Crassostrea gigas*) aquaculture in the central region of Vietnam. *J. Environ. Sci. Eng.* 8, 141–158. doi: 10.17265/2162-5298/2019.04.002

Conflict of Interest: JJ and LW are employees of the company CSS, Inc., and are under contract to NOAA.

The remaining authors declare that the research was conducted in the absence of any commercial or financial relationships that could be construed as a potential conflict of interest.

frontiers in Marine Science

ORIGINAL RESEARCH
published: 30 January 2020
doi: 10.3389/fmars.2020.00022

Sea Surface Temperature Imagery Elucidates Spatiotemporal Nutrient Patterns for Offshore Kelp Aquaculture Siting in the Southern California Bight

Jordan N. Snyder[1], Tom W. Bell[1], David A. Siegel[1,2], Nicholas J. Nidzieko[1,2] and Kyle C. Cavanaugh[3]*

[1] Earth Research Institute, University of California, Santa Barbara, Santa Barbara, CA, United States, [2] Department of Geography, University of California, Santa Barbara, Santa Barbara, CA, United States, [3] Department of Geography, University of California, Los Angeles, Los Angeles, CA, United States

OPEN ACCESS

Edited by:
Rodney Forster, University of Hull, United Kingdom

Reviewed by:
Daniel Louis Kamykowski, North Carolina State University, United States
Jonathan Peter Fram, Oregon State University, United States

***Correspondence:**
Jordan N. Snyder
jordan_snyder@ucsb.edu

Specialty section:
This article was submitted to Ocean Observation, a section of the journal Frontiers in Marine Science

Received: *26 September 2019*
Accepted: *13 January 2020*
Published: *30 January 2020*

Citation:
Snyder JN, Bell TW, Siegel DA, Nidzieko NJ and Cavanaugh KC (2020) Sea Surface Temperature Imagery Elucidates Spatiotemporal Nutrient Patterns for Offshore Kelp Aquaculture Siting in the Southern California Bight. Front. Mar. Sci. 7:22. doi: 10.3389/fmars.2020.00022

Offshore aquaculture of giant kelp (*Macrocystis pyrifera*) has been proposed by the US Department of Energy for large scale biofuel production along the west coast of California. The Southern Californian Bight provides an ideal area for offshore kelp aquaculture as the upwelling and advection of cool, nutrient-rich waters supports the growth of vast native giant kelp populations. However, concentrations of nutrients vary greatly across space, can be limiting for kelp growth over seasonal to interannual time scales, and inputs of nutrients to surface waters may be subject to local circulation processes. Therefore, it is important to understand both the spatiotemporal variability of seawater nitrate concentrations and the appropriate scale of observation in order for offshore kelp aquaculture to be successful. Here, we use a combination of satellite sea surface temperature imagery, *in situ* measurements, and modeling to determine seawater nitrate fields across multiple spatial and temporal scales. We then combine this information with known giant kelp physiological traits to develop a kelp stress index (KSI) for the optimal siting of offshore kelp aquaculture over seasonal to decadal scales. Temperature to nitrate relationships were determined from *in situ* measurements using generalized additive models and validated with buoy data. Summer and winter relationships were significantly different, and satellite-derived products compared well to buoy validations. Surface nitrate patterns, as derived from satellite temperature products, reveal the spatial variability in nitrate concentrations, and indicate areas that that may cause nutrient stress seasonally and during the negative phase of the North Pacific Gyre Oscillation. As the spatial scale of the surface nitrate product decreased, the negative bias increased and fine scale spatial variability was lost. Similarly, the averaging of daily nitrate concentration determinations over longer time scales increased

the negative bias. We found that daily, 1 km spatial resolution nitrate products were most sufficient for identifying localized upwelling and areas of consistently high surface nitrate concentrations, and that areas in the northern and western-most portions of the Southern California Bight are the most suitable for sustained offshore kelp aquaculture.

Keywords: sea surface temperature, remote sensing, kelp, spatiotemporal, aquaculture, scaling, modeling

INTRODUCTION

Satellite remote sensing allows for the daily determination of global sea surface temperature (SST), which can be used to estimate nutrient concentrations in the surface water via empirical temperature to nutrient relationships. Over the last four decades, the rapid increase in global satellite missions and freely available satellite-based data products have led to spatially explicit seawater nutrient estimates in many regions. Early work by Kamykowski and Zentara (1986) modeled temperature to nutrient relationships globally using *in situ* temperature, nitrate, phosphate, and silicic acid measurements for use with Coastal Zone Color Scanner SST imagery. Others have built upon this technique to include additional nutrients for marine flora and established time series over large spatial extents in various regions (Sathyendranath et al., 1991; Morin et al., 1993; Dugdale et al., 1997; Kamykowski et al., 2002; Son et al., 2006). The more recently launched Landsat 8 Operational Land Imager has the capability to monitor surface temperatures at a finer spatial resolution than traditional ocean observing satellites. Landsat 8 imagery is particularly useful for work in coastal environments because the thermal infrared sensor (TIRS) has a high signal-to-noise ratio and 100-m spatial resolution. High-resolution SST from Landsat 8 can be accurately determined after accounting for atmospheric effects using coincident satellite imagery and have been used to aid in the siting of aquaculture, such as oyster farms in Maine (Snyder et al., 2017).

Recently, the United States Department of Energy has invested in research to develop offshore giant kelp aquaculture farms for the production of biofuels and other products (e.g., fertilizer, animal feed, and chemicals). Thus, a temporospatial knowledge of nutrient availability in these often nutrient-poor offshore waters is required. The floating kelp canopy exists at the sea surface, so while nutrients at depth may fluctuate depending on seasonal stratification, year-round estimations of SST should be sufficient for this application. Seawater nitrate concentration is strongly and inversely related to seawater temperature in regions influenced by coastal upwelling and empirical temperature to nitrate relationships (T2N) have been developed for this region (Eppley et al., 1979; Dugdale et al., 1997; Kim and Miller, 2007; McPhee-Shaw et al., 2007; Omand et al., 2012; Jacox et al., 2015) to study ocean dynamics and biophysical interactions in a variety of ecosystems (Kamykowski and Zentara, 1986; Kamykowski et al., 2002; Edwards and Estes, 2006; Fram et al., 2008; Stewart et al., 2009).

The growth, distribution, and lifespan of giant kelp (*Macrocystis pyrifera*) fluctuates due to multiple environmental drivers, such as wave disturbance, temperature, nutrients, light availability, and herbivory (Gerard, 1982a; Graham et al., 2007; Parnell et al., 2010; Bell et al., 2015a). The spatial and temporal variability of these drivers must be quantified to optimize the spatial planning of these large-scale, offshore kelp aquaculture operations (Gentry et al., 2017; Lester et al., 2018). Two of these physical parameters, seawater temperature and nutrient concentration, are particularly relevant as upwelling processes deliver cool, nutrient-rich water to the surface and fuel giant kelp growth, while water temperatures >23°C can lead to severe reductions in canopy biomass (Zimmerman and Kremer, 1984; Deysher and Dean, 1986; Cavanaugh et al., 2019). The upwelling and advection of nutrient-rich seawater to the surface varies greatly across space and through time and is associated with seasonal to interannual fluctuations in giant kelp abundance over local to regional scales (Bell et al., 2015a). Ambient seawater nitrate accounts for a large portion of readily available inorganic nutrients and is a necessary ion for tissue building and photosynthesis, where frond elongation rate declines dramatically when nitrate concentrations are <1 μmol L^{-1} (Zimmerman and Kremer, 1984; Rodriguez et al., 2016). While seawater nitrate concentration is closely related to kelp frond elongation and biomass accumulation in natural kelp forest systems (Zimmerman and Kremer, 1984; Bell et al., 2018), other forms of nitrogen, such as ammonia and urea, have been proposed for the maintenance of photosynthetic processes during periods of low nitrate availability (Brzezinski et al., 2013; Smith et al., 2018). However, the benthic sources of these reduced forms of nitrogen (Brzezinski et al., 2013; Burkepile et al., 2013; Peters et al., 2019) suggest they will be less important in offshore areas. Furthermore, while kelp can absorb nitrogen throughout the water column, the photosynthetic condition of the canopy is strongly related to seawater nitrate concentrations at the surface (Fram et al., 2008; Konotchick et al., 2012; Bell et al., 2018; Bell and Siegel, in review). Since the surface canopy exists in a high light environment and provides the largest contribution to production, the assessment of surface seawater nitrate concentration is an essential first step in the aquaculture siting process (Colombo-Pallotta et al., 2006).

Since seawater nutrient concentrations are dynamic and can be limiting for kelp forest growth, this variability across space and through time needs to be well understood if offshore kelp aquaculture is to be successful. It is also necessary to understand the appropriate spatial and temporal scale to observe these nutrient dynamics, as local circulation processes may play a critical role in nutrient delivery to aquaculture farms. This is especially important as aquaculture farms are usually on the scale of 10's to 100's of meters and may be subject to processes operating over a variety of scales. Larger spatial and longer temporal resolution satellite data products may mask smaller scale nutrient inputs that may be important to kelp growth in

proposed offshore aquaculture areas. Since T2N relationships tend to be non-linear, the mean seawater temperature state across several days or over several kilometers may lead to a vastly different estimate of mean nitrate concentration when compared to estimates determined from sensors with increased temporal or spatial resolution. With the numerous spatial and temporal scale SST products available to the aquaculture community, a quantification of error associated with changes in spatial/temporal resolution is necessary. In order to determine the optimal spatial and temporal scale to observe seawater nitrate dynamics for use with offshore kelp aquaculture, we (1) used high spatial resolution (100 m) SST imagery from Landsat 8 to quantify the error associated with determining nitrate concentrations at several common spatial resolutions, (2) determined the error associated with averaging temperature data across various temporal scales, and (3) determined the optimal spatial/temporal scale of observation and combined these analyses with known kelp physiological traits to develop a kelp stress index (KSI) to aid in a siting analysis of offshore kelp farms in the Southern California Bight.

MATERIALS AND METHODS

Study Area

The United States portion of the Southern California Bight is a part of the California Current System that stretches from Point Conception to San Diego, California, and experiences a Mediterranean climate of cool, wet winters and warm, dry summers. Seasonal upwelling of cool, nutrient rich waters is driven by intensified winds in late winter and spring along the west coast of the United States (Harms and Winant, 1994; Otero and Siegel, 2004; Henderikx-Freitas et al., 2016). This season is followed by a period of reduced upwelling, when waters warm and stratify throughout the summer and fall months. The Santa Barbara Channel falls within the Southern California Bight and is defined by the Channel Islands to the south, Point Conception to the northwest, and the Santa Clara River to the southeast. A strong east/west gradient in seawater temperature (typically > 5°C) often exists in the Santa Barbara Channel in the late spring and early summer (e.g., Otero and Siegel, 2004).

Development of Temperature to Nitrate Relationships

In order to derive surface water temperature to nitrate relationships which can be applied to remotely sensed SST data, we used *in situ* seawater temperature and seawater nitrate concentration measurements across seasons and locations in the Southern California Bight. Generalized additive models (Wood, 2006) were used to model these relationships for nitrate + nitrite, hereafter referred to as nitrate (Kamykowski et al., 2002; Parnell et al., 2010; Bell et al., 2018). In previous studies of the Southern California Bight, nitrate represented the vast majority of nutrients in pooled nitrate + nitrite samples (Paulson, 1972; ∼98% CalCOFI). Input to the model was from all data collections spanning 1980–2018 at depths from 0 m to 3 m within the Southern California Bight (**Figure 1**). For analyses using Landsat 8 imagery of the Santa Barbara Channel, data were used from a subset of CalCOFI cruises within the boundaries of the Landsat 8 overpass over the Santa Barbara Channel (33.496°N to 35.706°N; and −118.594°E to −121.186°E), Santa Barbara Coastal Long Term Ecological Research cruises, and UCSB Plumes and Blooms cruises[1,2,3].

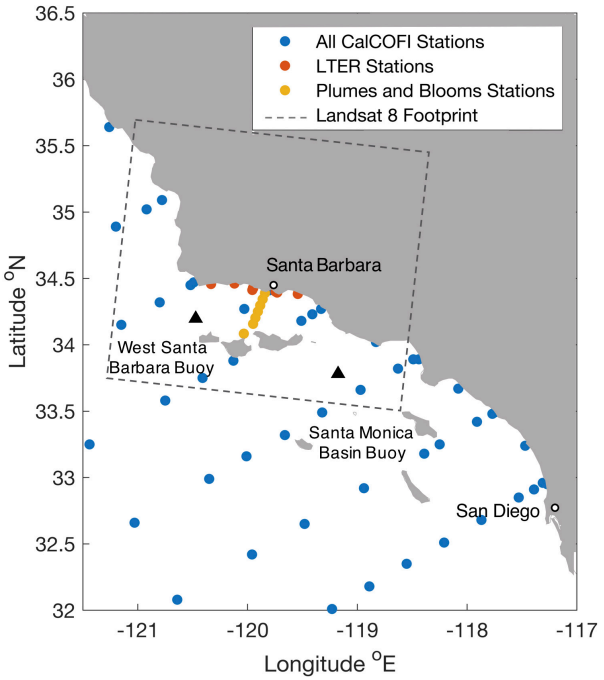

FIGURE 1 | *In situ* data collection sites (orange, yellow, and blue markers) in the Southern California Bight used for temperature to nitrate relationships in the Santa Barbara Channel, California.

Temperature and nitrate data from all cruises were binned into two groups according to a seasonal, climatological pattern in the Southern California Bight: cool and wet winter months (December – May), and warm and dry summer months (June – November) (Otero and Siegel, 2004). Temperature and nitrate data were also binned by coastal vs. offshore (at least 10 km from the nearest coast), and sub-regionally, (northern: >34.15°N and < −120.5°E, central: from 33.75°N to 34.41°N and −120.4°E to −119.3°E, and southern: < 34.03°N and > −119.3°E) inside the Southern California Bight (**Supplementary Figure S1**). A GAM was fit for the two seasonal, three regional, and coastal/offshore temperature and nitrate datasets using the mgcv package in R with a Tweedie error structure (power function = 1.3; $k = 10$).

Satellite Imagery

Sea surface temperature (SST) imagery from multiple satellite sensors were used to produce seawater nitrate estimates with the empirical seasonal T2N relationships developed in this

[1]CalCOFI.org
[2]http://sbc.lternet.edu/
[3]http://www.oceancolor.ucsb.edu/plumes_and_blooms/

study. One kilometer resolution SST imagery was obtained via a combined MODIS/VIIRS-derived product for the Southern California Bight[4]; while 100 m resolution data from the Landsat 8 TIRS thermal band was used to derive high spatial resolution SST products in the Santa Barbara Channel[5]. An atmospheric correction was applied to the Landsat 8 imagery by scaling brightness values with fully processed 1 km SST product data (Snyder et al., 2017). Clouds, cloud shadows and land were masked from the Landsat 8 SST imagery using the Fmask algorithm (Zhu et al., 2015), and fog banks and airplane contrails were manually removed. Imagery was processed for twelve clear Landsat 8 overpass dates between 2016 and 2018, and then five of these images that displayed the best results from the atmospheric correction step (as well as the greatest dynamic range in nutrient values throughout the Channel), were chosen to represent the highest spatial resolution imagery available. Landsat 8-derived SST imagery were validated with SST data from four NOAA ocean observing buoys in the Santa Barbara Channel (buoys 46218 Harvest, 46054 West Santa Barbara, 46053 East Santa Barbara, and 46217 Anacapa Passage; r^2 = 0.93, mean error = 0.23°C, mean absolute error = 0.59°C, and linear fit equation $y = 1.2x - 1.2$). Buoy temperature time series from the Santa Monica Basin and West Santa Barbara (**Figure 1**) were also converted to time series of nitrate concentration using the T2N relationships developed in this study. These buoy time series were used to validate seawater nitrate estimates from the 1 km MODIS/VIIRS-derived product described above.

Spatial Scaling Analysis

We performed a scaling analysis to examine the effect of using SST products with different spatial resolutions to produce maps of seawater nitrate concentration. We started with a processed Landsat 8 100 m SST image and degraded the spatial resolution to produce 1, 2, 4, 9, 15, and 25 km pixel scale imagery of nitrate concentration via two methods (**Figure 2**).

The first method preserves the high-resolution nitrate estimates by spatially degrading a 100 m nitrate product (assuming this product is "truth"), and the second method simulates the use of a lower resolution SST product by first spatially degrading the 100 m SST image before estimating the nitrate concentrations. We then found the difference in nitrate concentration between the two methods as the spatial resolution of the imagery was decreased. Differences in modeled seawater nitrate concentration were quantified using simple linear regressions. We also investigated the spatial error within a spatially degraded pixel by quantifying the fine scale physical processes hidden by using lower spatial resolution imagery. These fine scale (100 m) errors due to changing resolution were quantified by fitting normal probability distribution functions to the error distributions at each spatial scale.

Temporal Scaling Analysis

We performed a temporal scaling analysis to examine the effect of averaging SST through time on estimated seawater nitrate concentration. Temperature measurements were made every 10 min by the Santa Monica Basin buoy and West Santa Barbara buoy, and we sampled the timeseries (blue trace, **Figure 3**) at 1:30PM local time each day to mimic a satellite SST acquisition. These daily temperatures were then averaged over several time intervals (5, 10, 15, and 30 days) to simulate SST products at commonly available temporal resolutions (**Figure 3**).

These averaged temperature intervals were then converted to nitrate concentration and compared to the mean nitrate concentration estimated from the individual daily buoy temperatures over the same time period. The accuracy of the nitrate concentration estimate was determined using the mean absolute error for each temporal resolution (MAE_k), defined as:

$$MAE_k = \frac{1}{n}\sum_{i=1}^{n} |N_{k,i}^{Satellite} - N_{k,i}^{Buoy}| \quad (1)$$

where $N_{k,i}^{Satellite}$ is the estimated nitrate concentration from the simulated daily satellite SST averaged over each temporal resolution k, $N_{k,i}^{Buoy}$ is the estimated nitrate concentration from the continuous buoy temperature measurements, and n is the total number of absolute error determinations. Mean absolute error is an unambiguous measure of error compared to root mean squared error because it is less sensitive to the distribution of error magnitudes (Willmott and Matsuura, 2005). To quantify bias in the estimation of nitrate concentration, we determined the mean error for each temporal resolution (ME_k) which was calculated as:

$$ME_k = \frac{1}{n}\sum_{i=1}^{n} \left(N_{k,i}^{Satellite} - N_{k,i}^{Buoy}\right) \quad (2)$$

Cloud cover limits the ability of satellites to measure SST and varies seasonally. In order to account for the effect of variable cloud cover, a fraction of daily SST values (0.1, 0.2, 0.3, 0.4, 0.5, 0.6, 0.7, and 0.8) were randomly removed from each time interval before averaging was completed. Mean absolute error and mean error were then determined from these estimated nitrate concentrations as stated above.

Siting Analysis

We performed a siting analysis for all areas in the United States portion of the Southern CA Bight. Since the technology of farm design is changing rapidly, we included areas regardless of depth. We used daily, 1 km SST from the MODIS/VIIRS-derived product from 2002 to 2018 (see text footnote 4) and converted to nitrate concentration according to the seasonal T2N relationships derived in this study. We then calculated the mean and coefficient of variation of nitrate concentration in the surface water across all dates and the mean nitrate concentration for each season.

We also determined the proportion of time that giant kelp farms exist in nutrient conditions to support adequate growth rates. Giant kelp has internal nitrogen stores to support growth for roughly 2 to 3 weeks (Gerard, 1982a) and frond elongation rate maximizes at seawater nitrate concentrations of 1 μmol L^{-1} (Zimmerman and Kremer, 1984). Therefore, we examined the number of consecutive days when surface nitrate concentrations

[4]http://spg-satdata.ucsd.edu/

[5]earthexplorer.usgs.gov

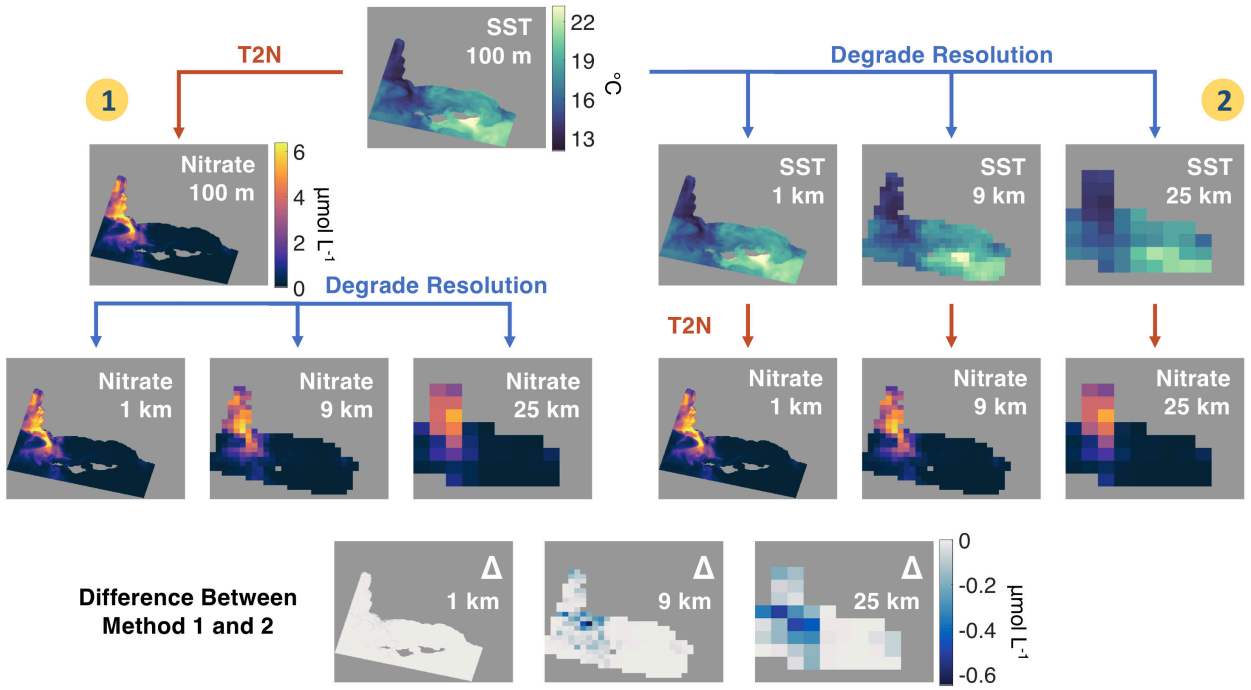

FIGURE 2 | Description of the two methods of estimating nitrate from sea surface temperature (SST) imagery for the Santa Barbara Channel region using Landsat 8 thermal images from October 22, 2017. Method 1 preserves the magnitude of nitrate estimations at the native 100 m scale by first passing the SST data through the empirical temperature to nitrate (T2N) relationship, then degrading the spatial resolution. Method 2 approximates a data user selecting a SST product at a commonly available spatial resolution and then applying the T2N relationship. The bottom rows show the difference in estimated nitrate concentrations between Method 1 and 2 at each spatial resolution.

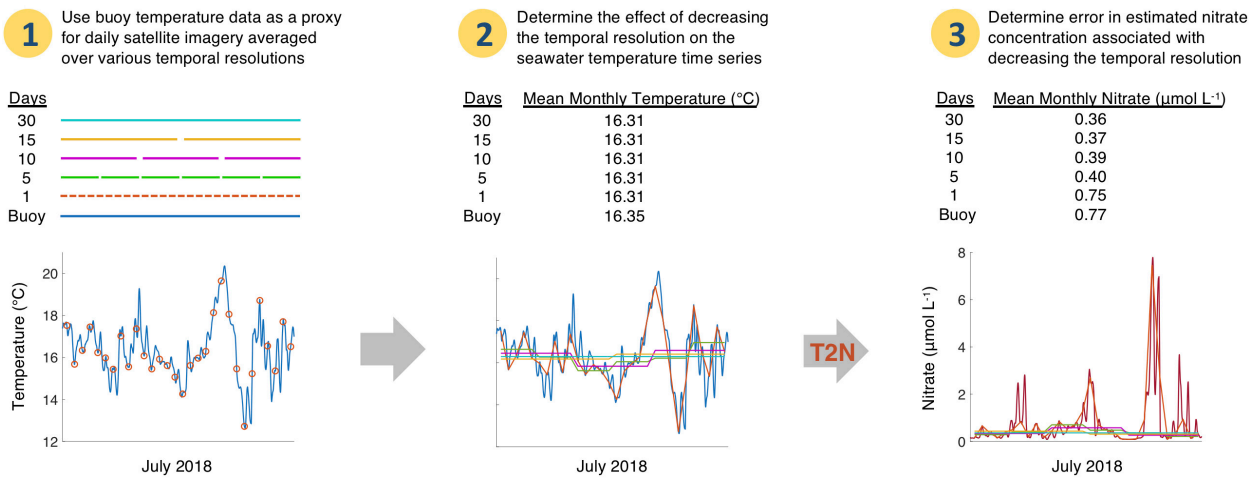

FIGURE 3 | (1) Continuous temperature data (blue line) from a buoy was sampled daily to simulate daily satellite SST determinations (red dots). **(2)** These daily temperatures are then averaged over four temporal resolutions (5, 10, 15, and 30 days; shown as colored lines plotted over the continuous buoy data). The mean SST across the entire time series for each temporal resolution is shown. **(3)** Use empirical temperature to nitrate relationship (T2N) to estimate time series of nitrate concentration which are plotted over the continuous estimated nitrate concentration derived from the buoy temperature data (maroon line). The mean estimated nitrate concentration across the entire time series for each temporal resolution is shown.

fell below 1 μmol L^{-1} after interpolating each 1 km pixel's SST time series with a piecewise cubic spline to remove missing values (Matlab function interp1 – "pchip"). When there were >21 days in a row below the 1 μmol L^{-1} nitrate concentration threshold, we counted those days as a period of giant kelp nutrient stress. We then found the fraction of days with kelp nutrient stress to determine the KSI for each season for the entire study area. Low frequency climate cycles, like the North Pacific Gyre Oscillation

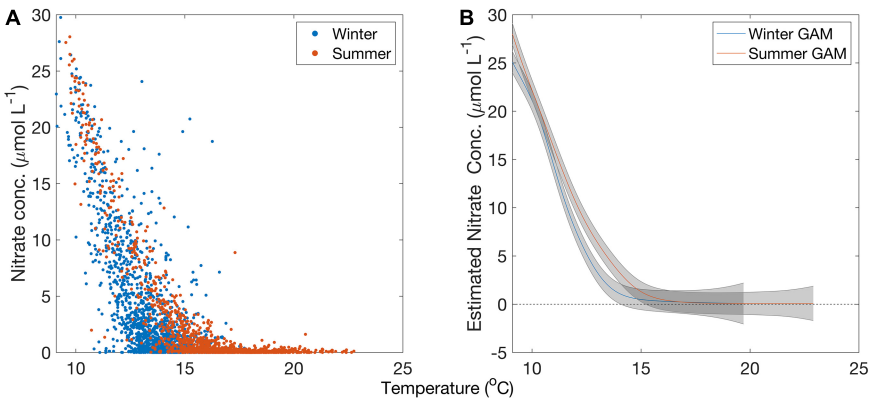

FIGURE 4 | (A) Temperature and nitrate measurements separated by season in the Southern California Bight. Blue markers are datapoints collected during wintertime, red markers are datapoints collected during summertime. **(B)** Generalized additive model fit for temperature to nitrate relationships in the winter and summer months in the Santa Barbara Channel from 1980 to 2018 above 3 m depth. Blue line is the winter GAM, and red line is the summer GAM. Gray bars are the standard error about the curve.

(NPGO), affects nitrate delivery to the Southern California Bight (Di Lorenzo et al., 2008; Parnell et al., 2010). Stronger winds drive increased upwelling during positive NPGO years, and greater concentrations of nutrients are delivered to the surface (Di Lorenzo et al., 2008). We also determined the difference in the KSI for each season when the NPGO was in a negative versus a positive mode.

RESULTS

Temperature to Nitrate Relationship and Satellite Imagery

There were significant seasonal differences found in the T2N relationships developed from *in situ* temperature and nitrate data. The winter GAM had an $R^2 = 0.83$; $p < 0.001$; $n = 2691$; and the summer GAM had an $R^2 = 0.91$; $p < 0.001$; $n = 2758$, with winter months defined as December – May and summer months defined as June – November (**Figure 4**). The summer T2N relationship showed higher nitrate concentrations than the winter T2N relationship between 11 and 15°C. These seasonally specific relationships were used for all further analyses.

There were no significant differences found between coastal and offshore T2N relationships, nor were significant differences found between the three sub-regional T2N relationships (**Supplementary Figure S1**). The results are qualitatively similar to prior work in the region (cf. Omand et al., 2012 or Jacox et al., 2015 for summaries of coastal and offshore T2N relationships derived from *in situ* observations).

High spatial resolution maps of SST and estimated nitrate concentration (**Figure 5**) were generated for the Santa Barbara Channel on five clear days between 2016 and 2018 (October 3, 2016, October 19, 2016, October 22, 2017, November 10, 2018, and December 28, 2018).

Landsat 8-derived temperature data compared well to buoy validation data in the Santa Barbara Channel ($r^2 = 0.93$). Surface nitrate concentrations followed an inverse pattern to SST, as expected, where nitrate concentrations in the Santa Barbara Channel are typically highest in the western half of the channel, where cold, nutrient rich waters upwelled along the central coast of California are advected southward toward the western Channel Islands (**Figure 5**). This is observed in all five sets of Landsat imagery analyzed (**Supplementary Figures S3–S6**).

Satellite retrievals of SST (1 km MODIS/VIIRS product) and estimated nitrate concentration matched the general patterns of variability estimated from the continuous data at both buoys (**Figure 6**). General temperature patterns followed a seasonal cycle of highest values in the summer and lower values in the winter, while nitrate concentrations had an inverse pattern of peaks during the spring/winter and lows during the summer/fall.

Comparisons of SST between the buoys (West Santa Barbara and Santa Monica Basin) and the satellite product were highly significant and more strongly correlated ($r^2 = 0.93$ and 0.95, $p < 0.001$) than the estimated seawater nitrate concentrations ($r^2 = 0.89$ and 0.79, $p < 0.001$) because nitrate estimates contain error from both satellite temperature estimates as well as the T2N relationship. Both mean absolute error and mean error were greater in magnitude for both SST and nitrate concentration for the West Santa Barbara buoy than the Santa Monica Basin buoy (**Table 1**).

Spatial Scaling Analysis

The spatial scaling analysis showed that values of T2N estimated nitrate concentrations were reduced as the spatial resolution of the image was decreased (**Figure 7**). As the spatial resolution was degraded from 1 km to 25 km, nitrate concentrations greater than 1 μmol L^{-1} were disproportionately underestimated and pixel nitrate concentration magnitude was reduced (**Figure 7** and **Supplementary Figures S3–S6**).

As the spatial resolution was degraded, local scale variations in nitrate concentration were lost. As spatial resolution decreased from 1 km to 25 km, the standard deviation of the distribution of errors became larger, indicating that the level of error increased over a greater number of pixels (**Figure 8**). The mean of the error

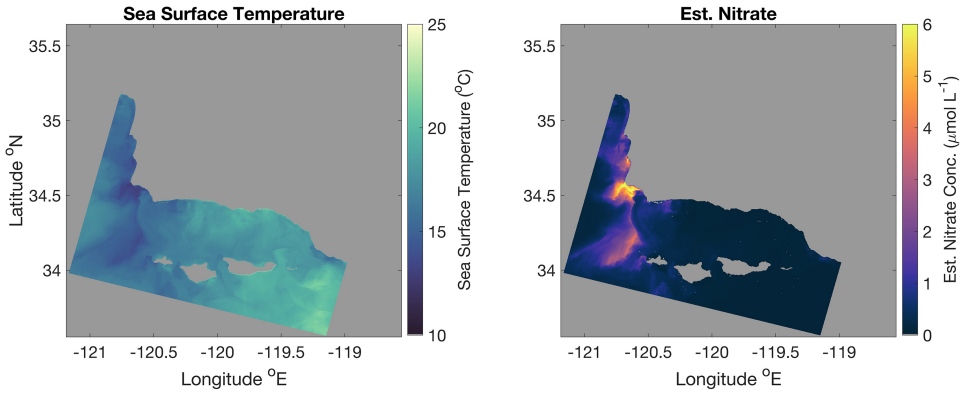

FIGURE 5 | Landsat 8-derived SST and T2N estimated nitrate concentration imagery of the Santa Barbara Channel on October 19, 2016. Spatial resolution is 100 m.

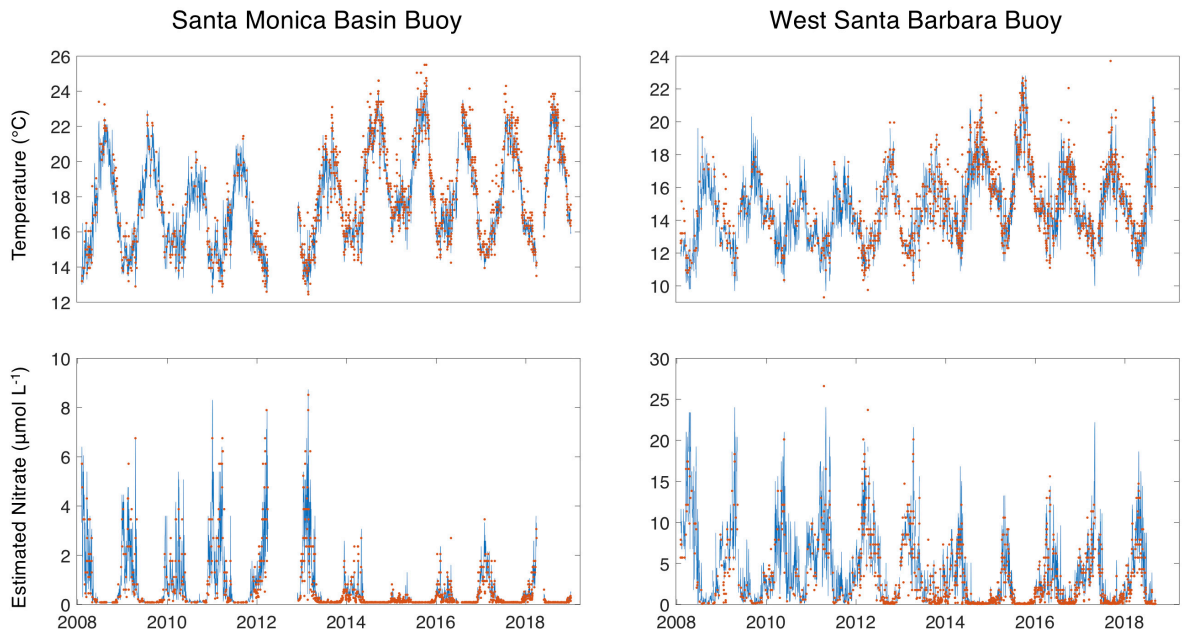

FIGURE 6 | Continuous temperature and estimated nitrate concentrations time series from the Santa Monica Basin and West Santa Barbara buoys are shown as blue lines. The red dots show the daily SST and daily estimated nitrate concentrations from the 1 km, MODIS/VIIRS-derived SST product.

distribution decreased from zero to negative values as the spatial scale increased from 1 km to 25 km, indicating that local scale nitrate concentration was more often underestimated.

Maps of the difference in estimated nitrate concentration between the 100 m product and the 25 km product show the higher values of nitrate were diminished, (up to 5 μmol L^{-1}) in places where there was higher spatial variability in SST, such as around Point Conception in the northwest and around the Channel Islands (**Figure 9**).

Temporal Analysis Results

The temporal scaling analysis showed that increasing the temporal averaging of daily SST imagery negatively biased nitrate concentration estimates (**Figure 10**). The average MAE (μmol L^{-1}) across all cloud contamination fractions did not show large changes as temporal scale increased for both buoys (West Santa Barbara, 0.66 to 0.64 and Santa Monica Basin, 0.13 to 0.14). However, there were large increases in MAE as the degree of cloud contamination increased, when averaged over all temporal scales (West Santa Barbara, 0.47 to 0.86 and Santa Monica Basin, 0.10 to 0.17), meaning that a reduction in the number of images due to cloud cover affected MAE more than averaging samples over a specific time period. The magnitude of the ME (μmol L^{-1}) increased and became more negative as the temporal scale increased (West Santa Barbara, −0.27 to −0.50 and Santa Monica Basin, −0.06 to −0.12) and displayed a smaller effect associated with increasing cloud contamination (West Santa Barbara, −0.42 to −0.32 and Santa Monica Basin,

TABLE 1 | The mean absolute error (MAE), mean error (ME), coefficient of determination (r^2), and linear equation for relationships between sea surface temperature (SST) and estimated nitrate concentration (Est. NO_3) between buoys and satellite determinations (1 km) MODIS/VIIRS-derived SST product.

Buoy	Variable	MAE	ME	r^2	Equation
Santa Monica Basin	SST (°C)	0.49	0.31	0.95	y = 1.00x + 0.04
	Est. NO_3 (μmol L^{-1})	0.23	−0.02	0.79	y = 0.91x + 0.04
West Santa Barbara	SST (°C)	0.51	0.23	0.93	y = 0.98x + 0.57
	Est. NO_3 (μmol L^{-1})	0.91	−0.52	0.89	y = 0.85x + 0.05

All relationships significant at the $p < 0.001$ level.

−0.09 to −0.07). Meaning that averaging samples over a specific time period led to a greater negative bias compared to a reduction in available imagery due to cloud cover.

Siting Analysis

The siting analysis shows areas in the Southern California Bight that maintain consistent nitrate levels above 1 μmol L^{-1} at the surface in all seasons, and some areas that exhibit seasonal and interannual differences. We found that nitrate concentrations remain elevated in areas north of Pt. Conception and in the western SB Channel throughout the time series, with a coefficient of variation of nitrate concentration close to 1 (**Figure 11**).

The coefficient of variation was higher in the rest of the SB Channel and close to 2 in much of the southeastern quadrant of our study area. Seasonal patterns of nitrate concentration were >1 μmol L^{-1} for most of the study area in winter with increased concentrations in the northern half of the study area in spring. Summer and fall were characterized by reduced nitrate concentrations over the vast majority of the study area.

The KSI was low during the winter and spring seasons, the fraction of nutrient stress was close to zero throughout most of the Santa Barbara Channel and into the open ocean beyond the Channel Islands (**Figure 12A**). In the summer season KSI values were high, especially in the eastern half of the Channel and close to shore, where the fraction of nutrient stress was well above 0.8. There was moderate nutrient stress in the fall season, the stress fraction was above 0.5 in most of the SB Channel and southward.

During the positive phase of the NPGO the spatial pattern of nutrient stress changed the most during the spring season (**Figure 12B**). There was a decrease in KSI in areas offshore and south of the channel, in some places by as much as 0.5. The winter season also had a strong reduction in stress fraction, especially along the coast and to the southeast. The summer only had weak reductions in KSI near Point Conception, and the fall had mild reductions in the channel and along the southeast coast.

DISCUSSION

Siting of Kelp Aquaculture Farms

Estimated surface nitrate concentration imagery show seasonal means that follow expectations for the Southern California Bight (**Figure 11**). Spring upwelling leads to elevated nitrate concentrations, especially in the northern and western halves of the study area. The SE quadrant of the study area can have less than 1 μmol L^{-1} nitrate in surface waters for much of the year; and with CV's of around 2, this area shows a great degree of variability through time. For kelp aquaculture, and especially farms fixed to the seafloor, areas with more stable nutrient conditions (both seasonally and interannually, i.e., the northern and western areas) should lead to more stable aquaculture production and should be considered in spatial planning analyses (Gentry et al., 2017; Lester et al., 2018). The Santa Barbara Channel is uniquely protected from exposure to wave action and high-resolution thermal imagery could be especially useful for identifying areas with nutrient concentrations high enough to support year-round kelp growth (Cabral et al., 2016).

The analysis of the KSI (i.e., fraction of days with kelp nutrient stress) shows that much of the study area is not under potential nitrate stress for the winter and spring seasons (**Figure 12**). During summer and fall the northern half of the study area can still display low kelp nutrient stress, but low nutrient surface waters dominate during summer in the SE quadrant and as they flow into the Santa Barbara Channel from the east and increase nutrient stress (Harms and Winant, 1994; Otero and Siegel, 2004). There are areas in the Southern California Bight that maintain less than ideal conditions for kelp growth (mean nitrate concentration stays below 1 μmol L^{-1} nitrate as indicated by the white contour line in **Figure 11**). Nevertheless, there are kelp forests that occur for periods of several years in the SE quadrant of the map despite a high average KSI, for example, along the coast of San Diego, CA.

By incorporating decadal forcing like NPGO into the siting analysis we found valuable information that may have otherwise been missed by the averaged data through time. When the NPGO was positive, areas in the southern portion of the study area increased in their proportion of time with adequate nutrients for kelp growth, especially in the winter and spring. In fact, the NPGO is an important interannual driver of kelp canopy biomass dynamics along the California coast and natural kelp forests in these southern areas may only form canopies during positive NPGO years (Parnell et al., 2010; Cavanaugh et al., 2011; Bell et al., 2015a). It follows that engineered kelp farms planted in areas that typically experience low nitrate conditions may only be successful during high NPGO periods. We can learn from the dynamics of natural kelp systems in these low nitrate areas, especially if planned aquaculture requires that no external fertilizers are applied. The KSI is modulated by factors other than mean seasonal temperature and nutrient concentrations, so it is helpful to consider low frequency marine climate oscillations, like the NPGO, that may allow kelp to persist (Di Lorenzo et al., 2008). In the Santa Barbara Channel the KSI never exceeds 0.5, except in the Summer and Fall seasons near the eastern section and along the mainland coast. This highlights the western Santa Barbara Channel as an ideal site for maintaining kelp growth at the surface in offshore aquaculture during both negative and positive NPGO years.

It is important to note that this study only covers nitrate concentrations at the surface, and stratification and internal

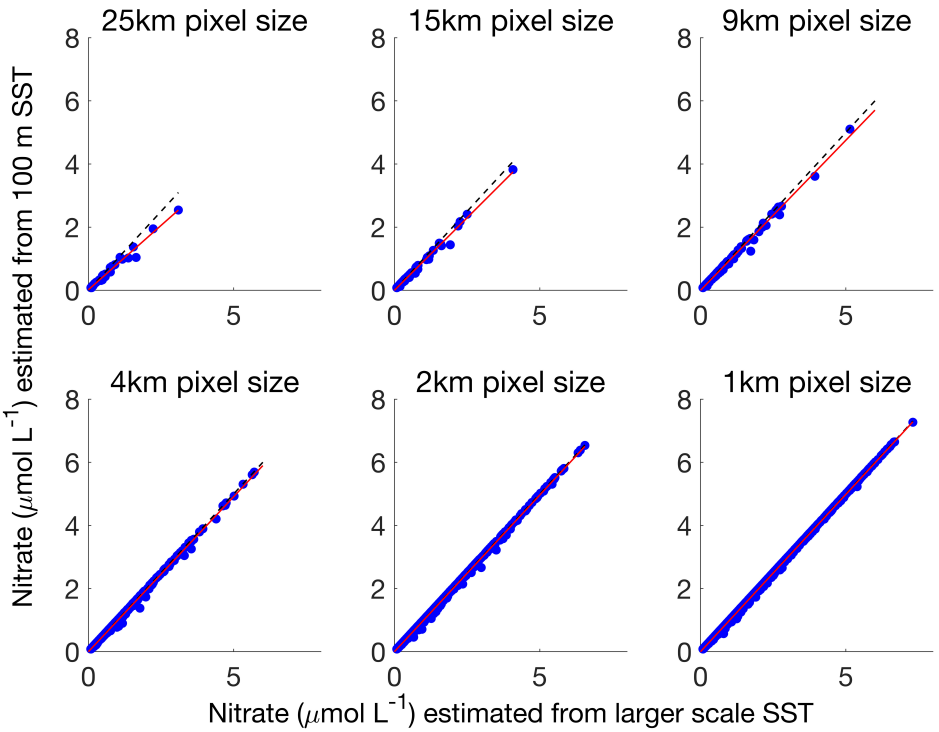

FIGURE 7 | Nitrate concentrations for 25, 15, 9, 4, 2, and 1 km spatial resolution nitrate products calculated from the 100 m Landsat 8 SST product (*x*-axis) and the larger spatial resolution Landsat 8 SST product (*y*-axis). Red line is regression fit, dashed black line is 1:1. Image was collected on October 19, 2016.

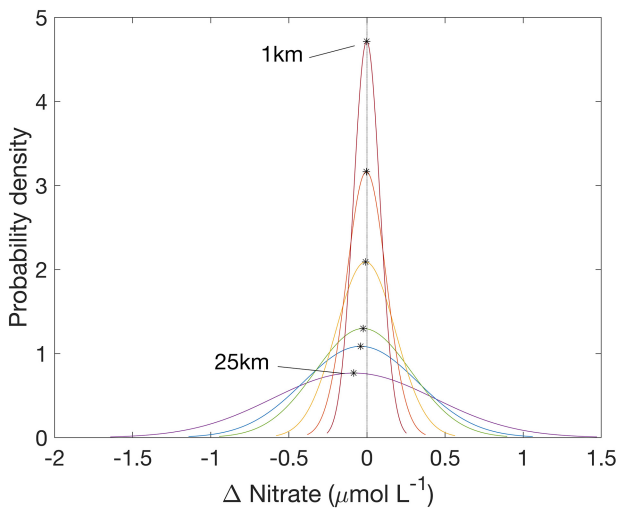

FIGURE 8 | Normal curve fit of error distribution in nitrate product from October 19, 2016. Black stars are the mean error at each spatial resolution.

waves may be responsible for translocation of nutrients at depth (Zimmerman and Kremer, 1984; McPhee-Shaw et al., 2007). Despite this, we know that kelp canopy health declines when surface waters warm and nitrate decreases, both seasonally and during marine heatwaves, and thus surface waters are very important to monitor for kelp canopy condition and growth (Bell et al., 2018; Cavanaugh et al., 2019). While the spatial resolution of the MODIS 1 km product adequately captures surface patterns of SST and nitrate, it is important to note that the temporal resolution of satellite imagery only provides a snapshot of conditions at a single moment during the day. As such, this daily measurement likely misses oceanographic events, some of which could be especially important for supporting kelp growth. Internal waves are strong at 12 h periods and drive influxes of upwelled water into the Santa Barbara Channel, so for siting purposes it would be advantageous to collect continuous or hourly measurements with moored sensors that can capture these events and supplement satellite datasets (Zimmerman and Kremer, 1984).

These maps do not directly identify the best overall areas to site a kelp farm, but they do offer spatially and temporally explicit information to help with the decision-making process, as several factors will come into play depending on farm design, permitting, economic forces, and environmental impacts. As a foundation species and ecosystem engineer, giant kelp serves as a habitat for bryozoans, bacterial colonies, fishes etc, and floating kelp farms in the open ocean could have positive and/or negative effects on surrounding ecosystems by modulating local nutrient availability. Rather than solely rely on nitrate concentration, it is better to map how the organism of interest will respond to these nutrient dynamics. Maps of nutrient stress periods show areas where kelp production may suffer seasonally. Sainz et al. (2019) showed that bivalve aquaculture is also expected to do poorly in the Southern

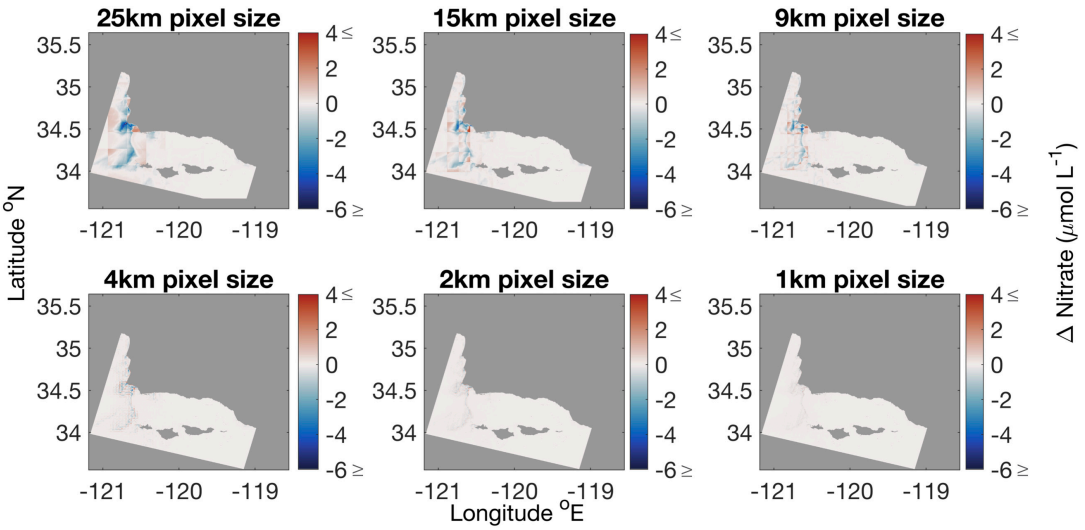

FIGURE 9 | Difference between nitrate calculated from 100 m SST product and nitrate calculated from coarser spatial resolution SST products. Lower spatial resolution products diminished areas with high nitrate levels. Original Landsat 8 imagery was collected on October 19, 2016.

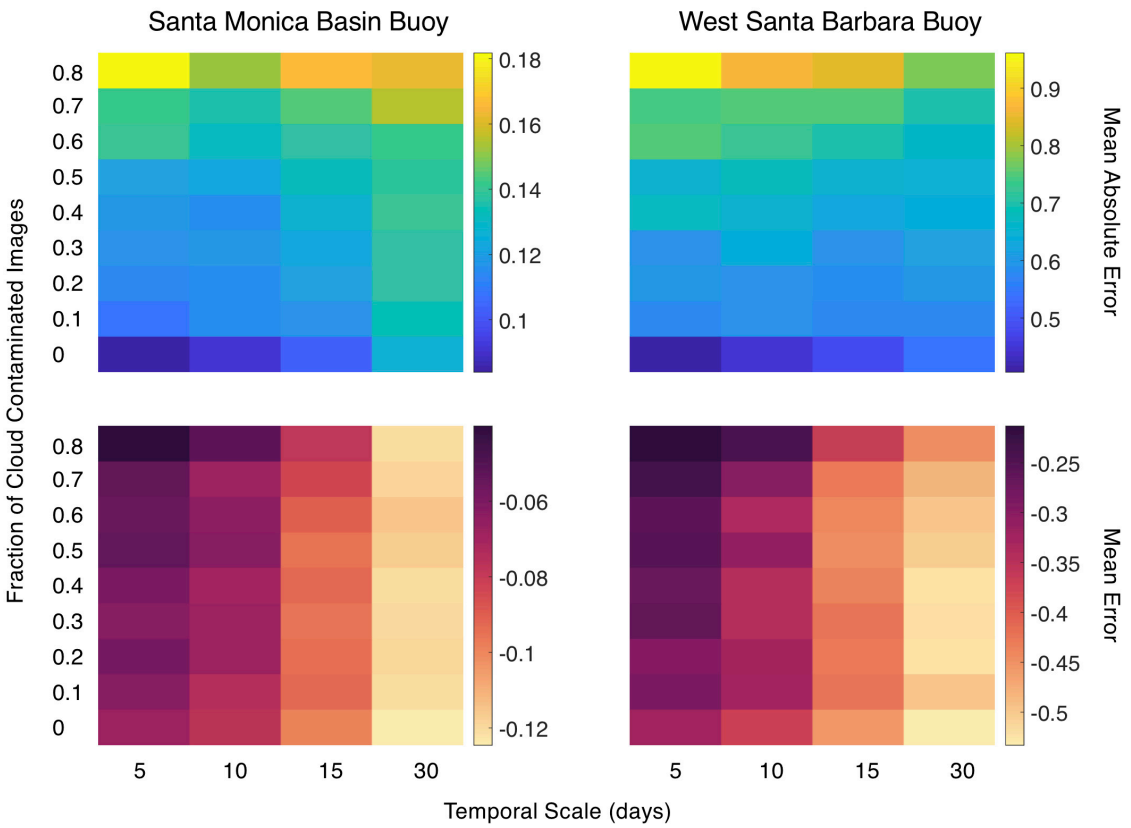

FIGURE 10 | Mean absolute error and mean error in estimated nitrate concentration (μmol L^{-1}) as a function of the temporal resolution of the simulated SST imagery and the fraction of daily temperature images contaminated with cloud cover.

California Bight during these negative NPGO periods, however, Lester et al. (2018), showed that finfish aquaculture may benefit from warmer waters, conditions that would be common during this period. Due to the nature of decadal climate cycles in the Southern California Bight, it may be worthwhile to examine a dynamic approach to marine spatial planning, where kelp

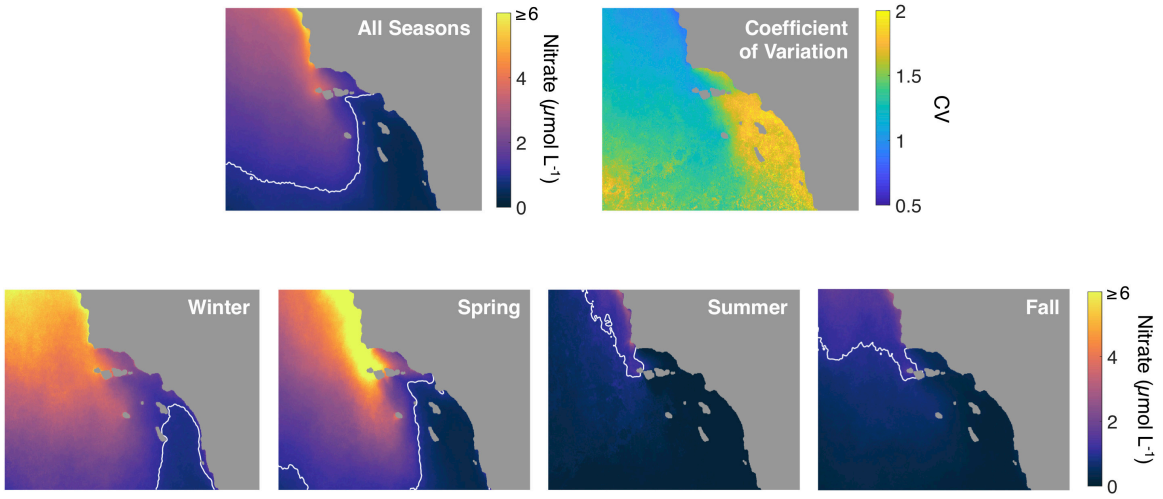

FIGURE 11 | Top row: Mean and coefficient of variation (CV) of estimated nitrate concentration over the study area across all seasons. **Bottom row:** Mean estimated nitrate concentration across each season over the study area. White contour line shows the location of the 1 μmol L^{-1} nitrate concentration front.

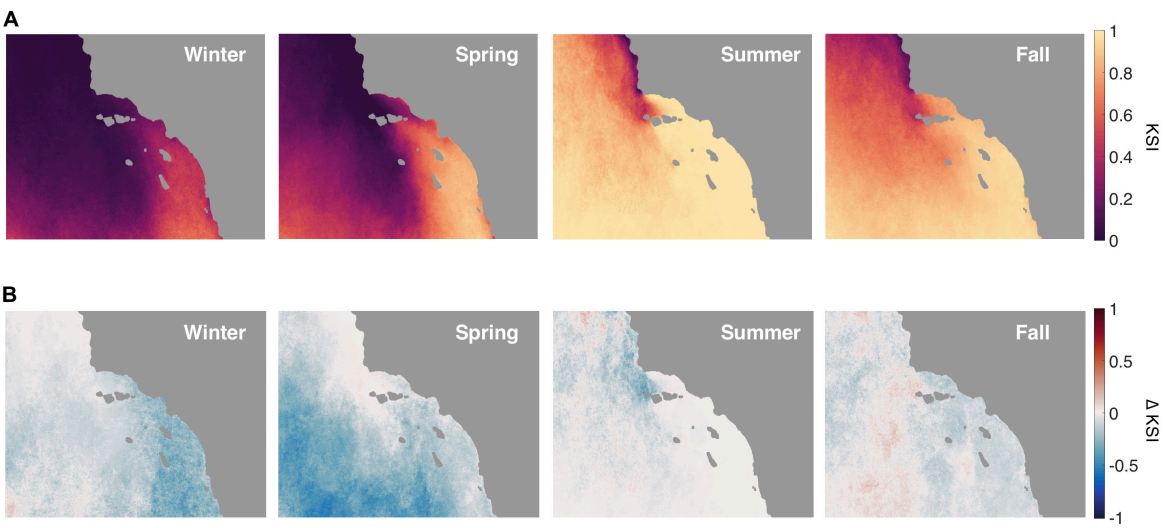

FIGURE 12 | (A) The Kelp Stress Index (KSI) for each season over the study area. The KSI is the proportion of the season where kelp is nutrient stressed. Nutrient stress is defined as greater than 21 consecutive days of seawater nitrate concentration less than 1 μmol L^{-1}. **(B)** The difference in the KSI for each season when the North Pacific Gyre Oscillation (NPGO) is in a positive versus a negative mode.

aquaculture could shift to other products during negative periods of the NPGO.

Effect of Spatial Scaling on Nitrate Estimates

Spatially degrading SST tends to underestimate the amount of nitrate in the surface waters due to the non-linearity of the T2N relationship. This is most apparent at the lowest spatial resolutions (25, 15, and 9 km in **Figure 7**) where the best fit line slope is lower than the 1:1 line. The largest effect is seen at nitrate values between 1 and 4 μmol L^{-1} because this area is located at the curve of the T2N relationship, where the relationship is the most non-linear (**Figure 4**). At low nitrate values there is less of an effect because there is little nitrate in the water from 16°C to 24°C, thus averaging does not affect these lower values as much. Accurate nitrate concentration estimates around 1 – 4 μmol L^{-1} are important because this is a critical concentration range for the growth of giant kelp (Gerard, 1982b; Bell et al., 2015a). Uptake rates by giant kelp vary non-linearly with ambient seawater nitrate concentration, and the nitrogen uptake rate changes the fastest over this 1 – 4 μmol L^{-1} range (Gerard, 1982b). Thus, an error in estimating sea surface nitrate concentration, especially at low spatial resolutions, can lead to disproportionate errors in estimating nitrogen uptake by kelp. As errors tend to underestimate nitrate concentrations, larger

spatial scale estimates may exclude areas as potential sites for kelp aquaculture.

Fine scale physical processes that bring cool, nutrient-rich water to specific sites can be hidden when the spatial resolution of remote sensing imagery is degraded. This is shown in the probability distribution functions (**Figure 8**) and maps of error (red and blue areas in **Figure 9**) at the 25, 15, and 9 km scale. Localized areas of upwelling, such as coastline and seamounts, or eddy formation (around the Channel Islands and headlands) may be good places for aquaculture but are often missed in lower spatial resolution imagery (Broitman and Kinlan, 2006; Bell et al., 2015b). The spatial scaling analysis showed that, under most circumstances, 1, 2, and 4 km resolution imagery compared well to the 100 m scale nitrate estimates for this study area.

Effect of Temporal Scaling on Nitrate Estimates

One-kilometer MODIS satellite retrievals performed well for SST and nitrate dynamics as seen in validation data by continuous buoy measurements in both cool and warm areas of the Southern California Bight (**Table 1**). The increased magnitude of MAE and ME of estimated nitrate concentrations in the West Santa Barbara buoy were likely caused by the higher magnitudes of nitrate at that site relative to the Santa Monica Basin site. As part of the temporal scaling analysis, higher values in MAE were due to the higher fraction of cloud contaminated daily SST estimates as opposed to the increase in temporal scale (**Figure 10**). Offshore areas to the west of the Channel Islands and Pt. Conception are generally cloudier than areas inside the Channel Islands (**Supplementary Figures S2A,B**), and overcast and cloudy conditions often persist throughout the summer and fall seasons over the Santa Barbara Channel. This makes it difficult to build an accurate climatology, as clear imagery are sometimes only available once or twice per week. We see that as new satellites come online, such as VIIRS in 2012, the increased number of passes allows at least one sensor to get a clear image of daily SST more often. The future launch of Landsat 9, scheduled for 2020, promises an improved TIRS-2 sensor that will reduce stray light issues in Landsat 8's thermal imagery, as well as increase global coverage and data collection. Improvements in future satellite missions, the addition of geostationary satellites, and greater cooperation between global space agencies will continue to mitigate this limitation (Castelao et al., 2006). For areas with persistent cloud cover and frequent storms (and thus lower SST and possibly higher nitrate concentrations) *in situ* monitoring will be necessary for farmers and stakeholders to observe local conditions.

On the contrary, increases in the ME are driven mostly by increases in temporal averaging and not cloud contamination. It is important to note that ME is always negative and becomes more negative as temporal scale (the averaging of daily SST determinations) increases. We cannot control the level of cloud contamination, but we can control the temporal scale at which we convert SST to nitrate concentrations. We would recommend that each daily determination of SST is converted to nitrate before averaging over time (**Figure 2**).

Conclusion

It is important to understand the implications of spatial and temporal scale of temperature data when estimating seawater nutrient fields for assessing the suitability of kelp aquaculture sites. We found that daily, 1 km SST imagery does an adequate job of replicating continuous buoy measurements. For studies in the NE Pacific, a merged daily 1 km multi-satellite product, like the one used in this study, captures a great deal of the variability in temperature and nitrate concentration in this system at a fine spatial and temporal scale. It is also important to remember that SST does not estimate temperature dynamics below the surface of the water, and that waters can be stratified in the summer. This stratification may hide subsurface dynamics of seawater nutrients. Future offshore aquaculture farms may use technology to overcome this, like farms which can alter buoyancy to sink below a nutricline or employ the use of artificial upwelling devices.

DATA AVAILABILITY STATEMENT

Publicly available datasets were used in this study. These data can be found here: http://spg-satdata.ucsd.edu/, http://sbc.lternet.edu/, http://www.oceancolor.ucsb.edu/plumes_and_blooms/, and https://calcofi.org/.

AUTHOR CONTRIBUTIONS

JS and TB developed the research concept and led the image and data analyses. JS and TB led the writing with contributions from DS, NN, and KC.

FUNDING

Funding was provided by the U.S. Department of Energy ARPA-E grant #DE-AR0000922, the NASA Plumes and Blooms grant #80NSSC18K0735 and MBON grant #NNX14AR62A, and the U.S. National Science Foundation grant for the SBC LTER – OCE #1831937.

ACKNOWLEDGMENTS

We would like to acknowledge the USGS for providing open source Landsat 8 imagery and Mati Kahru for providing the timeseries of processed SST imagery. We thank Nathalie Guillocheau and Stuart Halewood for data products from the Plumes and Blooms cruises, as well as the Santa Barbara LTER survey team and CALCOFI survey teams for their data collections and provisions.

SUPPLEMENTARY MATERIAL

The Supplementary Material for this article can be found online at: https://www.frontiersin.org/articles/10.3389/fmars.2020.00022/full#supplementary-material

REFERENCES

Bell, T. W., Cavanaugh, K. C., Reed, D. C., and Siegel, D. A. (2015a). Geographical variability in the controls of giant kelp biomass dynamics. *J. Biogeogr.* 42, 2010–2021. doi: 10.1111/jbi.12550

Bell, T. W., Cavanaugh, K. C., and Siegel, D. A. (2015b). Remote monitoring of giant kelp biomass and physiological condition: an evaluation of the potential for the Hyperspectral Infrared Imager (HyspIRI) mission. *Remote Sens. Environ.* 167, 218–228. doi: 10.1016/j.rse.2015.05.003

Bell, T. W., Reed, D. C., Nelson, N. B., and Siegel, D. A. (2018). Regional patterns of physiological condition determine giant kelp net primary production dynamics. *Limnol. Oceanogr.* 63, 472–483. doi: 10.1002/lno.10753

Broitman, B. R., and Kinlan, B. P. (2006). Spatial scales of benthic and pelagic producer biomass in a coastal upwelling ecosystem. *Mar. Ecol. Progre. Ser.* 327, 15–25. doi: 10.3354/meps327015

Brzezinski, M., Reed, D., and Harrer, S. (2013). Multiple sources and forms of nitrogen sustain year-round kelp growth on the inner continental shelf of the Santa Barbara Channel. *Oceanography* 26, 114–123. doi: 10.5670/oceanog.2013.53

Burkepile, D. E., Allgeier, J. E., Shantz, A. A., Pritchard, C. E., Lemoine, N. P., Bhatti, L. H., et al. (2013). Nutrient supply from fishes facilitates macroalgae and suppresses corals in a Caribbean coral reef ecosystem. *Sci. Rep.* 3:1493. doi: 10.1038/srep01493

Cabral, R. B., Gaines, S. D., Johnson, B. A., Bell, T. W., and White, C. (2016). Drivers of redistribution of fishing and non- fishing effort after the implementation of a marine protected area network. *Ecol. Appl.* 27, 416–428. doi: 10.1002/eap.1446

Castelao, R. M., Mavor, T. P., Barth, J. A., and Breaker, L. C. (2006). Sea surface temperature fronts in the California current system from geostationary satellite observations. *J. Geophys. Re.: Oceans* 111, 1–13. doi: 10.1029/2006JC003541

Cavanaugh, K. C., Reed, D. C., Bell, T. W., Castorani, M. C. N., and Beas-Luna, R. (2019). Spatial variability in the resistance and resilience of giant kelp in Southern and Baja California to a Multiyear Heatwave. *Fron. Mar. Sci.* 6:413. doi: 10.3389/fmars.2019.00413

Cavanaugh, K. C., Siegel, D. A., Reed, D. C., and Dennison, P. E. (2011). Environmental controls of giant-kelp biomass in the santa barbara channel. California. *Mar. Ecol. Progr. Ser.* 429, 1–17. doi: 10.3354/meps09141

Colombo-Pallotta, M. F., García-Mendoza, E., and Ladah, L. B. (2006). Photosynthetic performance, light absorption, and pigment composition of Macrocystis pyrifera (Laminariales. Phaeophyceae) blades from different depths. *J. Phycol.* 42, 1225–1234. doi: 10.1111/j.1529-8817.2006.00287

Deysher, L. E., and Dean, T. A. (1986). In situ recruitment of sporophytes of the giant kelp, Macrocystis pyrifera (L.) C.A. Agardh: effects of physical factors. *J. Exp. Mar. Biol. Ecol.* 103, 41–63. doi: 10.1016/0022-0981(86)90131-0

Di Lorenzo, E., Schneider, N., Cobb, K. M., Franks, P. J. S., Chhak, K., Miller, A. J., et al. (2008). North pacific gyre oscillation links ocean climate and ecosystem change. *Geophysi. Res. Lett.* 35, 2–7. doi: 10.1029/2007GL032838

Dugdale, R. C., Davis, C. O., and Wilkerson, F. P. (1997). Assessment of new production at the upwelling center at point conception, California, using nitrate estimated from remotely sensed sea surface temperature. *J. Geophys. Res.*102, 8573–8585. doi: 10.1029/96jc02136

Edwards, M. S., and Estes, J. A. (2006). Catastrophe, recovery and range limitation in NE Pacific kelp forests: a large-scale perspective. *Mar. Ecol. Progr. Seri.* 320, 79–87. doi: 10.3354/meps320079

Eppley, R. W., Renger, E. H., and Harrison, W. G. (1979). Nitrate and phytoplankton production in southern California coastal waters. *Limnol Oceanogr.* 24, 483–494. doi: 10.4319/lo.1979.24.3.0483

Fram, J. P., Stewart, H. L., Brzezinski, M. A., Gaylord, B., Reed, D. C., Williams, S. L., et al. (2008). Physical pathways and utilization of nitrate supply to the giant kelp, Macrocystis pyrifera. *Limnol. Oceanogr.* 53, 1589–1603. doi: 10.4319/lo.2008.53.4.1589

Gentry, R. R., Lester, S. E., Kappel, C. V., White, C., Bell, T. W., Stevens, J., et al. (2017). Offshore aquaculture: spatial planning principles for sustainable development. *Ecol. Evol.* 7, 733–743. doi: 10.1002/ece3.2637

Gerard, V. A. (1982a). Macrocystis pyrifera in a Low-Nitrogen Environment. *Mar. Biol.* 66, 27–35. doi: 10.1007/BF00397251

Gerard, V. A. (1982b). In situ rates of nitrate uptake by giant kelp, Macrocystis pyrifera (L.) C. Agardh: tissue differences, environmental effects, and predictions of nitrogen-limited growth. *J. Exp. Mar. Biol. Ecol.* 62, 211–224. doi: 10.1007/s00442-016-3641-2

Graham, M. H., Vasquez, J. A., and Buschmann, A. H. (2007). Global ecology of the giant kelp Macrocystis: from ecotypes to ecosystems. *Oceanogr. Mar. Biol.*45, 39–88. doi: 10.1201/9781420050943.ch2

Harms, S., and Winant, C. D. (1994). Synthetic subsurface pressure derived from bottom pressure and tide gauge observations. *J. Atmos. Oceanic Technol.* 11, 1625–1637. doi: 10.1175/1520-0426(1994)011<1625:sspdfb>b2.0.co;2

Henderikx-Freitas, F., Siegel, D. A., Maritorena, S., and Fields, E. (2016). Satellite assessment of particulate matter and phytoplankton variations in the Santa Barbara Channel and its surrounding waters: role of surface waves. *J. Geophys. Res.: Oceans* 122, 355–371. doi: 10.1002/2016JC012152

Jacox, M. G., Bograd, S. J., Hazen, E. L., and Fiechter, J. (2015). Sensitivity of the California current nutrient supply to wind, heat, and remote ocean forcing. *Geophys. Res. Lett.* 42, 5950–5957. doi: 10.1002/2015gl065147

Kamykowski, D., and Zentara, S. (1986). Predicting plant nutrient concentrations from temperature and sigma-t in the upper kilometer of the world ocean. *Deep Sea Res.* 33, 89–105. doi: 10.1016/0198-0149(86)90109-3

Kamykowski, D., Zentara, S., Morrison, J. M., and Switzer, A. C. (2002). Dynamic global patterns of nitrate, phosphate, silicate, and iron availability and phytoplankton community composition from remote sensing data. *Global Biogeoch. Cycles* 16:25-1-25-29. doi: 10.1029/2001GB001640

Kim, H. J., and Miller, A. J. (2007). Did the thermocline deepen in the California Current after the 1976/77 climate regime shift? *J. Phys. Oceanogr.* 37, 1733–1739. doi: 10.1175/jpo3058.1

Konotchick, T., Parnell, P. E., Dayton, P. K., and Leichter, J. J. (2012). Vertical distribution of Macrocystis pyrifera nutrient exposure in southern California. *Estuar.Coast. Shelf Sci.* 106, 85–92. doi: 10.1016/j.ecss.2012.04.026

Lester, S. E., Stevens, J. M., Gentry, R. R., Kappel, C. V., Bell, T. W., Costello, C. J., et al. (2018). Marine spatial planning makes room for offshore aquaculture in crowded coastal waters. *Nat. Commun.* 9, 945. doi: 10.1038/s41467-018-03249-1

McPhee-Shaw, E. E., Siegel, D. A., Washburn, L., Brzezinski, M. A., Jones, J. L., Leydecker, A., et al. (2007). Mechanisms for nutrient delivery to the inner shelf: observations from the santa barbara channel. *Limnol. Oceanogr.* 52, 1748–1766. doi: 10.4319/lo.2007.52.5.1748

Morin, P., Wafar, M. V. M., and Corre, P. (1993). Estimations of nitrate flux in a tidal front from satellite-derived temperature data. *J. Geophys. Res.* 98, 4689–4695. doi: 10.1029/92jc02445

Omand, M. M., Feddersen, F., Guza, R., and Franks, P. J. (2012). Episodic vertical nutrient fluxes and nearshore phytoplankton blooms in Southern California. *Limnol. Oceanogr.* 57, 1673–1688. doi: 10.4319/lo.2012.57.6.1673

Otero, M. P., and Siegel, D. A. (2004). Spatial and temporal characteristics of sediment plumes and phytoplankton blooms in the Santa Barbara Channel. *Deep Sea Res.* 51, 1129–1149. doi: 10.1016/j.dsr2.2004.04.004

Parnell, P. E., Miller, E. F., Lennert-Cody, C. E., Dayton, P. K., Carter, M. L., and Stebbins, T. D. (2010). The response of giant kelp (Macrocystis pyrifera) in southern California to low-frequency climate forcing. *Limnol. Oceanogr.* 55, 2686–2702. doi: 10.4319/lo.2010.55.6.2686

Paulson, G. O. (1972). *A study of Nutrient Variations in the Surface and Mixed Layer of Monterey Bay Using Automated Analysis Techniques*. M.S. thesis, Nav. Postgraduate School, Monterey, CA.

Peters, J. R., Reed, D. C., and Burkepile, D. E. (2019). Climate and fishing drive regime shifts in consumer-mediated nutrient cycling in kelp forests. *Glob. Chang. Biol.* 25, 3179–3192. doi: 10.1111/gcb.14706

Rodriguez, G. E., Reed, D. C., and Holbrook, S. J. (2016). Blade life span, structural investment, and nutrient allocation in giant kelp. *Oecologia* 182, 397–404. doi: 10.1007/s00442-016-3674-6

Sainz, J. F., Di Lorenzo, E., Bell, T. W., Gaines, S., Lenihan, H., and Miller, R. J. (2019). Spatial planning of marine aquaculture under climate decadal variability: a case study for mussel farms in southern California. *Front. Mar. Sci.* 6:253. doi: 10.3389/fmars.2019.00253

Sathyendranath, S., Platt, T., Horne, E. P. W., Harrison, W. G., Ulloa, O., Outerbridge, R., et al. (1991). Estimation of new production in the ocean

by compound remote sensing. *Nature* 353, 129–133. doi: 10.1038/353129a0

Smith, J. M., Brzezinski, M. A., Melack, J. M., Miller, R. J., and Reed, D. C. (2018). Urea as a source of nitrogen to giant kelp (Macrocystis pyrifera). *Limnol. Oceanogr. Lett.* 3, 365–373. doi: 10.1002/lol2.10088

Snyder, J., Boss, E., Weatherbee, R., Thomas, A. C., Brady, D., and Newell, C. (2017). Oyster aquaculture site selection using landsat 8-Derived sea surface temperature, turbidity, and chlorophyll a. *Front. Mar. Sci.* 4:190. doi: 10.3389/fmars.2017.00190

Son, S., Platt, T., Bouman, H., and Lee, D. (2006). Satellite observation of chlorophyll and nutrients increase induced by Typhoon Megi in the Japan/East Sea. *Geophys. Res. Lett.* 33, 4–7. doi: 10.1029/2005GL025065

Stewart, H. L., Fram, J. P., Reed, D. C., Williams, S. L., Brzezinski, M. A., Maclntyreb, S., et al. (2009). Differences in growth, morphology and tissue carbon and nitrogen of Macrocystis pyrifera within and at the outer edge of a giant kelp forest in California. USA. *Mar. Ecol. Progr. Ser.* 375, 101–112. doi: 10.3354/meps07752

Willmott, C. J., and Matsuura, K. (2005). Advantages of the mean absolute error (MAE) over the root mean square error (RMSE) in assessing average model performance. *Clim. Res.* 30, 79–82. doi: 10.3354/cr00799

Wood, S. N. (2006). *Generalized Additive Models: An Introduction With R*. London: Chapman and Hall/CRC.

Zhu, Z., Wang, S., and Woodcock, C. E. (2015). Remote Sensing of Environment Improvement and expansion of the Fmask algorithm: cloud, cloud shadow, and snow detection for Landsats 4 – 7, 8, and Sentinel 2 images. *Remote Sens. Environ.* 159, 269–277. doi: 10.1016/j.rse.2014.12.014

Zimmerman, R. C., and Kremer, J. N. (1984). Episodic nutrient supply to a kelp forest ecosystem in Southern California. *J. Mar. Res.* 42, 591–604. doi: 10.1357/002224084788506031

Conflict of Interest: The authors declare that the research was conducted in the absence of any commercial or financial relationships that could be construed as a potential conflict of interest.

frontiers in Marine Science

ORIGINAL RESEARCH
published: 14 February 2020
doi: 10.3389/fmars.2020.00061

Satellite Ocean Color Based Harmful Algal Bloom Indicators for Aquaculture Decision Support in the Southern Benguela

Marié E. Smith[1]* *and Stewart Bernard*[1,2]

[1] Earth Observation, CSIR, Cape Town, South Africa, [2] Department of Oceanography, University of Cape Town, Cape Town, South Africa

The aquaculture industry of southern Africa faces environmental threats from harmful algal blooms (HABs), which have the potential to cause devastating economic losses (Pitcher et al., 2019). Satellite earth observation offers a systematic and cost effective method for operational monitoring of HABs over large areas. Whilst the chlorophyll-a concentration ([Chl-a]) product, often used as a proxy for phytoplankton biomass, can be used to indicate high biomass blooms (elevated biomass against a background signal of 5–10 mgChl m^{-3}), there is a clear need for value-added products that not only alert on bloom presence, but also on the bloom type and persistence. This study demonstrates the identification of different phytoplankton communities that can feasibly be identified in bloom concentrations from space, relevant to the aquaculture industry of South Africa. In terms of water-leaving reflectance, 76 % of the variance in the red and NIR spectral region is significantly positively correlated to phytoplankton abundance, [Chl-a], and the maximum line height (MLH) (defined as the height of the maximum reflectance peak above a baseline between 665 and 753 nm). The MLH is related to dominant phytoplankton types derived from phytoplankton count data, in order to identify thresholds which represent blooms that pose a high hypoxia and/or toxicity risk; whilst $0.0016 < MLH < 0.003$ represent low to moderate concern mixed assemblage blooms, $MLH > 0.003$ has a strong likelihood of indicating high biomass dinoflagellate or *Pseudo-nitzschia* blooms. These techniques are routinely used by the aquaculture industry in South Africa for decision support and risk mitigation. The high biomass nature of the South African regional waters provide strong assemblage-related spectral variability, which can be exploited with the spectral bands of OLCI and MERIS. Application to these sensors not only ensures future monitoring capability, but also allows the creation of a historical risk climatology that can guide the site selection of industries sensitive to the presence of HABs, such as aquaculture facilities and desalination plants.

Keywords: ocean color, remote sensing, HABs, aquaculture, OLCI, MERIS, South Africa, Southern Benguela

OPEN ACCESS

Edited by:
Pierre Gernez, Université de Nantes, France

Reviewed by:
Michelle Christine Tomlinson, National Centers for Coastal Ocean Science (NOAA), United States
Blake Schaeffer, Office of Research and Development, United States Environmental Protection Agency, United States

***Correspondence:**
Marié E. Smith
msmith2@csir.co.za

Specialty section:
This article was submitted to Ocean Observation, a section of the journal Frontiers in Marine Science

Received: *31 October 2019*
Accepted: *28 January 2019*
Published: *14 February 2020*

Citation:
Smith ME and Bernard S (2020) Satellite Ocean Color Based Harmful Algal Bloom Indicators for Aquaculture Decision Support in the Southern Benguela. Front. Mar. Sci. 7:61. doi: 10.3389/fmars.2020.00061

1. INTRODUCTION

Aquaculture is a burgeoning industry in South Africa and plays a vital role in the country's blue economy. The marine aquaculture sector centers around mussel *Mytilus galloprovincialis*, Pacific oyster *Crassostrea gigas* and abalone *Haliotis midae* farming (DAFF, 2017), with most facilities situated along the west coast in close proximity to the productive Benguela current upwelling system.

Most mussel and oyster farms utilize in-water culture methods such as rafts and cages (DAFF, 2017) located in Saldanha Bay (**Figure 1**). Abalone are farmed commercially along the west and southwest coasts of the country, with the majority of abalone operations situated near Walker Bay; the most common production methods utilize land-based flow-through systems (Urban-Econ Development Economists, 2018) which necessitates a close proximity to the ocean to allow large volumes of sea-water to be pumped up to the farm for optimal water exchange, temperature control, and removal of metabolic waste.

The global marine aquaculture sector faces environmental threats from harmful algal blooms (HABs), with impacts from these events amounting to approximately 8 $billion/yr (Brown et al., 2019). Within the South African aquaculture industry the HAB-related risk factors and mitigation strategies differs within the various sub-sectors. Whilst the herbivorous abalone are at risk of physical damage and paralysis attributed to some dinoflagellate species (e.g., Pitcher et al., 2019), the filter-feeders (i.e., mussels and oysters) are vulnerable to growth arrest (Pitcher and Calder, 2000) and the accumulation of biotoxins which affects their safety of consumption and can cause poisoning syndromes in humans. On a larger environmental scale, some non-toxic dinoflagellate blooms can result in marine mortalities and anoxia following the collapse of blooms with very high biomass (e.g., Ndhlovu et al., 2017).

Routine management and risk assessment at aquaculture facilities includes monitoring the flesh of mussels and oysters for specific biotoxins and regular phytoplankton counts of water samples. Counts include total abundance counts and HAB species monitoring focusing on toxic dinoflagellates known to cause paralytic shellfish poisoning (PSP) (e.g., *Alexandrium* spp.) and diarrhetic shellfish poisoning (DSP) (e.g., *Dinophysis* spp.), diatoms known to cause amnesic shellfish poisoning (ASP) (e.g., some *Pseudo-nitzschia* spp.), as well as dinoflagellates known to produce yessotoxins (e.g., *Lingulodinium polyedrum*).

HABs have the potential to cause devastating economic losses in the aquaculture and fisheries industries. The Saldanha Bay mussel aquaculture industry was first affected in 1994 due to PSP (Pitcher et al., 1994), while the presence of brown tides in 1997–1999 resulted in reduced growth rates of the filter feeding bivalves and 80 % reduction in monthly sales (Probyn et al., 2001); in 2015 farms were closed 13 times due to the presence of bio-toxins in shellfish flesh above acceptable regulatory limits (DAFF, 2017). Dinoflagellate blooms have previously impacted wild and farmed abalone (Pitcher et al., 2001; Botes et al., 2003) in South Africa, even leading to mortalities of wild adult abalone (Horstman et al., 1991); abalone have been known to contain paralytic shellfish toxins following some dinoflagellate blooms (Harwood et al., 2014; Hallegraeff and Bolch, 2016). HABs can also pose a threat to the physical condition of sardines and associated fisheries (Van der Lingen et al., 2016). The decay of high biomass dinoflagellate blooms have often lead to marine mortalities and mass rock-lobster strandings in the St Helena Bay region (e.g., Pitcher et al., 2011, 2014) with losses valued up to 50 million US dollars in some cases (Ndhlovu et al., 2017).

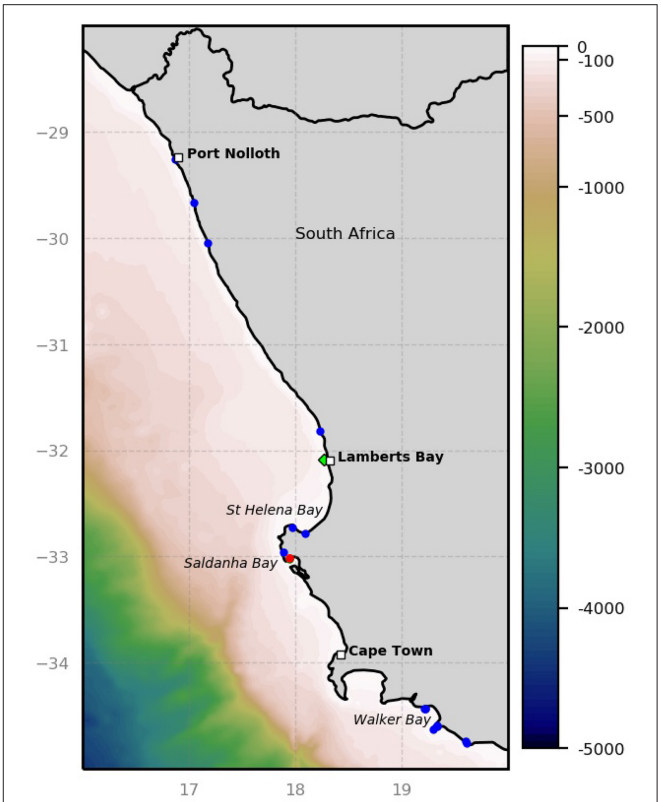

FIGURE 1 | Map showing the west coast aquaculture facilities, with important bays and towns for reference. The location of the sampling station off Lamberts Bay is indicated by a green diamond. Abalone farms are shown as blue dots and mussel farms are shown in red (adapted from DAFF, 2017).

Ocean color remote sensing provides a cost-effective and valuable tool in the detection and monitoring of various types of phytoplankton blooms (see references in Blondeau-Patissier et al., 2014). The most common method, using the concentration of Chlorophyll *a* ([Chl-a]) as a proxy for biomass, has often been used to define blooms as anomalous [Chl-a] above a pre-determined threshold (e.g., Stumpf et al., 2003). [Chl-a] has traditionally been used to detect phytoplankton blooms and HABs in the southern Benguela (Bernard et al., 2014; Smith and Bernard, 2018) where concentrations in the coastal waters are known to vary from <1 mg m^{-3} in newly upwelled water (Barlow, 1982) to well over 100 mg m^{-3} in bloom conditions (Pitcher and Weeks, 2006). Although [Chl-a] is routinely derived from satellite reflectance using regionally optimized algorithms (e.g., Smith and Bernard, 2018), it does not provide direct information about inherent phytoplankton-related risk.

The optical environment off the west coast of South Africa can be described as phytoplankton dominated, with other constituents (e.g., colored dissolved organic matter and suspended inorganic material) contributing relatively little to the water-leaving reflectance signal (Bernard et al., 2009). The blue-green water-leaving reflectance signal generally dominates in low biomass open ocean environments, which is considered to be [Chl-a] < 1 mg m^{-3} in the context of this study. As the phytoplankton biomass increases, the reflectance signal is increasingly affected by a combination of the peaks of Chl-a absorption near 465 and 665 nm, the Chl-a fluorescence peak near 685 nm, as well as increased phytoplankton-related backscattering and the absorption of water; these effects result in the shift of the dominant reflectance signal to the red-NIR spectral region at Chlorophyll *a* concentrations ([Chl-a]) of approximately >15 mg m^{-3} (Robertson Lain et al., 2014).

It should be noted that the term "bloom" and "HAB" should be considered within a specific ecological and environmental context; some HABs can be toxic at low biomass or do not manifest as high [Chl-a], and there are generally no set abundance values to define when a HAB species is considered to be a "bloom" (Glibert et al., 2018). When contextualized within the highly productive waters of the southern Benguela, a phytoplankton "bloom" needs to be identifiable against a background biomass signal of approximately [Chl-a] of 5 to 10 mg m^{-3} (Demarcq et al., 2003); since a variety of different phytoplankton types commonly reach [Chl-a] of 20–50 mg m^{-3} and above (Bernard et al., 2014), a detection technique focusing on the red/NIR was deemed most appropriate for regional harmful bloom identification.

Spectral band difference algorithms are often used to relate the reflectance peak in the red/NIR to phytoplankton biomass, the most well-known version of which is arguably the fluorescence line height (FLH) (Letelier and Abbott, 1996; Gower et al., 1999); FLH provides a quantification of the height of the Chl-a fluorescence peak above a baseline formed by the Chl-a absorption trough near 665 and a NIR wavelength (usually near 750 nm). Several studies have used a variant of this line height detection method, whether on its own or in combination with other optical properties (e.g., backscattering) or true color imagery, for the detection of HABs in coastal waters using ocean color remote sensing (Gower et al., 2005; Ryan et al., 2008; Matthews et al., 2012; Al Shehhi et al., 2013; Ghanea et al., 2016).

This study aims to relate spectral features of water-leaving reflectance in the red-NIR directly to phytoplankton types of particular concern to the marine aquaculture industry of South Africa. We focus on application to reflectance data from the MEdium Resolution Imaging Spectrometer (MERIS) and the Ocean and Land Colour Imager (OLCI), as both sensors have good spectral covarage in the red-NIR region and high (300 m) spatial resolution. The objective is to determine probabilistic ecosystem-contextualized identifiers for waters dominated by either dinoflagellates or the diatom *Pseudo-nitzschia* (*PN*) as these are high risk HAB types that offer distinct ocean color signals.

2. MATERIALS AND METHODS

In situ water samples were collected at a station in St Helena Bay approximately 4 km off of Lambert's bay (32.0845°S 18.2691°E) in late summer (between February and April) of 2004–2008. Chlorophyll *a* concentration was measured by fluorometric analysis (Holm-Hansen et al., 1965) using 90% acetone with the use of a Turner Designs 10-AU Fluorometer according to accepted protocols (Knap et al., 1996; Mueller et al., 2003). Phytoplankton samples were taken at the surface, fixed in buffered formalin to a concentration of 0.5%, and counted using the Utermöhl method (Hasle, 1978). Count data were grouped into diatoms, dinoflagellates, flagellates, cilliates, and coccolithophores; *PN* was treated separately, in an attempt to determine unique spectral characteristics. A >50 % abundance threshold was used as the primary simplistic phytoplankton population metric.

In-water radiometric measurements were made with a hyperspectral Tethered Satlantic Radiometric Buoy (TSRB); further details on measurements, processing, and uncertainties can be found in Smith and Bernard (2018). The *in situ* radiometric data (N = 68) were resampled to MERIS/OLCI wavelength bands centered at 665, 681.25, 708.75, and 753.75 nm.

A line height (or spectral band difference) algorithm, similar to the fluorescence line height (Gower et al., 1999), with a baseline formed by the water-leaving reflectance (ρ_w) between 665 and 753 nm was applied to all spectra. In the case of the hyperspectral *in situ* data the remote sensing reflectance (R_{rs}) were converted to ρ_w by multiplying spectra by π (Antoine and Morel, 2005) prior to application of the line height algorithms. The line heights at both 681 (*LH*681) and 709 nm (*LH*709) were calculated as follows:

$$LH(\lambda) = \rho_w(\lambda) - \rho_w(665) - [(\rho_w(753) - \rho_w(665)) \times (\frac{\lambda - 665}{753 - 665})] \quad (1)$$

The maximum line height (MLH) was calculated as follows:

$$MLH = max[LH681, LH709] \quad (2)$$

The reflectance peak at 681 nm is generally associated with Chl-a fluorescence emission; however, at higher biomass this peak shifts to longer wavelengths due to the combined effects of increased phytoplankton absorption and backscattering, as well as pure water absorption. The ratio of *LH*709 to *LH*681, also known as the line height ratio (LHR) (Tao et al., 2011), provides an indication of this red shift, and was calculated as follows:

$$LHR = \frac{LH709}{LH681} \quad (3)$$

Principal component analysis (PCA) was applied as an exploratory data analysis step in order to assess the variance structure within the dataset. This analysis technique reduces the dimensionality of a dataset by breaking it down into a set of geometrically independent (orthogonal) modes of oscillation

which represent all the variability in the data (Craig et al., 2012). PCA was performed on the resampled and standardized (i.e., removing the mean and scaling to unit variance) reflectance data using eigenvalue decomposition of the data covariance matrix. The scores of the first three principal components (modes) of variance were use in correlation analysis with the following variables: [Chl-a], MLH, LHR, the percentage compositions by abundance of diatoms, *PN*, dinoflagellates, flagellates, cilliates, coccolithophores, and the total cell counts for each sample. The authors note that although *PN* is a diatom it was assessed separately in an attempt to find an unique identification criteria given that is the only potentially toxic diatom genus appearing in the Benguela.

Satellite data from the Ocean and Land Colour Imager (OLCI) on board Sentinel-3A (processing baseline 2.23; IPF version 06.11) were obtained from the Copernicus online data access website (https://coda.eumetsat.int/) while data from the 3rd reprocessing for the Medium Resolution Imaging Spectrometer (MERIS) were obtained from the MERIS catalog and inventory (MERCI) website. In the case of both sensors the bright pixel (atmospheric) correction (Moore and Lavender, 2011) is universally applied over the coastal waters of the southern Benguela. The water-leaving reflectance (ρ_w) from the Level 2 data files were used in all calculations. The flags that were applied to maintain the quality of the data during the phytoplankton type detection algorithm application to MERIS data included "CLOUD," "LAND," uncorrected sun glint ("HIGLINT"), and reflectance confidence flags ("PCD1_13"); for OLCI data these included land and cloud flags ("LAND," "CLOUD," "CLOUD_AMBIGUOUS," "CLOUD_MARGIN") missing, invalid or transmission errors ("INVALID," "SUSPECT," and "COSMETIC"), suspect atmospheric correction and saturated pixels ("AC_FAIL," "SATURATED"), and unreliable sun glint correction flags ("RISKGLINT").

3. RESULTS

The first three principal components accounted for 98.8 % of the total variance in the red-NIR region of the remote sensing reflectance (R_{rs}) dataset (**Figure 2**). The first mode, which accounts for 76% of the total variance within the dataset, represents an amplitude effect with a significant positive correlation to MLH, total cell count, [Chl-a] and LHR; this indicates that the biomass drives the magnitude of the R_{rs} spectra in the red-NIR. The second mode indicates significant yet opposing spectral responses between $R_{rs}(665)$ and $R_{rs}(709)$ to variations in [Chl-a], LHR, MLH, and total cell counts. Mode two also had a significant positive correlation to the percentage coccolithophores in the sample; the highly scattering nature of these cells tend to increase the magnitude of the reflectance in the green, which in turn can partially mask some of the Chl-a absorption near 665 nm. The third mode, although contributing to a relatively small percentage of the total variance, is significantly negatively and positively related to the percentage composition of *PN* and dinoflagellates respectively; increases in the percentage of *PN* and dinoflagellates in water samples respectively are associated with increases in the LH681 and LH709, respectively, indicating a potential approach for the optical distinction of these two phytoplankton types.

Figure 3 shows the statistics of the MLH, LHR, and [Chl-a] associated with the dominance (i.e., >50 %) of diatoms, *PN*, and dinoflagellates respectively; only samples with total cell concentration over 10^6 cells L^{-1} were included in order to capture scenarios of likely phytoplankton bloom conditions. As the sample sizes were quite small, the Kruskal-Wallis H Test was used to compare the distributions of the three samples (diatom, *PN*, and dinoflagellates) for each variable (MLH, LHR, and [Chl-a]); this test found no significant differences between any of the samples. Bloom conditions dominated by diatoms tend to have a MLH < 0.0038; thus there is a high probability that conditions with MLH > 0.0038 is either *PN* or dinoflagellate dominated. For all three phytoplankton types approximately 75 % of the bloom samples had MLH > 0.0019; this was chosen as the lower threshold for mixed bloom conditions. Approximately half of the *PN* and 25 % of the diatom bloom samples had a MLH > 0.0027; this was chosen as the lower threshold for mixed bloom conditions that have a slightly higher potential for harm. All bloom conditions dominated by diatoms and *PN* displayed a LHR under 0.6; thus it is very likely that LHR > 0.6 would be dinoflagellate dominated. Similarly, valid samples of blooms dominated by either *PN* or other diatoms had maximum [Chl-a] under approximately 30 mg m^{-3}. Therefore, it is very likely that a bloom with [Chl-a]>30 mg m^{-3} is dinoflagellate dominated; Bernard et al. (2014) also defined the lower end of the probabilistic range of dinoflagellate dominance as [Chl-a] above 30 mg m^{-3}. It should be noted that dinoflagellate dominance is entirely possible at lower [Chl-a] and/or LHR<0.6, but would most likely be associated with low total cell concentrations and related risk.

Some of the key values indicated above are used as baseline thresholds for a reflectance classification framework to determining phytoplankton types, which is presented in **Table 2**. An LHR > 0.6 is used as a probabilistic dinoflagellate identifier, while the MLH of 0.0019, 0.0027, and 0.0038 is used to represent increasing likelihood and potential severity of either dinoflagellates or *PN* blooms. **Figure 4** shows the total cell counts and [Chl-a] that roughly corresponds to these *in situ* MLH thresholds; when using the regression lines of these figures there is a 63 % chance that a MLH of 0.0038 relates to total cell counts of approximately 6.4 million cells L^{-1}, and a 70% chance of it relating to [Chl-a] of approximately 23 mg m^{-3}. A small sample (N = 19) of coincident MERIS reflectance data were available to enable the comparison of satellite-derived MLH to *in situ* total cell counts and [Chl-a] (**Figure 5**); the coefficient of determination decreased from 0.63 to 0.52 for total cell counts, but increased from 0.70 to 0.74 for [Chl-a]. The thresholds for MLH were adjusted using the [Chl-a] associated with the original threshold values in **Figure 3** and the new regression equation between satellite MLH and *in situ* [Chl-a]; the adjusted thresholds are shown in bold in **Table 2**, and are used for all satellite image classification.

Assessing the performance of algorithms designed to classify satellite data into discrete groups can be challenging, particularly

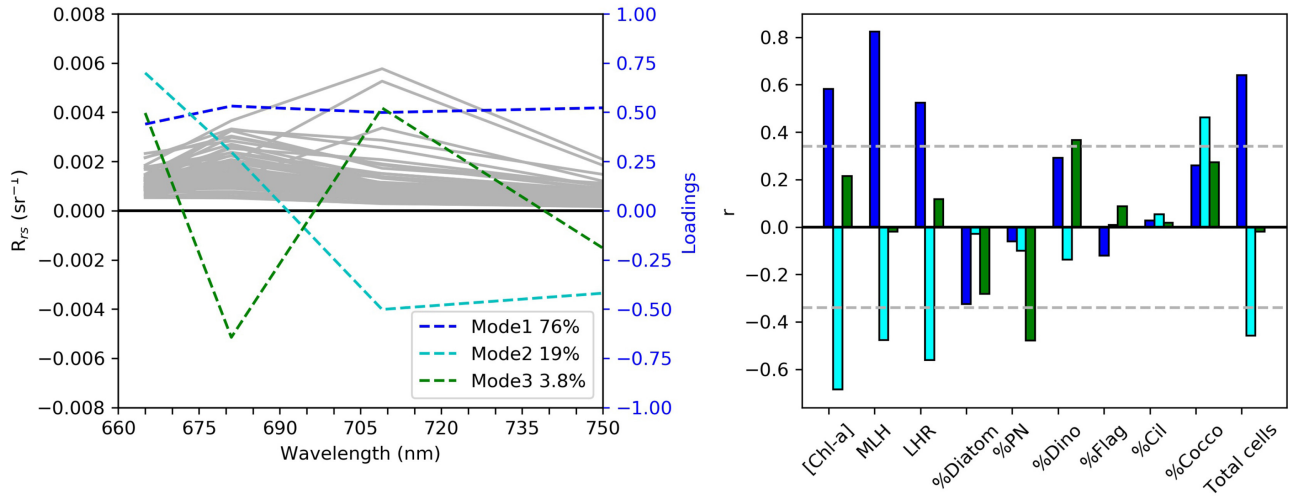

FIGURE 2 | Results from the principal component analysis of the *in situ* reflectance between 665 and 754 nm (N = 68). In the left panel the gray lines indicate individual R_{rs} samples, while the colored lines show the loadings of the top three modes of variability in the R_{rs} dataset. In the right panel the bars are color-coded according to the corresponding modes of variance to show the correlation with [Chl-a], maximum line height, line height ratio, percentage composition of diatoms, *Pseudo-nitzschia*, dinoflagellates, flagellates, ciliates, and coccolithophores, as well as the total cell counts per sample. The gray horizontal lines indicate the 95 % significance level.

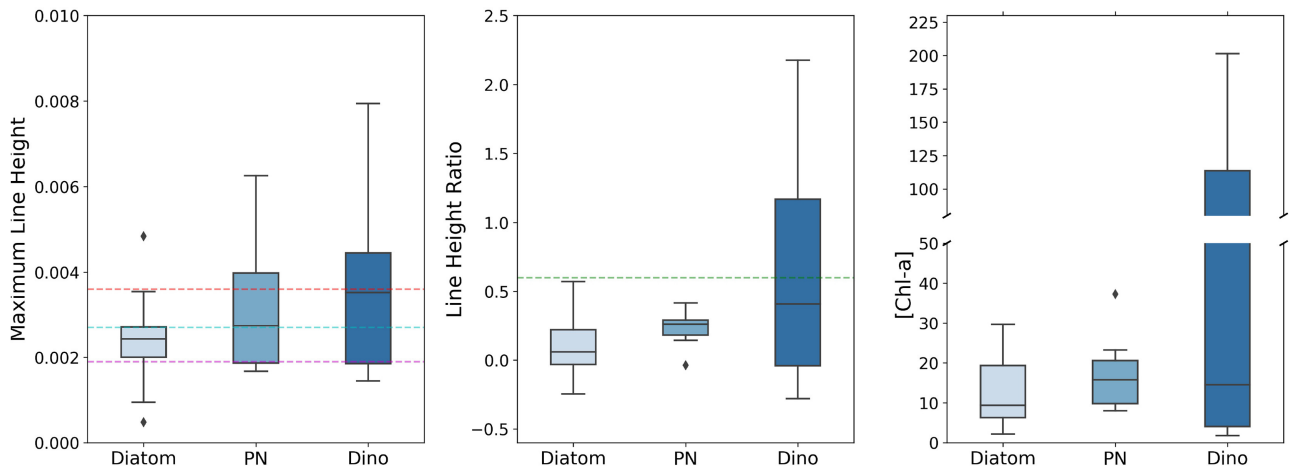

FIGURE 3 | Boxplots of the MLH, LHR, and [Chl-a] for samples with total cell concentration over 10^6 cells L^{-1}. Each column represents the statistics associated with the dominance (i.e., >50 % composition as relative abundance to the total cell count) of a given phytoplankton type, i.e., diatoms, *Pseudo-nitzschia*, and dinoflagellates. The horizontal lines of the boxes represent the 25th, 50th (median), and 75th percentiles, whereas the whiskers represent the valid minimum and maximum; outliers are indicated as diamonds. The colored dashed horizontal lines indicate the thresholds used in the initial probabilistic phytoplankton community classification.

when sample sizes are small, and often requires indicators other than the standard metrics (e.g., bias, RMSD) used for ocean color product validation (Melin et al., 2019); in these cases confusion/contingency/error matrices can be more useful (e.g., Carvalho et al., 2011; Wang and Hu, 2017). In the present study the performance of the satellite classification algorithm was assessed (in terms of correctly identifying pixels as either "bloom" or "non-bloom") using **Figure 5D** as a reference; three confusion matrices (depicted in **Table 1**) were created to represent classification results of samples with *in situ* [Chl-a] above approximately 8.9, 14.2, and 22.1 mg m^{-3}, corresponding to MLH above the thresholds of 0.0016, 0.0022, and 0.003, respectively. Note that for the purpose of this assessment it is assumed that all samples above the specified [Chl-a] are true "blooms". The classification accuracy is lowest (64%) at the low [Chl-a], with the satellite-derived classification indicating some false negatives; classification accuracy increases with increasing [Chl-a], with the highest accuracy obtained at [Chl-a] > 22.1 mg

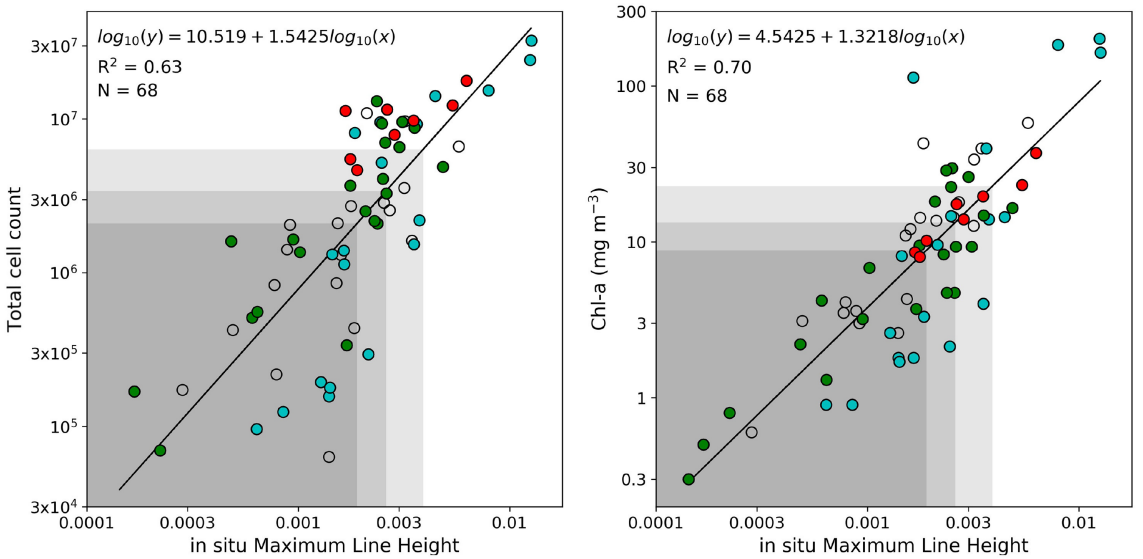

FIGURE 4 | Linear regression analysis between maximum line height and total cell counts **(left)** and between maximum line height and [Chl-a] **(right)**; all data were log-transformed before analysis. The black line represents the regression line with the corresponding equation, coefficient of determination (R^2) and the sample size (N). Samples with more than 50% *Pseudo-nitzschia*, diatoms, or dinoflagellates are shown in red, green, and blue, respectively. The shaded areas represent cell counts and [Chl-a] associated with MLH below 0.0019, 0.0027, and 0.0038, respectively.

m^{-3}. These results are based on very small sample sizes and are only used to provide an indication of the classification algorithm's operational limits.

Several studies have noted that the line height algorithms operating in the red/NIR can be affected by high concentrations of suspended sediment or atmospheric dust, producing apparent reflectance peaks in this spectral region (e.g., Zhao et al., 2015) or masking the reflectance peak signal (e.g., McKee et al., 2007; Gilerson et al., 2008). For the purposes of this study the area under the baseline of the MLH, i.e., the integral of the water-leaving reflectance values between the 665 and 753 nm wavebands, was used as a quality control measure for highly scattering (possibly inorganic) substances. The maximum MLH baseline integral of both the *in situ* and satellite-derived reflectance datasets was 0.5; thus for satellite application the classification algorithm was not applied to pixels where the integral was > 0.5 (i.e., these pixels are displayed as unclassified).

4. DISCUSSION

4.1. HABs in the Southern Benguela

The southern Benguela is a wind-driven, pulsed upwelling system forced by equatorward winds from the south Atlantic high pressure system, and modulated by low-pressure systems moving eastwards past the southern tip of Africa; these conditions supports elevated phytoplankton biomass over the wide continental shelf (Verheye et al., 2016) dominated by primarily large celled diatoms (Hutchings et al., 2012) that thrive in the nutrient-rich turbulent environment of upwelling systems (Sathyendranath et al., 2014). Succession within the system generally follows known conceptual frameworks (Margalef, 1987) where diatoms dominate during turbulent upwelling phases, followed by a shift to dinoflagellate dominance during quiescent periods. A decrease in upwelling-favorable winds toward the end of austral summer (between January and May) are usually associated with more frequent dinoflagellate-dominance in the near-shore waters of the southern Benguela during the latter stages of the upwelling season (Pitcher and Calder, 2000). HABs within the southern Benguela are largely attributable to dinoflagellates (Pitcher and Weeks, 2006). Although the prevalence of *PN* has been established in both the northern (Louw et al., 2016) and the southern (Fawcett et al., 2007) Benguela, there are no recorded impacts to the aquaculture industry (Pitcher et al., 2014). The type of harm caused by HABs within upwelling systems are diverse, with the impact attributed to organism type, concentrations they occur in, and whether toxins are present (Pitcher et al., 2017).

Whilst HABs were considered to be relatively scarce along the southern coastline of South Africa prior to 1997 (Pitcher and Calder, 2000), several extensive dinoflagellate blooms, some consisting of previously unobserved species, have notably impacted the region in recent years (Pitcher et al., 2014); these events included *Gonyaulax polygramma* blooms that negatively affected physical condition of the regional sardine stock in 2011 (Van der Lingen et al., 2016), and blooms of *Lingulodinium polyedrum* impacting hundreds of kilometers along the south coast during 2013/2014 (Pitcher et al., 2014). Most notably for the aquaculture industry was the bloom co-dominated by *Lingulodinium polyedrum* and *Gonyaulax spinifera* at the end of 2016 which lead to the mortalities of over 250 tons of farmed abalone by February 2017 (Pitcher et al., 2019).

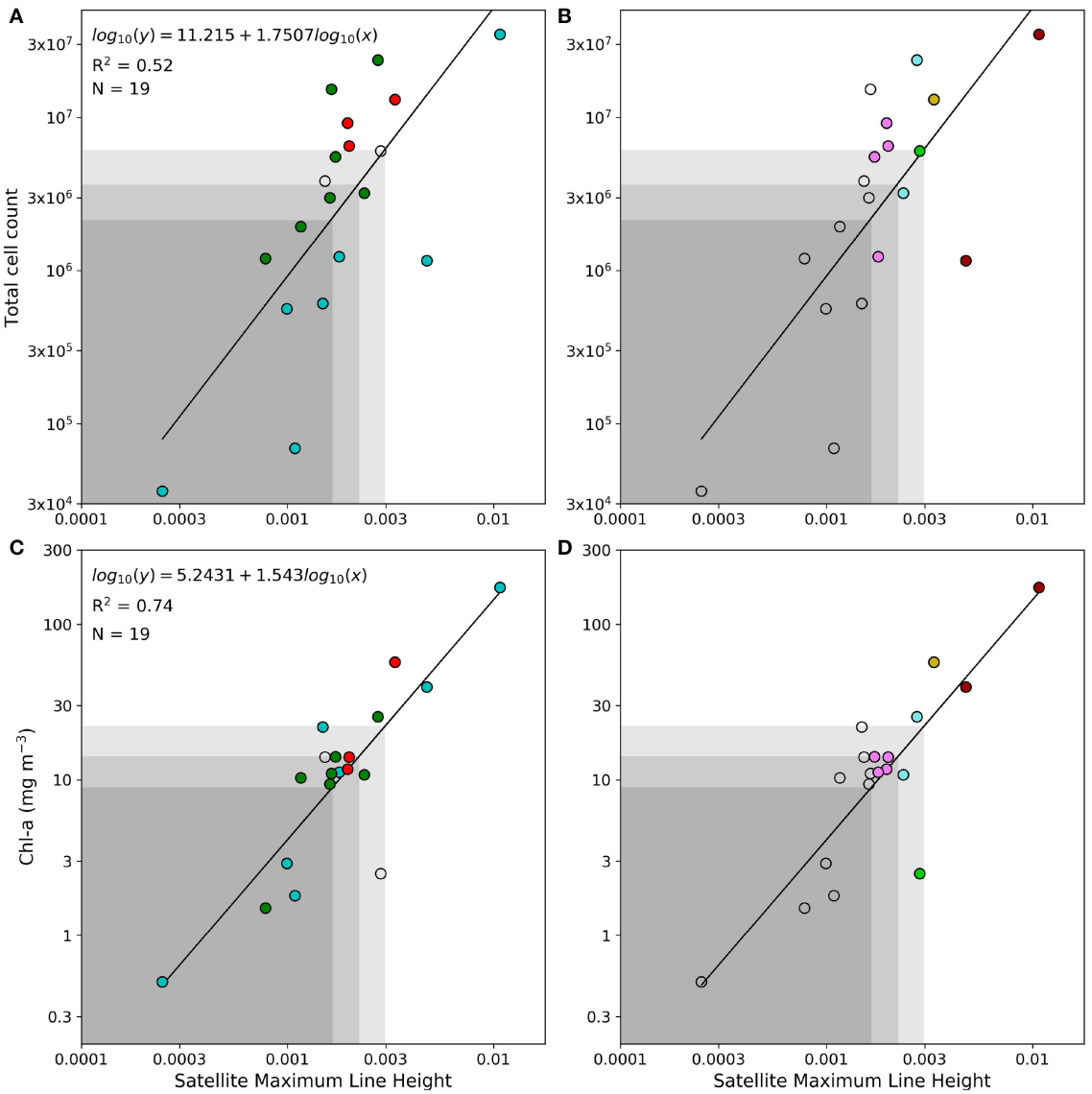

FIGURE 5 | (A–D) Linear regression analysis between maximum line height and *in situ* total cell counts **(top)** and between maximum line height and [Chl-a] **(bottom)**; all data were log-transformed before analysis. The black line represents the regression line with the corresponding equation, coefficient of determination (R^2) and the sample size (*N*). The shaded areas represent cell counts and [Chl-a] associated with MLH below 0.0016, 0.0022, and 0.003, respectively. Samples with more than 50% *Pseudo-nitzschia*, diatoms, or dinoflagellates are shown in red, green, and blue, respectively in the left panels. Right-hand panels show the classification of these samples using the satellite derived MLH and LHR. Please refer to **Table 2** for a detailed color key.

The occurrence and frequency of HABs are thought to be increasing worldwide, and within the context of a changing climate the global distribution and occurrence of different HAB species are likely to change in the future (Glibert and Burford, 2017). Pitcher et al. (2017) noted the continuously changeable nature of the species that constitute HABs in upwelling systems, and the inherently diverse threats posed to industries and humans relying on these systems. These concepts support the notion that the southern Benguela aquaculture industries requires adaptable and robust HAB monitoring strategies to safeguard the economic viability of these facilities.

4.2. Probabilistic Phytoplankton Community Classification (PPCC) Algorithm Functioning and Suitability

There are a multitude of methods to obtain information on phytoplankton functional types from remotely sensed ocean color data (see Sathyendranath et al., 2014), however many of these techniques were designed for oligotrophic and mesotrophic waters and/or operate in the blue-green spectral region. At lower biomass levels the spectral features in the blue-green wavelengths are potentially more useful for distinguish certain HABs from non-harmful blooms and other water types from an ocean color

TABLE 1 | Confusion matrices describing the performance of the satellite classification model in terms of correctly identifying satellite-derived pixels as either "bloom" or "non-bloom."

Example 1			**Satellite prediction**		
			Non-bloom	*Bloom*	
	In situ	*Non-bloom*	TN = 0	FP = 0	
	measurement	*Bloom*	FN = 0	TP = 4	
					Classification accuracy =100%
Example 2			**Satellite prediction**		
			Non-bloom	*Bloom*	
	In situ	*Non-bloom*	TN = 0	FP = 0	
	measurement	*Bloom*	FN = 2	TP = 6	
					Classification accuracy =75%
Example 3			**Satellite prediction**		
			Non-bloom	*Bloom*	
	In situ	*Non-bloom*	TN = 0	FP = 0	
	measurement	*Bloom*	FN = 5	TP = 9	
					Classification accuracy =64%

*Examples 1, 2, and 3 represent samples with in situ [Chl-a] above 22.1, 14.2, and 8.9 mg m^{-3} respectively as depicted in **Figure 5D**. TP, TN, FP, and FN represent conditions of true positive (i.e., correctly classified as a bloom), true negative (i.e., correctly classified as non-bloom), false positive and false negative classification, respectively. Classification accuracy is calculated as (TP + TN) / (TP + TN + FP + FN).*

perspective (e.g., Cannizzaro et al., 2008; Kurekin et al., 2014; Tao et al., 2015); particularly the phytoplankton backscaterring-driven signal in the 520–600 nm range has shown potential for phytoplankton functional type applications (Lain and Bernard, 2018). However, at the relatively high concentration of biomass that regularly occurs in the southern Benguela, the largest spectral signal is often found in the red/NIR.

It was shown in **Figure 2** that the variability in the red-NIR is largely driven by total phytoplankton biomass, and has the greatest correlation with the MLH. The position of the reflectance peak in the red/NIR, indicated in this study by the LHR, together with the MLH, provides some information on the phytoplankton communities present in the water. Diatoms have developed rapid photo-protective capability in response to the dynamic light levels of a high-mixing upwelling environment, which can manifest as elevated fluorescence (Lavaud et al., 2002); it appears as though *PN* might have additional spectrally-based advantage linked to its fluorescence quantum yield (Brunet et al., 2014). As a result, also impacted by differences in IOPs, the fluorescence peak remains evident even at relatively high concentrations, meaning that the fluorescence signal (LH681) exceeds the phytoplankton backscattering-related signal (LH709), producing lower LHR values.

TABLE 2 | The framework for probabilistic phytoplankton community classification (PPCC), based on thresholds of maximum line height (MLH) and line height ratio (LHR).

MLH	**LHR<0.6**	**LHR>0.6**
> **0.0016** (0.0019)	Mixed assemblage diatoms, low concern [pink]	Dinoflagellate dominated [green]
> **0.0022** (0.0027)	Mixed assemblage diatoms, moderate concern [blue]	Dinoflagellate dominated [green]
> **0.003** (0.0038)	High likelihood of *Pseudo-nitzschia* dominance [yellow]	High likelihood of dinoflagellate dominance, very high biomass [red]

MLH thresholds based on in situ regression analysis are shown in brackets, and the adjusted values for application to satellite data are shown in bold text. The colors in square brackets represent the color-key used during PPCC algorithm application.

For application to the MERIS and OLCI sensors, the traditional FLH utilizes wavebands centered at 665, 681, and 709 nm, while the Maximum Chlorophyll Index (MCI) uses 681, 709, and 753 nm (Gower et al., 2005). This relatively narrow positioning of the baseline and signal bands limits the application of the FLH to low-moderate biomass waters, whereas the MCI only functions in high biomass waters (i.e., [Chl-a] >20 mg m^{-3} when the red-shift, associated with increasing phytoplankton biomass, produces a discernible reflectance peak in the red/NIR). Zhao et al. (2015) found that using a wide baseline modified FLH provided improved results compared to either the traditional FLH or MCI for qualitatively distinguish HABs from other blooms in the Arabian Gulf. The wide baseline and the dominant peak selection method are similar in functioning to the maximum peak-height (MPH) algorithm (Matthews et al., 2012) and the adaptive reflectance peak height (ARPH) algorithm (Ryan et al., 2014), which are both used in the operational quantification of different phytoplankton populations in eutrophic waters.

The generally weaker positive correlation between total cell counts, dominant phytoplankton types, and the reflectance-based signal in the red-NIR indicates that this relationship is not straight-forward, and that care should be taken when attempting to quantify phytoplankton abundance from remotely sensed information. Although not directly related to probabilistic phytoplankton community information, accurate [Chl-a] can provide a valuable supplementary indication on phytoplankton-related risk.

4.3. Phytoplankton Community Identification Using Remote Sensing

Both MERIS and OLCI offer good spectral resolution in the red/NIR region as well as high spatial resolution (300 m) which is often necessary at the small spatial scale and near coastal aquaculture applications. With two satellites in orbit (Sentinel 3A and 3B), the OLCI sensor provides near daily coverage. In the generally eutrophic conditions of the southern Benguela it is useful to avoid the blue-green spectral region when using satellite-derived reflectance data, where the uncertainty resulting from aerosol extrapolation can be more extreme than in the red-NIR. The use of thresholds based on line height algorithms and

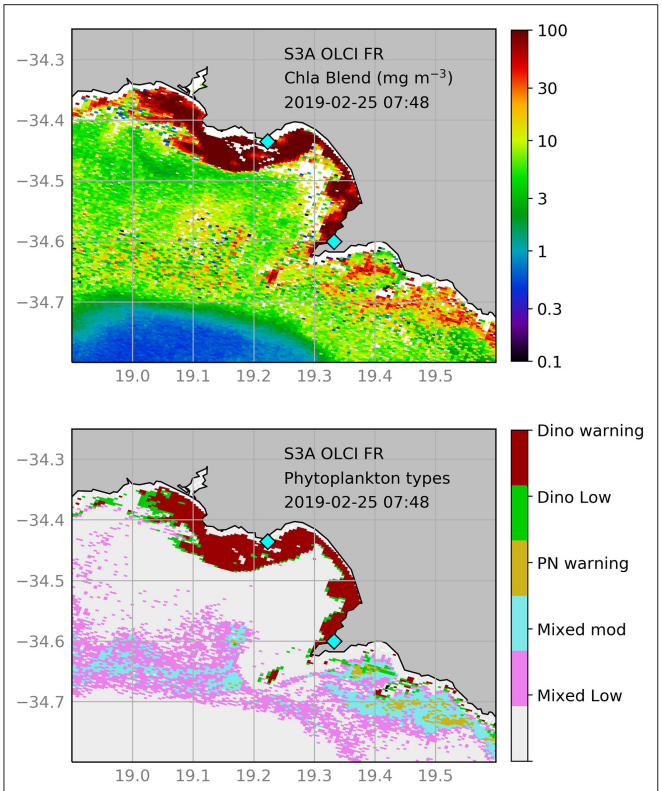

FIGURE 6 | Satellite products derived from full resolution S3A-OLCI for the 25th of February 2019. The top panel shows [Chl-a], whilst the bottom panel shows the probabilistic phytoplankton community classification (PPCC); classes include dinoflagellate (red) and *Pseudo-nitzschia* (yellow) dominated waters, as well as high (green) and moderate (blue) biomass mixed assemblages. Please refer to **Table 2** for a detailed PPCC color key. The locations of two of the primary water intake pipes for abalone farms in the area are indicated by blue diamonds.

ratios, instead of absolute reflectance values, also mitigates the potential spectral offsets and errors that might result from the atmospheric correction process. MERIS and OLCI utilize the bright pixel correction (Moore and Lavender, 2011) in addition to the standard atmospheric correction, which was universally applied across the satellite images. This atmospheric correction is considered generally appropriate for the southern Benguela (Bernard et al., 2014), as it is capable of adjusting for non-zero reflectance in the NIR.

Although the algorithm was validated with MERIS matchup data, the similar radiometric heritage between sensors means that this classification scheme is applicable to OLCI (example image shown in **Figure 7**), ensuring utility of this classification technique for the next 20 years, whilst also being application to ten years of archive MERIS data. In the current study we demonstrate the application of the PPCC to MERIS and OLCI images representing two different HAB events.

Yessotoxin producing blooms of *Lingulodinium polyedrum* and *Gonyaulax spinifera* impacted the Walker Bay abalone industry in December 2016 to February 2017 (Pitcher et al., 2019). A similar dinoflagellate bloom was recorded in the Walker Bay area during February of 2019, which persisted until May 2019; during the stages of the bloom depicted in **Figure 6**, cell concentrations of over 2 million cells L^{-1} (dominated by *Gonyaulax spinifera*) were measured at some of the aquaculture farm intake pipes (personal communication with farm managers). The probabilistic classification clearly shows the spatial extent and associated patches of this dinoflagellate bloom; the [Chl-a] map shows good spatial coherence with the classification while providing an indication of bloom intensity.

The probabilistic classification method was applied to four MERIS images (**Figure 7**) that coincided with the March 2006 field campaign where a *Pseudo-nitzschia* bloom was sampled off Lambert's Bay (Fawcett et al., 2007). The PPCC correctly identified the presence of PN at the sampling station on the 12th of March, where [Chl-a] of 57.1 mg m^{-3} and PN concentrations of 8 million cells L^{-1} were measured *in situ*. Although the highest number of PN cells were measured on the 18th of March, the PPCC indicated only a high biomass mixed assemblage; this could potentially be due to the relatively lower *in situ* [Chl-a] (compared to the 12th of March), producing a poorer optical signal in the red/NIR. Both the 15th and 22nd of March coincided with decreased phytoplankton counts and [Chl-a], which were similarly reflected in the unclassified pixels over the sampling site. It is clear that the highest chance of successful classification is achieved under conditions of the highest biomass (i.e., on the 12th of March). Special precaution is also advised for regions classified as "high biomass mixed assemblages," as they could likely contain high concentrations of PN.

4.4. Algorithm Limitations

This study is based on a relatively small *in situ* dataset ($N = 68$) with only a limited number of samples that included coincident radiometric measurements and phytoplankton counts; however, it did comprise a wide range of phytoplankton types and biomass concentrations enabling a first order determination of ecosystem-contextualized thresholds. Although these thresholds are based upon statistical indicators, the algorithm is not specifically meant to be a quantitative translation between MLH and cell counts or [Chl-a]. The aim was to provide simple intuitive map-based indication of probabilistic phytoplankton-related risk to the aquaculture industry of southern Africa. If/when more data become available these classification methods and detection accuracy could potentially be refined further.

The application of the PPCC to coincident satellite reflectance demonstrated that there was the highest likelihood of correct classification of phytoplankton community dominance at [Chl-a] > 23 mg m^{-3}. Although it is possible that HAB identification could be more straight-forward at lower biomass levels under mono-specific bloom conditions, it is unlikely for any one species of phytoplankton to out-compete others under nutrient-rich upwelling conditions. DSP toxin producing species of the genus *Dinophysis*, usually *D. acuminata* or *D. fortii*, often form small components of blooms dominated by other dinoflagellates in the southern Benguela (Pitcher and Calder, 2000); these species also pose different threat levels to shellfish cultivation, as mussels are more susceptible to the accumulation of DSP toxins (Pitcher et al., 2011). Conversely it is also possible for

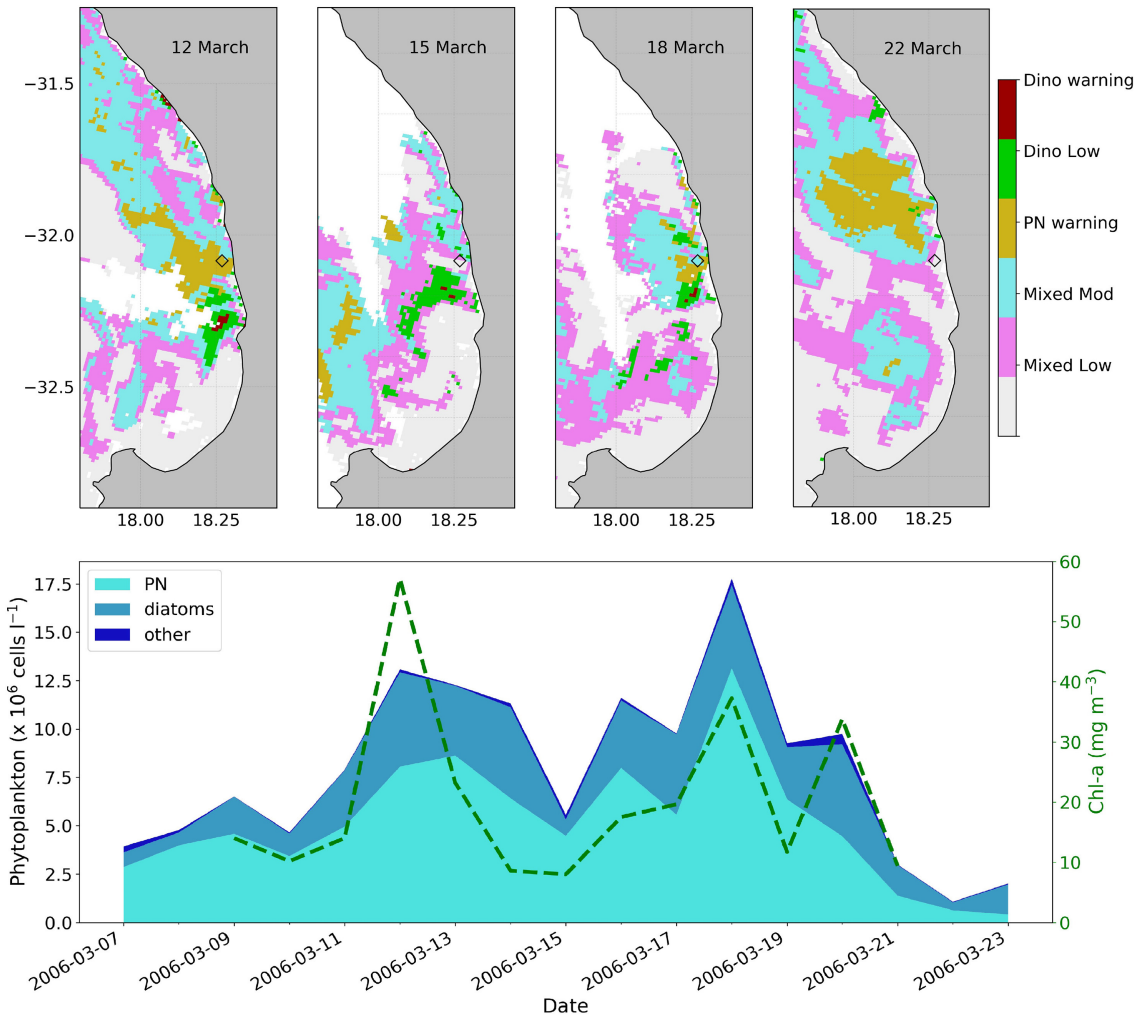

FIGURE 7 | The top panels show the satellite-derived probabilistic phytoplankton community classification (PPCC) from MERIS for the 12th, 15th, 18th, and 22nd of March 2006, with the location of the Lambert's Bay sampling station indicated by a diamond; classes include high biomass dinoflagellate blooms (red), dinoflagellate dominated blooms of moderate biomass (green), *Pseudo-nitzschia* (yellow) dominated waters, as well as high (blue) and low (pink) biomass mixed assemblages. Please refer to **Table 2** for a detailed PPCC color key. The lower panel provides the phytoplankton count data at the Lambert's Bay station for the 2006 sampling period (adapted from Fawcett et al., 2007), with available *in situ* [Chl-a] overlayed.

some very high biomass dinoflagellate blooms to not result in any harmful impacts.

It should be noted that *in situ* and *in vitro* techniques far outweigh current remote sensing capabilities when it comes to phytoplankton identification at the species level. The strength of using remote sensing for HAB detection lies in the repeatability of measurements over the same location at higher spatial scales than is attainable by *in situ* methods. The utility of ocean color remote sensing for in HAB monitoring is most powerful when informed by coincident *in situ* information such as species-level phytoplankton identification and abundance, and toxicity. Remote sensing should ideally be utilized as part of a larger multi-scale monitoring approach: where a bloom has been identified as harmful, the PPCC method can aid in the continued monitoring of the bloom's spatial extent, trajectory, and possible intensification or dissipation, thereby supporting decision making and risk mitigation processes at environmental and aquaculture management level.

The successful application of the algorithm to remote sensing data is dependent on the appropriate and successfully applied atmospheric correction and the resultant reflectance product quality. The algorithm functions in the red/NIR where the problems associated with aerosol correction are generally less than in the blue-green wavelengths. Line height algorithms are also generally less affected by absolute magnitude changes than ratios. Caution is advised when interpreting the Chl-a fluorescence signal from phytoplankton for quantitative determination of phytoplankton biomass, as the fluorescence efficiency of phytoplankton can be affected by various factors including taxonomy, physiology,

nutrient availability, light history, and temperature (Babin et al., 1996). Increased backscattering across the red/NIR, as might be caused by inorganic matter, could dampen the effect of the red/NIR reflectance peaks by increasing the reflectance of the baseline; studies have demonstrated that the FLH signal could be masked by non-algal materials in turbid waters (McKee et al., 2007; Gilerson et al., 2008).

4.5. Concluding Remarks and Future Outlook

This study represents a spectral classification scheme, applicable to both *in situ* and satellite reflectance, for the detection of phytoplankton communities relevant to the aquaculture industry of South Africa. Although the classification is primarily qualitative, it is based on species-related optical signatures and abundance data, and provides more direct risk-related information for aquaculture management than traditional maps of [Chl-a]. Future models could potentially incorporate environmental and/or nutrient information within the phytoplankton risk probability, as changes in these variables have been linked with bloom toxicity (e.g., Torres Palenzuela et al., 2019).

Whilst the classification system was contextualized for the southern Benguela, its utility is potentially appropriate to similar upwelling systems; for instance the northern Benguela is also known to experience frequent occurrences of toxic dinoflagellates (Dijerenge, 2015) and *PN* blooms (Louw et al., 2016), which could negatively impact regional marine aquaculture in Namibia. Following several years of severe drought in the western Cape province, there has been a rise in the number of planned desalination plants in the region; these facilities require appropriate phytoplankton monitoring practices, as both toxic and non-toxic algae can impact operations by clogging pre-treatment filters, causing saltwater reverse osmosis membrane fouling, and affecting the taste and odor of the water (Al Shehhi et al., 2017; Anderson et al., 2017). The PPCC could potentially be applied to 10 years of MERIS data and recent OLCI data to produce probability maps (e.g., Ryan et al., 2008) which could be used to guide future aquaculture and desalination site selection.

The routine high spatial information provided by the PPCC, used together with corroborative *in situ* phytoplankton cell counts, provides a powerful combination for operational HAB monitoring and daily decision support within the aquaculture industry. It is important that the limitations and strengths of the classifier be clearly delineated to users to ensure the appropriate level of response and mitigation, allowing different industries to use the information as they see fit.

DATA AVAILABILITY STATEMENT

The datasets generated for this study are available on request to the corresponding author.

AUTHOR CONTRIBUTIONS

MS and SB conceptualized the study. MS prepared figures, conducted analyses, and wrote the first draft of the manuscript. All authors contributed to the manuscript revision, read, and approved the submitted version.

ACKNOWLEDGMENTS

Grant Pitcher, Andre du Randt, and Trevor Probyn from the department of agriculture, forestry and fisheries for *in situ* data; GMES&Africa MarCOSouth and OCIMS for project funding. The original concept of this work was presented at the 2018 International Ocean Optics conference in Dubrovnik, Croatia (Smith and Bernard, 2018), and has been expanded upon in this manuscript.

REFERENCES

Al Shehhi, M. R., Gherboudj, I., and Ghedira, H. (2017). "Chapter 9 - Satellites-based monitoring of harmful algal blooms for sustainable desalination," in *Desalination Sustainability*, ed H. A. Arafat (Elsevier), 341–366. doi: 10.1016/B978-0-12-809791-5.00009-2

Al Shehhi, M. R., Gherboudj, I., Zhao, J., Mezhoud, N., and Ghedira, H. (2013). "Evaluating the performance of MODIS FLH ocean color algorithm in detecting the Harmful Algae Blooms in the Arabian Gulf and the Gulf of Oman," in *Oceans-San Diego, 2013* (San Diego, CA: IEEE), 1–7.

Anderson, D. M., Boerlage, S. F. E., and Dixon, M. (2017). *Harmful Algal Blooms (HABs) and Desalination: A Guide to Impacts, Monitoring, and Management*. Paris: Intergovernmental Oceanographic Commission of UNESCO. doi: 10.25607/OBP-203

Antoine, D., and Morel, A. (2005). Atmospheric correction of the meris observations over ocean case 1waters. *MERIS ATBD 2.7*.

Babin, M., Morel, A., and Gentili, B. (1996). Remote sensing of sea surface sun-induced chlorophyll fluorescence: consequences of natural variations in the optical characteristics of phytoplankton and the quantum yield of chlorophyll a fluorescence. *Int. J. Remote Sens.* 17, 2417–2448. doi: 10.1080/01431169608948781

Barlow, R. (1982). Phytoplankton ecology in the southern Benguela current. I. Biochemical composition. *J. Exp. Mar. Biol. Ecol.* 63, 209–227. doi: 10.1016/0022-0981(82)90179-4

Bernard, S., Pitcher, G., Evers-King, H., Robertson, L., Matthews, M., Rabagliati, A., et al. (2014). "Ocean colour remote sensing of harmful algal blooms in the Benguela system," in *Remote Sensing of the African Seas*, eds V. Barale and M. Gade (Dordrecht: Springer), 185–203.

Bernard, S., Probyn, T., and Quirantes, A. (2009). Simulating the optical properties of phytoplankton cells using a two-layered spherical geometry. *Biogeosci. Discuss.* 6, 1497–1563. doi: 10.5194/bgd-6-1497-2009

Blondeau-Patissier, D., Gower, J. F., Dekker, A. G., Phinn, S. R., and Brando, V. E. (2014). A review of ocean color remote sensing methods and statistical techniques for the detection, mapping and analysis of phytoplankton blooms in coastal and open oceans. *Prog. Oceanogr.* 123, 123–144. doi: 10.1016/j.pocean.2013.12.008

Botes, L., Sym, S. D., and Pitcher, G. C. (2003). *Karenia cristata* sp. nov. and *Karenia bicuneiformis* sp. nov. (*Gymnodiniales*, *Dinophyceae*): two new *Karenia* species from the South African coast. *Phycologia* 42, 563–571. doi: 10.2216/i0031-8884-42-6-563.1

Brown, A. R., Lilley, M., Shutler, J., Lowe, C., Artioli, Y., Torres, R., et al. (2019). Assessing risks and mitigating impacts of harmful algal blooms on mariculture and marine fisheries. *Rev. Aquacult.* doi: 10.1111/raq.12403. [Epub ahead of print].

Brunet, C., Chandrasekaran, R., Barra, L., Giovagnetti, V., Corato, F., and Ruban, A. V. (2014). Spectral radiation dependent photoprotective mechanism in the diatom *Pseudo-nitzschia multistriata*. *PLoS ONE* 9:e87015. doi: 10.1371/journal.pone.0087015

Cannizzaro, J. P., Carder, K. L., Chen, F. R., Heil, C. A., and Vargo, G. A. (2008). A novel technique for detection of the toxic dinoflagellate, *Karenia brevis*, in the Gulf of Mexico from remotely sensed ocean color data. *Continent. Shelf Res.* 28, 137–158. doi: 10.1016/j.csr.2004.04.007

Carvalho, G. A., Minnett, P. J., Banzon, V. F., Baringer, W., and Heil, C. A. (2011). Long-term evaluation of three satellite ocean color algorithms for identifying harmful algal blooms (*Karenia brevis*) along the west coast of Florida: a matchup assessment. *Remote Sens. Environ.* 115, 1–18. doi: 10.1016/j.rse.2010.07.007

Craig, S. E., Jones, C. T., Li, W. K., Lazin, G., Horne, E., Caverhill, C., et al. (2012). Deriving optical metrics of coastal phytoplankton biomass from ocean colour. *Remote Sens. Environ.* 119, 72–83. doi: 10.1016/j.rse.2011.12.007

DAFF (2017). *Aquaculture Yearbook 2016, South Africa*. Department of Agriculture, Forestry and Fisheries, Cape Town, South Africa.

Demarcq, H., Barlow, R. G., and Shillington, F. A. (2003). Climatology and variability of sea surface temperature and surface chlorophyll in the Benguela and Agulhas ecosystems as observed by satellite imagery. *Afr. J. Mar. Sci.* 25, 363–372. doi: 10.2989/18142320309504022

Dijerenge, K. J. (2015). *Analysis of marine biotoxins: paralytic and lipophilic shellfish toxins in Mussels (Mytilus Galloprovincialis) along the Namibia coastline* (Ph.D. thesis). University of Namibia, Windhoek, Namibia.

Fawcett, R., Pitcher, G., Bernard, S., Cembella, A., and Kudela, R. (2007). Contrasting wind patterns and toxigenic phytoplankton in the southern Benguela upwelling system. *Mar. Ecol. Prog. Ser.* 348, 19–31. doi: 10.3354/meps07027

Ghanea, M., Moradi, M., and Kabiri, K. (2016). A novel method for characterizing harmful algal blooms in the Persian Gulf using MODIS measurements. *Adv. Space Res.* 58, 1348–1361. doi: 10.1016/j.asr.2016.06.005

Gilerson, A., Zhou, J., Hlaing, S., Ioannou, I., Gross, B., Moshary, F., et al. (2008). Fluorescence component in the reflectance spectra from coastal waters. II. performance of retrieval algorithms. *Opt. Express* 16, 2446–2460. doi: 10.1364/OE.16.002446

Glibert, P. M., Berdalet, E., Burford, M. A., Pitcher, G. C., and Zhou, M., (eds.). (2018). "Harmful algal blooms and the importance of understanding their ecology and oceanography," in *Global Ecology and Oceanography of Harmful Algal Blooms*, (Cham: Springer), 9–25.

Glibert, P. M., and Burford, M. A. (2017). Globally changing nutrient loads and harmful algal blooms: recent advances, new paradigms, and continuing challenges. *Oceanography* 30, 58–69. doi: 10.5670/oceanog.2017.110

Gower, J., Doerffer, R., and Borstad, G. (1999). Interpretation of the 685nm peak in water-leaving radiance spectra in terms of fluorescence, absorption and scattering, and its observation by MERIS. *Int. J. Remote Sens.* 20, 1771–1786. doi: 10.1080/014311699212470

Gower, J., King, S., Borstad, G., and Brown, L. (2005). Detection of intense plankton blooms using the 709 nm band of the MERIS imaging spectrometer. *Int. J. Remote Sens.* 26, 2005–2012. doi: 10.1080/01431160500075857

Hallegraeff, G., and Bolch, C. (2016). Unprecedented toxic algal blooms impact on Tasmanian seafood industry. *Microbiol. Aust.* 37, 143–144. doi: 10.1071/MA16049

Harwood, D. T., Selwood, A. I., van Ginkel, R., Waugh, C., McNabb, P. S., Munday, R., et al. (2014). Paralytic shellfish toxins, including deoxydecarbamoyl-STX, in wild-caught Tasmanian abalone (*Haliotis rubra*). *Toxicon* 90, 213–225. doi: 10.1016/j.toxicon.2014.08.058

Hasle, G. R. (1978). "The inverted-microscope method," in *Phytoplankton Manual*, ed A. Sournia (Paris: Unesco Monographs on Oceanographic Methodology), 88–96.

Holm-Hansen, O., Lorenzen, C. J., Holmes, R. W., and Strickland, J. D. (1965). Fluorometric determination of chlorophyll. *J. Conseil* 30, 3–15. doi: 10.1093/icesjms/30.1.3

Horstman, D., McGibbon, S., Pitcher, G., Calder, D., Hutchings, L., and Williams, P. (1991). Red tides in False Bay, 1959-1989, with particular reference to recent blooms of *Gymnodinium* sp. *Trans. R. Soc. South Afr.* 47, 611–628.

Hutchings, L., Jarre, A., Lamont, T., Van den Berg, M., and Kirkman, S. (2012). St Helena Bay (southern Benguela) then and now: muted climate signals, large human impact. *Afr. J. Mar. Sci.* 34, 559–583. doi: 10.2989/1814232X.2012.689672

Knap, A., Michaels, A., Close, A., Ducklow, H., and Dickson, A. (1996). "Protocols for the joint global ocean flux study (JGOFS) core measurements," in *JGOFS, Reprint of the IOC Manuals and Guides No. 29*, JGOFS Report, 19 (Paris: UNESCO).

Kurekin, A., Miller, P., and Van der Woerd, H. (2014). Satellite discrimination of *Karenia mikimotoi* and *Phaeocystis harmful* algal blooms in European coastal waters: merged classification of ocean colour data. *Harmful Algae* 31, 163–176. doi: 10.1016/j.hal.2013.11.003

Lain, L. R., and Bernard, S. (2018). The fundamental contribution of phytoplankton spectral scattering to ocean colour: implications for satellite detection of phytoplankton community structure. *Appl. Sci.* 8:2681. doi: 10.3390/app8122681

Lavaud, J., Rousseau, B., Van Gorkom, H. J., and Etienne, A.-L. (2002). Influence of the diadinoxanthin pool size on photoprotection in the marine planktonic diatom *Phaeodactylum tricornutum*. *Plant Physiol.* 129, 1398–1406. doi: 10.1104/pp.002014

Letelier, R. M., and Abbott, M. R. (1996). An analysis of chlorophyll fluorescence algorithms for the moderate resolution imaging spectrometer (MODIS). *Remote Sens. Environ.* 58, 215–223. doi: 10.1016/S0034-4257(96)00073-9

Louw, D. C., Doucette, G. J., and Voges, E. (2016). Annual patterns, distribution and long-term trends of *Pseudo-nitzschia* species in the northern Benguela upwelling system. *J. Plankton Res.* 39, 35–47. doi: 10.1093/plankt/fbw079

Margalef, R. (1987). Life-forms of phytoplankton as survival alternatives in an unstable environment. *Oceanol. Acta* 1, 493–509.

Matthews, M. W., Bernard, S., and Robertson, L. (2012). An algorithm for detecting trophic status (chlorophyll-a), cyanobacterial-dominance, surface scums and floating vegetation in inland and coastal waters. *Remote Sens. Environ.* 124, 637–652. doi: 10.1016/j.rse.2012.05.032

McKee, D., Cunningham, A., and Dudek, A. (2007). Optical water type discrimination and tuning remote sensing band-ratio algorithms: application to retrieval of chlorophyll and Kd (490) in the Irish and Celtic Seas. *Estuar. Coast. Shelf Sci.* 73, 827–834. doi: 10.1016/j.ecss.2007.03.028

Melin, F., Wang, M., Werdell, J., and Hiroshi, K. (2019). *Uncertainties in Ocean Colour Remote Sensing*. Reports of the International Ocean-Colour Coordinating Group (IOCCG); 18. International Ocean-Colour Coordinating Group.

Moore, G., and Lavender, S. (2011). "Case IIS bright pixel atmospheric correction," in *MERIS ATBD, 2. MERIS ATBD, 2.6* (Plymouth: ARGANS).

Mueller, J. L., Pietras, C., Hooker, S. B., Austin, R.W., Miller, M., Knobelspiesse, K. D., et al. (2003) *Ocean Optics Protocols for Satellite Ocean Color Sensor Validation, Revision 5. Volume V: Biogeochemical and Bio-Optical Measurements and Data Analysis Protocols (NASA/TM-2003)*. Greenbelt, MD: Goddard Space Flight Space Center. 1–43.

Ndhlovu, A., Dhar, N., Garg, N., Xuma, T., Pitcher, G. C., Sym, S. D., et al. (2017). A red tide forming dinoflagellate *Prorocentrum triestinum*: identification, phylogeny and impacts on St Helena Bay, South Africa. *Phycologia* 56, 649–665. doi: 10.2216/16-114.1

Pitcher, G., and Calder, D. (2000). Harmful algal blooms of the southern Benguela Current: a review and appraisal of monitoring from 1989 to 1997. *South Afr. J. Mar. Sci.* 22, 255–271. doi: 10.2989/025776100784125681

Pitcher, G., Calder, D., Davis, G., and Nelson, G. (1994). Harmful algal blooms and mussel farming in Saldanha Bay. *Proc. Aquacult. Assoc. Southern Afr.* 5, 87–93.

Pitcher, G., Krock, B., and Cembella, A. (2011). Accumulation of diarrhetic shellfish poisoning toxins in the oyster *Crassostrea gigas* and the mussel *Choromytilus meridionalis* in the southern Benguela ecosystem. *Afr. J. Mar. Sci.* 33, 273–281. doi: 10.2989/1814232X.2011.600372

Pitcher, G. C., Foord, C. J., Macey, B. M., Mansfield, L., Mouton, A., Smith, M. E., et al. (2019). Devastating farmed abalone mortalities attributed to yessotoxin-producing dinoflagellates. *Harmful Algae* 81, 30–41. doi: 10.1016/j.hal.2018.11.006

Pitcher, G. C., Franco, J. M., Doucette, G. J., Powell, C. L., and Mouton, A. (2001). Paralytic shellfish poisoning in the abalone *Haliotis midae* on the west coast of South Africa. *J. Shellfish Res.* 20, 895–904.

Pitcher, G. C., Jiménez, A. B., Kudela, R. M., and Reguera, B. (2017). Harmful algal blooms in eastern boundary upwelling systems: a GEOHAB core research project. *Oceanography* 30, 22–35. doi: 10.5670/oceanog.2017.107

Pitcher, G. C., Probyn, T. A., du Randt, A., Lucas, A., Bernard, S., Evers-King, H., et al. (2014). Dynamics of oxygen depletion in the nearshore of a coastal embayment of the southern Benguela upwelling system. *J. Geophys. Res. Oceans* 119, 2183–2200. doi: 10.1002/2013JC009443

Pitcher, G. C., and Weeks, S. J. (2006). The variability and potential for prediction of harmful algal blooms in the southern Benguela ecosystem. *Large Mar. Ecosyst.* 14, 125–146. doi: 10.1016/S1570-0461(06)80012-1

Probyn, T., Pitcher, G., Pienaar, R., and Nuzzi, R. (2001). Brown tides and mariculture in Saldanha Bay, South Africa. *Mar. Pollut. Bull.* 42, 405–408. doi: 10.1016/S0025-326X(00)00170-3

Robertson Lain, L., Bernard, S., and Evers-King, H. (2014). Biophysical modelling of phytoplankton communities from first principles using two-layered spheres: Equivalent Algal Populations (EAP) model. *Opt. Express* 22, 16745–16758. doi: 10.1364/OE.22.016745

Ryan, J., Davis, C., Tufillaro, N., Kudela, R., and Gao, B.-C. (2014). Application of the hyperspectral imager for the coastal ocean to phytoplankton ecology studies in Monterey Bay, CA, USA. *Remote Sens.* 6, 1007–1025. doi: 10.3390/rs6021007

Ryan, J. P., Gower, J. F. R., King, S. A., Bissett, W. P., Fischer, A. M., Kudela, R. M., et al. (2008). A coastal ocean extreme bloom incubator. Geophys. *Res. Lett.* 35:L12602. doi: 10.1029/2008GL034081

Sathyendranath, S., Aiken, J., Alvain, S., Barlow, R., Bouman, H., Bracher, A., et al. (2014). *Phytoplankton Functional Types From Space*. Reports of the International Ocean-Colour Coordinating Group (IOCCG); 15 (International Ocean-Colour Coordinating Group), 1–156.

Smith, M., and Bernard, S. (2018). Satellite ocean colour based harmful algal bloom identification for improved risk assessment and mitigation. *Environ. Sci.* doi: 10.1002/essoar.10500045.1. [Epub ahead of print].

Stumpf, R., Culver, M., Tester, P., Tomlinson, M., Kirkpatrick, G., Pederson, B., et al. (2003). Monitoring *Karenia brevis* blooms in the Gulf of Mexico using satellite ocean color imagery and other data. *Harmful Algae* 2, 147–160. doi: 10.1016/S1568-9883(02)00083-5

Tao, B., Mao, Z., Lei, H., Pan, D., Shen, Y., Bai, Y., et al. (2015). A novel method for discriminating *Prorocentrum donghaiense* from diatom blooms in the East China Sea using MODIS measurements. *Remote Sens. Environ.* 158, 267–280. doi: 10.1016/j.rse.2014.11.004

Tao, B., Mao, Z., Wang, D., Lu, J., and Huang, H. (2011). "Remote sensing of the ocean, sea ice, coastal waters, and large water regions 2011," in *Proceedings of SPIE, Vol. 8175* (Prague).

Torres Palenzuela, J. M., González Vilas, L., Bellas, F. M., Garet, E., González-Fernández, Á., and Spyrakos, E. (2019). *Pseudo-nitzschia* blooms in a coastal upwelling system: Remote sensing detection, toxicity and environmental variables. *Water* 11:1954. doi: 10.3390/w11091954

Urban-Econ Development Economists (2018). *Abalone Feasibility Study, Final report*. Report prepared for the Department of Agriculture, Forestry and Fisheries, South Africa.

Van der Lingen, C., Hutchings, L., Lamont, T., and Pitcher, G. (2016). Climate change, dinoflagellate blooms and sardine in the southern Benguela Current Large Marine Ecosystem. *Environ. Dev* 17, 230–243. doi: 10.1016/j.envdev.2015.09.004

Verheye, H. M., Lamont, T., Huggett, J. A., Kreiner, A., and Hampton, I. (2016). Plankton productivity of the Benguela current large marine ecosystem (BCLME). *Environ. Dev.* 17, 75–92. doi: 10.1016/j.envdev.2015.07.011

Wang, M., and Hu, C. (2017). Predicting Sargassum blooms in the Caribbean Sea from MODIS observations. *Geophys. Res. Lett.* 44, 3265–3273. doi: 10.1002/2017GL072932

Zhao, J., Temimi, M., and Ghedira, H. (2015). Characterization of harmful algal blooms (habs) in the Arabian Gulf and the Sea of Oman using MERIS fluorescence data. *ISPRS J. Photogrammetr. Remote Sens.* 101, 125–136. doi: 10.1016/j.isprsjprs.2014.12.010

Conflict of Interest: The authors declare that the research was conducted in the absence of any commercial or financial relationships that could be construed as a potential conflict of interest.

frontiers in Marine Science

ORIGINAL RESEARCH
published: 26 May 2020
doi: 10.3389/fmars.2020.00337

Current and Future Remote Sensing of Harmful Algal Blooms in the Chesapeake Bay to Support the Shellfish Industry

Jennifer L. Wolny[1], Michelle C. Tomlinson[2], Stephanie Schollaert Uz[3], Todd A. Egerton[4], John R. McKay[5], Andrew Meredith[6], Kimberly S. Reece[7], Gail P. Scott[7] and Richard P. Stumpf[2]*

[1] Resource Assessment Service, Maryland Department of Natural Resources, Annapolis, MD, United States, [2] National Centers for Coastal Ocean Science, National Oceanic and Atmospheric Administration, Silver Spring, MD, United States, [3] Earth Science Division, Goddard Space Flight Center, National Aeronautics and Space Administration, Greenbelt, MD, United States, [4] Division of Shellfish Safety, Virginia Department of Health, Norfolk, VA, United States, [5] Water and Science Administration, Maryland Department of the Environment, Annapolis, MD, United States, [6] Consolidated Safety Services, Inc., Fairfax, VA, United States, [7] Aquatic Health Sciences, Virginia Institute of Marine Science, William & Mary, Gloucester Point, VA, United States

OPEN ACCESS

Edited by:
Pierre Gernez, Université de Nantes, France

Reviewed by:
Clarissa Anderson, University of California, San Diego, United States
Hayley Louise Evers-King, Plymouth Marine Laboratory, United Kingdom

***Correspondence:**
Jennifer L. Wolny
jennifer.wolny@maryland.gov

Specialty section:
This article was submitted to Ocean Observation, a section of the journal Frontiers in Marine Science

Received: *07 December 2019*
Accepted: *22 April 2020*
Published: *26 May 2020*

Citation:
Wolny JL, Tomlinson MC, Schollaert Uz S, Egerton TA, McKay JR, Meredith A, Reece KS, Scott GP and Stumpf RP (2020) Current and Future Remote Sensing of Harmful Algal Blooms in the Chesapeake Bay to Support the Shellfish Industry. Front. Mar. Sci. 7:337. doi: 10.3389/fmars.2020.00337

Harmful algal bloom (HAB) species in the Chesapeake Bay can negatively impact fish, shellfish, and human health via the production of toxins and the degradation of water quality. Due to the deleterious effects of HAB species on economically and environmentally important resources, such as oyster reef systems, Bay area resource managers are seeking ways to monitor HABs and water quality at large spatial and fine temporal scales. The use of satellite ocean color imagery has proven to be a beneficial tool for resource management in other locations around the world where high-biomass, nearly monospecific HABs occur. However, remotely monitoring HABs in the Chesapeake Bay is complicated by the presence of multiple, often co-occurring, species and optically complex waters. Here we present a summary of common marine and estuarine HAB species found in the Chesapeake Bay, *Alexandrium monilatum*, *Karlodinium veneficum*, *Margalefidinium polykrikoides*, and *Prorocentrum minimum*, that have been detected from space using multispectral data products from the Ocean and Land Colour Imager (OLCI) sensor on the Sentinel-3 satellites and identified based on *in situ* phytoplankton data and ecological associations. We review how future hyperspectral instruments will improve discrimination of potentially harmful species from other phytoplankton communities and present a framework in which satellite data products could aid Chesapeake Bay resource managers with monitoring water quality and protecting shellfish resources.

Keywords: aquaculture, Chesapeake Bay, harmful algal bloom (HAB), ocean color, OLCI, remote sensing, shellfish

INTRODUCTION

The Chesapeake Bay is the largest estuary in the United States. The annual temperature cycle combined with numerous freshwater inputs and the tidal influx of high salinity ocean water makes it a suitable habitat for many juvenile and adult stages of important commercial and recreational fish and shellfish species and one of the country's most productive estuaries. Maintaining a viable,

Bay-wide population of the eastern oyster (*Crassostrea virginica*) is of particular concern because of its role in supporting ecosystem health (Kennedy et al., 2011; Grabowski et al., 2012) and regional economies (Hicks et al., 2004; Haddaway-Riccio, 2019). Virginia shellfish aquaculture, which produces the most eastern oysters on the United States East Coast, had a farm gate value of $53.3 million in 2018 and is first in the United States for production of hard clams (*Mercenaria mercenaria*) (Hudson, 2019). Similarly, Maryland's oyster industry was valued at $10.6 million between 2016 and 2017 (Tarnowski, 2017) and Maryland has modest soft shell (*Mya arenaria*), stout razor (*Tagelus plebeius*), and hard clam industries (Roegner and Mann, 1991; Glaspie et al., 2018).

Abundant Chesapeake Bay oyster populations were cataloged in the early 1900s, with approximately 250,000 acres of oyster reefs in both Maryland and Virginia (Mann, 2000). However, beginning in the late 1950s extensive oyster mortality events occurred Bay-wide due to outbreaks of the diseases MSX (*Haplosporidium nelsoni*) and Dermo (*Perkinsus marinus*) as drought conditions changed salinity gradients in the Bay and its tributaries (Mann, 2000; Carnegie and Burreson, 2011). While the threat from disease remains (Powell et al., 2012; Tarnowski, 2017), over the past 15–20 years oyster populations have been additionally stressed by reduced water quality and habitat loss (Kemp et al., 2005; Harding et al., 2019) and episodic harmful algal blooms (HABs) (Tango et al., 2005; Glibert et al., 2007; Mulholland et al., 2009; May et al., 2010; Griffith and Gobler, 2020).

Assessment of the state of the health of the Chesapeake Bay includes results from routine water quality and phytoplankton monitoring. Monthly water quality and phytoplankton monitoring throughout the Chesapeake Bay has occurred since the mid-1980s through the auspices of the Chesapeake Bay Program (CBP) (Marshall et al., 2005, 2009) by officials at the Maryland Department of Natural Resources (MDNR), Morgan State University (MSU), Old Dominion University (ODU) and the Virginia Department of Environmental Quality (VDEQ). Currently, the phytoplankton community at 32 stations in the Chesapeake Bay and its tributaries is monitored monthly from above pycnocline or from whole water column composited samples[1]. Surface water samples collected routinely throughout the Bay and its tributaries are also examined for phytoplankton community composition as part of monitoring and research programs at MDNR, ODU, the Virginia Department of Health (VDH), and the Virginia Institute of Marine Science (VIMS). In Maryland, Chesapeake Bay shellfish harvesting areas are monitored by the Maryland Department of Environment (MDE) for water quality and bacteria concentrations. In Virginia these activities are conducted by VDH. The state agencies responsible for shellfish health and safety regularly monitor for fecal coliforms at 800 sites in Maryland and 2,500 sites in Virginia for the purpose of classifying shellfish growing areas for wild harvest and aquaculture in the Bay and estuarine portion of its tributaries. This routine sampling is based off guidelines provided in the National Shellfish Sanitation Program (NSSP) in which a systematic random sampling strategy is used to visit shellfish sites six to twelve times per year (National Shellfish Sanitation Program [NSSP], 2017). Additionally, in accordance with NSSP guidelines, each state has a marine biotoxin contingency plan to facilitate response and monitoring strategies in the event of a toxigenic HAB outbreak and/or human illness.

Phytoplankton data collected via the CBP between 1984 and 2004 indicated a phytoplankton community dominated by diatoms throughout the year with periodic dinoflagellate blooms (Kemp et al., 2005; Marshall et al., 2005, 2009). In 2002, a bloom of the dinoflagellate *Dinophysis acuminata* in the Potomac River and its sub-estuaries at concentrations $> 200{,}000$ cells$\cdot L^{-1}$ caused the first and only precautionary closure of Chesapeake Bay shellfish harvesting areas due to a toxigenic algal species (Marshall et al., 2004; Tango et al., 2004). This precautionary closure of regional oyster harvesting areas in the Potomac River was issued while water samples and oyster tissues were assayed for the presence of okadaic acid (OA), a diarrhetic shellfish poisoning (DSP) toxin produced by many *Dinophysis* species. Marshall and Egerton (2009a,b), Li et al. (2015), and Wolny et al. (2020) have summarized common marine and estuarine HAB species in Bay waters that have historically been present but are increasing in abundance and extent: *Alexandrium monilatum, Dinophysis acuminata, Karlodinium veneficum, Margalefidinium polykrikoides,* and *Prorocentrum minimum*. Each of these bloom-forming dinoflagellate species have different harmful or toxic properties that can negatively impact larval oyster development and recruitment and cause physiological stress in adult oysters or threaten human health due to toxin accumulation in shellfish harvested for consumption. Additionally, Chesapeake Bay populations of *A. monilatum* and *M. polykrikoides* have been shown to produce cysts, a resting stage that ensures long-term survival and can seed future blooms (Seaborn and Marshall, 2008; Pease, 2016; Van Hauwaert, 2016).

Both Marshall and Egerton (2009b) and Li et al. (2015) reported that HABs occur more frequently in the mesohaline and polyhaline regions of the tributaries and the Bay shoreline than in the mainstem of the Chesapeake. These are the same geographic regions that are conducive to productive oyster reefs (Smith et al., 2005; Carnegie and Burreson, 2011). In the mid-2000s, meetings and surveys conducted jointly with government officials and shellfish growers from Maryland and Virginia identified several needs of the shellfish industry. One of the most critical needs identified was the establishment and maintenance of good water quality specific to the shellfish species being grown (Oesterling and Luckenbach, 2008; Webster, 2009). Growers also identified a need for technology that would detect blooms more rapidly in order to better assess human health risks and respond if there was a need to conduct shellfish relays between aquaculture sites (Webster, 2009; Sea Grant Association [SGA], 2016). Incorporating satellite technology to improve monitoring for HAB communities was outlined as a priority by the Interstate Shellfish Sanitation Commission (Interstate Shellfish Sanitation Commission [ISSC], 2016). Shellfish industry members want government agencies to provide timely information about water quality and HABs from remote sensing, yet challenges

[1]https://www.chesapeakebay.net/what/downloads/baywide_cbp_plankton_database for sample collection metadata

remain (Schaeffer et al., 2013; National Aeronautics and Space Administration Goddard Space Flight Center [NASA GSFC], 2018, 2019; Schollaert Uz et al., 2019). However, the need for near-real time and high-resolution water quality and HAB data is expected to grow as the shellfish industry is projected to increase in economic value and geographic expanse into the next decade in both Maryland (Kobell, 2017) and Virginia (Hudson, 2019).

While the sampling approaches currently used by state agencies appear to be historically successful, and no biotoxin-related human illnesses resulting from shellfish consumption have been reported from either state, the scale and variability of algal blooms exceeds what is fully captured by the states' phytoplankton, water quality, and shellfish health monitoring programs. HAB species can remain cryptic in the environment, blooms can initiate and intensify over the course of days or weeks, and may occur in areas that are not routinely monitored by state agencies (Anderson et al., 2012). Bloom patterns also respond to regional climatic variations (Miller and Harding, 2007; Morse et al., 2014). Hence, state officials could augment current monitoring systems with greater spatial and temporal coverage from satellites. During blooms, a timely view from space could guide resource manager sampling strategies and help inform the decision-making process that safeguard natural resources, shellfish industry assets, and the public. Satellite data can also be used to fill data gaps when routine *in situ* monitoring plans are seriously interrupted, such as during the COVID-19 outbreak that disrupted the United States workforce beginning in March 2020.

Over the past decade, satellite ocean color imagery has proven to be a useful tool to identify and track HABs globally (Stumpf and Tomlinson, 2005; Davidson et al., 2016). In the United States, several optical techniques pertaining to absorption, backscatter, and chlorophyll-*a* (chl-*a*) anomalies have been used for the detection of the toxic dinoflagellate *Karenia brevis* in the Gulf of Mexico (Tomlinson et al., 2004, 2009; Cannizzaro et al., 2008; Soto et al., 2015). Currently, shellfish resource managers in Florida incorporate satellite data products produced by the National Oceanic and Atmospheric Administration (NOAA) and the National Atmospheric and Space Administration (NASA) into their decision-making processes when monitoring for *K. brevis* blooms (Heil, 2009). In California, a joint academic and government monitoring program, the California-Harmful Algae Risk Mapping (C-HARM) System, incorporates ecological models, Moderate Resolution Imaging Spectroradiometer (MODIS) remote sensing reflectance (R_{rs}) ratios and chl-*a* data to better inform coastal resource managers about *Pseudo-nitzschia* blooms and domoic acid toxicity risks (Anderson et al., 2011, 2016). A spectral shape algorithm that identifies the unique spectral signature of cyanobacteria is being used to forecast *Microcystis aeruginosa* blooms in Lake Erie, as well as to monitor cyanobacteria blooms in other large lakes around the United States (Wynne et al., 2010, 2013; Schaeffer et al., 2015; Clark et al., 2017). The Ohio Environmental Protection Agency has incorporated the use of this cyanobacteria-specific satellite data product into the monitoring plan for the state's public drinking water supply (Ohio Environmental Protection Agency [Ohio EPA], 2019).

The suitability of similar data products for the Chesapeake Bay region is still being investigated as both a research application and a monitoring tool. New hyperspectral sensors currently being studied, designed, and built for satellites will change the way we monitor water quality from space with increased spectral, temporal, and spatial resolution. The NASA Plankton, Aerosol, Cloud, ocean Ecosystem (PACE) mission, scheduled to launch by 2023, will fly the Ocean Color Imager (OCI) with a spatial resolution of 1 km, 1–2 days global repeat, spanning 340 to 890 nm with a spectral resolution (bandwidth) of 5 nm, plus seven short-wave infrared bands at wider spectral resolution. The OCI instrument performance specifications for water-leaving reflectances constrain the errors, i.e., 350–400 nm at 20% uncertainty; 400–600 nm at 5% uncertainty; 600–710 nm at 10% uncertainty (Werdell et al., 2019). This sensitivity will enable PACE to improve the identification of phytoplankton community composition and to separate phytoplankton pigment absorption from that of colored dissolved organic matter (CDOM) (Blough and Del Vecchio, 2002; Catlett and Siegel, 2018). Furthermore, the spectral slope of CDOM absorption will provide an indication of its terrestrial or aquatic source (Siegel et al., 2002, 2005). Less sensitive, the Geostationary Littoral Imaging and Monitoring Radiometer (GLIMR) instrument will be delivered to NASA in 2023/2024 and launched into geosynchronous orbit above the Gulf of Mexico and southeastern United States, including the Chesapeake Bay, with the potential for up to seven observations per day at 300 m spatial resolution, 350–890 nm spectral resolution at less than 10 nm, plus one near-infrared band at 1020 nm (National Aeronautics and Space Administration [NASA], 2019). A NASA Surface Biology and Geology observable platform recommended in the 2017 Decadal Survey (National Academies of Sciences, Engineering, and Medicine [NASEM], 2018) for studying coastal and inland aquatic ecosystems worldwide, among other variables, is currently in architecture study with a potential launch around 2027 and is likely to have PACE-like spectral range and sensitivity with higher spatial resolution (tens of meters) but less frequent revisit (16-day). Combining these new observations with others from sub-orbital and *in situ* sensors through assimilation and modeling will help overcome limitations, such as cloud gaps.

In advance of the expanded capability afforded by these future hyperspectral missions, we examined the suitability of existing multispectral satellite ocean color products, particularly from the Ocean Land Colour Instrument (OLCI) on the Copernicus Sentinel-3 satellite constellation, to detect the spatial and temporal extent of several HAB species common to the Chesapeake Bay. OLCI currently has the most spectral bands of any satellite-based routine monitoring sensor, as well as nearly daily coverage, making it the best sensor for timely response and for evaluation of capabilities that will only be enhanced with the hyperspectral data products that are anticipated after 2022. Red-edge algorithms, which use the strong spectral variability in chlorophyll and reflectance from 650 to 750 nm, have been developed with OLCI. Some algorithms, such as the Maximum Chlorophyll Index (MCI) of Gower et al. (2008) and the Red Band Difference (RBD) of Amin et al. (2009), do not require a full atmospheric correction and have also been designed

specifically to locate algal blooms. As red-edge bands are much less sensitive to interference by non-algal pigments (dissolved or particulate), they can provide more specific information on algal blooms. However, scattering by sediments may still interfere with algorithms like the MCI (Zeng and Binding, 2019), a potential problem in an estuary, such as Chesapeake Bay, with large tributary rivers and multiple turbidity maxima. The RBD was designed to detect chl-*a* fluorescence in a harmful algal bloom (*K. brevis*) without interference from sediment (Amin et al., 2009). This method, applied to OLCI data, provides a HAB monitoring tool for resource managers supporting aquaculture in the Chesapeake Bay. Here, we present some preliminary work that shows the use of multispectral OLCI data from the Sentinel-3 satellite constellation to detect HABs in Chesapeake Bay and we propose how model development and hyperspectral data will improve bloom detection.

MATERIALS AND METHODS

Satellite Product Generation

Imagery from OLCI on the Sentinel-3 satellites covering Chesapeake Bay (36–39°N, 75–77°W) were obtained from EUMETSAT. OLCI has 300 m pixels, which provide useful information for the Chesapeake Bay and its tributaries. The level 1 granules were processed using the NOAA satellite automated processing system, which incorporates the NASA standard ocean color satellite processing software distributed within the Sea-viewing Wide Field-of-view Sensor (SeaWiFS) Data Analysis System (SeaDAS) package (version 7.5.3) and the European Space Agency's (ESA) Sentinel Application Platform (SNAP) package (version 6). The R_{rs} and top-of-atmosphere reflectance (R_{rhos}) products corrected for molecular scattering (Rayleigh) and absorption were created for the visible and near-infrared bands using SeaDAS l2gen with the system defaults except for cloud, stray light, and high light masking disabled. Products were mapped to a Universal Transverse Mercator (zone 18N) projection at 300 m pixel resolution to produce level 3 multi-band GeoTiffs. Multiple granules overlapping the area of interest from the same day were composited based on time of swath.

During product generation from the level 3 files, a custom flagging algorithm was applied to identify clouds, glint, mixed pixels, and snow and ice (Wynne et al., 2018). Clouds were flagged using NIR albedo, with the threshold adjusted for the presence of turbid water. For atmospheric correction, we used R_{rs} determined from R_{rhos} with a fixed maritime aerosol (Stumpf and Pennock, 1989, after Gordon et al., 1983). With dense, highly reflective biomass and the optically complex water of Chesapeake Bay, the standard (complex) coastal atmospheric corrections often lead to areas of negative or anomalous R_{rs} fields. As a result, algorithms that require accurate R_{rs} of the water, such as the neural network algorithms available for Sentinel-3, perform inconsistently or can fail.

The typical ocean color algorithms developed for open ocean waters use blue and green spectral bands to determine chl-*a* concentration. These algorithms confuse CDOM and sediment as chlorophyll, which can lead to high rates of false positive bloom detections. Chl-*a* fluorescence in the red has been shown to be useful in detecting dense blooms of *K. brevis*, providing a way to avoid high CDOM conditions (Hu et al., 2005; Amin et al., 2009). While some fluorescence algorithms also respond to sediment, the RBD fluorescence algorithm described in Amin et al. (2009) is insensitive to interference from sediment, making it a particularly useful detection method in Chesapeake Bay, which frequently has strong sediment/turbidity gradients near areas of dense blooms. The RBD was modified for OLCI R_{rhos} bands as:

$$RBD = R_{\mathrm{rhos}}(681) - R_{\mathrm{rhos}}(665) \quad (1)$$

to highlight areas of high algal biomass, using only pixels within the valid R_{rhos} range (0–1). The differencing method is a variant of a derivative, which produces an implicit atmospheric correction over this short (16 nm) difference in wavelength (Philpot, 1991). Due to the increase in reflectance caused by chl-*a* fluorescence at 681 nm, the RBD will be positive in areas of chl-*a* fluorescence.

The Cyanobacteria Index (CI), an algorithm developed by Wynne et al. (2008), identifies blooms that combine strong scattering and chl-*a* absorption with weak chl-*a* fluorescence – optical characteristics of cyanobacterial blooms (Stumpf et al., 2016). The CI has also proven useful in identifying weakly fluorescing algae within the Chesapeake Bay (detailed in Wynne et al., 2018). To summarize, the spectral shape around 681 nm [SS(681)] product, later renamed the Cyanobacteria Index by Wynne et al. (2010), was developed for Lake Erie using Medium Resolution Imaging Spectrometer (MERIS) data to detect large monospecific blooms of cyanobacteria, primarily *M. aeruginosa*. Cyanobacteria typically show negligible chl-*a* fluorescence at 681 nm, so the CI captures the chl-*a* absorption peak, which also occurs around 681 nm. The CI is calculated based on a spectral shape (SS) around 681 nm using the following equation:

$$CI = -SS = \left(\rho_{\lambda_1} - \rho_{\lambda_2}\right) + \left(\rho_{\lambda_3} - \rho_{\lambda_1}\right) * \frac{(\lambda_2 - \lambda_1)}{(\lambda_3 - \lambda_1)} \quad (2)$$

Where ρ_λ is the R_{rhos} measured at wavelength λ, and subscripts 1 = 665 nm, 2 = 681 nm, and 3 = 709 nm, and values less than zero are assumed to be non-detect and linearly related to the biomass (Lunetta et al., 2015). While the CI was developed for blooms of cyanobacteria in Lake Erie, it will detect strongly scattering and weakly fluorescing algae (Stumpf et al., 2016). As such it can be applied to areas with more complex phytoplankton assemblages, such as Chesapeake Bay, to look for potential physiological (fluorescence) differences in the algal blooms, even where there are no reported occurrences of cyanobacteria.

In situ Data

Phytoplankton and water quality data collected between 2016 and 2018 through the CBP were downloaded from https://datahub.chesapeakebay.net/ and sorted for cell concentrations of *A. monilatum*, *K. veneficum*, *M. polykrikoides*, and *P. minimum*. Cell concentration data collected at the same station location, on the same date, and at sampling depths ≤ 1.0 m were selected for satellite ocean color imagery match ups. Additional phytoplankton and water quality observations collected between

2016 and 2020 as part of Maryland[2] and Virginia[3] routine environmental monitoring and HAB event response activities were also included to increase the spatial and temporal distribution of *in situ* cell concentration data. Data retrieval parameters for these data were the same as described above for the CBP data. The phytoplankton cell concentration data retrieved from the CBP, MDNR, and VDH data portals are comparable as the sample processing methods between these agencies are similar. Phytoplankton samples (0.5–1 L) were preserved with a 5% Lugol's iodine solution. A known sample volume was allowed to settle in a settling chamber for a minimum of 60 min before species were identified and enumerated using an inverted light microscope, following the modified Utermöhl method of Marshall and Alden (1990). Species identifications were based on morphological characteristics (see Tomas, 1997), enumerated as individual cells per volume, and then extrapolated to a per L concentration.

In situ phytoplankton cell concentration data determined using light microscopy were augmented with cell concentration data obtained through quantitative PCR (qPCR) assays. For each sample a known volume of water, 25–100 ml, was filtered through a 3 μm Isopore membrane filter (Millipore Corp., Darmstadt, Germany) using sterile technique for DNA extraction and PCR analysis. Filters were placed into 5 ml centrifuge tubes and frozen at −20°C until DNA extraction. DNA was extracted from the filters using the QIAamp Fast Stool Mini Kit (QIAGEN, Inc., Germantown, MD, United States) according to the manufacturer's protocol with the following modifications. Rather than centrifuging the sample and using only 200 μL of the lysate, per the manufacturer's instructions, the entire sample was retained and carried through the extraction protocol. Reagent volumes were increased in the subsequent steps to maintain a ratio of sample to reagent consistent with that in the manufacturer's protocol. The eluted DNA was stored at −20°C until needed. A "blank" extraction (reagents only) was performed alongside each set of environmental samples to ensure there was no contamination.

A previously published TaqMan® qPCR assay was used to target *A. monilatum* (see Vandersea et al., 2017). We developed a new TaqMan qPCR assay to target *M. polykrikoides*. The *M. polykrikoides* primers are MpolyLSU_703F (5′-TCTTTCCGACCCGTCTTGAA-3′) and MpolyLSU_875R (5′-CCATCTTTCGGGTCCTAGCA-3′). The probe is MpolyLSU 828Pr (5′FAM -TTGCGAGACGTTTGAGTGTG-3′ MGBNFQ). Stock cultures of York River *A. monilatum* and *M. polykrikoides* were maintained at VIMS. The cell concentration of *A. monilatum* and *M. polykrikoides* cultures were determined and DNA was extracted from a known number of cells to use as positive control material and to generate standard curves by serially diluting the DNA to achieve a range of cell number equivalents. The qPCR assays were done on 7500 Fast, QuantStudio 6, or QuantStudio 3 Real-Time PCR systems (Applied Biosystems, Thermo Fisher, Foster City, CA, United States) using the following cycling parameters: an initial denaturation step at 95°C for 20 s followed by 40 cycles of 95°C for 3 s to denature and 60°C for 30 s to anneal and extend. All reactions were run in duplicate with reagent concentrations for each reaction at 0.9 μM for each primer, 0.1 μM for the probe, and 1X of the TaqMan Fast Advanced Master Mix (Applied Biosystems, Thermo Fisher) in a 10 μL final volume.

Satellite Imagery Comparison With *in situ* Data

In situ field data were used to perform same day pixel extractions from imagery at bloom sample locations. Cell concentration data > 50,000 cells·L^{-1} [the limit of detection for Gulf of Mexico *K. brevis* blooms via legacy satellites (Tester et al., 1998)] were compared with same day Sentinel-3 scenes. The mean R_{rhos} spectra from the level 3 OLCI satellite data products within a 3 pixel × 3 pixel window centered on the location of each field sample were extracted and plotted for each wavelength, by individual species (**Figure 1**). Match ups containing invalid pixels (e.g., cloud, land, and mixed pixels) were excluded. Separate spectral plots from the match up data were created for *A. monilatum*, *K. veneficum*, *M. polykrikoides*, and *P. minimum*.

RESULTS AND DISCUSSION

While the analysis of historic phytoplankton datasets indicates a phytoplankton community dominated by diatoms, the Chesapeake Bay can experience blooms dominated by the dinoflagellates *A. monilatum, K. veneficum, M. polykrikoides,* and *P. minimum*, throughout the year. Each of these species have unique harmful or toxic properties which are of concern for the region's shellfish industry. Due to the optical complexity of Chesapeake Bay waters, remote sensing has not previously been used extensively to detect and track these blooms for resource management applications. However, the 2016 launch of the Copernicus Sentinel-3 constellation of satellites that are flying the OLCI sensor has given us the opportunity to investigate the possibility of monitoring these species in the Chesapeake Bay using multispectral ocean color satellite data. We speculate how the hyperspectral assets expected after 2022, through the launch of several new NASA satellites, will improve our ability to monitor blooms and will increase the data available to couple ocean color satellite imagery, water quality, and ecological associations.

Alexandrium monilatum and *Margalefidinium polykrikoides*

Margalefidinium polykrikoides (formerly *Cochlodinium polykrikoides* and *C. heterolobatum*) blooms have been reported in the York River, Virginia since the 1960s (Mackiernan, 1968). Since the 1990s there has been an increase in bloom occurrence and intensity throughout Virginia waters (Marshall, 1996; Marshall et al., 2005) with a geographic expansion of the blooms from the York River, primarily southwards to the James River (Marshall and Egerton, 2009a), and to a lesser degree northwards to the Rappahannock River (Marshall and Egerton, 2009b).

[2]http://eyesonthebay.dnr.maryland.gov/eyesonthebay/DataInfo.cfm

[3]http://www.vdh.virginia.gov/environmental-health/environmental-health-services/shellfish-safety/

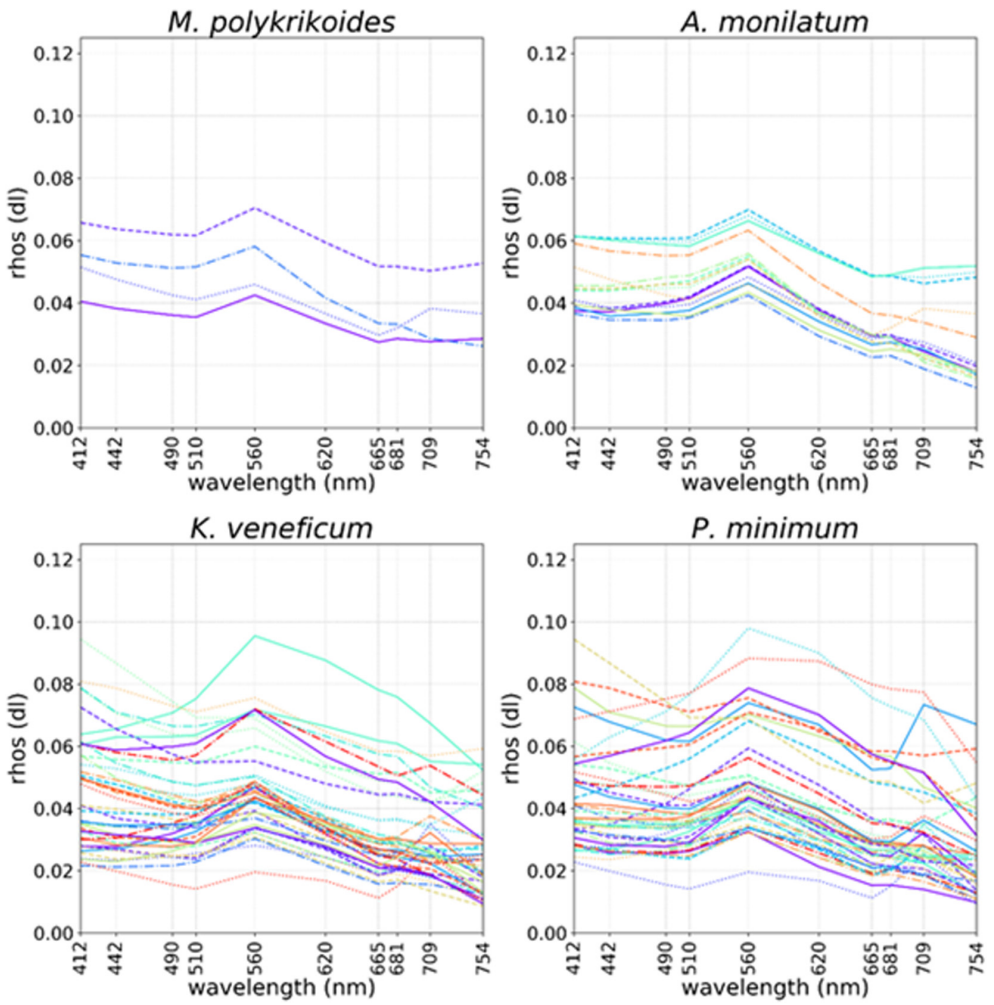

FIGURE 1 | Ocean and Land Colour Imager (OLCI) R_{rhos} spectral plots coinciding with locations of *in situ* cell concentrations > 50,000 cells L^{-1} collected on the same day for *Margelefidinium polykrikoides* **(top left)**, *Alexandrium monilatum* **(top right)**, *Karlodinium veneficum* **(bottom left)**, and *Prorocentrum minimum* **(bottom right)**. Colored lines and random linestyles were used for better separation of individual spectra.

Globally, *M. polykrikoides* blooms upward of 10^6 cells·L^{-1} generally occur when the water temperature is >20°C and when the salinity ranges from 30–33 (Kudela et al., 2008; Kudela and Gobler, 2012). However, in the Chesapeake Bay these blooms occur at lower salinities (21–28) (Mulholland et al., 2009). Mulholland et al. (2009) documented that *M. polykrikoides* blooms caused mortalities in both juvenile oysters and fish exposed to live cells. Tang and Gobler (2009) demonstrated that cell toxicity was tied to bloom stage, with the early exponential growth phase being more toxic than late exponential growth or stationary phases. More recently Griffith et al. (2019) showed, using juvenile oysters, hard clams, and bay scallops (*Argopecten irradians*) contained in bags on grow-out rafts, that shellfish position within the water column impacts animal susceptibility to *M. polykrikoides* blooms. In their study, animals in surface waters had higher mortality rates than those at depth and reduced growth rates were exhibited in animals exposed to *M. polykrikoides* blooms, regardless of position in the water column, thus having implications for aquaculture management in regions where *M. polykrikoides* blooms are common (Griffith et al., 2019). The timing of *M. polykrikoides* blooms often coincide with the region's maximum water temperatures (July–September) and blooms intensify after strong rain events during drought conditions (Mulholland et al., 2009). These are climatic scenarios predicted to increase in frequency within the Chesapeake Bay region (Najjar et al., 2010; Reidmiller et al., 2018); Mulholland et al. (2009) and Griffith and Gobler (2016) hypothesize that this shift could cause a longer and more toxic *M. polykrikoides* bloom season that would overlap with the shellfish larval recruitment and growing season within Chesapeake Bay.

In 2007, *A. monilatum* blooms were first reported in the York River (Harding et al., 2009; Marshall and Egerton, 2009b). Since 2007, *A. monilatum* has bloomed nearly annually in the late summer, typically co-occurring with or following *M. polykrikoides* blooms, when water temperatures are >24°C

and the salinity is 18–24 (Mulholland et al., 2018). Blooms have been measured at concentrations $> 10^8$ cells·L^{-1} and have intensified and expanded from the York River basin southwards to the Hampton Roads area and Virginia Beach coastline (Pease, 2016; Robison, 2019). The 2007 bloom in the lower York River was responsible for a veined rapa whelk (*Rapana venosa*) mortality event wherein whelk tissues tested positive for elevated concentrations of the hemolytic and neurotoxic toxin goniodomin A, produced by *A. monilatum* (Harding et al., 2009). Subsequent laboratory experiments conducted by May et al. (2010) indicated that adult oysters exposed to *A. monilatum* cells and cell extracts had decreased clearance rates and reduced valve gapes, which influences the animals' pumping rate. In studies focusing on larval oysters May et al. (2010) demonstrated that animals were not affected by the presence of *A. monilatum* cells, but that larval mortality rates increased when exposed to *A. monilatum* cell extracts that contained extracellular toxins. Through field and laboratory studies, Pease (2016) found that extended exposure (>96 h) to both *A. monilatum* cells and cell extracts caused erosion to gill and mantle tissues in 94% of adult oysters and led to a 67% mortality rate.

Alexandrium monilatum and *M. polykrikoides* bloom in the same geographic regions of the lower Chesapeake Bay and at similar times of the year. While these blooms are detectable by satellite imagery through the RBD algorithm (**Figures 2A,B**), they cannot be distinguished from each other with existing satellite ocean color data products alone (**Figure 1**). *In situ* monitoring by state agencies is needed to confirm species identification. Currently, by applying the RBD algorithm to Sentinel-3 image products, NOAA officials are able to alert resource managers to the presence of a high biomass phytoplankton bloom in these areas. With the addition of space-based hyperspectral sensors in the future, we hope to develop the capability to further differentiate these blooms. From a resource management perspective, knowing which dinoflagellate species is blooming, where it is blooming, and the duration of blooms for each species would be useful to shellfish industry partners who may be able to mitigate damage to shellfish crops by adjusting spat planting schedules, conducting shellfish relays, adjusting crop position in the water column, or avoiding moving shellfish crops or gear from areas with blooms to areas without blooms to limit the spread of HAB cells or cysts.

Karlodinium veneficum

Discolored water caused by a bloom of *K. veneficum* (reported as *Gyrodinium galatheanum*) was first noted in the Chesapeake Bay in 1994 (Li et al., 2000). In 1996, a striped bass (*Morone* spp.) mortality event was caused by this same organism (reported as *Karlodinium micrum*) in an aquaculture facility on the Bay's eastern coast (Deeds et al., 2002). This mixotrophic dinoflagellate was identified (as *Gymnodinium estuariale* and *Gyrodinium estuariale*) in the Chesapeake Bay phytoplankton community in the late 1970s by Marshall (1980) and Chrost and Faust (1983); however, annual blooms were not reported until the mid-2000s (Marshall et al., 2005; Place et al., 2012). Since the mid-2000s there has been an increase in bloom occurrence and intensity, though fish kills remain sporadic as *K. veneficum* toxicity seems to be regulated by a series of environmental conditions such as increased CO_2 concentrations and P-limitation (Fu et al., 2010), water column stratification that alters salinity and nutrient flow regimes (Hall et al., 2008), and the abundance and nutritional status of cryptophyte prey (Adolf et al., 2008; Lin et al., 2017). Since first being documented in the mainstem of the Chesapeake Bay and in the Tangier Sound region of the Bay's eastern coast, *K. veneficum* has been found as far north as the Bush River in Maryland and as far south as the western branch of the Elizabeth River in Virginia. While *K. veneficum* cells can be found year-round in waters with temperatures of 7–28°C and salinities of 3–29, blooms with cell concentrations $> 5 \times 10^5$ cells·L^{-1} typically occur between May and September (Glibert et al., 2007; Li et al., 2015), though more recently blooms also have been detected in Maryland waters in winter months (November–December) (J. Wolny, unpublished data).

Karlodinium veneficum produces strong ichthyotoxic and hemolytic compounds, called karlotoxins, that disrupt osmoregulatory processes across gill tissues and lead to acute fish kills, as well as cause deformations in shellfish larvae that impact larval development, dispersal, and recruitment (Deeds et al., 2006; Glibert et al., 2007). Thus, *K. veneficum* blooms pose a risk to both finfish and shellfish populations, but are not a risk to human health (Place et al., 2012, 2014). Deeds et al. (2002, 2006) showed that larval, juvenile, and adult stages of various finfish species are all susceptible to the effects of karlotoxin. Pre-bloom concentrations as low as 6.2×10^4 cells·L^{-1} increased immune system stress responses in adult blue mussels (*Mytilus edulis*) indicating that exposure to background concentrations of *K. veneficum* may negatively impact shellfish health before blooms occur (Galimany et al., 2008). Brownlee et al. (2008) showed that oyster spat exposed to *K. veneficum* cells at a concentration of 10^7 cells·L^{-1} had depressed growth rates and reduced organ development. Glibert et al. (2007) and Lin et al. (2017) demonstrated that oyster spawning and the early life stages of oysters are very susceptible (as shown through larval deformation and mortality > 80%) to *K. veneficum* cells and to karlotoxin exposure at concentrations of 10^7 cells·L^{-1} and that the nutritional status of the cryptophyte prey plays a role in *K. veneficum* toxicity. Because the risk to finfish and shellfish can be severe and acute at both high ($>10^7$ cells·L^{-1}) and low (10^5 cells·L^{-1}) *K. veneficum* cell densities, monitoring schemes that identify temperature and salinity fronts, assess nutrient concentrations, and cryptophyte abundance may be more critical than monitoring for *K. veneficum* cell concentrations alone if toxin risks are to be forecasted or mitigated for the aquaculture industry.

Currently, *K. veneficum* blooms are identified by resource managers as fish kills occur and are reported to state agencies. However, recent blooms of *K. veneficum* have been identified through remote sensing using both the RBD (fluorescence) (**Figure 3A**) and CI (weakly fluorescing) algorithms (**Figure 3B**). While this result appears contradictory and OLCI spectra from *K. veneficum* blooms are inconsistent in the red bands (**Figure 1**), it may be explained by a few simple hypotheses. The detection of bloom presence with the RBD algorithm indicates some chl-*a* fluorescence, as the radiance returned at 681 nm is greater than

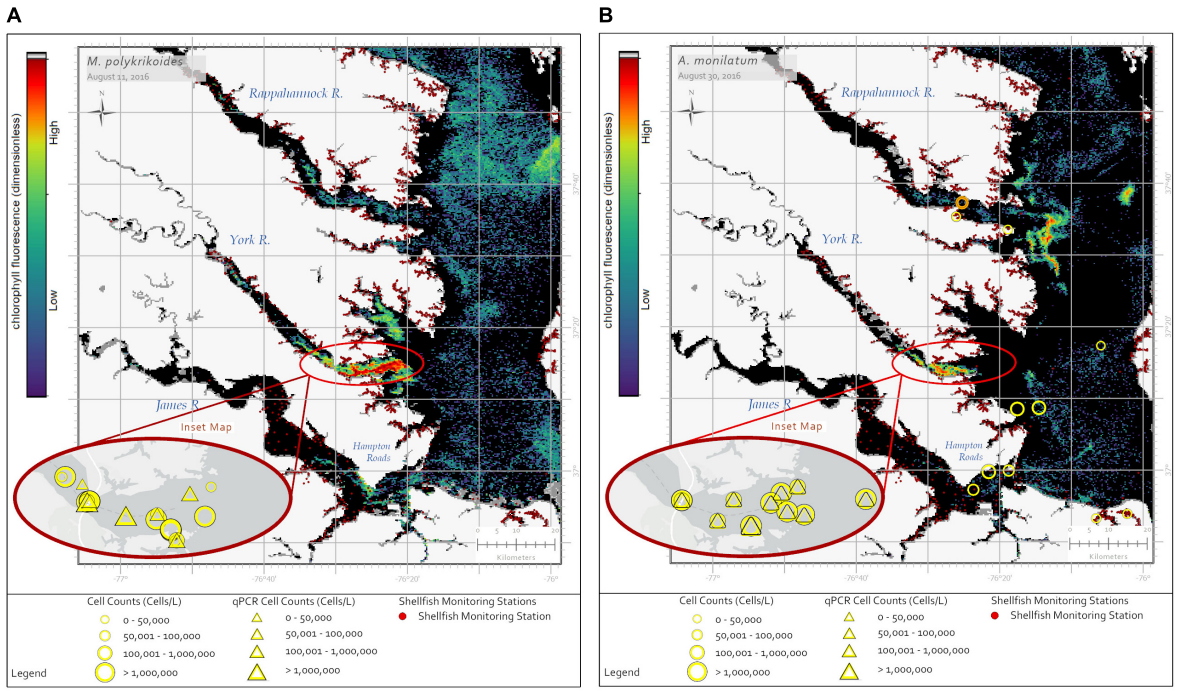

FIGURE 2 | Sentinel-3a OLCI images with RBD algorithm captured two dinoflagellate blooms in late summer 2016. **(A)** The image from August 11, 2016 shows a bloom of *M. polykrikoides* in the southern Chesapeake Bay with a concentrated bloom patch off the York River. Yellow circles show *in situ* cell concentration data obtained using light microscopy for water samples collected August 11–15, 2016. Yellow triangles represent cell concentrations measured using qPCR for the same date range. **(B)** The image from August 30, 2016 shows a bloom of *A. monilatum* in the Rappahannock, York, and James Rivers. Yellow circles show *in situ* cell concentration data obtained using light microscopy for water samples collected August 28 – September 02, 2016. Yellow triangles represent cell concentrations measured using qPCR for the same date range. Data from September 09, 2016 (orange circle) indicate *A. monilatum* was confirmed in the Rappahannock River a week later. Black pixels indicate no bloom detected. Yellow symbol size represents cell concentration ranges for *in situ* data. The dark red dots indicate shellfish growing area classification locations.

that returned from 665 nm, even though 681 nm also includes strong chl-*a* absorption. Near-surface blooms reflect the red-edge, 709 nm band, strongly. A weakly fluorescing bloom would combine a slight increase in 681 nm with a large increase at 709 nm, leading to identification with the CI algorithm.

Why might this occur with *K. veneficum* blooms? Field and laboratory studies need to be conducted with *K. veneficum* specifically, but Dower and Lucas (1993) and Gasol et al. (2016) suggested that photosynthetic irradiance measurements could provide information about spatial and temporal variability in light-dependent phytoplankton reactions. This information would aid in explaining the factors influencing the variability, including regionality and seasonality in environmental or growth conditions. Accordingly, at least four hypotheses could be considered when examining *K. veneficum* blooms with RBD and CI algorithms: heterotrophy vs. autotrophy, turbidity, seasonal light availability, and/or nutrient availability. *K. veneficum* blooms only fluoresce when cells are photosynthesizing and their optical characteristics change to a high-biomass, non-fluorescing algae under heterotrophic conditions. However, we cannot dismiss ecological considerations; *K. veneficum* blooms occur in high turbidity areas within Chesapeake Bay tributaries and may not receive enough light to emit excess photons as fluorescence. For example, on November 16, 2017 OLCI imagery showed a sediment plume [as shown by R_{rs}(665 nm)] from the Susquehanna River impacting the Bay's northwestern tributaries where the CI algorithm more accurately identified *K. veneficum* blooms (**Figures 3B,C**). Similarly, time of year could also be a factor due to light availability (low light near the winter solstice). **Figure 3A** shows an example where *K. veneficum* appears to be detected using the RBD algorithm in mid-spring (May); however, the CI algorithm was more useful in detecting it in late fall (November) when *Karlodinium* cells were documented to be actively feeding on cryptophytes (**Figure 3B**). Finally, the concentration and availability of nutrients may influence how *K. veneficum* cells respond to light. Gameiro et al. (2011) demonstrated that increased water column turbidity led to increased photosynthetic efficiency and low light-saturation photosynthetic rates in algal cells. Vonshak et al. (2000) showed an increase in photosynthetic efficiency when cultured algal cells were grown mixotrophically as opposed to phototrophically. Similarly, Skovgaard et al. (2000) showed that when the prey of the dinoflagellate *Fragilidium subglobosum* is abundant most of the carbon uptake occurs through mixotrophic feeding, not photosynthesis, even when photosynthetic irradiance is at sufficient levels. In a laboratory study with phototrophically grown *K. veneficum* cultures, Cui et al. (2017) showed that the capacity to dissipate excess light energy was correlated with

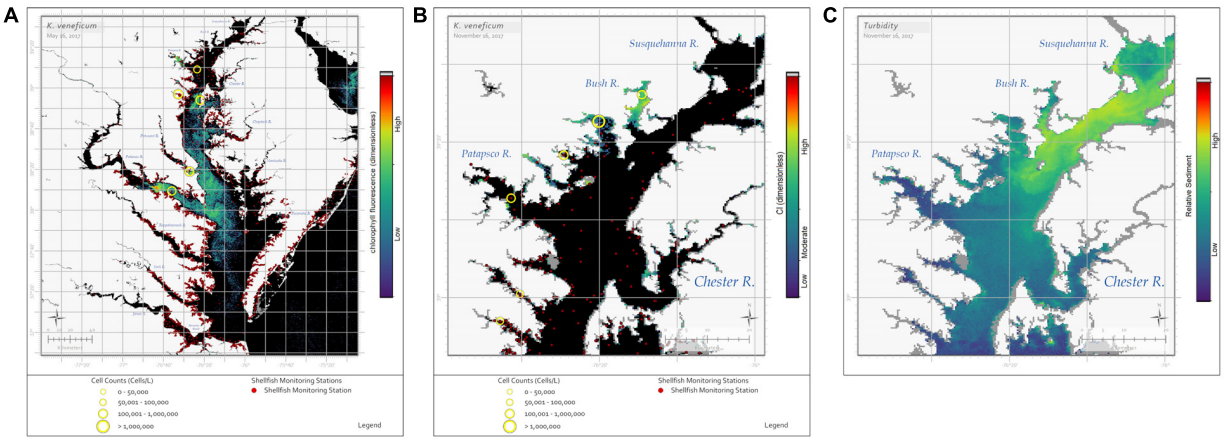

FIGURE 3 | Sentinel-3a OLCI images showing blooms of the dinoflagellate *K. veneficum*. **(A)** The RBD algorithm captured a bloom on May 16, 2017 throughout the Maryland portion of the Chesapeake Bay. Yellow circles indicate *in situ* cell concentrations determined using light microscopy for water samples collected on the same day, with symbol size representing cell concentration ranges. **(B)** The CI algorithm captured a bloom on November 16, 2017 in the Bush River, Maryland. Yellow circles indicate *in situ* cell concentrations determined using light microscopy for water samples collected November 13–16, 2017, with symbol size representing cell concentration ranges. *K. veneficum* cells in the Bush River bloom were documented to be actively feeding on cryptophyte prey. **(C)** The R_{rs}(665 nm) image from November 16, 2017 shows a sediment plume from the Susquehanna River, with warmer colors indicating higher sediment concentrations. Black pixels indicate no bloom detected. The dark red dots on **(A,B)** indicate shellfish growing area classification locations.

phosphorus concentrations; in Chesapeake Bay the availability of phosphorus varies seasonally (Li et al., 2017). If the cells' feeding state is a factor, it may be possible to use the visualization of the bloom with the RBD or CI algorithm to estimate high or low toxicity risks as *K. veneficum* is known to be more toxic when in a heterotrophic state (Adolf et al., 2008, 2009; Place et al., 2012).

Prorocentrum minimum

In his summary of 30 years of phytoplankton data, Marshall (1996) reported *P. minimum* as the most common dinoflagellate in the Chesapeake Bay. Reports of *P. minimum* blooms within Bay and tributary waters date back to the 1960s (Mackiernan, 1968). In a more recent analysis using Chesapeake Bay Program data, Li et al. (2015) determined that in the 1990s an average of 13 *P. minimum* blooms (cell concentrations $\geq 10^8$ cells·L^{-1}) were reported annually and in the 2000s this number increased to 23 blooms annually. While *P. minimum* is found throughout the year in the Bay and its tributaries when water temperatures are between 6–28°C and 5–14 salinity, blooms occur most frequently April through June when waters are between 13–19°C and 6–10 salinity (Marshall and Egerton, 2009a; Li et al., 2015). Recently, high biomass blooms (10^8 cells·L^{-1}) of *P. minimum* were documented in the Maryland portion of the Bay from December 2017 to January 2018 and again in December 2019 to January 2020 (**Figure 4**). Both Tango et al. (2005) and Marshall and Egerton (2009a) reported that the cell concentrations of *P. minimum* blooms were considerably greater in the 2000s (10^7–10^8 cells·L^{-1}) than in the 1980s and 1990s (10^6 cells·L^{-1}) and that temporally extensive blooms contributed to degraded water quality conditions, especially with regards to dissolved oxygen concentrations, which lead to finfish and shellfish mortalities and the loss of submerged aquatic vegetation due to decreased water clarity.

In short-term (2–3 days) laboratory exposure experiments, embryonic, juvenile, and adult oysters exposed to *P. minimum* concentrations $\leq 10^7$ cells·L^{-1} did not exhibit any negative impacts to growth or survival (Stoecker et al., 2008). Similarly, Brownlee et al. (2005, 2008) found that growth rates of oyster spat were comparable between *P. minimum* and a commercial hatchery food mix in both laboratory and field settings. However, Glibert et al. (2007) reported that at a cell concentration of 10^7 cells·L^{-1} *P. minimum* caused the mortality of days-old oysters after a 48 h exposure and reduced motility after 2-week-old oysters were exposed for 72 h. Tango et al. (2005) reported that a week-long *P. minimum* bloom in the lower Potomac River caused the mortality of 78% of juvenile oysters at an aquaculture facility. The different effects of *P. minimum* on shellfish has been hypothesized to be the result of the growth stage of the bloom, with blooms in decline to be more detrimental than those exponentially growing (Wikfors, 2005). If the stage of the bloom is as critical as monitoring for cell concentrations, then future remote sensing assets that offer greater spectral, temporal, and spatial coverage should aid the monitoring of *P. minimum* blooms within the framework of safeguarding aquaculture interests. As dinoflagellates tend to produce ultraviolet photo-protective mycosporine-like amino acids (MAAs), UV remote sensing from instruments like OCI on PACE may help in distinguishing these blooms and associated physiological effects (Korbee et al., 2010; Carreto et al., 2018).

Future Remote Sensing Strategies

In addition to distinguishing HABs that have unique spectral signatures, it may be possible to detect indicators of harmful species through other means, such as the unique optical signatures of prey and associated environmental monitoring. For example, multiple species within the heterotrophic genus

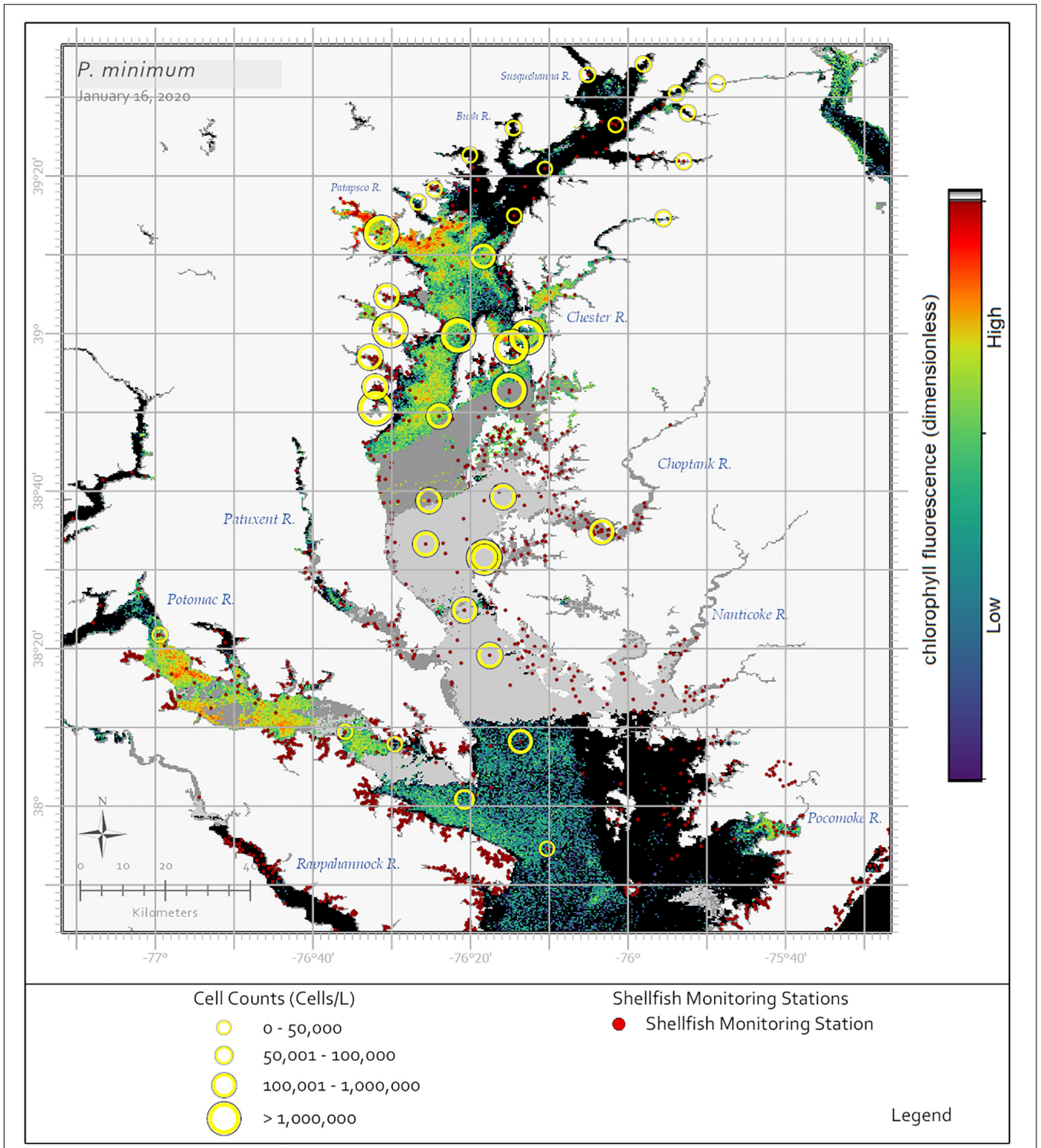

FIGURE 4 | Sentinel-3a OLCI image with RBD algorithm captured on January 16, 2020 showing a bloom of the dinoflagellate *P. minimum* throughout the Maryland portion of the Chesapeake Bay. *In situ* data indicated a widespread *P. minimum* bloom, however, the satellite ocean color data collected during this time were limited by cloud cover. Yellow circles indicate cell concentrations determined using light microscopy for samples collected January 13–16, 2020, with symbol size representing cell concentration ranges. Medium and dark gray pixels represent no retrievals due to clouds. Black pixels indicate no bloom detected. The dark red dots indicate shellfish growing area classification locations.

Dinophysis have been reported in the lower Chesapeake Bay since the late 1970s (Marshall, 1980, 1982). *Dinophysis* can produce OA and/or dinophysistoxins (DTXs), all of which contribute to DSP, a human illness consisting of severe vomiting, diarrhea, and abdominal pain shortly after the consumption of contaminated shellfish (Barceloux, 2008). The region's first *D. acuminata* bloom and precautionary shellfish harvesting area closure occurred in 2002 (Marshall et al., 2004; Tango et al., 2004). *Dinophysis* can be toxic at cell concentrations well below the limit of detection by satellite sensors (e.g., 200 cells·L^{-1} for *Dinophysis fortii*; Yasumoto et al., 1985). To date, the toxicity of *Dinophysis* spp. in Maryland and Virginia waters appears to be minimal compared to other regions (Wolny et al., 2020). However, there recently has been a precedent for blooms of these species to intensify in cell concentration and toxicity in New York and New England waters (Hattenrath-Lehmann et al., 2013, 2015; J. Deeds, unpublished data). This elevated human health risk necessitates a more robust monitoring system.

The use of ocean color imagery to visualize *Dinophysis* blooms directly for resource management applications is unlikely as these species can be highly toxic at low cell densities. The detection of *D. acuminata* within the phytoplankton community at the low concentrations it is typically found in the Chesapeake Bay region (average of 403 cells·L^{-1}; Wolny et al., 2020), may be aided by using its prey items as a proxy. *Dinophysis* prey, the ciliate *Mesodinium rubrum* which feeds on cryptophytes, has unique bio-optical properties (Guzmán et al., 2016) and can co-occur with *Dinophysis* in thin layers within the water column (González-Gil et al., 2010; Sjöqvist and Lindholm, 2011) or can form distinctive surface features (Dierssen et al., 2015; Guzmán et al., 2016). Because *M. rubrum* is found in Chesapeake Bay waters year-round (Johnson et al., 2013) detection of *M. rubrum* blooms with satellite imagery would have to be coupled with regionally tuned ecological models that characterize both the *Dinophysis* and *Mesodinium* population patterns observed in this region. Using the ecological patterns of *M. rubrum* blooms as predictive guidelines for *Dinophysis ovum* blooms has proven successful along the Texas coast (Harred and Campbell, 2014). Over the past two decades artificial neural networks, hydrodynamic and lagrangian models, as well as satellite-derived sea surface temperature (SST) data has been used to predict blooms of *Dinophysis* along the European Atlantic coast (Velo-Suárez and Gutiérrez-Estrada, 2007; Reguera et al., 2014; Díaz et al., 2016; Moita et al., 2016; Ruiz-Villarreal et al., 2016). Dierssen et al. (2015) demonstrated the successful use of the Hyperspectral Imager for the Coastal Ocean (HICO) that flew aboard the International Space Station from 2009 to 2014 to detect a bloom of *M. rubrum* in Long Island Sound, NY. The successful exploitation of future hyperspectral satellite missions to distinguish a HAB, such as *Dinophysis*, from above a background community in the optically complex Chesapeake Bay and to differentiate *M. rubrum* and cryptophytes from other phytoplankton constituents, will require a combination of efforts and many *in situ* observations for validation. Finer-scale oceanographic observations available through a combination of future satellite platforms may aid in the development of similar systems for the Chesapeake Bay that have proven beneficial in other waters.

SUMMARY

We have outlined emerging optical remote sensing techniques being used to identify the most common marine and estuarine HABs in the Chesapeake Bay. Although challenges remain, the methodology continues to improve with the implementation of new technology and the incorporation of ecological data either gathered from long-standing data archives (i.e., Chesapeake Bay Program, 2019) or in real-time (i.e., radiometry) as blooms occur. Utilizing remote sensing to its maximum potential is of increased importance as more frequent, potentially toxic blooms are projected to occur at the same time that the region's shellfish aquaculture industry is growing. Additionally, the state agencies that manage these resources need to increase their efficiencies in order to monitor these systems more often with fewer assets and funding. The launch of orbiting and geostationary satellites with hyperspectral sensors after 2022 could further enhance our ability to distinguish blooms and improve upon these efforts. The HAB detection and monitoring systems developed for the optically complex Chesapeake Bay have the potential to provide a framework for monitoring HABs in other bodies of water with mixed harmful algae assemblages, elevated turbidity, and frequent sediment plumes.

The preliminary use of the RBD algorithm to help guide state agencies in detecting and monitoring dinoflagellate blooms in the Chesapeake Bay has been presented here. Our cursory examination of other algorithms in the red-edge portion of the electromagnetic spectrum, such as the Algal Bloom Index (ABI; Hu and Feng, 2016), which is another algorithm that includes fluorescence, and Maximum Peak Height (MPH) chlorophyll (Matthews and Odermatt, 2015) indicates that RBD is more useful at delineating these blooms when they are fluorescing. The RBD, as a fluorescence algorithm, requires algae to fluoresce to be detected, so false negatives are possible for blooms that are not fluorescing. Additionally, while the RBD algorithm is successful in detecting large biomass blooms, mismatches between *in situ* data and satellite imagery have occurred (e.g., within the August 2016 *A. monilatum* bloom, **Figure 2B**). This is also visible in the variability in the slope between 665 and 681 nm in **Figure 1**, indicative of the RBD algorithm. Patchiness of these dinoflagellate blooms (Mackiernan, 1968; Marshall and Egerton, 2009a; Mulholland et al., 2009) or sub-pixel variability, coupled with tidal flow and the difference between the time of *in situ* data collection and satellite overpass may be causing these discrepancies. More work will need to be done to determine the frequency of these mismatches in shellfish aquaculture areas. Numerous studies have shown the utility and statistical rigor of determining cell concentrations using qPCR compared to other visual detection methods for the HAB species presented here (e.g., Handy et al., 2008; Eckford-Soper and Daugbjerg, 2015; Lee et al., 2017; Vandersea et al., 2017). Our

preliminary assessment of *A. monilatum* and *M. polykrikoides in situ* cell concentrations collected using both qPCR and light microscopy versus relative cell abundance determined from pixel retrievals shows promise for the algorithms under development. This review highlights current uses of the RBD algorithm for fluorescing algal blooms in the Chesapeake Bay. A more rigorous analysis is underway to determine the success of the method for not only detecting, but for quantifying these HABs.

Higher spatial resolution can be of value in smaller tributaries. The Multispectral Imager (MSI) on the Sentinel-2 satellites has some red-edge bands, with 20 m pixels and 5-day repeat but is potentially glint-limited in summer, when the majority of Chesapeake Bay HABs occur. Landsat-8, while having 30 m pixels, has only 16-day repeat, and only one red band, greatly limiting its value for monitoring blooms. The MSI does not have a band at the chl-*a* fluorescence peak, but other red-edge algorithms have been applied to the MSI data. Algorithms, such as the ratio of 704–665 nm (Gilerson et al., 2010) and a form of the MCI from Gower et al. (2008), can be applied to Sentinel-2/MSI data and have the potential for identifying high biomass blooms in Chesapeake Bay. Gernez et al. (2017) demonstrated how satellite data could be used to monitor shellfish health through a unique application of suspended particulate matter and chl-*a* algorithms to Sentinel-2 imagery. The resulting model allowed the effects of tide-driven dynamics on oyster feeding rates to be examined in Bourgneuf Bay, along the French Atlantic coast. Further validation studies of these various approaches and the utility of higher spatial resolution (20 m) Sentinel-2 products are warranted to provide increased monitoring into narrower portions of Chesapeake Bay tributaries where aquaculture operations often occur. A key question for future research will be to determine the minimum algal cell concentrations that can be detected with these different algorithms.

The CI algorithm has also been proposed as a way to detect weakly fluorescing blooms, which occasionally occur in Chesapeake Bay estuarine waters. A more rigorous validation to determine accuracy in detection and a detailed comparison with these other algorithms is underway. It is possible that an ensemble approach, including turbidity, SST, and salinity, may provide improved bloom separation during scenarios when algal cells are weakly fluorescing and the RBD algorithm fails. In addition, these other algorithms are being investigated to provide general chlorophyll concentration information for the Bay as the currently available ocean color algorithms are insufficient in these complex waters.

While many of the high-biomass algal blooms in the optically complex Chesapeake Bay are detected with OLCI image products, such as the RBD and CI, further discrimination to genus or species level is unlikely with current satellite-derived products. The alternative is to combine ecological associations (i.e., salinity/temperature regimes, nutrient preferences, time of year, and location within Chesapeake Bay), with near real-time daily satellite imagery. This combination would allow us to develop a monitoring system for individual blooms across the Bay. Such an approach was developed to detect *K. brevis* blooms along the Florida West Coast (Stumpf et al., 2003), where seasonality and geography were combined with an algorithm for bloom detection. Habitat models are also being applied for *Pseudo-nitzschia* blooms and domoic acid events in California (Anderson et al., 2011, 2016) and are likely suitable for some HAB species found in Chesapeake Bay (Brown et al., 2013). The output of these heuristic (rule-based) models can be further combined with remote-sensing products to develop a classified product for individual blooms. Therefore, future work will investigate combinations of model outputs and remote-sensing products that could provide resource managers and the shellfish industry a method to monitor a suite of potentially harmful species throughout Chesapeake Bay. The launch of satellites with hyperspectral sensors after 2022 will further enhance these efforts.

DATA AVAILABILITY STATEMENT

The datasets generated for this study are available on request to the corresponding author.

AUTHOR CONTRIBUTIONS

JW, TE, JM, GS, and KR participated in the collection and analysis of field and laboratory *in situ* data. MT, SS, AM, and RS participated in the analysis and presentation of ocean color satellite data. JW, MT, and SS wrote the first draft of the manuscript. All authors contributed to manuscript revisions and approved the submitted version.

FUNDING

Support for data collection was provided by the Virginia Department of Environmental Quality (Grant #16879), Virginia Department of Health (Grants #VIMSHAB617 and #VDH-20-102-0046), and through the NOAA ECOHAB grant #NA17NOS4780182 to KR (VIMS). This is VIMS contribution #3896 and ECOHAB contribution #958.

ACKNOWLEDGMENTS

In memory of Hunter M. Horn (1994–2020), MDNR colleague and friend.

We gratefully acknowledge Ann McManus (MDE) for her assistance with creating the satellite image figures. James Bailey and Kerry Maguire (MDNR) were invaluable in providing *in situ* data and data management. Field staff at MDNR, MDE, ODU, VDH, VDEQ, and VIMS are thanked for their efforts to collect and process bloom samples. Thoughtful input from two peer reviewers and Amy Hamilton (MDNR) helped to improve this manuscript. We also acknowledge the support of the NASA Earth Science Division and collaborations developed through the Interagency Chesapeake Bay Group hosted at NASA GSFC.

REFERENCES

Adolf, J. E., Bachvaroff, T. R., and Place, A. R. (2008). Can cryptophyte abundance trigger toxic *Karlodinium veneficum* blooms in eutrophic estuaries? *Harmful Algae* 8, 119–128.

Adolf, J. E., Bachvaroff, T. R., and Place, A. R. (2009). Environmental modulation of karlotoxin levels in strains of the cosmopolitan dinoflagellate, *Karlodinium veneficum* (Dinophyceae). *J. Phycol.* 45, 176–192. doi: 10.1111/j.1529-8817.2008.00641.x

Amin, R., Zhou, J., Gilerson, A., Moshary, F., and Ahmed, S. (2009). Novel optical techniques for detecting and classifying toxic dinoflagellate *Karenia brevis* blooms using satellite imagery. *Opt. Express* 17, 9126–9144. doi: 10.1364/oe.17.009126

Anderson, C. R., Kudela, R. M., Benitez-Nelson, C., Sekula-Wood, E., Burrell, C. T., Chao, Y., et al. (2011). Detecting toxic diatom blooms from ocean color and a regional ocean model. *Geophys. Res. Lett.* 38:LO4603. doi: 10.1029/2010GL045858

Anderson, C. R., Kudela, R. M., Kahru, M., Chao, Y., Rosenfeld, L. K., Bahr, F. L., et al. (2016). Initial skill assessment of the California harmful algae risk mapping (C-HARM) System. *Harmful Algae* 59, 1–18. doi: 10.1016/j.hal.2016.08.006

Anderson, D. M., Cembella, A. D., and Hallegraeff, G. M. (2012). Progress in understanding harmful algal blooms (HABs): paradigm shifts and new technologies for research, monitoring and management. *Ann. Rev. Mar. Sci.* 4, 143–176. doi: 10.1146/annurev-marine-120308-081121

Barceloux, D. G. (2008). "Diarrhetic shellfish poisoning and okadaic acid," in *Medical Toxicology of Natural Substances: Foods, Fungi, Medicinal Herbs, Plants, and Venomous Animals*. Hoboken, NJ: John Wiley & Sons, 222–226.

Blough, N. V., and Del Vecchio, R. (2002). "Chromophoric DOM in the coastal environment," in *Biogeochemistry of Marine Dissolved Organic Matter*, eds D. A. Hansell and C. A. Carlson (San Diego, CA: Academic Press), 509–545.

Brown, C. W., Hood, R. R., Long, W., Jacobs, J., Ramers, D. L., Wazniak, C., et al. (2013). Ecological forecasting in Chesapeake Bay: using a mechanistic-empirical modeling approach. *J. Mar. Syst.* 125, 113–125.

Brownlee, E. F., Sellner, S. G., and Sellner, K. G. (2005). *Prorocentrum minimum* blooms: potential impacts on dissolved oxygen and Chesapeake Bay oyster settlement and growth. *Harmful Algae* 4, 593–602.

Brownlee, E. F., Sellner, S. G., Sellner, K. G., Nonogaki, H., Adolf, J. E., Bachvaroff, T. R., et al. (2008). Responses of *Crassostrea virginica* (Gmelin) and *C. ariakensis* (Fujita) to bloom-forming phytoplankton including ichthyotoxic *Karlodinium veneficum* (Ballantine). *J. Shellfish Res.* 27, 581–591.

Cannizzaro, J. P., Carder, K. L., Chen, F. R., Heil, C. A., and Vargo, G. A. (2008). A novel technique for detection of the toxic dinoflagellate, *Karenia brevis*, in the Gulf of Mexico from remotely sensed ocean color data. *Cont. Shelf. Res.* 28, 137–158.

Carnegie, R. B., and Burreson, E. M. (2011). Declining impact of an introduced pathogen: *Haplosporidium nelsoni* in the oyster *Crassostrea virginica* in Chesapeake Bay. *Mar. Ecol. Prog. Ser.* 432, 1–5.

Carreto, J. I., Carignan, M. O., Montoya, N. G., Cozzolino, E., and Akselman, R. (2018). Mycosporine-like amino acids and xanthophyll-cycle pigments favour a massive spring bloom development of the dinoflagellate *Prorocentrum minimum* in Grande Bay (Argentina), an ozone hole affected area. *J. Mar. Syst.* 178, 15–28.

Catlett, D., and Siegel, D. A. (2018). Phytoplankton pigment communities can be modeled using unique relationships with spectral absorption signatures in a dynamic coastal environment. *J. Geophys. Res. Oceans* 123, 246–264.

Chesapeake Bay Program (2019). *Baywide CBP Plankton Database*. Available online at: https://www.chesapeakebay.net/what/downloads/baywide_cbp_plankton_database (accessed November, 3 2019).

Chrost, R. H., and Faust, M. A. (1983). Organic carbon release by phytoplankton: its composition and utilization by bacterioplankton. *J. Plankton Res.* 5, 477–493.

Clark, J. M., Schaeffer, B. A., Darling, J. A., Urquhart, E. A., Johnston, J. M., Ignatius, A. R., et al. (2017). Satellite monitoring of cyanobacterial harmful algal bloom frequency in recreational waters and drinking water sources. *Ecol. Indic.* 80, 84–95. doi: 10.1016/j.ecolind.2017.04.046

Cui, Y., Zhang, H., and Lin, S. (2017). Enhancement of non-photochemical quenching as an adaptive strategy under phosphorus deprivation in the dinoflagellate *Karlodinium veneficum*. *Front. Microbiol.* 8:404. doi: 10.3389/fmicb.2017.00404

Davidson, J., Mateus, M., Reguera, B., Silke, J., and Sourisseau, M. (2016). Applied simulations and integrated modelling for the understanding of toxic and harmful algal blooms (ASIMUTH). *Harmful Algae* 53, 1–166. doi: 10.1016/j.hal.2015.11.006

Deeds, J. R., Reimschuessel, R., and Place, A. R. (2006). Histophathological effects in fish exposed to the toxins from *Karlodinium micrum*. *J. Aquat. Anim. Health* 18, 136–148.

Deeds, J. R., Terlizzi, D. E., Adolf, J. E., Stoecker, D. K., and Place, A. R. (2002). Toxic activity from cultures of *Karlodinium micrum* (=*Gyrodinium galatheanum*) (Dinophyceae) – a dinoflagellate associated with fish mortalities in an estuarine aquaculture facility. *Harmful Algae* 1, 169–189.

Díaz, P. A., Ruiz-Villarreal, M., Pazos, Y., Moita, M. T., and Reguera, B. (2016). Climate variability and *Dinophysis acuta* blooms in an upwelling system. *Harmful Algae* 53, 145–159. doi: 10.1016/j.hal.2015.11.007

Dierssen, H., McManus, G. B., Chlus, A., Qiu, D., Gao, B.-C., and Lin, S. (2015). Space station image captures a red tide ciliate bloom at high spectral and spatial resolution. *Proc. Natl. Acad. Sci. U.S.A.* 112, 14783–14787. doi: 10.1073/pnas.1512538112

Dower, K. M., and Lucas, M. I. (1993). Photosynthesis-irradiance relationships and production associated with a warm-core ring shed from the Agulhas Retroflection south of Africa. *Mar. Ecol. Prog. Ser.* 95, 141–154.

Eckford-Soper, L. K., and Daugbjerg, N. (2015). Development of a multiplex real-time qPCR assay for simultaneous enumeration of up to four marine toxic bloom-forming microalgal species. *Harmful Algae* 48, 37–43. doi: 10.1016/j.hal.2015.06.009

Fu, F. X., Place, A. R., Garcia, N. S., and Hutchins, D. A. (2010). CO_2 and phosphate availability control the toxicity of the harmful bloom dinoflagellate *Karlodinium veneficum*. *Aquat. Microb. Ecol.* 59, 55–65.

Galimany, E., Place, A. R., Ramón, M., Jutson, M., and Pipe, R. K. (2008). The effects of feeding *Karlodinium veneficum* (PLY #103; *Gymnodinium veneficum* Ballantine) to the blue mussel *Mytilus edulis*. *Harmful Algae* 7, 91–98.

Gameiro, C., Zwolinski, J., and Brotas, V. (2011). Light control on phytoplankton production in a shallow and turbid estuarine system. *Hydrobiologia* 669, 249–263.

Gasol, J. M., Cardelús, C., Morán, X. A. G., Balagué, V., Forn, I., Marrasé, C., et al. (2016). Seasonal patterns in phytoplankton photosynthetic parameters and primary production at a coastal NW Mediterranean site. *Sci. Mar.* 80S1, 63–77.

Gernez, P., Doxaran, D., and Barille, L. (2017). Shellfish aquaculture from space: potential of Sentinel2 to monitor tide-driven changes in turbidity, chlorophyll concentrations and oyster physiological response at the scale of an oyster farm. *Front. Mar. Sci.* 4:137. doi: 10.3389/fmars.2017.00137

Gilerson, A. A., Zhou, J., Gurlin, D., Moses, W., Iannou, I., and Ahmed, S. (2010). Algorithms for remote estimation of chlorophyll-a in coastal and inland waters using red and near infrared bands. *Opt. Express* 18, 24109–24124. doi: 10.1364/OE.18.024109

Glaspie, C. N., Seitz, R. D., Ogburn, M. B., Dungan, C. F., and Hines, A. H. (2018). Impacts of habitat, predators, recruitment, and disease on soft-shell clams *Mya arenaria* and stout razor clams *Tagelus plebeius* in Chesapeake Bay. *Mar. Ecol. Prog. Ser.* 603, 117–133.

Glibert, P. M., Alexander, J., Meritt, D. M., North, E. W., and Stoecker, D. K. (2007). Harmful algae pose additional challenges for oyster restoration: impacts of the harmful algae *Karlodinium veneficum* and *Prorocentrum minimum* on early life stages of the oyster *Crassostrea virginica* and *Crassostrea ariakensis*. *J. Shellfish Res.* 26, 919–925.

González-Gil, S., Velo-Suárez, L., Gentien, P., Ramilo, I., and Reguera, B. (2010). Phytoplankton assemblages and characterization of a *Dinophysis acuminata* population during an upwelling-downwelling cycle. *Aquat. Microb. Ecol.* 58, 273–286. doi: 10.3354/ame01372

Gordon, H. R., Clark, D. K., Brown, J. W., Brown, O. B., Evans, R. H., and Broenkow, W. W. (1983). Phytoplankton pigment concentrations in the Middle Atlantic Bight: comparison of ship determinations and CZCS estimates. *Appl. Opt.* 22, 20–36. doi: 10.1364/ao.22.000020

Gower, J., King, S., and Goncalves, P. (2008). Global monitoring of plankton blooms using MERIS MCI. *Int. J. Remote Sens.* 29, 6209–6216.

Grabowski, J. H., Brumbaugh, R. D., Conrad, R. F., Keeler, A. G., Opaluch, J. J., Peterson, C. H., et al. (2012). Economic valuation of ecosystem services

provided by oyster reefs. *Bioscience* 62, 900–909. doi: 10.1371/journal.pone.0167694

Griffith, A. W., and Gobler, C. J. (2016). Temperature controls the toxicity of the ichthyotoxic dinoflagellate *Cochlodinium polykrikoides*. *Mar. Ecol. Prog. Ser.* 545, 63–76.

Griffith, A. W., and Gobler, C. J. (2020). Harmful algal blooms: a climate change co-stressor in marine and freshwater ecosystems. *Harmful Algae* 91:101590. doi: 10.1016/j.hal.2019.03.008

Griffith, A. W., Shumway, S. E., and Gobler, C. J. (2019). Differential mortality of North Atlantic bivalve molluscs during harmful algal blooms caused by the dinoflagellate, *Cochlodinium* (a.k.a. *Margalefidinium*) *polykrikoides*. *Estuar. Coast.* 42, 190–203.

Guzmán, L., Varela, R., Muller-Karger, F., and Lorenzoni, L. (2016). Bio-optical characteristics of a red tide induced by *Mesodinium rubrum* in the Cariaco Basin. *Venezuela. J. Marine Syst.* 160, 17–25.

Haddaway-Riccio, J. (2019). *Maryland Oyster Management Plan*. Annapolis, MD: Maryland Department of Natural Resources Report No. 17-012319-117. 93.

Hall, N. S., Litaker, R. W., Fensin, E., Adolf, J. E., Bowers, H. A., Place, A. R., et al. (2008). Environmental factors contributing to the development and demise of a toxic dinoflagellate (*Karlodinium veneficum*) bloom in a shallow, eutrophic, lagoonal estuary. *Estuar. Coast.* 31, 402–418.

Handy, S. M., Demir, E., Hutchins, D. A., Portune, K. J., Whereat, E. B., Hare, C. E., et al. (2008). Using quantitative real-time PCR to study competition and community dynamics among Delaware Inland Bays harmful algae in field and laboratory studies. *Harmful Algae* 7, 599–613.

Harding, J. M., Mann, R., Moeller, P., and Hsia, M. (2009). Mortality of the veined rapa whelk, *Rapana venosa*, in relation to a bloom of *Alexandrium monilatum* in the York River, United States. *J. Shellfish Res.* 28, 363–367.

Harding, L. W., Mallonee, M. E., Perry, E. S., Miller, W. D., Adolf, J. E., Gallegos, C. L., et al. (2019). Long-term trends, current status, and transitions of water quality in Chesapeake Bay. *Sci. Rep*. 9:6709. doi: 10.1038/s41598-019-43036-6

Harred, L. B., and Campbell, L. (2014). Predicting harmful algal blooms: a case study with *Dinophysis ovum* in the Gulf of Mexico. *J. Plankton Res.* 36, 1434–1445.

Hattenrath-Lehmann, T. K., Marcoval, M. A., Berry, D. L., Fire, S., Wang, Z., Morton, S. L., et al. (2013). The emergence of *Dinophysis acuminata* blooms and DSP toxins in shellfish in New York waters. *Harmful Algae* 26, 33–44.

Hattenrath-Lehmann, T. K., Marcoval, M. A., Mittlesdorf, H., Goleski, J. A., Wang, Z., Haynes, B., et al. (2015). Nitrogenous nutrients promote the growth and toxicity of *Dinophysis acuminata* during estuarine bloom events. *PLoS One* 10:e0124148. doi: 10.1371/journal.pone.0124148

Heil, D. C. (2009). *Karenia brevis* monitoring, management, and mitigation for Florida molluscan shellfish harvesting areas. *Harmful Algae* 8, 608–610.

Hicks, R. L., Haab, T. C., and Lipton, D. (2004). *The Economic Benefits of Oyster Reef Restoration in the Chesapeake Bay*. Annapolis, MD: Chesapeake Bay Foundation. 113.

Hu, C., and Feng, L. (2016). Modified MODIS fluorescence line height data product to improve image interpretation for red tide monitoring in the eastern Gulf of Mexico. *J. Appl. Remote Sens.* 11:012003. doi: 10.1117/1.JRS.11.012003

Hu, C., Muller-Karger, F. E., Taylor, C. J., Carder, K. L., Kelble, C., Johns, E., et al. (2005). Red tide detection and tracing using MODIS fluorescence data: a regional example in SW Florida coastal waters. *Remote Sens. Environ.* 97, 311–321.

Hudson, K. (2019). *Virginia Shellfish Aquaculture Situation and Outlook Report: Results of the 2018 Virginia Shellfish Aquaculture Crop Reporting Survey*. VIMS Marine Resource Report No. 2019-8. Gloucester Point, VA: Virginia Sea Grant. 20.

Interstate Shellfish Sanitation Commission [ISSC] (2016). *ISSC Priorities to Improve Shellfish Monitoring for Harmful Algal Bloom Toxins*. Available online at: http://www.issc.org/harmfulalgaebloominformation (accessed November 3, 2019).

Johnson, M. D., Stoecker, D. K., and Marshall, H. G. (2013). Seasonal dynamics of *Mesodinium rubrum* in Chesapeake Bay. *J. Plankton Res.* 35, 877–893.

Kemp, W. M., Boynton, W. R., Adolf, J. E., Boesch, D. F., Boicourt, W. C., Brusch, G., et al. (2005). Eutrophication of Chesapeake Bay: historical trends and ecological interactions. *Mar. Ecol. Prog. Ser.* 303, 1–29.

Kennedy, V. S., Breitburg, D. L., Christman, M. C., Luckenbach, M. W., Paynter, K., Kramer, J., et al. (2011). Lessons learned from efforts to restore oyster populations in Maryland and Virginia, 1990-2007. *J. Shellfish Res.* 30, 719–731.

Kobell, R. (2017). Bay's oyster aquaculture harvest closing in on wild fishery. *Bay J.* 27:17224.

Korbee, N., Mata, M. T., and Figueroa, F. L. (2010). Photoprotection mechanisms against ultraviolet radiation in *Heterocapsa* sp. (Dinophyceae) are influenced by nitrogen availability: Mycosporine-like amino acids vs. xanthophyll cycle. *Limnol. Oceanogr.* 55, 899–908.

Kudela, R. M., and Gobler, C. J. (2012). Harmful dinoflagellate blooms caused by *Cochlodinium* sp.: Global expansion and ecological strategies facilitating bloom formation. *Harmful Algae* 14, 71–86.

Kudela, R. M., Ryan, J. P., Blakely, M. D., Lane, J. Q., and Peterson, T. D. (2008). Linking the physiology and ecology of *Cochlodinium* to better understand harmful algal bloom events: a comparative approach. *Harmful Algae* 7, 278–292.

Lee, S. Y., Jeong, H. J., Seong, K. A., Lim, A. S., Kim, J. H., Lee, K. H., et al. (2017). Improved real-time PCR method for quantification of the abundance of all known ribotypes of the ichthyotoxic dinoflagellate *Cochlodinium polykrikoides* by comparing 4 different preparation methods. *Harmful Algae* 63, 23–31. doi: 10.1016/j.hal.2017.01.006

Li, A., Stoecker, D. K., and Coats, D. W. (2000). Spatial and temporal aspects of *Gyrodinium galatheanum* in Chesapeake Bay: distribution and mixotrophy. *J. Plankton Res.* 22, 2105–2124.

Li, J., Bai, Y., Bear, K., Joshi, S., and Jaisi, D. (2017). Phosphorus availability and turnover in the Chesapeake Bay: insights from nutrient stoichiometry and phosphate oxygen isotope ratios. *J. Geophys. Res. Biogeol.* 122, 811–824.

Li, J., Glibert, P. M., and Gao, Y. (2015). Temporal and spatial changes in Chesapeake Bay water quality and relationships to *Prorocentrum minimum*, *Karlodinium veneficum*, and CyanoHAB events, 1991-2008. *Harmful Algae* 42, 1–14.

Lin, C. H. M., Accoroni, S., and Glibert, P. M. (2017). *Karlodinium veneficum* feeding responses and effects on larvae of the eastern oyster *Crassostrea virginica* under variable nitrogen:phosphorus stoichiometry. *Aquat. Microb. Ecol.* 79, 101–114.

Lunetta, R. S., Schaeffer, B. A., Stumpf, R. P., Keith, D., Jacobs, S. A., and Murphy, M. S. (2015). Evaluation of cyanobacteria cell count detection derived from MERIS imagery across the eastern USA. *Remote Sens. Environ.* 157, 24–34.

Mackiernan, G. B. (1968). *Seasonal Distribution of Dinoflagellates in the Lower York River, Virginia*. M.A. Thesis, William & Mary, Williamsburg, VA, 104.

Mann, R. (2000). Restoring the oyster reef communities in the Chesapeake Bay: a commentary. *J. Shellfish Res.* 19, 335–339.

Marshall, H., and Alden, R. (1990). A comparison of phytoplankton assemblages and environmental relationships in three estuarine rivers of the lower Chesapeake Bay. *Estuaries* 13, 287–300.

Marshall, H. G. (1980). Phytoplankton composition in the lower Chesapeake Bay and Old Plantation Creek, Cape Charles, Virginia. *Estuaries* 3, 207–216.

Marshall, H. G. (1982). The composition of phytoplankton within the Chesapeake Bay Plume and adjacent waters off the Virginia coast, USA. *Estuar. Coast. Shelf Sci.* 15, 29–43.

Marshall, H. G. (1996). Toxin producing phytoplankton in Chesapeake Bay VA. *J. Sci.* 47, 29–37.

Marshall, H. G., Burchardt, L., and Lacouture, R. (2005). A review of phytoplankton composition within Chesapeake Bay and its tidal estuaries. *J. Plankton Res.* 27, 1083–1102.

Marshall, H. G., Egerton, T., Stem, T., Hicks, J., and Kokocinski, M. (2004). "Extended bloom concentration of the toxic dinoflagellate *Dinophysis acuminata* in Virginia estuaries during late winter through early spring 2002," in *Harmful Algae 2002*, eds K. A. Steidinger, J. H. Landsberg, C. R. Tomas, and G. A. Vargo (Tallahassee, FL: Florida Fish and Wildlife Conservation Commission), 364–366.

Marshall, H. G., and Egerton, T. A. (2009a). "Increasing occurrence and development of potentially harmful algal blooms in Virginia tidal rivers," in *Proceedings of the Water Resources in Changing Climates. Virginia Water Research Conference October 15-16, 2009*, ed. P. Fay (Virginia: Virginia Polytechnic Institute and State University), 89–99.

Marshall, H. G., and Egerton, T. A. (2009b). Phytoplankton blooms: their occurrence and composition within Virginia's tidal tributaries. *VA. J. Sci.* 60, 149–164.

Marshall, H. G., Lane, M. F., Nesius, K. K., and Burchardt, L. (2009). Assessment and significance of phytoplankton species composition within Chesapeake Bay and Virginia tributaries through a long-term monitoring program. *Environ. Monit. Assess.* 150, 143–155. doi: 10.1007/s10661-008-0680-0

Matthews, M. W., and Odermatt, D. (2015). Improved algorithm for routine monitoring of cyanobacteria and eutrophication in inland and near-coastal waters. *Remote Sens. Environ.* 156, 374–382.

May, S. P., Burkholder, J. M., Shumway, S. E., Hegaret, H., Wikfors, G. H., and Frank, D. (2010). Effects of the toxic dinoflagellate *Alexandrium monilatum* on survival, grazing and behavioral response of three ecologically important bivalve molluscs. *Harmful Algae* 9, 281–293.

Miller, W. D., and Harding, L. W. Jr. (2007). Climate forcing of the spring bloom in Chesapeake Bay. *Mar. Ecol. Prog. Ser.* 331, 11–22.

Moita, M. T., Pazos, Y., Rocha, C., Nolasco, R., and Oliveira, P. B. (2016). Towards predicting *Dinophysis* blooms off NW Iberia: a decade of events. *Harmful Algae* 52, 17–32. doi: 10.1016/j.hal.2015.12.002

Morse, R. E., Mulholland, M. R., Egerton, T. A., and Marshall, H. G. (2014). Phytoplankton and nutrient dynamics in a tidally dominated eutrophic estuary: daily variability and controls on bloom formation. *Mar. Ecol. Prog. Ser.* 503, 59–74.

Mulholland, M. R., Morse, R., Egerton, T., Bernhardt, P. W., and Filippino, K. C. (2018). Blooms of dinoflagellate mixotrophs in a lower Chesapeake Bay tributary: carbon and nitrogen uptake over diurnal, seasonal, and interannual timescales. *Estuar. Coast.* 41, 1744–1765.

Mulholland, M. R., Morse, R. E., Boneillo, G. E., Bernhardt, P. W., Filippino, K. C., Procise, L. A., et al. (2009). Understanding causes and impacts of the dinoflagellate, *Cochlodinium polykrikoides*, blooms in the Chesapeake Bay. *Estuar. Coast.* 32, 734–747.

Najjar, G., Pyke, C. R., Adams, M. B., Breitburg, D., Hershner, C., Kemp, M., et al. (2010). Potential climate-change impacts on the Chesapeake Bay. *Estuar. Coast. Shelf Sci.* 86, 1–20.

National Academies of Sciences, Engineering, and Medicine [NASEM] (2018). *Thriving on Our Changing Planet: A Decadal Strategy for Earth Observation from Space*. Washington, DC: The National Academies Press, doi: 10.17226/24938

National Aeronautics and Space Administration [NASA] (2019). *NASA Targets Coastal Ecosystems with New Space Sensor, NASA Press Release, 1 Aug. 2019*. Available online at: https://www.nasa.gov/press-release/nasa-targets-coastal-ecosystems-with-new-space-sensor (accessed October 21, 2019).

National Aeronautics and Space Administration Goddard Space Flight Center [NASA GSFC] (2018). *Interagency Workshop on Societal Applications of Satellite Data for the Chesapeake Bay*. Available online at: https://science.gsfc.nasa.gov/610/applied-sciences/chesapeake_bay_workshop.html (accessed November 28, 2019).

National Aeronautics and Space Administration Goddard Space Flight Center [NASA GSFC] (2019). *Interagency Chesapeake Bay Water Quality Modelling Workshop*. Available online at: https://science.gsfc.nasa.gov/610/applied-sciences/chesapeake_bay_modeling_workshop.html (accessed November 28, 2019).

National Shellfish Sanitation Program [NSSP] (2017). *Guide for the Control of Molluscan Shellfish 2017 Revision*. Available online at: http://www.fda.gov/Food/GuidanceRegulation/FederalStateFoodPrograms/ucm2006754.htm (accessed November 3, 2019).

Oesterling, M., and Luckenbach, M. (2008). *Best Management Practices for the Virginia Shellfish Culture Industry*. Marine Resource Report No. 2008-10. Silver Spring, MA: NOAA, 12.

Ohio Environmental Protection Agency [Ohio EPA] (2019). *Public Water System Harmful Algal Bloom Response Strategy*. Available online at: https://epa.ohio.gov/Portals/28/documents/habs/2019-PWS-HAB-Response-Strategy.pdf (accessed November 4, 2019).

Pease, S. K. (2016). *Alexandrium monilatum in the Lower Chesapeake Bay: Sediment Cyst Distribution and Potential Health Impacts on Crassostrea virginica*. Master's Thesis, William & Mary, Williamsburg, VA, 158.

Philpot, W. D. (1991). The derivative ratio algorithm: avoiding atmospheric effects in remote sensing. *IEEE Trans. Geosci. Remote Sens.* 29, 350–357.

Place, A. R., Bowers, H. A., Bachvaroff, T. R., Adolf, J. E., Deeds, J. R., and Sheng, J. (2012). *Karlodinium veneficum*—The little dinoflagellate with a big bite. *Harmful Algae* 14, 179–195.

Place, A. R., Munday, R., and Munday, J. S. (2014). Acute toxicity of karlotoxins to mice. *Toxicon* 90, 184–190. doi: 10.1016/j.toxicon.2014.08.003

Powell, E. N., Klinck, J. M., Ashton-Alcox, K., Hofmann, E. F., and Morson, J. (2012). The rise and fall of *Crassostrea virginica* oyster reefs: the role of disease and fishing in their demise and a vignette on their management. *J. Mar. Res.* 70, 505–558.

Reguera, B., Velo-Suárez, L., Raine, R., and Park, M. G. (2014). Harmful *Dinophysis* species: a review. *Harmful Algae* 14, 87–106.

Reidmiller, D. R., Avery, C. W., Easterling, D. R., Kunkel, K. E., Lewis, K. L. M., Maycock, T. K., et al. (2018). *Impacts, Risks, and Adaptation in the United States: Fourth National Climate Assessment, U.S.* Washington, DC: Global Change Research Program, doi: 10.7930/NCA4.2018

Robison, C. L. (2019). *Impacts of Margalefidinium polykrikoides and Alexandrium monilatum on oysters cultured in lower Chesapeake Bay*. Master's Thesis, William & Mary, Williamsburg, VA, 103.

Roegner, G. C., and Mann, R. (1991). "Hard clam *Mercenaria mercenaria*," in *Habitat Requirements for Chesapeake Bay Living Resources*, eds S. L. Funderburk, J. A. Mihursky, S. J. Jordan, and D. Riley (Pasadena, MD: Chesapeake Research Consortium, Inc), 19.

Ruiz-Villarreal, M., García-García, L. M., Cobas, M., Díaz, P. A., and Reguera, B. (2016). Modelling the hydrodynamic conditions associated with *Dinophysis* blooms in Galicia (NW Spain). *Harmful Algae* 53, 40–52. doi: 10.1016/j.hal.2015.12.003

Schaeffer, B. A., Loftin, K. A., Stumpf, R. P., and Werdell, P. J. (2015). Agencies collaborate, develop a cyanobacteria assessment network. *Eos, Earth Space Sci. News* 96, 16–20.

Schaeffer, B. A., Schaeffer, K. G., Keith, D., Lunetta, R. S., Conmy, R., and Gould, R. W. (2013). Barriers to adopting satellite remote sensing for water quality management. *Int. J. Rem. Sens.* 34, 7534–7544.

Schollaert Uz, S., Kim, G., Mannino, A., Werdell, P. J., and Tzortziou, M. (2019). Developing a community of practice for applied uses of future PACE data to address marine food security challenges. *Front. Earth Sci.* 7:283. doi: 10.3389/feart.2019.00283

Sea Grant Association [SGA] (2016). *NOAA Sea Grant 10-Year Aquaculture Vision. MASGP-16-015*. Ocean Springs, MS: Sea Grant Association, 16.

Seaborn, D. W., and Marshall, H. G. (2008). Dinoflagellate cysts within sediment collections from the southern Chesapeake Bay, and tidal regions of the James. York, and Rappahannock Rivers, Virginia. *VA J. Sci.* 59, 138–141.

Siegel, D. A., Maritorena, S., Nelson, N. B., and Behrenfeld, M. J. (2005). Independence and interdependencies among global ocean color properties: reassessing the bio-optical assumption. *J. Geophys. Res.* 110:C07011. doi: 10.1029/2004JC002527

Siegel, D. A., Maritorena, S., Nelson, N. B., Hansell, D. A., and Lorenzi-Kayser, M. (2002). Global distribution and dynamics of colored dissolved and detrital organic materials. *J. Geophys. Res.* 107:3228. doi: 10.1029/2001JC000965

Sjöqvist, C. O., and Lindholm, T. J. (2011). Natural co-occurrence of *Dinophysis acuminata* (Dinoflagellata) and *Mesodinium rubrum* (Ciliophora) in thin layers in a coastal inlet. *J. Eukaryot. Microbiol.* 58, 365–372. doi: 10.1111/j.1550-7408.2011.00559.x

Skovgaard, A., Hansen, P. J., and Stoecker, D. K. (2000). Physiology of the mixotrophic dinoflagellate *Fragilidium subglobosum*. I. Effects of phagotrophy and irradiance on photosynthesis and carbon content. *Mar. Ecol. Prog. Ser.* 201, 129–136.

Smith, G. F., Bruce, D. G., Roach, E. B., Hansen, A., Newell, R. I. E., and McManus, A. M. (2005). Assessment of recent habitat conditions of Eastern Oyster *Crassostrea virginica* bars in mesohaline Chesapeake Bay. *N. Am. J. Fish. Manag.* 25, 1569–1590. doi: 10.1577/m04-058.1

Soto, I. M., Cannizarro, J., Muller-Karger, F. E., Hu, C., Wolny, J., and Goldgof, D. (2015). Evaluation and optimization of remote sensing techniques for detection of *Karenia brevis* blooms on the West Florida Shelf. *Remote Sens. Environ.* 170, 239–254.

Stoecker, D. K., Adolf, J. E., Place, A. R., Glibert, P. M., and Merritt, D. W. (2008). Effects of the dinoflagellates *Karlodinium veneficum* and *Prorocentrum minimum* on early life stages of the eastern oyster (*Crassostrea virginica*). *Mar. Biol.* 154, 81–90.

Stumpf, R. P., Culver, M. E., Tester, P. A., Tomlinson, M. C., Kirkpatrick, G. J., Pederson, B. A., et al. (2003). Monitoring *Karenia brevis* blooms in the Gulf of Mexico using satellite ocean color imagery and other data. *Harmful Algae* 2, 147–160.

Stumpf, R. P., Davis, T. W., Wynne, T. T., Graham, J. L., Loftin, K. A., Johengen, T. H., et al. (2016). Challenges for mapping cyanotoxin patterns from remote sensing of cyanobacteria. *Harmful Algae* 54, 160–173. doi: 10.1016/j.hal.2016.01.005

Stumpf, R. P., and Pennock, J. R. (1989). Calibration of a general optical equation for remote sensing of suspended sediments in a moderately turbid estuary. *J. Geophys. Res.* 94, 14363–14371.

Stumpf, R. P., and Tomlinson, M. C. (2005). "Remote sensing of harmful algal blooms," in *Remote Sensing of Coastal Aquatic Environments*, eds R. L. Miller, C. E. del Castillo, and B. A. McKee (Dordrecht: Springer), 347. doi: 10.2175/106143014x13975035526149

Tang, Y. T., and Gobler, C. J. (2009). Characterization of the toxicity of *Cochlodinium polykrikoides* isolates from Northeast US estuaries to finfish and shellfish. *Harmful Algae* 8, 454–462.

Tango, P., Butler, W., Lacouture, R., Goshorn, D., Magnien, R., Michael, B., et al. (2004). "An unprecedented bloom of *Dinophysis acuminata* in Chesapeake Bay," in *Harmful Algae 2002*, eds K. A. Steidinger, J. H. Landsberg, C. R. Tomas, and G. A. Vargo (Tallahassee, FL: Florida Fish and Wildlife Conservation Commission), 358–360.

Tango, P. J., Magnien, R., Butler, W., Luckett, C., Luckenbach, M., Lacouture, R., et al. (2005). Impacts and potential effects due to *Prorocentrum minimum* blooms in Chesapeake Bay. *Harmful Algae* 4, 525–531.

Tarnowski, M. (2017). *Maryland Oyster Population Status Report*. Annapolis, MD: Chesapeake Bay Foundation, 64.

Tester, P. A., Stumpf, R. P., and Steidinger, K. A. (1998). "Ocean color imagery: what is the minimum detection level for *Gymnodinium breve* blooms?," in *Harmful Algae, Proceedings of the VII International Conference on Harmful Algae*, eds B. Reguera, J. Blanco, and M. Fernandez (Paris: Xunta de Galicia and Intergovernmental Oceanographic Commission of UNESCO), 149–151.

Tomas, C. R. (1997). *Identifying Marine Phytoplankton*. New York, NY: Academic Press, 858.

Tomlinson, M. C., Stumpf, R. P., Ransibrahmanakul, V., Truby, E. W., Kirkpatrick, G. J., Pederson, B. A., et al. (2004). Evaluation of the use of SeaWiFS imagery for detecting *Karenia brevis* harmful algal blooms in the eastern Gulf of Mexico. *Remote Sens. Environ.* 91, 293–303.

Tomlinson, M. C., Wynne, T. T., and Stumpf, R. P. (2009). An evaluation of remote sensing techniques for enhanced detection of the toxic dinoflagellate, *Karenia brevis*. *Remote Sens. Environ.* 113, 598–609.

Van Hauwaert, T. (2016). Recent dinoflagellate cysts from the Chesapeake estuary (Maryland and Virginia, USA): taxonomy and ecological preferences. Master's Thesis, University of Ghent, 97.

Vandersea, M. W., Kibler, S. R., Van Sant, S. B., Tester, P. A., Sullivan, K., Eckert, G., et al. (2017). qPCR assays for *Alexandrium fundyense* and *A. ostenfeldii* (Dinophyceae) identified from Alaskan waters and a review of species-specific *Alexandrium* molecular assays. *Phycologia* 56, 303–320.

Velo-Suárez, L., and Gutiérrez-Estrada, J. C. (2007). Artificial neural network approaches to one-step weekly prediction of *Dinophysis acuminata* blooms in Huelva (Western Andalucía Spain). *Harmful Algae* 6, 361–371.

Vonshak, A., Cheung, S. M., and Chen, F. (2000). Mixotrophic growth modifies the response of *Spirulina* (*Arthospira*) *platensis* (Cyanobacteria) cells to light. *J. Phycol.* 36, 675–679. doi: 10.1046/j.1529-8817.2000.99198.x

Webster, D. (2009). *Shellfish Aquaculture Development in Maryland and Virginia*. Silver Spring, MD: NOAA SeaGrant Report No. NA06OAR4171076, 47.

Werdell, P. J., Behrenfeld, M. J., Bontempi, P. S., Boss, E., Cairns, B., Davis, G. T., et al. (2019). The Plankton, Aerosol, Cloud, ocean Ecosystem (PACE) mission: status, science, advances. *Bull. Amer. Meteorol. Soc.* 100, 1775–1794. doi: 10.1175/BAMS-D-18-0056.1

Wikfors, G. H. (2005). A review and new analysis of trophic interactions between *Prorocentrum minimum* and clams, scallops, and oysters. *Harmful Algae* 4, 585–592.

Wolny, J. L., Egerton, T. A., Handy, S. M., Stutts, W. L., Smith, J. L., Whereat, E. B., et al. (2020). Characterization of *Dinophysis* spp. (Dinophyceae, Dinophysiales) from the mid-Atlantic region of the United States. *J. Phycol.* 56, 404–424. doi: 10.1111/jpy.12966

Wynne, T., Meredith, A., Briggs, T., Litaker, W., and Stumpf, R. (2018). "Harmful algal bloom forecasting branch ocean color satellite imagery processing guidelines," in *Proceedings of the NOAA Technical Memorandum NOS NCCOS 252*, Silver Spring, MD, 48. doi: 10.25923/twc0-f025

Wynne, T. T., Stumpf, R. P., Tomlinson, M. C., and Dyble, J. (2010). Characterizing a cyanobacterial bloom in western Lake Erie using satellite imagery and meteorological data. *Limnol. Oceanogr.* 55, 2025–2036.

Wynne, T. T., Stumpf, R. P., Tomlinson, M. C., Fahnenstiel, G. L., Dyble, J., Schwab, D. J., et al. (2013). Evolution of a cyanobacterial bloom forecast system in western Lake Erie: development and initial evaluation. *J. Great Lakes Res.* 39, 90–99.

Wynne, T. T., Stumpf, R. P., Tomlinson, M. C., Warner, R. A., Tester, P. A., Dyble, J., et al. (2008). Relating spectral shape to cyanobacterial blooms in the Laurentian Great Lakes. *Int. J. Remote Sens.* 29, 3665–3672.

Yasumoto, T., Murata, M., Oshima, Y., Sano, M., Matsumoto, G., and Clardy, J. (1985). Diarrhetic shellfish toxins. *Tetrahedron* 41, 1019–1025.

Zeng, C., and Binding, C. (2019). The effect of mineral sediments on satellite chlorophyll-a retrievals from line-height algorithms using red and near-infrared bands. *Remote Sens.* 11:2306. doi: 10.3390/rs11192306

Conflict of Interest: AM was employed by company Consolidated Safety Services, Inc.

The remaining authors declare that the research was conducted in the absence of any commercial or financial relationships that could be construed as a potential conflict of interest.

frontiers in Marine Science

ORIGINAL RESEARCH
published: 21 December 2020
doi: 10.3389/fmars.2020.520223

The Utility of Satellites and Autonomous Remote Sensing Platforms for Monitoring Offshore Aquaculture Farms: A Case Study for Canopy Forming Kelps

Tom W. Bell[1], Nick J. Nidzieko[2], David A. Siegel[1,2], Robert J. Miller[3], Kyle C. Cavanaugh[4], Norman B. Nelson[1], Daniel C. Reed[3], Dmitry Fedorov[5], Christopher Moran[1], Jordan N. Snyder[1], Katherine C. Cavanaugh[4], Christie E. Yorke[3] and Maia Griffith[1]*

[1] *Earth Research Institute, University of California, Santa Barbara, Santa Barbara, CA, United States,* [2] *Department of Geography, University of California, Santa Barbara, Santa Barbara, CA, United States,* [3] *Marine Science Institute, University of California, Santa Barbara, Santa Barbara, CA, United States,* [4] *Department of Geography, University of California, Los Angeles, Los Angeles, CA, United States,* [5] *ViQi Inc., Santa Barbara, CA, United States*

OPEN ACCESS

Edited by:
Yoann Thomas, Institut de Recherche Pour le Développement (IRD), France

Reviewed by:
Wiebe Nijland, Utrecht University, Netherlands
Anthony L. E. Bris, Centre d'étude et de Valorisation des Algues, France

***Correspondence:**
Tom W. Bell
tbell@ucsb.edu

Specialty section:
This article was submitted to Ocean Observation, a section of the journal Frontiers in Marine Science

Received: *14 December 2019*
Accepted: *17 November 2020*
Published: *21 December 2020*

Citation:
Bell TW, Nidzieko NJ, Siegel DA, Miller RJ, Cavanaugh KC, Nelson NB, Reed DC, Fedorov D, Moran C, Snyder JN, Cavanaugh KC, Yorke CE and Griffith M (2020) The Utility of Satellites and Autonomous Remote Sensing Platforms for Monitoring Offshore Aquaculture Farms: A Case Study for Canopy Forming Kelps. Front. Mar. Sci. 7:520223. doi: 10.3389/fmars.2020.520223

The emerging sector of offshore kelp aquaculture represents an opportunity to produce biofuel feedstock to help meet growing energy demand. Giant kelp represents an attractive aquaculture crop due to its rapid growth and production, however precision farming over large scales is required to make this crop economically viable. These demands necessitate high frequency monitoring to ensure outplant success, maximum production, and optimum quality of harvested biomass, while the long distance from shore and large necessary scales of production makes in person monitoring impractical. Remote sensing offers a practical monitoring solution and nascent imaging technologies could be leveraged to provide daily products of the kelp canopy and subsurface structures over unprecedented spatial scales. Here, we evaluate the efficacy of remote sensing from satellites and aerial and underwater autonomous vehicles as potential monitoring platforms for offshore kelp aquaculture farms. Decadal-scale analyses of the Southern California Bight showed that high offshore summertime cloud cover restricts the ability of satellite sensors to provide high frequency direct monitoring of these farms. By contrast, daily monitoring of offshore farms using sensors mounted to aerial and underwater drones seems promising. Small Unoccupied Aircraft Systems (sUAS) carrying lightweight optical sensors can provide estimates of canopy area, density, and tissue nitrogen content on the time and space scales necessary for observing changes in this highly dynamic species. Underwater color imagery can be rapidly classified using deep learning models to identify kelp outplants on a longline farm and high acoustic returns of kelp pneumatocysts from side scan sonar imagery signal an ability to monitor the subsurface development of kelp fronds. Current sensing technologies can be used to develop additional machine learning and spectral algorithms to monitor outplant health and canopy macromolecular content, however future developments in vehicle and infrastructure technologies are necessary to reduce costs and transcend operational limitations for continuous deployment in an offshore setting.

Keywords: autonomous vehicles, remote sensing, sUAS, giant kelp, side scan sonar, deep learning (DL), drones (unmanned aerial vehicles or UAVs), biofuel

INTRODUCTION

As the global population grows, so do food and energy demands. One possibility for meeting these demands is aquaculture in offshore areas (Lovatelli et al., 2013; Gentry et al., 2017a). This challenging marine environment has become a viable option due to recent developments in engineering, while advancements in offshore marine spatial planning can serve to reduce conflicts and environmental impacts (Shainee et al., 2012; Gentry et al., 2017b; Lester et al., 2018).

Giant kelp (*Macrocystis pyrifera*) is an ideal candidate for offshore aquaculture because it is among the world's fastest growing autotrophs, with elongation rates in excess of 0.5 m d^{-1} under ideal conditions, biomass turnover rates of ∼12 times per year, and year-round production (Clendenning, 1971; Graham et al., 2007; Reed et al., 2008; Correa et al., 2016; Rassweiler et al., 2018). Biomass can be used as a biofuel feedstock, fertilizer, and animal feed, which all require specific tissue nutrients and sugars to be maximized (Neushul, 1987; Gutierrez et al., 2006; Wargacki et al., 2012). However, the same high growth rate and versatility that makes giant kelp an attractive aquaculture crop necessitates high frequency monitoring to ensure outplant success, maximize production, and optimize the nutritional content of harvested biomass for its various uses.

Since distance from shore, labor costs, and the necessary scale of production makes in person monitoring unrealistic, remote sensing is a practical monitoring solution. Fortunately, the use of remote sensing for the quantification of giant kelp biomass dynamics and tissue composition has progressed in step with advancements in sensor technology and data availability. The advent of freely available, multispectral Landsat imagery in 2008 (Woodcock et al., 2008) enabled the monitoring of the floating surface canopy of giant kelp over large space and time scales. Cavanaugh et al. (2011) used linear unmixing methods to produce a time series of kelp canopy biomass in the Santa Barbara Channel, calibrated using a monthly time series of diver-estimated canopy biomass. Airborne imaging spectroscopy was used to estimate the physiological condition of the floating canopy, which is related to tissue nitrogen content and frond senescence and has implications for optimizing biomass quality and timing of harvest (Card et al., 1988; Bell et al., 2015, 2018; Rodriguez et al., 2016). Acoustic sensors have also been used to successfully estimate the density of subsurface giant kelp plants (Zabloudil et al., 1991; Parnell, 2015). While much of this work has focused on natural populations of giant kelp, these methods are readily adaptable to offshore kelp aquaculture farms and provide an excellent foundation to innovate with emerging technologies.

Leveraging existing and nascent technologies may allow for the development of effective monitoring platforms for offshore kelp aquaculture farms. Several new multispectral satellite systems have started acquiring free, publicly available imagery with increases in pixel resolution and sensor sensitivity (Drusch et al., 2012; Markham et al., 2018). Additionally, a global, repeat imaging spectrometer will likely start acquiring imagery in the mid-2020's (National Academies of Sciences, Engineering, and Medicine, 2018). Furthermore, cloud-based archive and analysis platforms, such as Google Earth Engine, have democratized the processing of satellite imagery by removing the need for expensive software and local computing resources (Gorelick et al., 2017). Nascent autonomous vehicle technologies deploying both optical and acoustic sensors have the potential to provide rapid, repeat monitoring capabilities both above and below the ocean surface (Ackleson et al., 2017; Hardin et al., 2019). Small Unoccupied Aircraft Systems (sUAS; aerial drones) have been rapidly adopted for high temporal and spatial scale monitoring of agriculture and advances in sensor miniaturization have allowed a suite of multispectral and hyperspectral sensors to be carried by these lightweight vehicles (Zhang and Kovacs, 2012). The recent increase in availability of low-cost remotely operated vehicles (ROVs) and autonomous underwater vehicles (AUVs) along with machine learning-based image processing, signal future innovations in subsurface monitoring capabilities (Salman et al., 2016; Fedorov et al., 2017; Manley and Smith, 2017; Lund-Hansen et al., 2018). All of these technologies possess unique advantages that could be leveraged to develop an offshore aquaculture monitoring system.

To assess the ability of spaceborne, aerial, and subsurface remote sensing technologies to provide products necessary for the monitoring of offshore kelp aquaculture farms we ask the following questions: (1) Does cloud cover limit the ability of satellite sensors to monitor kelp farms in the offshore areas of the Southern California Bight? (2) Can commercially available sUAS-mounted optical sensors provide spatial estimates of kelp canopy area, biomass, and tissue nitrogen content? (3) Are deep learning classified underwater color imagery and side scan sonar able to identify kelp outputs on a longline aquaculture farm? Based on the monitoring capabilities of these remote sensing platforms on natural kelp forest canopies and nearshore kelp farms we determine the optimal use of each sensor platform and discuss the operational risks and limitations of these platforms for use in an offshore aquaculture setting.

MATERIALS AND METHODS

Overview

Here, we use three approaches to examine the capabilities of various remote sensing platforms to monitor offshore kelp aquaculture farms. First, we examine the feasibility of spaceborne monitoring by analyzing several decades of Landsat imagery to produce maps of the mean seasonal cloud cover over the United States portion of the Southern California Bight (SCB). Second, we deploy multiple sUAS-mounted sensors (color camera, multispectral, hyperspectral) to image a natural kelp forest canopy located in the western Santa Barbara Channel (Arroyo Quemado; 34.467°N 120.118°W) and show monitoring products developed using the different types of imagery. All sUAS imagery was acquired on June 30, 2019 between 9 a.m. and 12 p.m. local time with clear skies and light wind at an altitude of 120 m above ground level, and concurrent with a Landsat satellite overpass. Tidal height fell from 1.05 to 0.67 m over the 3-h period as recorded from the Santa Barbara, CA tide station. Third, we image juvenile giant kelp outplants with underwater color imagery and side scan sonar on a longline

aquaculture farm located approximately 1.2 km off the coast of Santa Barbara, California (Santa Barbara Mariculture; 34.392°N 119.759°W). We develop deep learning models to classify kelp from the color imagery and assess the acoustic returns before and after the formation of pneumatocysts (gas bladders). Juvenile giant kelp sporophytes (outplanted between microscopic and ∼2 cm in length; $n = 2{,}500$) were outplanted along long lines over 5 days from May 5 through May 9, 2019 to assess the growth and production of different giant kelp genotypes under farmed conditions. All underwater imagery and diver measurements were collected along a subset of the farm lines between July 11 and August 1, 2019.

Cloud Cover Analysis to Examine Satellite Monitoring Potential

Mean seasonal cloud cover over the SCB was determined using Landsat satellite imagery from 1984 to 2019. The Landsat satellite sensors provide multispectral imagery at a 30 m pixel resolution with a repeat frequency of 16 days during periods with one satellite sensor and 8 days when two sensors are in orbit. Three Landsat sensors were used: Landsat 5 Thematic Mapper (TM; 1984–2011), Landsat 7 Enhanced Thematic Mapper Plus (ETM+; 1999 – present), and Landsat 8 Operational Land Imager (OLI; 2013 – present). Due to the scan line corrector error on the Landsat 7 ETM+ instrument, only data from 1999–May 2003 were used in the cloud cover analysis. All Landsat images were acquired as atmospherically corrected surface reflectance images and the pixel quality assessment band associated with each image was used to determine cloud containing pixels. The analysis was completed for the four Landsat tiles which cover the SCB (path/row: 042/036, 041/036, 041/037, 040/037). Mean cloud cover was then determined for each offshore pixel (USA federal waters; >3 nautical miles from the coast) for each season across all years. All cloud cover analysis was completed in Google Earth Engine (Gorelick et al., 2017).

In order to estimate the number of seasonal cloud-free views of each remote sensing pixel in the offshore region we used:

$$S = (1 - \bar{x}) \times (L/r) \tag{1}$$

where S is the mean number of usable satellite views per season, $\bar{x}$ is the mean cloud covered fraction of all offshore pixels, L is the length of the season in days, and r is each satellite sensor's repeat period in days. Repeat periods for several medium resolution (10–30 m pixel resolution) satellite sensors were used, including the multispectral Landsat sensors (16 days) and Sentinel-2 sensors (twin satellites; 5 days), and the hyperspectral sensor on the planned Surface Biology and Geology (SBG) designated observable (*proposed* 16 days; **Table 1**).

Canopy Analysis Using Landsat Imagery

Landsat 7 ETM+ imagery from June 30, 2019 was downloaded from the USGS Earth Explorer website (**Table 2**; earthexplorer.usgs.gov) as atmospherically corrected surface reflectance imagery. Kelp canopy fraction was determined following methods described in Cavanaugh et al. (2011) and Bell et al. (2020). Briefly, Landsat pixels were classified as containing kelp canopy using a binary decision tree using spectral bands 1–5, and 7. The fractional cover of kelp canopy inside each pixel was determined using Multiple Endmember Spectral Mixture Analysis (MESMA; Roberts et al., 1998), where the reflectance spectrum (spectral bands 1–4) of each pixel is iteratively modeled as a linear combination of one kelp canopy spectral endmember and one of 30 seawater endmembers. The 30 seawater endmembers were taken from Landsat pixels classified as seawater to account for varying spectral qualities due to sun glint, phytoplankton blooms, and suspended sediment. The optimal model, and resulting kelp canopy fraction estimate, minimizes the root mean squared error between the modeled and observed pixel reflectance spectrum. Kelp canopy fraction has been found to be linearly correlated with canopy biomass density using the empirical relationship between a time series of Landsat kelp canopy fraction estimates and monthly diver estimated canopy biomass at two permanent transects in the Santa Barbara Channel from 2003 to 2017 (Cavanaugh et al., 2011; Bell et al., 2020).

Canopy Analysis Using sUAS Color Imagery

Aerial color digital imagery was obtained for the Arroyo Quemado kelp forest using a DJI Phantom 4 Pro sUAS, which is equipped with a 20 MP (1″ CMOS sensor, 84° FOV) color camera and can image areas of ∼40 hectares in one flight (**Table 2**). All camera settings were set to automatic and there was no spectral calibration using calibration targets. Photogrammetric software (Agisoft Metashape Pro Version 1.5.0) was used to produce a georeferenced orthomosaic from the color imagery. Georeferencing was validated using known ground control points on land, approximately 200 m from the inshore edge of the kelp canopy. After land and breaking waves were removed from the color orthomosaic, floating kelp canopy was classified using a simple band ratio where *Red* is the red band and *Blue* is the blue band of the color image:

$$\textit{Kelp Canopy}, \quad \frac{Red}{Blue} \geq 1 \tag{2}$$

$$\textit{Seawater}, \quad \frac{Red}{Blue} < 1 \tag{3}$$

Canopy Analysis Using sUAS Multispectral Imagery

Multispectral aerial imagery was collected for the Arroyo Quemado kelp forest using the MicaSense Altum sensor mounted on a DJI Matrice 200 sUAS, which can also image areas of ∼40 hectares in one flight (**Table 2**). The Altum sensor has five individual 3.2 MP cameras which simultaneously capture images across five spectral bands: blue (475 nm center, 32 nm bandwidth), green (560 nm center, 27 nm bandwidth), red (668 nm center, 14 nm bandwidth), red edge (717 nm center, 12 nm bandwidth), near infrared (840 nm center, 57 nm bandwidth). A 50% gray panel with a known reflectance across each of the five spectral bands was captured before and after the flight to convert each image to reflectance. Agisoft Metashape Pro software was used to produce a georeferenced

TABLE 1 | Various current and planned satellites systems which are potentially useful for kelp aquaculture.

Satellite system	Sensor type	Spatial resolution (m)	Repeat period (days)	Winter	Spring	Summer	Fall
Landsat (1 satellite)	Multispectral	30	16	4.1 (0.37)	3.0 (0.6)	1.9 (1.1)	3.7 (0.5)
Landsat (2 satellites)*	Multispectral	30	8	8.1 (0.74)	6.0 (1.1)	3.7 (2.3)	7.4 (1.0)
Sentinel-2	Multispectral	10	5	13.0 (1.2)	9.6 (1.8)	5.9 (3.7)	11.8 (1.6)
SBG†	Hyperspectral†	30†	16†	4.1 (0.37)	3.0 (0.6)	1.9 (1.1)	3.7 (0.5)

"Sensor Type" and "Spatial Resolution" refer to the sensors' visible and near infrared bands. Seasonal values show the estimated mean number of usable views per season (standard deviation) of the offshore region of the Southern California Bight (USA federal waters; >3 nautical miles from the coast). SBG is the initialization for the Surface Biology and Geology designated observable, whose targeted observation capabilities include a global, repeat imaging spectrometer.
**Landsat 7 ETM+ & Landsat 8 OLI (2013 – present), Landsat 8 OLI & Landsat 9 OLI-2 (starting 2021). †Planned (mid-2020's).*

TABLE 2 | Remote sensing technologies that can be used to monitor giant kelp aquaculture farms and the products which can be derived from the imagery.

Application	Vehicle	Sensor type	Sensor	Spatial scale	Products
Canopy	Satellite	Multispectral	Sentinel-2/Landsat	10 m /30 m	Area[a], Biomass[b]
		Hyperspectral†	SBG†	30 m†	Pigment[c]/Nitrogen§/ Sugar‡ Content, Age‡
	sUAS	Color Camera	1″ sensor, 84° FOV, 20 MP	3.2 cm*	Area§
		Multispectral	Micasense Altum	6.5 cm*	Area[a], Biomass[b]
		Hyperspectral	Headwall Nano-Spec	7.5 cm*	Pigment[c]/ Nitrogen§/Sugar‡ Content, Age‡
Subsurface	ROV/AUV/ surface craft	Color Camera	1/2.9″ sensor, 80° FOV, 1,080 p	2.6 mm at 3 m distance	Identification§, Size‡, Disease‡, Herbivory‡
		Sidescan Sonar	Edgetech 4215/Marine Sonic MKII (900 kHz)	1 cm across track	Identification§, Size‡, Biomass‡

*†Planned, ‡in principle, §this study, *120 m above ground level altitude.*
[a]Hamilton et al. (2020).
[b]Cavanaugh et al. (2011).
[c]Bell et al. (2015).

orthomosaic for each spectral band (version 1.5.0). Kelp canopy density was determined using MESMA across all five spectral bands using one kelp spectral endmember and 10 seawater spectral endmembers (similar to the methods used with Landsat imagery in section Canopy Analysis Using Landsat Imagery). The kelp spectral endmember was determined using the mean spectrum of the 100 kelp canopy pixels with the highest near infrared reflectance (**Supplementary Figure 1**). Kelp canopy, like all photosynthetic material, displays a high reflectance in the near infrared, while seawater rapidly attenuates near infrared radiation (Cavanaugh et al., 2011; Bell et al., 2015). The 10 seawater endmembers were randomly chosen from seawater areas at least 50 m from the nearest kelp canopy (**Supplementary Figure 1**).

Canopy Analysis Using sUAS Hyperspectral Imagery

Hyperspectral aerial imagery was collected over the Arroyo Quemado kelp forest using a Headwall Nano-Hyperspec VNIR sensor mounted on a DJI Matrice 600 Pro sUAS, which can image areas of ∼20 hectares in one flight (**Table 2**). The Nano-Hyperspec VNIR sensor measures a continuous reflectance spectrum from 400 to 1,000 nm across 270 contiguous 2.2 nm spectral bands. The sensor is a push broom scanner with 640 spatial bands and a 12 mm focal length lens, delivering a 7.2 cm pixel resolution at an altitude of 120 m. The sensor was calibrated before each flight by capturing a dark reference and a white reference using a 50% gray panel with a known spectral reflectance from 400 to 1,000 nm. A 3 × 3 m spectral reflectance calibration tarp comprised of three 3 × 1 m gray sections (11, 32, and 56% reflectance) was placed on the beach approximately 175 m inshore of the kelp canopy and was captured in the hyperspectral imagery. Image swaths were processed to surface reflectance data by first converting the recorded digital numbers to radiance using the dark reference and a sensor specific radiometric calibration file. Second, radiance was converted to surface reflectance using the three panels of the spectral reflectance calibration tarp captured in the imagery. The processed surface reflectance image swaths were individually orthorectified and georeferenced, and the positioning of each swath was then adjusted to match overlapping pixels between neighboring image swaths.

All image processing was completed using the Headwall SpectralView software.

Each georeferenced image swath was then processed further using Matlab (version 2018b) first by smoothing all reflectance spectra using a Savitzky-Golay filter with a three-band window (Savitsky and Golay, 1964). Pixels containing glint were identified as all pixels where reflectance was >30% at the band centered at 731 nm and removed. Pixels were classified as kelp canopy where the ratio of reflectance at the band centered at 731 nm to the band centered at 509 nm was >3. Kelp canopy density was determined using MESMA across the entire reflectance spectrum using one kelp spectral endmember and 10 seawater spectral endmembers. The kelp spectral endmember was determined as the mean of the 100 kelp canopy pixels with the highest near infrared reflectance across all image swaths. The 10 seawater endmembers were randomly chosen from seawater areas at least 50 m from the nearest kelp canopy. After these additional processing steps, the resulting hyperspectral image was then georeferenced for a second time using the orthomosaic captured by the color camera sUAS to correct any spatial discrepancies.

Nitrogen Content Spectral Algorithm Development

In order to use spectral imagery to assess the condition of the kelp canopy using metrics such as tissue nitrogen content, empirical relationships must be developed between the spectra and the condition metric of interest. We used data of giant kelp blade reflectance with corresponding data of blade tissue nitrogen content collected monthly from 2012 to 2015 at three kelp forests in the Santa Barbara Channel to develop these relationships (see Bell et al., 2018 *for detailed methods*). Briefly, every month 15 mature canopy blades were collected at each of the three sites and their reflectance between 350 and 800 nm (1 nm intervals) was measured in the laboratory using a Shimadzu UV 2401PC spectrometer with an integrating sphere attachment. A 5 cm^2 disc was excised from the central portion of each blade and placed in a drying oven at 60°C for several days until completely dry. The dried discs were then combined, weighed, ground to a fine powder, and analyzed for nitrogen content using an elemental analyzer (Carlo-Erba Flash EA 1112 series, Thermo-Finnigan Italia, Milano, Italy). The mean reflectance spectra averaged over the 15 blades collected monthly for each site was paired with the pooled tissue nitrogen content of the 15 blades for the purpose of assessing the relationship between blade reflectance spectra and nitrogen content ($n = 101$ paired reflectance & nitrogen samples).

We focused on changes in the shape of the reflectance spectrum rather than the magnitude since sun glint or the proportion of kelp canopy inside an imaged pixel can have a large effect on reflectance magnitude (Cavanaugh et al., 2011). We first interpolated the 1 nm laboratory reflectance onto the 2.2 nm spectral bands associated with the Nano-Hyperspec sensor (full width at half maximum = 6.6 nm). Normalized reflectance (*Nr*) was determined by scaling reflectance (between 0 and 1) based on the maximum and minimum reflectance values of the spectral bands between 596 and 670 nm, an area of the spectrum important for diagnosing kelp physiological condition (Bell et al., 2015), and then adding a value of 1 to all spectral bands so that all values were positive. The bands in the range used for normalization represent wavelengths with low and relatively flat seawater reflectance and avoid the rapid increase in reflectance associated with the red edge of kelp canopy reflectance.

The ratio of *Nr* for all band pairs between 596 and 670 nm were iteratively compared to tissue nitrogen content across all 101 samples using linear and generalized additive models (GAMs; R package mgcv; Wood, 2017). Each GAM was fit between tissue nitrogen content and the predictor variable(s) with a Tweedie error structure (power function = 1.01; $k = 5$). In the visible light bands, differences in the spectral shape of reflectance are not a direct function of the tissue nitrogen content itself but are due to the additive absorption and fluorescence properties of various pigments (Gates et al., 1965; Woolley, 1971; Gausman, 1983; Hochberg et al., 2004). Photosynthetic pigment concentrations are modulated by both the ambient seawater nitrate concentration and available light, and different relationships may exist between pigment concentration and nitrogen content under nutrient vs. light limited conditions (Laws and Bannister, 1980). Due to these potential differences, photosynthetically active radiation (PAR) during the 30 days prior to sample collection was included as a predictor in the models. We compared model parsimony using the Akaike information criterion (AIC). Photosynthetically active radiation was determined using the closest 4 km daily MODIS Aqua product to each site (oceandata.sci.gsfc.nasa.gov; Bell et al., 2018).

Application of Nitrogen Algorithm to sUAS Hyperspectral Imagery

In order to create maps of kelp canopy nitrogen content, the tissue nitrogen content algorithm must be applied to the reflectance spectra measured by the Nano-Hyperspec VNIR. The hyperspectral image spectra were first normalized in the same manner as the laboratory reflectance spectra. Since each 7.2 cm pixel is a combination of kelp canopy and seawater, we used MESMA to estimate the fractional cover of kelp canopy and removed all pixels with a relative canopy fraction of <0.1 to minimize the effect of seawater on the reflectance spectra. Pixels with excessive noise were removed if the mean coefficient of variation of *Nr* between 565 and 610 nm (an area of the spectrum with low absorption by chlorophyll *a*) exceeded 10%. The nitrogen content spectral algorithm determined from the laboratory spectra was then applied to the hyperspectral imagery.

Subsurface Analysis Using Side Scan Sonar Imagery

Acoustic imagery of the aquaculture farm was captured using an Edgetech 4125 400/900 kHz side scan sonar system mounted 1 m below the water surface along the side of a 22-foot vessel moving at 3 km h^{-1} (**Table 2**). The system's 900 kHz Compressed High-Intensity Radiated Pulse (CHIRP) pulse delivers an across track resolution of 1 cm and an onboard inertial measurement unit allows for correction of the imagery due to surface motion side scan imagery was collected on July 12 and July 30, 2019 along the

length of one of the longlines of the Santa Barbara Mariculture giant kelp facility.

Subsurface Analysis Using Color Imagery

Underwater color imagery and video was captured by a high definition 1,080 p (1/2.9″ sensor, 80° FOV) color camera mounted on a Blue Robotics Remotely Operated Vehicle (ROV) on July 11 and July 29, 2019 along a portion of the same longline surveyed using side-scan sonar (**Table 2**). Visual analysis of the juvenile kelp growing on the longlines (number of pneumatocysts individual^{-1}) were performed for the portion of the longline surveyed on both dates using video collected by the ROV. The length of each kelp individual growing on the longline was measured by divers on July 12 and August 1, 2019. Elongation rate was determined for each individual kelp outplant that was measured on both dates by dividing the difference in maximum length by the number of days between surveys.

The images collected by the ROV were automatically analyzed for subsurface kelp outplant distribution using deep learning models trained from a set of human annotated imagery (ViQi, Inc.). The models used a Convolutional Neural Network (CNN; CaffeNet), which was pre-trained on the ImageNet dataset and used transfer learning techniques to train the models. Transfer learning was optimized to retrain the neural network while only fine-tuning the convolutional, feature retrieval, layers. This approach is especially useful when training with a small number of samples and when visual features created for natural image recognition are descriptive for the task in hand. Our training dataset consisted of five classes including ocean, kelp, longline, tag, and wire tie (plants were individually marked with tags affixed to the line with wire ties). Each class was manually annotated using polygonal outlines (405 ocean, 370 kelp, 316 long line, 338 tag, and 230 wire tie polygons). Since small numbers of training samples require additional methods to render good models, we exacted multiple samples from polygons using uniform gridding. The final training set consisted of >125,000 samples of ocean, >11,000 of kelp, >12,000 longline, >4,000 tags and >2,000 wire ties. The augmented dataset was then randomly partitioned into a training subset using 60% of the samples, withholding 20% for testing, and the final 20% for validation.

RESULTS

Effect of Cloud Cover on the Usefulness of Satellite Observations

Cloud cover, which limits the ability of satellites to observe the ocean surface, displayed seasonal variability in the SCB over decadal time scales. Cloud cover over offshore areas was generally lowest in the winter ($\overline{x} = 29.0\%$), increased in spring ($\overline{x} = 47.2\%$) to a maximum in summer ($\overline{x} = 67.5\%$) and declined in fall ($\overline{x} = 35.4\%$). The seasonal pattern of cloud cover varied spatially (**Figure 1**), as cloud cover was fairly consistent in winter, spring, and fall ($\sigma = 3.3,\ 5.0,$ and 4.3%, respectively), while offshore areas and windward coasts were generally cloudier than the leeward coasts of the mainland and islands during the summer ($\sigma = 10.0\%$). The various satellite systems produced different numbers of usable images ranging from ∼2 to 13 per season depending on their repeat time, number of satellites in a system, and seasonal cloud cover (**Table 1**).

Kelp Canopy Nitrogen Content Spectral Algorithm

Several spectral band ratios displayed strong linear and non-linear relationships with tissue nitrogen content. The ratio of *Nr* for any band located between 603 and 644 nm, and any band located between 665 and 680 nm was significantly and strongly linearly correlated with tissue nitrogen content. The changes in spectral shape in this region of the spectrum were superior for the estimation of tissue nitrogen content compared to spectral features in the blue, green, and near infrared wavelengths (**Figure 2**). The use of GAMs to incorporate the non-linearity of the relationship between the spectral band ratios and tissue nitrogen content led to the selection of the bands centered at 640 and 670 nm as the optimized wavelengths for the model:

$$Nr_{670nm} \,/\, Nr_{640nm} \tag{4}$$

where Nr_{670nm} and Nr_{640nm} are the normalized reflectance at the bands centered at 670 and 640 nm, respectively ($r^2 = 0.57$; $p < 0.0001$; **Figure 3A**). Using both Nr_{670nm} / Nr_{640nm} and PAR as predictor variables ($R^2 = 0.60$; $p < 0.0001$, $p = 0.015$, respectively) decreased the AIC from 142.9 to 130.9, indicating a more parsimonious model. The effect of PAR on tissue nitrogen is demonstrated by the different relationships between Nr_{670nm} / Nr_{640nm} and tissue nitrogen content during high light (April–September) and low light (October–March) periods of the year (**Figure 3A**). The non-linear relationship between Nr_{670nm} / Nr_{640nm} and tissue nitrogen content displayed an effect size range of −0.48 to 0.68, and the relationship became positive at values >0.62 (**Figure 3B**). Photosynthetically active radiation displayed a linear relationship with tissue nitrogen content where the effect size of the relationship became positive at values >41 E m^{-2} d^{-1}, with an effect size range of −0.11 to 0.09 (**Figure 3C**).

Assessment of Kelp Canopy Characteristics From Satellite and Aerial Imagery

In order to compare the various types of imagery and derived products, we surveyed a 10-hectare area containing kelp forest canopy with four different sensors over the course of a 3-h period. We first imaged the kelp canopy using the color camera on the Phantom 4 Pro sUAS, which produced a color orthomosaic with a final pixel resolution of 3.2 cm (**Figure 4A**). Kelp canopy and seawater were then classified from the color orthomosaic using (Equations 2 and 3) for a total estimated canopy area of 1.39 hectares (**Figure 4B**). The multispectral sensor onboard the Matrice 200 sUAS then imaged the study area, which produced an orthomosaic with a final pixel resolution of 6.5 cm. Kelp canopy fraction was then estimated using MESMA for the entire survey area ($\overline{x} = 0.059$; $\sigma = 0.174$) and from all pixels containing kelp canopy (kelp canopy fraction >0; $\overline{x} = 0.424$; $\sigma = 0.250$) for a total estimated canopy area of 1.41 hectares (**Figure 4C**). The hyperspectral sensor on the Matrice 600 Pro sUAS then imaged

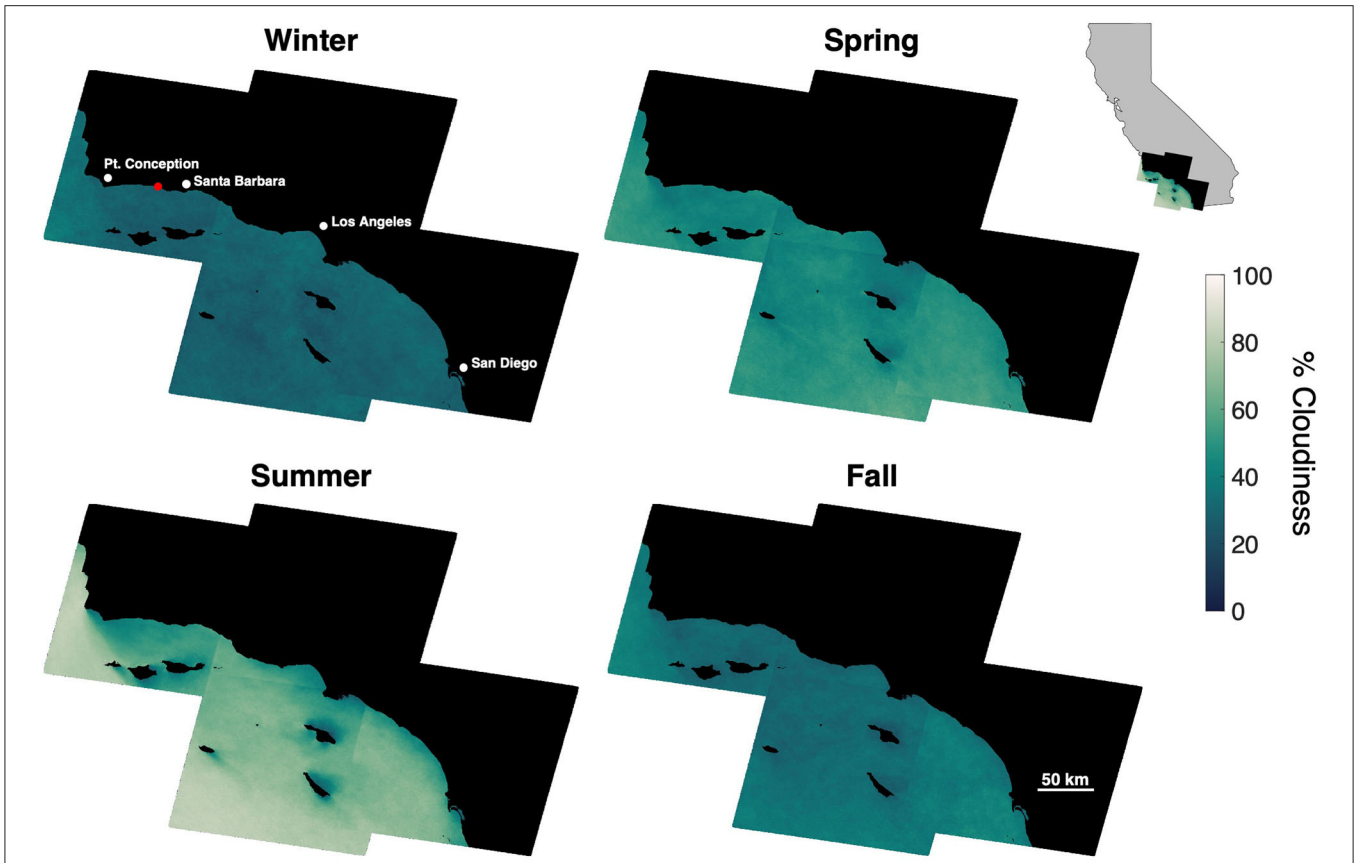

FIGURE 1 | Mean seasonal cloud cover for areas offshore of Southern California at a 30 × 30 m pixel resolution, determined from 35 years of Landsat imagery (1984–2019). Red dot shows the location of the kelp forest in **Figure 4**.

the study area to produce a map of canopy tissue nitrogen content ($\bar{x}$ = 2.32%; σ = 0.465%). The native 7.2 cm pixels were then interpolated onto a 25 cm grid, and all grid cells with less than three tissue nitrogen estimates were discarded (**Figure 4D**).

The Landsat 7 ETM+ satellite sensor imaged the survey area simultaneous to the sUAS flights and kelp canopy fraction was estimated from the entire survey area (**Figure 4F**; $\bar{x}$ = 0.037; σ = 0.088) and for all pixels classified as containing kelp canopy ($\bar{x}$ = 0.196; σ = 0.099). Kelp canopy fraction ranged from 0.074 to 0.523, corresponding to a 0.78–3.71 kg m^{-2} range of canopy biomass density. Kelp canopy fractions from the multispectral sUAS imagery (6.5 cm) were interpolated to the 30 m Landsat grid and were compared using a linear regression (**Figures 4E–G**; r^2 = 0.853, $p < 0.0001$; y = 1.087 + 0.015). Overall, Landsat underestimated kelp canopy fractional cover by 33% when fractions were summed (6.71 vs. 4.50 summed kelp canopy fraction, respectively).

Acoustic Analysis of Juvenile Kelp Outplants on Farm Longlines

Kelp outplants increased in size between the two acoustic survey dates and diver measurements of the kelp outplants displayed an average elongation rate of 0.55 cm d^{-1} (σ = 0.38; n = 50). Video analysis showed an increase in the number of pneumatocysts per outplant from 1.15 (σ = 1.87; n = 108) on July 11 to 6.18 (σ = 6.12; n = 97) on July 29, 2019 (**Figure 5A**). Side scan sonar imagery showed high acoustic returns for the longline and its structural buoys and weights during the survey on July 12, 2019. The subsequent side scan sonar survey on Jul 30, 2019 showed high acoustic returns for the same farm structures, as well as many objects attached to the top of the farm line (**Figure 5B**). These high acoustic returns were regularly spaced along the farm line and correspond to the general distance between the kelp outplants (∼0.5 m).

Kelp Outplant Visualization Using Deep Learning Models

The resulting deep learning classification model, which included all five object classes, detected kelp with 72% accuracy (percent of kelp class polygons correctly identified) and 32% error (percent of non-kelp class polygons incorrectly identified as kelp). After initial validation, we refined the model by disabling poorly performing classes (accuracy <25%). Since our primary objective was to detect kelp outplants, we also disabled classes deemed unnecessary (background ocean and wire tie). Disabling the ocean and wire tie classes reduced errors introduced to other classes and positively affected model performance, with the final model detecting kelp with 91% accuracy and 7% error, while

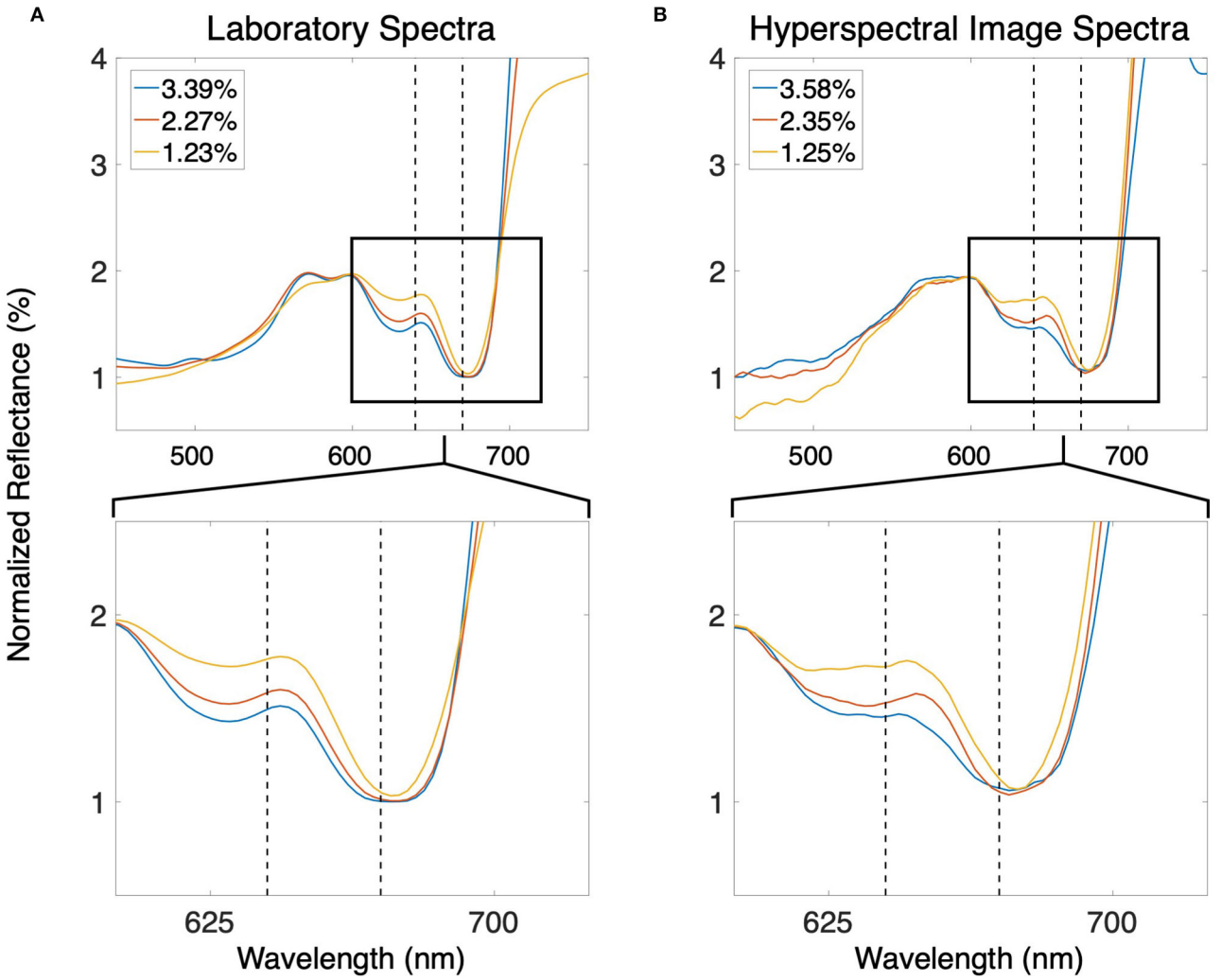

FIGURE 2 | (A) Smoothed normalized reflectance spectra of giant kelp canopy blades with different tissue nitrogen contents measured in the laboratory. **(B)** Smoothed normalized reflectance spectra of the giant kelp canopy using the sUAS hyperspectral sensor. Tissue nitrogen content estimated using the ratio of the spectral bands centered at 670 and 640 nm (dashed black lines). The bottom panels show enlargements of the areas inside the black boxes in the top panels.

longline detection demonstrated 68% accuracy and 2% error. The model produced polygonal annotations of kelp and longline classes that visually resembled human annotations (**Figure 6**).

DISCUSSION

Remote Monitoring of the Kelp Canopy

Aerial and spaceborne imaging of the floating kelp canopy have the potential to deliver several actionable products to offshore aquaculture managers (**Table 2** and **Figure 4**). Satellite observations of the kelp canopy represent the most mature sector of the aquaculture monitoring platforms examined in this study as these sensors have been used to assess natural kelp forest dynamics over 100's of km (Cavanaugh et al., 2019). The spectral and spatial resolution (30 m) of the Landsat satellite sensors can provide estimates of canopy biomass that compare well to over a decade of *in situ* diver estimates (Bell et al., 2020). However, because existing operational multispectral satellites were primarily designed for terrestrial targets (**Table 1**), only the area or biomass of canopy forming kelp species can be determined. The mixture of kelp canopy and seawater in each 10–30 m pixel limits their ability to use common multispectral band ratios to estimate plant physiological condition or the elemental content of the tissue (**Table 2**; Cavanaugh et al., 2010, Cavanaugh et al., 2011; Bell et al., 2015). In the near future, opportunities exist for more comprehensive spaceborne monitoring of kelp aquaculture farms using global, repeat hyperspectral imaging. The Surface Biology and Geology (SBG) designated observable (a set of targeted observation capabilities from a future spaceborne mission) will provide the spectral coverage and resolution necessary to estimate the physiology and macromolecular content of the kelp canopy in the presence of seawater (Bell et al., 2015; Lee et al., 2015). For example, the spectral bands centered at 640 and 670 nm will be measured by

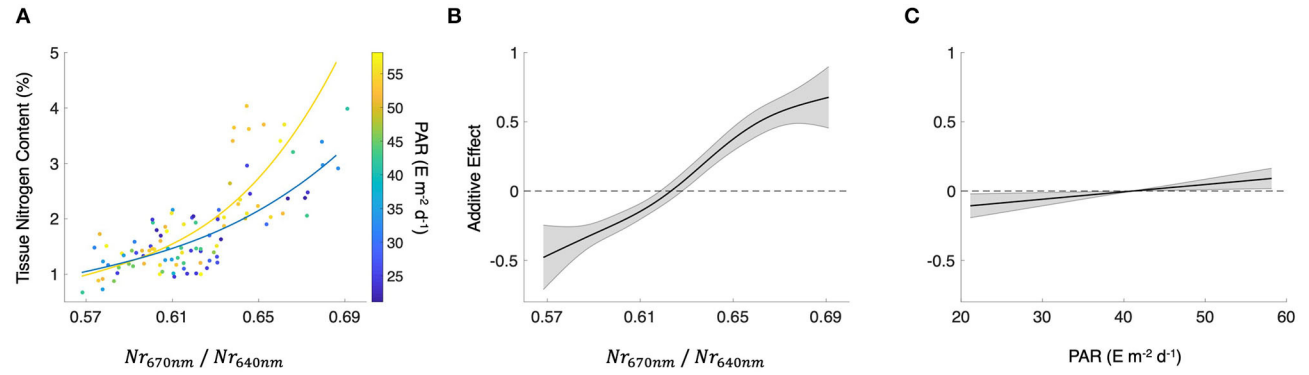

FIGURE 3 | (A) Scatterplot of the spectral band ratio of normalized reflectance for bands centered at 670 and 640 nm (Nr_{670nm}/Nr_{640nm}) and tissue nitrogen content. Colored lines represent best fit lines between Nr_{670nm}/Nr_{640nm} and tissue nitrogen content in the high light season (yellow; April–September) and low light season (blue; October–March). Mean photosynthetically active radiation (PAR) for 30 days prior to the sampling date. **(B)** The additive effect of Nr_{670nm}/Nr_{640nm} on tissue nitrogen content and **(C)** the additive effect of PAR on tissue nitrogen content produced using a generalized additive model estimating tissue nitrogen content from both Nr_{670nm}/Nr_{640nm} and PAR. Black lines show the mean relationship and shaded gray areas show the standard error.

the proposed satellite sensor and can assess the physiological condition and nitrogen content of the kelp canopy without relying on bands in the red edge (680–750 nm) and near infrared (>750 nm) regions, which are rapidly attenuated by seawater (Mobley, 1994).

The temporal resolution of satellite imagery and the lack of flexibility in image acquisition timing restrict the monitoring capabilities of satellite imagery for offshore aquaculture. Publicly available imagery (**Table 1**) are acquired on a 5 to 16 day repeat cycle regardless of cloud cover. Cloud cover in offshore areas of the Southern California Bight is considerably higher than coastal areas especially in the summer (**Figure 1**), a period when frequent monitoring may be vital to optimize production and harvest timing. However, by combining the imagery of multiple satellite systems there is an enhanced opportunity of a cloud-free view in any season (Li and Roy, 2017). Additionally, spatial resolution may also be problematic since pixel resolution is typically between 10 and 30 m (**Table 2**). Fine scale canopy features will likely be lost as the reflectance signal is averaged over larger areas, which may include floating farm structures (**Figures 4E–G**; Cui et al., 2019). Higher resolution satellite imagery (0.5–3 m) can be expensive to acquire, not publicly available, and/or not feasible for repeat imaging on the time scales necessary to deliver actionable information (Fan et al., 2018; Fu et al., 2019; Zhu et al., 2019). Despite the increased cloud cover in the offshore zone, moderate spatial resolution satellite sensors (daily repeat interval, more consistent coverage) could be used to monitor the farm environment (e.g., sea surface temperature). While these sensors cannot provide direct observations of the kelp canopy, valuable products such as seawater nitrate concentration can be empirically derived from satellite determinations of sea surface temperature (Kamykowski and Zentara, 1986; Snyder et al., 2020).

While there has been an increased use of sUAS for agricultural crop monitoring over the past decade (reviewed in Puri et al., 2017), their use in aquaculture has been rare (Reshma and Kumar, 2016). Despite their paucity of use, quality imagery of the kelp canopy can be acquired with a variety of sUAS mounted sensors, delivering maps of canopy area, canopy biomass, and physiological metrics such as tissue nitrogen content (**Figures 4A–D**). Commercially available color and multispectral sensors can rapidly capture imagery over ∼40 hectares in a single flight, and canopy area can be classified without the need for sophisticated analysis or expensive sensors (**Figure 4B**). The considerable differences in reflectance between seawater and the floating kelp canopy allows for a simple band ratio of the red and blue spectral bands to differentiate the classes. Furthermore, the high spatial resolution (∼5 cm) of this imagery can quantify sparse canopy which may be missed by the lower resolution imagery acquired by satellite sensors (**Figures 4E–G**). Hyperspectral sensors can provide the spectral data necessary to estimate the physiological and tissue content metrics of the kelp canopy through the quantification of photosynthetic pigment concentrations (**Figure 4D**; Bell et al., 2015; Adão et al., 2017). The chlorophyll *a* pigment absorbs blue and red wavelengths to drive the photosynthetic process, with absorption peaks at 430 nm and 662 nm. Giant kelp lacks the chlorophyll *b* pigment (absorption peaks at 453 and 642 nm) but possesses the chlorophyll *c* pigment (absorption peaks at 444 and 626 nm; Wheeler, 1980). The absence of the chlorophyll *b* pigment produces a peak in the kelp reflectance spectrum at ∼640 nm and provides a reference point to assess the relative spectral absorption associated with the chlorophyll *a* pigment at ∼670 nm (**Figure 2**). While the spectral information at 640 and 670 nm can be used to assess the concentration of the chlorophyll *a* pigment (Bell et al., 2015), the relationship between pigment concentration and tissue nitrogen content is also a function of the amount of sunlight reaching the surface canopy (**Figure 4**). Marine photosynthetic organisms optimize pigment concentrations in response to available light through photoacclimation, where increased solar irradiance lessens the need for high pigment concentrations to maximize

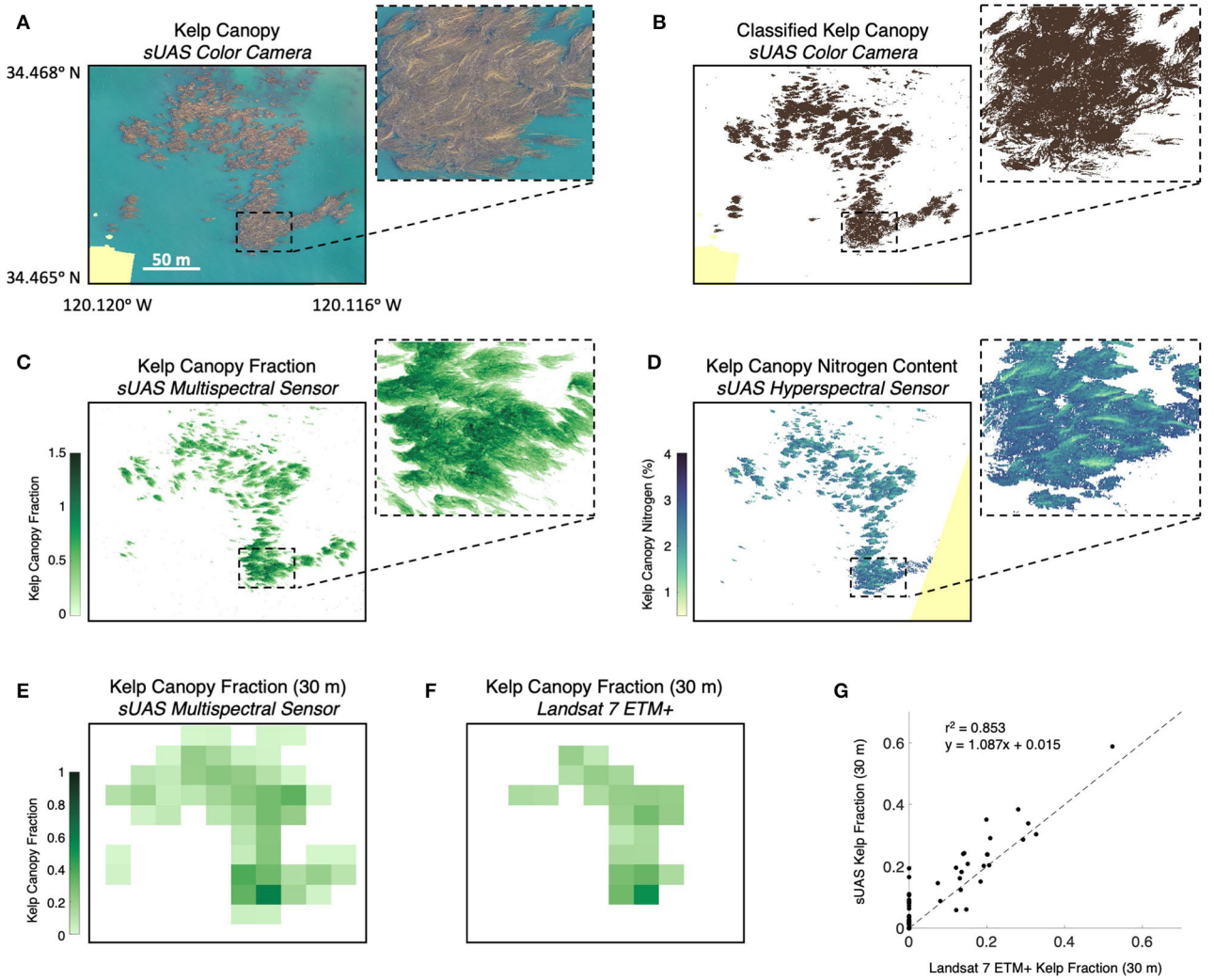

FIGURE 4 | (A) Color orthomosaic of the Arroyo Quemado kelp forest canopy using the color camera on the Phantom 4 Pro sUAS (pixel resolution of 3.2 cm). **(B)** Kelp canopy classified from the color orthomosaic. **(C)** Fraction of each pixel covered by kelp canopy determined using Multiple Endmember Spectral Mixture Analysis (MESMA) with imagery from the sUAS multispectral sensor (pixel resolution of 6.5 cm). **(D)** Kelp canopy nitrogen content determined using the nitrogen content spectral algorithm with imagery from the sUAS hyperspectral sensor (pixel resolution 25 cm). **(E)** The mean kelp canopy fraction from the multispectral sensor binned into 30 m pixels to compare with **(F)**. Kelp canopy fraction determined from the Landsat 7 ETM+ multispectral satellite sensor. **(G)** Comparison of the kelp canopy fraction from the multispectral sUAS sensor binned into 30 m pixels and the Landsat 7 ETM+ sensor. Pale yellow color shows areas not imaged by the sensor. All imagery acquired between 9:30 a.m. and 12 p.m. local time on June 30, 2019.

photosynthesis (Laws and Bannister, 1980). While an increase in photosynthetic pigment is positively associated with a higher tissue nitrogen content, this relationship is modulated by light (**Figure 3**), and these functions can be applied to spectral imagery to generate maps of tissue nitrogen content across large areas of kelp canopy (**Figure 4D**). Knowledge of the spatial patterns of physiological condition and tissue content metrics of the kelp canopy can be used to map farm production and time harvest to maximize desired biomass quality (i.e., nitrogen content). However, the sheer volume of data collected by hyperspectral sensors is immense, spectra are difficult to process, and pre-flight calibration procedures make these sensors challenging to use in an operational capacity. Research using hyperspectral imaging to identify the specific spectral bands necessary for the simultaneous estimation of valuable canopy traits (e.g., biomass, nitrogen/sugar content, age) could lead to user-friendly multispectral sensors with specific bands tailored for kelp canopy monitoring (**Figure 2**).

Remote Quantification of Subsurface Kelp Outplants

Since juvenile kelp stages are especially sensitive to changing environmental conditions, competition, and herbivory, it may be important to assess the state of kelp outplants prior to canopy development using subsurface sensors (Dean et al., 1984; Hernández-Carmona et al., 2001; Gorman and Connell, 2009).

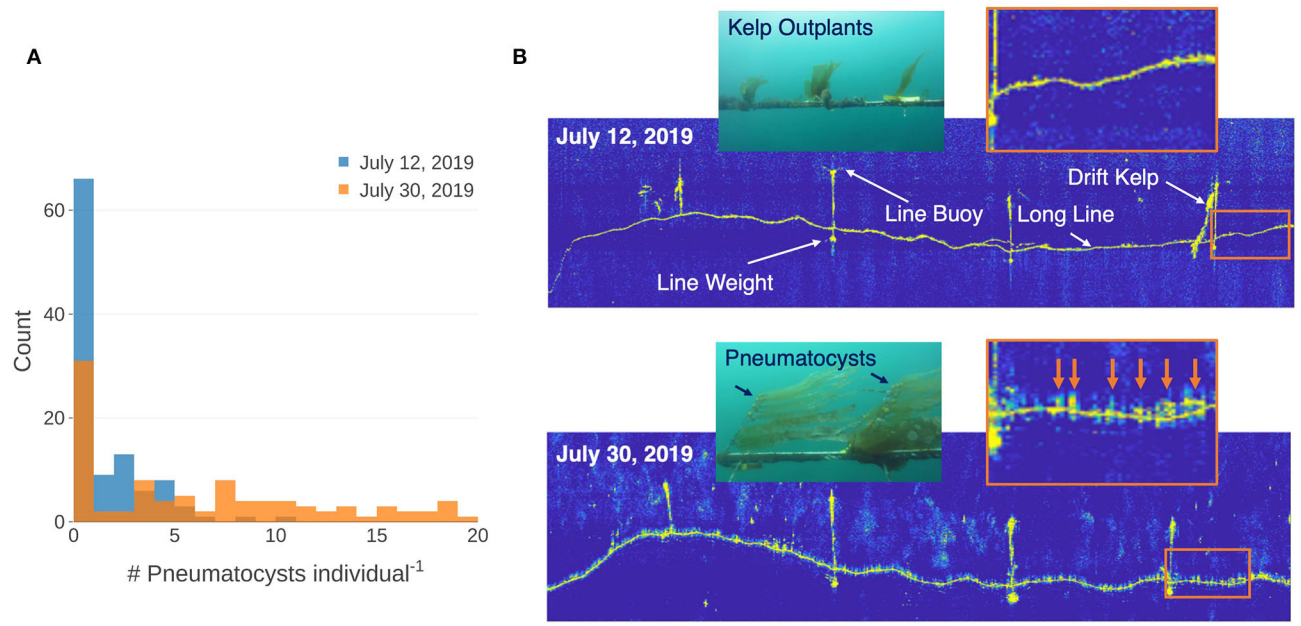

FIGURE 5 | (A) Histogram showing the number of pneumatocysts per individual determined from video captured by a remotely operated vehicle (ROV) on a section of each line at each date. **(B)** Side scan sonar imagery of the line on July 12 and July 30, 2019 showing farm structures and a drifting kelp frond caught on the farm buoy. Insets inside the orange boxes show enlarged areas of sonar returns along the farm lines between the two dates. Orange arrows show high acoustics returns at the locations of probable kelp outplants. Color images captured by the ROV showing typical size of individual kelp outplants for each date.

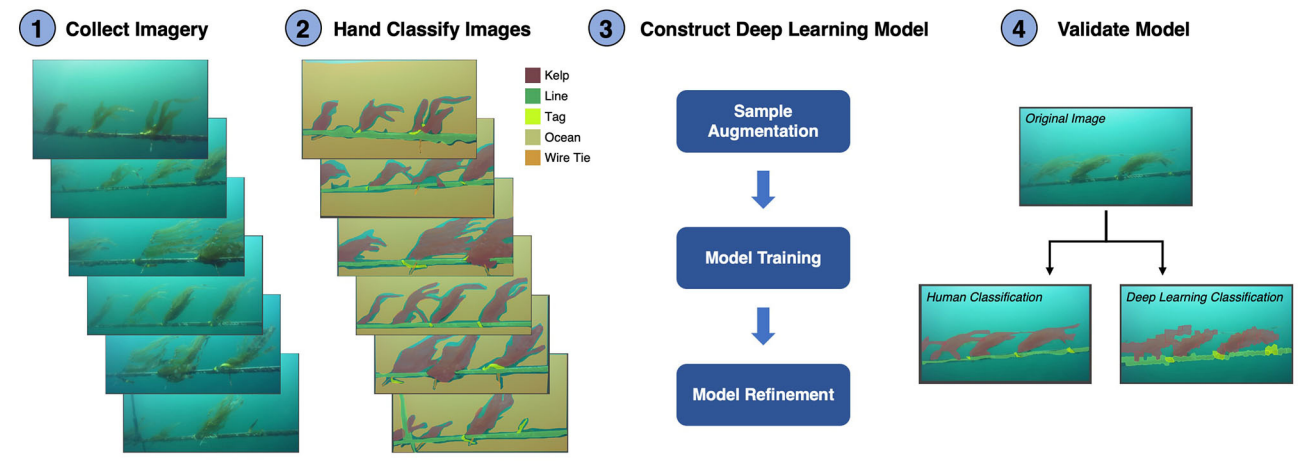

FIGURE 6 | Schematic showing the steps to develop and validate the deep learning model used to automatically classify giant kelp juveniles on an aquaculture farm. (1) Collect imagery of the farm lines using a color camera mounted on an underwater vehicle. (2) The images ($n = 137$) were classified by hand into five classes: Kelp, Line, Tag, Ocean, and Wire Tie. Light blue areas show sections of the background ocean which were not classified by hand. (3) The number of samples for model training was augmented by extracting multiple samples from inside the polygons of each class. The model was then trained using 60% of the images with a convolutional neural network and refined using 20% of the images. Model refinement involves identifying and removing poorly performing classes. (4) The final model was validated using the final 20% of the imagery by comparing hand classifications to the deep learning classifications.

The automated analysis of underwater color imagery using deep learning models could enable repeat monitoring of kelp juveniles on offshore farms. Machine learning based methods have already been successfully applied to underwater color imagery to classify fish species and quantify the biodiversity of marine sessile communities (Rahimi et al., 2014; Salman et al., 2016). In this study, a small set of underwater imagery collected by an inexpensive color camera mounted on an ROV was used to train a deep learning model and successfully classify kelp, tags, and longlines despite changes in kelp orientation due to water motion (**Figure 6**). These methods have advantages over spectral analyses as depth, bottom reflectance, and standoff distance of the sensor can significantly change the measured reflectance spectrum (Mobley, 1994). These tools should also be adaptable to other

kelp aquaculture monitoring tasks such as quantifying epibiont load or identifying the presence of herbivores. Capturing usable underwater color imagery requires clear water and sufficient solar illumination to produce satisfactory results. Fortunately, suspended particle concentrations are reduced in the offshore environments off the Southern California coast which should lead to greater opportunities for underwater image collection (Henderikx Freitas et al., 2017). Additionally, offshore farm structures can be equipped with inexpensive turbidity or light sensors in order to optimize the timing of image acquisition.

Acoustic measurements do not require light and are also less sensitive to water clarity than optical imaging and high-quality measurements can be acquired at any time of day and across a range of seawater conditions (Gonzalez-Socoloske et al., 2009). Side scan sonar is particularly useful to identify kelp outplants once the juveniles produce gas filled pneumatocysts, which lead to enhanced acoustic returns (**Figure 5**; Wilson, 2011). Since a pneumatocyst exists at the base of each giant kelp blade, there is a strong linear relationship between total gas volume and kelp biomass, such that acoustic imagery is ideal for monitoring the spatial arrangement and growth of subsurface stages of giant kelp on aquaculture farms (Wilson, 2011). Future development of these technologies also brings new opportunities, as many farmed kelp species never produce a floating canopy and require subsurface monitoring using acoustic sensors or color imaging (Fischell et al., 2019). These techniques could be deployed to survey numerous species and have potential for monitoring across aquaculture industries.

Operational Risks and Limitations

While the use of remote sensing platforms for offshore aquaculture monitoring reduces risks and costs related to *in situ* monitoring there are several limitations to these platforms that must be addressed before they are used in an operational context (**Table 3**). At the present time, monitoring with satellite platforms presents the fewest operational limitations. Sensor hardware failures are rare, though they may occasionally lead to missing data or failure of the sensor system (Markham et al., 2004; Chan et al., 2018). While the advent of freely available imagery has led to massive increases in both research and commercial remote sensing applications, there is no guarantee that these policies will exist in perpetuity (Zhu, 2019).

A major limiting factor for sUAS monitoring of offshore kelp aquaculture farms is the lack of available docking, charging, and data downlink infrastructure necessary for the autonomous and repeat deployment of these systems. However, there are several recent patents outlining the design of these systems, suggesting that such capabilities may be available in the near future (Garrec and Cornic, 2012; Yu et al., 2016; Gentry et al., 2018). While consumer grade sUAS equipped with color cameras are relatively inexpensive (<$1,500 USD), multispectral sensors can cost several thousand dollars. Processing of the individual images (e.g., orthorectification, mosaicking) is the responsibility of the user and precise georeferencing and radiometric calibration must be performed before mosaics and their derived products can be compared (Cruzan et al., 2016; Doughty and Cavanaugh, 2019). These tasks have been greatly simplified for users without image analysis training by several companies who offer cloud-based image processing through subscription services. Any autonomous vehicle carries a risk of loss associated with mechanical failure, GPS signal interference, and an inability to react to novel situations (Milanés et al., 2008). Additionally, while the U.S. Federal Aviation Administration adopted regulations allowing for extensive agricultural monitoring activities by sUAS in 2016, current regulations only allow for 'line of sight' operation where the pilot must maintain visual observation of the vehicle (Patel, 2016). Such rules will need to be adjusted for the sUAS monitoring of offshore aquaculture to become a reality.

While autonomous underwater vehicles are a promising monitoring platform for both acoustic and color imaging, there are both significant cost and operational risk barriers that must be crossed before these systems become viable monitoring options. Research-grade side scan sonar systems cost tens of thousands of dollars, although there has been recent success in monitoring submerged aquatic vegetation with less expensive consumer-grade systems (Greene et al., 2018). While the cost of autonomous underwater vehicles is currently prohibitive to most aquaculture operations, several small and low-cost vehicles are entering the market space and may revolutionize the collection of acoustic and color imagery in the coming years, and the development cost-effective infrastructure for docking, charging, and data downlink for these vehicles is an active area of research (Hobson et al., 2003; Pyle et al., 2012; Manley and Smith, 2017). Due to these high costs, the loss of underwater vehicles and their associated sensors a paramount concern. New statistical approaches to inform the probability of vehicle loss could be used to determine low risk conditions and provide adaptive mission management for these autonomous platforms (Brito and Griffiths, 2016).

Additionally, it is important to assess the risks these monitoring platforms and large-scale offshore aquaculture farms present to the environment. While sUAS carry limited risk to the environment outside of vehicle loss, their potential effects on the behavior of seabirds is an often-cited concern. Studies have found minimal negative effects of sUAS while censusing nesting colonies (Brisson-Curadeau et al., 2017) however aquaculture operations should be situated away from wildlife areas to avoid potential interactions. Below water, the acoustic imaging systems examined in this study (side scan sonar) generate high-frequency sound at the upper limit of the audible spectrum and are unlikely to cause a behavioral response from marine mammals (MacGillivray et al., 2013). Potential negative impacts of large-scale offshore aquaculture structures including wildlife interactions, shipping hazards, and the generation of marine debris are valid concerns and robust spatial planning should be prioritized to reduce conflicts and avoid environmental impacts (Gentry et al., 2017b; Lester et al., 2018).

CONCLUSIONS

This examination of remote sensing technologies guides the best uses of these platforms to deliver actionable products for offshore kelp aquaculture farms. Kelp outplant viability and growth are most readily assessed using underwater color imagery classified with deep learning models. This combination of inexpensive cameras and machine learning leads to the rapid

TABLE 3 | The advantages, disadvantages, risks, and future opportunities of various remote sensing technologies applicable to offshore kelp aquaculture farms.

Application	Tool	Advantages	Disadvantages	Risks	Future opportunities
Canopy	Satellite Imagery	- Extensive prior work - Free/publicly available - Cloud-based processing - Large areal coverage	- Spatial resolution (10's m) - Cloud cover - No flexibility in timing - Only canopy species	- Funding dependent - Sensor malfunction	- Higher spectral resolution - High spatial/temporal resolution constellations
	sUAS Imagery	- Flexibility on timing - Spatial resolution (cm's) - Farm scale (10's hectares) - Multiple sensors avail. - Consumer-grade inexpensive	- Depend on infrastructure - Only canopy species - Expensive sensors - Image processing	- Vehicle/sensor loss - Government regulation	- Vehicle improvements - Specific kelp aquaculture sensor development
Subsurface	Acoustic Imagery	- Monitoring of juvenile stages - Water clarity less important	- Expensive vehicles - Expensive sensors - Depend on infrastructure - Image processing	- Vehicle/sensor loss	- Potential for lower cost vehicles/sensors - Applications for multiple aquaculture sectors
	Deep Learning Classifications of Imagery	- Monitoring of juvenile stages - Tools are nascent - Customizable/multiple uses - Inexpensive sensors	- Water clarity important - Development of specific algorithm	- Vehicle/sensor loss	- Potential for lower cost vehicles - Stereo cameras - Applications for multiple aquaculture sectors

identification and sizing of small juvenile kelps, measuring survivorship and growth much earlier than other subsurface monitoring technologies. The use of deep learning models to detect kelp in color imagery could be enhanced by future research developing additional models that quantify the abundance of kelp herbivores and epibionts. Acoustic imaging from side scan sonar is most effective once pneumatocysts have developed and used to track the growth of subsurface kelp fronds that are too large to be imaged using color imagery (Wilson, 2011). While the monitoring of kelp farms with underwater side scan sonar and color imaging shows great promise, their implementation relies on the development of low-cost AUVs and docking infrastructure (Hobson et al., 2003; Pyle et al., 2012; Manley and Smith, 2017). Additional research using consumer-grade side scan sonar sensors to quantify subsurface kelp will also reduce costs (Greene et al., 2018). Due to high summertime cloud cover in offshore areas, satellite imagery is most useful for large-scale monitoring of the farm environment using daily, moderate spatial resolution estimates of sea surface temperature and derived products such as seawater nitrate concentration (Snyder et al., 2020). Due to the rapid growth, turnover, and senescence rates of giant kelp, observations of kelp canopy biomass quantity and condition, such as tissue nitrogen content, are most readily achieved using sUAS imagery (Clendenning, 1971; Rodriguez et al., 2013; Rassweiler et al., 2018). Improvements in sUAS infrastructure, multispectral sensors customized for estimating kelp canopy traits, and a relaxation of the 'line of sight' regulation for offshore areas will strengthen the role of kelp canopy monitoring by sUAS.

DATA AVAILABILITY STATEMENT

The datasets generated for this study are available on request to the corresponding author.

AUTHOR CONTRIBUTIONS

TB, RM, NNi, and DS conceived the study and wrote the manuscript. TB, JS, and MG processed satellite imagery for the cloud cover analysis. TB, JS, and CM collected and processed the sUAS imagery of kelp canopy. DS, TB, KyC, and KaC developed the color and multispectral sUAS algorithms. TB, JS, NNe, and DR collected the laboratory spectral measurements and performed the pigment and elemental analyses. TB, NNe, and MG developed the tissue nitrogen content spectral algorithm. NNi and CM collected and processed the underwater color and acoustic imagery of the kelp outplants. DF and CM developed the deep learning algorithms. DR, RM, and CY collected and processed the *in situ* data of the kelp outplants. All authors contributed to interpreting the results and revising the manuscript.

FUNDING

This was supported by the US Department of Energy's Advanced Research Projects Agency–Energy (ARPA-E; DE-AR0000922 and DE-AR0000914), the US National Science Foundation (OCE 1831937), and by the National Aeronautics and Space Administration (NNX14AR62A).

ACKNOWLEDGMENTS

We would like to thank all individuals involved with the UCSB/USC/UWM ARPA-E MARINER kelp genetics project who outplanted and maintained the kelp farm off the coast of Santa Barbara. We would also like to extend a sincere thanks to the many field technicians and student volunteers who conduct field and laboratory work for the Santa Barbara Coastal LTER. Special thanks go to guest editors Dr. Stephanie Palmer, Dr. Pierre Gernez, Dr. Rodney Forster, and Dr. Yoann Thomas.

SUPPLEMENTARY MATERIAL

The Supplementary Material for this article can be found online at: https://www.frontiersin.org/articles/10.3389/fmars.2020.520223/full#supplementary-material

REFERENCES

Ackleson, S. G., Smith, J. P., Rodriguez, L. M., Moses, W. J., and Russell, B. J. (2017). Autonomous coral reef survey in support of remote sensing. *Front. Mar. Sci.* 4:325. doi: 10.3389/fmars.2017.00325

Adão, T., Hruška, J., Pádua, L., Bessa, J., Peres, E., Morais, R., et al. (2017). Hyperspectral imaging: a review on uav-based sensors, data processing and applications for agriculture and forestry. *Remote Sens.* 9:1110. doi: 10.3390/rs9111110

Bell, T. W., Allen, J. G., Cavanaugh, K. C., and Siegel, D. A. (2020). Three decades of variability in California's giant kelp forests from the Landsat satellites. *Remote Sens. Environ.* 238:110811. doi: 10.1016/j.rse.2018.06.039

Bell, T. W., Cavanaugh, K. C., and Siegel, D. A. (2015). Remote monitoring of giant kelp biomass and physiological condition: an evaluation of the potential for the Hyperspectral Infrared Imager (HyspIRI) mission. *Remote Sens. Environ.* 167, 218–228. doi: 10.1016/j.rse.2015.05.003

Bell, T. W., Reed, D. C., Nelson, N. B., and Siegel, D. A. (2018). Regional patterns of physiological condition determine giant kelp net primary production dynamics. *Limnol. Oceanogr.* 63, 472–483. doi: 10.1002/lno.10753

Brisson-Curadeau, É., Bird, D., Burke, C., Fifield, D. A., Pace, P., Sherley, R. B., et al. (2017). Seabird species vary in behavioural response to drone census. *Sci. Rep.* 7:17884. doi: 10.1038/s41598-017-18202-3

Brito, M., and Griffiths, G. (2016). A Bayesian approach for predicting risk of autonomous underwater vehicle loss during their missions. *Reliab. Eng. Syst. Saf.* 146, 55–67. doi: 10.1016/j.ress.2015.10.004

Card, D. H., Peterson, D. L., Matson, P. A., and Aber, J. D. (1988). Prediction of leaf chemistry by the use of visible and near infrared reflectance spectroscopy. *Remote Sens. Environ.* 26, 123–147. doi: 10.1016/0034-4257(88)90092-2

Cavanaugh, K., Siegel, D., Kinlan, B., and Reed, D. (2010). Scaling giant kelp field measurements to regional scales using satellite observations. *Mar. Ecol. Prog. Ser.* 403, 13–27. doi: 10.3354/meps08467

Cavanaugh, K., Siegel, D., Reed, D., and Dennison, P. (2011). Environmental controls of giant kelp biomass in the Santa Barbara Channel, California. *Mar. Ecol. Prog. Ser.* 429, 1–17. doi: 10.3354/meps09141

Cavanaugh, K. C., Reed, D. C., Bell, T. W., Castorani, M. C. N., and Beas-Luna, R. (2019). Spatial variability in the resistance and resilience of giant kelp in southern and Baja California to a multiyear heatwave. *Front. Mar. Sci.* 6:413. doi: 10.3389/fmars.2019.00413

Chan, S. K., Bindlish, R., O'Neill, P., Jackson, T., Njoku, E., Dunbar, S., et al. (2018). Development and assessment of the SMAP enhanced passive soil moisture product. *Remote Sens. Environ.* 204, 931–941. doi: 10.1016/j.rse.2017.08.025

Clendenning, K. A. (1971). "Photosynthesis and general development," in The *Biology of Giant Kelp Beds (Macrocystis) in California. Beihefte Zur Nova Hedwigia. Lehre*, ed W. J. North (Coley: Verlag Von J. Cramer), 169–190.

Correa, T., Gutiérrez, A., Flores, R., Buschmann, A. H., Cornejo, P., and Bucarey, C. (2016). Production and economic assessment of giant kelp *Macrocystis pyrifera* cultivation for abalone feed in the south of Chile. *Aquac. Res.* 47, 698–707. doi: 10.1111/are.12529

Cruzan, M. B., Weinstein, B. G., Grasty, M. R., Kohrn, B. F., Hendrickson, E. C., Arredondo, T. M., et al. (2016). Small unmanned aerial vehicles (micro-uavs, drones) in plant ecology. *Appl. Plant Sci.* 4:1600041. doi: 10.3732/apps.1600041

Cui, B., Fei, D., Shao, G., Lu, Y., and Chu, J. (2019). Extracting raft aquaculture areas from remote sensing images via an improved U-Net with a PSE structure. *Remote Sens.* 11:2053. doi: 10.3390/rs11172053

Dean, T. A., Schroeter, S. C., and Dixon, J. D. (1984). Effects of grazing by two species of sea urchins (*Strongylocentrotus franciscanus* and *Lytechinus anamesus*) on recruitment and survival of two species of kelp (*Macrocystis pyrifera* and *Pterygophora californica*). *Mar. Biol.* 78, 301–313. doi: 10.1007/BF00393016

Doughty, C., and Cavanaugh, K. (2019). Mapping coastal wetland biomass from high resolution unmanned aerial vehicle (UAV) imagery. *Remote Sens.* 11:540. doi: 10.3390/rs11050540

Drusch, M., Del Bello, U., Carlier, S., Colin, O., Fernandez, V., Gascon, F., et al. (2012). Sentinel-2: ESA's Optical High-Resolution Mission for GMES Operational Services. *Remote Sens. Environ.* 120, 25–36. doi: 10.1016/j.rse.2011.11.026

Fan, J., Zhao, J., Song, D., Wang, X., Wang, X., and Su, X. (2018). Marine floating raft aquaculture dynamic monitoring based on multi-source GF Imagery. in *2018 7th International Conference on Agro-geoinformatics (Agro-geoinformatics)* (Hangzhou: IEEE), 1–4. doi: 10.1109/Agro-Geoinformatics.2018.8476085

Fedorov, D. V., Kvilekval, Kristian, G., Doheny, B., Sampson, S., Miller, R. J., and Manjunath, B. S. (2017). *Deep Learning for All: Managing and Analyzing Underwater and Remote Sensing Imagery on the Web Using BisQue*. UC Santa Barbara. Retrieved from: https://escholarship.org/uc/item/9z73t7hv (accessed November 29, 2020).

Fischell, E. M., Gomez-ibanez, D., Lavery, A., Stanton, T., and Kukulya, A. (2019). "Autonomous underwater vehicle perception of infrastructure and growth for aquaculture," in *IEEE ICRA Workshop, Underwater Robotic Perception 2019* (Montreal, QC), 1–7

Fu, Y., Ye, Z., Deng, J., Zheng, X., Huang, Y., Yang, W., et al. (2019). Finer resolution mapping of marine aquaculture areas using worldview-2 imagery and a hierarchical cascade convolutional neural network. *Remote Sens.* 11:1678. doi: 10.3390/rs11141678

Garrec, P., and Cornic, P. (2012). *Autonomous and Automatic Landing System for Drones*. U.S. Patent No. 8,265,808 B2. Washington, DC: U.S. Patent and Trademark Office.

Gates, D. M., Keegan, H. J., Schleter, J. C., and Weidner, V. R. (1965). Spectral properties of plants. *Appl. Opt.* 4:11. doi: 10.1364/AO.4.000011

Gausman, H. W. (1983). Visible light reflectance, transmittance, and absorptance of differently pigmented cotton leaves. *Remote Sens. Environ.* 13, 233–238. doi: 10.1016/0034-4257(83)90041-X

Gentry, N., Hsieh, R., and Nguyen, L. (2018). *Multi-Use UAV Docking Station Systems and Methods*. U.S. Patent No. 9,387,928 B1. Washington, DC: U.S. Patent and Trademark Office.

Gentry, R. R., Froehlich, H. E., Grimm, D., Kareiva, P., Parke, M., Rust, M., et al. (2017a). Mapping the global potential for marine aquaculture. *Nat. Ecol. Evol.* 1, 1317–1324. doi: 10.1038/s41559-017-0257-9

Gentry, R. R., Lester, S. E., Kappel, C. V., White, C., Bell, T. W., Stevens, J., et al. (2017b). Offshore aquaculture: spatial planning principles for sustainable development. *Ecol. Evol.* 7:2637. doi: 10.1002/ece3.2637

Gonzalez-Socoloske, D., Olivera-Gomez, L. D., and Ford, R. E. (2009). Detection of free-ranging West Indian manatees *Trichechus manatus* using side-scan sonar. *Endanger. Species Res.* 8, 249–257. doi: 10.3354/esr00232

Gorelick, N., Hancher, M., Dixon, M., Ilyushchenko, S., Thau, D., and Moore, R. (2017). Google earth engine: planetary-scale geospatial analysis for everyone. *Remote Sens. Environ.* 202, 18–27. doi: 10.1016/j.rse.2017.06.031

Gorman, D., and Connell, S. D. (2009). Recovering subtidal forests in human-dominated landscapes. *J. Appl. Ecol.* 46, 1258–1265. doi: 10.1111/j.1365-2664.2009.01711.x

Graham, M. H., Vasquez, J. A., and Buschmann, A. H. (2007). Global ecology of the giant kelp *Macrocystis*: from ecotypes to ecosystems. *Oceanogr. Mar. Biol. An Annu. Rev.* 45, 39–88. doi: 10.1201/9781420050943.ch2

Greene, A., Rahman, A. F., Kline, R., and Rahman, M. S. (2018). Side scan sonar: A cost-efficient alternative method for measuring seagrass cover in shallow environments. *Estuar. Coast. Shelf Sci.* 207, 250–258. doi: 10.1016/j.ecss.2018.04.017

Gutierrez, A., Correa, T., Muñoz, V., Santibañez, A., Marcos, R., Cáceres, C., et al. (2006). Farming of the giant kelp *Macrocystis pyrifera* in southern chile for development of novel food products. *J. Appl. Phycol.* 18, 259–267. doi: 10.1007/s10811-006-9025-y

Hamilton, S. L., Bell, T. W., Watson, J. R., Grorud-Colvert, K. A., and Menge, B. A. (2020). Remote sensing: generation of long-term kelp bed data sets for evaluation of impacts of climatic variation. *Ecology* 101:e03031. doi: 10.1002/ecy.3031

Hardin, P. J., Lulla, V., Jensen, R. R., and Jensen, J. R. (2019). Small Unmanned Aerial Systems (sUAS) for environmental remote sensing: challenges and opportunities revisited. *GIScience Remote Sens.* 56, 309–322. doi: 10.1080/15481603.2018.1510088

Henderikx Freitas, F., Siegel, D. A., Maritorena, S., and Fields, E. (2017). Satellite assessment of particulate matter and phytoplankton variations in the Santa Barbara Channel and its surrounding waters: role of surface waves. *J. Geophys. Res. Ocean.* 122, 355–371. doi: 10.1002/2016JC012152

Hernández-Carmona, G., Robledo, D., and Serviere-Zaragoza, E. (2001). Effect of nutrient availability on *Macrocystis pyrifera* recruitment and survival near its southern limit off Baja California. *Bot. Mar.* 44, 221–229. doi: 10.1515/BOT.2001.029

Hobson, B., Schulz, B., Pinnix, H., and Moody, R. (2003). *Low-Cost UUVs for Task Specific and Expendable Missions.* Technol. [C/CD], 2–5. Available online at: https://www.researchgate.net/publication/228902666_Low-cost_UUVs_for_task_specific_and_expendable_missions (accessed November 29, 2020).

Hochberg, E. J., Atkinson, M. J., Apprill, A., and Andréfouët, S., (2004). Spectral reflectance of coral. *Coral Reefs* 23, 84–95. doi: 10.1007/s00338-003-0350-1

Kamykowski, D., and Zentara, S.-J. (1986). Predicting plant nutrient concentrations from temperature and sigma-t in the upper kilometer of the world ocean. *Deep Sea Res. Part A Oceanogr. Res. Pap.* 33, 89–105. doi: 10.1016/0198-0149(86)90109-3

Laws, E., and Bannister, T. (1980). Nutrient and light-limited growth of Thalassiosira fluviatilis in continuous culture, with implications for phytoplankton growth in the ocean. *Limnol. Oceanogr.* 25, 457–473. doi: 10.4319/lo.1980.25.3.0457

Lee, C. M., Cable, M. L., Hook, S. J., Green, R. O., Ustin, S. L., Mandl, D. J., et al. (2015). An introduction to the NASA hyperspectral InfraRed imager (HyspIRI) mission and preparatory activities. *Remote Sens. Environ.* 167, 6–19. doi: 10.1016/j.rse.2015.06.012

Lester, S. E., Stevens, J. M., Gentry, R. R., Kappel, C. V., Bell, T. W., Costello, C. J., et al. (2018). Marine spatial planning makes room for offshore aquaculture in crowded coastal waters. *Nat. Commun.* 9:945. doi: 10.1038/s41467-018-03249-1

Li, J., and Roy, D. P. (2017). A global analysis of sentinel-2A, sentinel-2B and landsat-8 data revisit intervals and implications for terrestrial monitoring. *Remote Sens.* 9:902. doi: 10.3390/rs9090902

Lovatelli, A., Aguilar-Manjarrez, J., and Soto, D. (2013). *Expanding mariculture farther offshore: Technical, environmental, spatial and governance challenges.* FAO Technical Workshop (p. 73). Orbetello: FAO Fisheries and Aquaculture Department.

Lund-Hansen, L. C., Juul, T., Eskildsen, T. D., Hawes, I., Sorrell, B., Melvad, C., et al. (2018). A low-cost remotely operated vehicle (ROV) with an optical positioning system for under-ice measurements and sampling. *Cold Reg. Sci. Technol.* 151, 148–155. doi: 10.1016/j.coldregions.2018.03.017

MacGillivray, A. O., Racca, R., and Li, Z. (2013). Marine mammal audibility of selected shallow-water survey sources. *J. Acoust. Soc. Am.* 135, EL35–EL40. doi: 10.1121/1.4838296

Manley, J. E., and Smith, J. (2017). *Rapid Development and Evolution of a Micro-UUV. Ocean. 2017* – Anchorage.

Markham, B., Barsi, J., Montanaro, M., McCorkel, J., Gerace, A., Pedelty, J., et al. (2018). "Landsat-8 on-orbit and Landsat-9 pre-launch sensor radiometric characterization," in *Proc. SPIE 10781, Earth Observing Missions and Sensors: Development, Implementation, and Characterization*, Vol. 1078104. doi: 10.1117/12.2324715

Markham, B. L., Storey, J. C., Williams, D. L., and Irons, J. R. (2004). Landsat sensor performance: history and current status. *IEEE Trans. Geosci. Remote Sens.* 42, 2691–2694. doi: 10.1109/TGRS.2004.840720

Milanés, V., Naranjo, J. E., González, C., Alonso, J., and De Pedro, T. (2008). Autonomous vehicle based in cooperative GPS and inertial systems. *Robotica* 26, 627–633. doi: 10.1017/S0263574708004232

Mobley, C. D. (1994). *Light and Water: Radiative Transfer in Natural Waters*. New York, NY: Academic Press.

National Academies of Sciences, Engineering, and Medicine (2018). *Thriving on Our Changing Planet: A Decadal Strategy for Earth Observation from Space*. Washington, DC: The National Academies Press.

Neushul, M. (1987). "Energy from marine biomass: the historical record," *in Seaweed Cultivation for Renewable Resources, eds* K. T. Bird and *P. H. Benson (Amsterdam:* Elsevier Science Publishers*)*, 1–37.

Parnell, P. E. (2015). The effects of seascape pattern on algal patch structure, sea urchin barrens, and ecological processes. *J. Exp. Mar. Biol. Ecol.* 465, 64–76. doi: 10.1016/j.jembe.2015.01.010

Patel, P. (2016). Agriculture drones are finally cleared for takeoff [News]. *IEEE Spectr.* 53, 13–14. doi: 10.1109/MSPEC.2016.7607013

Puri, V., Nayyar, A., and Raja, L. (2017). Agriculture drones: a modern breakthrough in precision agriculture. *J. Stat. Manag. Syst.* 20, 507–518. doi: 10.1080/09720510.2017.1395171

Pyle, D., Granger, R., Geoghegan, B., Lindman, R., and Smith, J. (2012). "Leveraging a large UUV platform with a docking station to enable forward basing and persistence for light weight AUVs," in *OCEANS 2012 MTS/IEEE: Harnessing the Power of the Ocean* (Hampton Roads, VA: IEEE), 1–8. doi: 10.1109/OCEANS.2012.6404932

Rahimi, A. M., Miller, R. J., Fedorov, D. V., Sunderrajan, S., Doheny, B. M., Page, H. M., et al. (2014). "Marine biodiversity classification using dropout regularization," *in Proceedings - 2014 ICPR Workshop on Computer Vision for Analysis of Underwater Imagery, CVAUI 2014* (Stockholm), 80–87. doi: 10.1109/CVAUI.2014.17

Rassweiler, A., Reed, D. C., Harrer, S. L., and Nelson, J. C. (2018). Improved estimates of net primary production, growth, and standing crop of *Macrocystis pyrifera* in Southern California. *Ecology* 99, 2132–2132. doi: 10.1002/ecy.2440

Reed, D. C., Rassweiler, A., and Arkema, K. K. (2008). Biomass rather than growth rate determines variation in net primary production by giant kelp. *Ecology* 89, 2493–2505. doi: 10.1890/07-1106.1

Reshma, B., and Kumar, S. S. (2016). "Precision aquaculture drone algorithm for delivery in sea cages," *Proc. 2nd IEEE Int. Conf. Eng. Technol. ICETECH 2016* (Coimbatore), 1264–1270. doi: 10.1109/ICETECH.2016.7569455

Roberts, D., Gardner, M., Church, R., Ustin, S., Scheer, G., and Green, R. O. (1998). Mapping chaparral in the Santa Monica Mountains using multiple endmember spectral mixture models. *Remote Sens. Environ.* 65, 267–279. doi: 10.1016/S0034-4257(98)00037-6

Rodriguez, G., Rassweiler, A., Reed, D., and Holbrook, S. (2013). The importance of progressive senescence in the biomass dynamics of giant kelp (*Macrocystis pyrifera*). *Ecology* 94, 1848–1858. doi: 10.1890/12-1340.1

Rodriguez, G. E., Reed, D. C., and Holbrook, S. J. (2016). Blade life span, structural investment, and nutrient allocation in giant kelp. *Oecologia* 182, 397–404. doi: 10.1007/s00442-016-3674-6

Salman, A., Jalal, A., Shafait, F., Mian, A., Shortis, M., Seager, J., et al. (2016). Fish species classification in unconstrained underwater environments based on deep learning. *Limnol. Oceanogr. Methods* 14, 570–585. doi: 10.1002/lom3.10113

Savitsky, A., and Golay, M. J. E. (1964). Smoothing and differentiation of data by simplified least squares procedures. *Anal. Chem.* 36, 1627–1639. doi: 10.1021/ac60214a047

Shainee, M., Haskins, C., Ellingsen, H., and Leira, B. J. (2012). Designing offshore fish cages using systems engineering principles. *Syst. Eng.* 15, 396–406. doi: 10.1002/sys.21200

Snyder, J. N., Bell, T. W., Siegel, D. A., Nidzieko, N. J., and Cavanaugh, K. C. (2020). Sea surface temperature imagery elucidates spatiotemporal nutrient patterns and serves as a tool for offshore aquaculture siting in the Southern California Bight. *Front. Marine Sci.* 7, 1–14. doi: 10.3389/fmars.2020.00022

Wargacki, A. J., Leonard, E., Win, M. N., Regitsky, D. D., Santos, C. N. S., Kim, P. B., et al. (2012). An engineered microbial platform for direct biofuel production from brown macroalgae. *Science* 335, 308–313. doi: 10.1126/science.1214547

Wheeler, W. N. (1980). Pigment content and photosynthetic rate of the fronds of macrocystis pyrifera. *Mar. Biol.* 56, 97–102. doi: 10.1007/BF00397127

Wilson, C. J. (2011). *The acoustic ecology of submerged macrophytes* (Ph.D. dissertation), Department of Marine Science. University of Texas at Austin. Available online at: https://repositories.lib.utexas.edu/handle/2152/ETD-UT-2011-12-4742 (accessed November 29, 2020).

Wood, S. N. (2017). *Generalized Additive Models: An Introduction with R, 2nd Edn.* New York, NY: Chapman and Hall/CRC.

Woodcock, C. E., Allen, R., Anderson, M., Belward, A., Bindschadler, R., Cohen, W., et al. (2008). Free access to landsat imagery. *Science* 320:1011. doi: 10.1126/science.320.5879.1011a

Woolley, J. T. (1971). Reflectance and transmittance of light by leaves. *Plant Physiol.* 47, 656–662. doi: 10.1104/pp.47.5.656

Yu, Y., Lee, S., Lee, J., Cho, K., and Park, S. (2016). Design and implementation of wired drone docking system for cost-effective security system in IoT environment. *2016 IEEE Int. Conf. Consum. Electron. ICCE 2016* (Las Vegas, NV), 369–370. doi: 10.1109/ICCE.2016.7430651

Zabloudil, K. F., Reitzel, S., Schroeter, S. C., Dixon, D., Dean, T. A., and Norall, T. L. (1991). "Sonar mapping of giant kelp density and distribution, coastal zone '91," in *Proc., 7th Symp. on Coast. and Dc. Mgmt., ASCE* (New York, NY).

Zhang, C., and Kovacs, J. M. (2012). The application of small unmanned aerial systems for precision agriculture: a review. *Precis. Agric.* 13, 693–712. doi: 10.1007/s11119-012-9274-5

Zhu, H., Li, K., Wang, L., Chu, J., Gao, N., and Chen, Y. (2019). spectral characteristic analysis and remote sensing classification of coastal aquaculture areas based on GF-1 data. *J. Coast. Res.* 90:49. doi: 10.2112/SI90-007.1

Zhu, Z. (2019). Science of landsat analysis ready data. *Remote Sens.* 11:2166. doi: 10.3390/rs11182166

Conflict of Interest: DF was employed by the company ViQi, Inc.

The remaining authors declare that the research was conducted in the absence of any commercial or financial relationships that could be construed as a potential conflict of interest.

Advantages of publishing in Frontiers

OPEN ACCESS
Articles are free to read for greatest visibility and readership

FAST PUBLICATION
Around 90 days from submission to decision

HIGH QUALITY PEER-REVIEW
Rigorous, collaborative, and constructive peer-review

TRANSPARENT PEER-REVIEW
Editors and reviewers acknowledged by name on published articles

Frontiers
Avenue du Tribunal-Fédéral 34
1005 Lausanne | Switzerland

Visit us: www.frontiersin.org
Contact us: frontiersin.org/about/contact

REPRODUCIBILITY OF RESEARCH
Support open data and methods to enhance research reproducibility

DIGITAL PUBLISHING
Articles designed for optimal readership across devices

FOLLOW US
@frontiersin

IMPACT METRICS
Advanced article metrics track visibility across digital media

EXTENSIVE PROMOTION
Marketing and promotion of impactful research

LOOP RESEARCH NETWORK
Our network increases your article's readership